UHE Neutrino Detection using the Lunar Čerenkov Technique

Rebecca Angela McFadden

Submitted in total fulfilment of the requirements
of the degree of Doctor of Philosophy

School of Physics
University of Melbourne

September, 2009

Abstract

This thesis investigates Ultra High Energy (UHE) neutrino detection using the lunar Čerenkov technique. UHE neutrinos may hold the key to understanding the origin of the most energetic particles observed in nature, the UHE Cosmic Rays (CR). UHECR traveling over distances larger than ∼80 Mpc will lose energy to photo-pion production, causing a suppression of the cosmic ray spectrum at the highest energies. However, significant information is preserved in the spectrum of neutrinos produced as a result of these interactions and UHE neutrino astronomy may therefore be able to provide more insight into the origin of the UHECR.

Direct detection of UHE neutrinos is very difficult due to their extremely small interaction cross-sections. Instead, they may be detected indirectly via observation of the Askaryan effect (1) in the lunar regolith. Using the Moon as a large volume neutrino detector, coherent radio Čerenkov emission from neutrino-induced cascades in the lunar regolith can be observed with ground-based telescopes. This thesis explores detection issues associated with using this technique including an investigation into alternative planetary detectors, the phenomenology of the radio Čerenkov emission and the effect of ionospheric dispersion on Čerenkov pulse propagation.

The results of this investigation were used to design a detector system for a series of experiments performed at the Australia Telescope Compact Array. The experiments made use of a 600-MHz RF signal available at the ATCA which required the development of custom-designed ionospheric dedispersion and pulse detection hardware. Approximately 36.5 hours of lunar data were taken over three observations. Earlier runs were scheduled to target a broad region surrounding the galactic centre, which was chosen as it harbors the closest super massive black hole and potential accelerator of UHECR. Scheduling of the final ATCA experiment in May 2008 was influenced by results published by the Pierre Auger Observatory in late 2007, which showed a statistical correlation between observations of the highest energy CR and the matter distribution in the local universe as represented by nearby active galactic nuclei (2). These experiments offered an increase in exposure to the regions of Sagittarius A* and Centaurus A. However, analysis of the data revealed that most of the candidate events could be attributed to terrestrial RFI and no candidates events were suspected as potential lunar Čerenkov pulses.

A new method to calibrate the dispersive effect of the ionosphere on lunar Čerenkov pulses is also presented. This method exploits radial symmetries of the lunar polarisation distribution to make Faraday rotation measurements in the visibility domain of synthesis array data. The Faraday rotation measurements are combined with geomagnetic field models to estimate the ionospheric Total Electron Content (TEC). An accurate knowledge of the ionospheric TEC can be used to perform pulse dedispersion and recover maximum Čerenkov pulse amplitude before detection. This method of ionospheric calibration is particularly attractive for the lunar Čerenkov technique as it can be used in real time to give values of the ionospheric TEC which are line-of-sight to the Moon.

Declaration

The declaration.

This is to certify that:

- This thesis entitled “UHE Neutrino Detection using the Lunar Čerenkov Technique” comprises only my original work, except where indicated in the preface.
- Due acknowledgement has been made in the text to all other material used.
- The thesis is less than 100,000 words in length, exclusive of tables, maps, bibliographies and appendices.

. . . .

Rebecca Angela McFadden

Preface

While the work presented herein is essentially my own, there is some that is the result of collaborative work, or the result of the work of others. Any such data used are acknowledged in the text, and other specific details are listed here:

- Chapter 3 makes extensive use of ionospheric data products from the International Global Navigation Satellite System Service. Ionospheric TEC maps, derived from dual frequency GPS data, are available online from NASA's Crustal Dynamics Data Information System (at http://cddisa.gsfc.nasa.gov/gnss_datasum.html).

- Chapter 4 describes a series of UHE neutrino detection experiments performed at the ATCA. These experiments were designed and executed by the LUNASKA collaboration; R. Ekers, R. Protheroe, J. Alvarez-Muñiz, C. James, R. McFadden, C. Phillips, S. Tingay, R. Bhat and J. Bray. In particular, the pulse detection hardware was designed by P. Roberts, the software interface between this hardware and the control room was implemented by C. Phillips and the data analysis (summarised in Section 4.6) was performed by C. James. These experiments are described in a number of papers by the LUNASKA collaboration (For *e. g.* (3), (4)).

- The *Miriad* software package (see Ref. (5)) was used for data reduction in Chapter 5 and to develop a model of the Moon's polarised emission in Chapter 6.

- The angular spatial filtering technique, described in Chapter 6, was developed in collaboration with R. Sault and R. Ekers. Publications of this result are in preparation.

- This work was not possible without the radio telescope facilities of the Compact Array in Narrabri. The Compact Array is part of the Australia Telescope which is funded by the Commonwealth of Australia for operation as a national facility managed by the CSIRO.

Acknowledgements

This thesis would not have been possible without the support and guidance that I received from a number of people during my candidature.

Most of all I would like to thank my supervisor Professor Ron Ekers. I feel very privileged to have been part of such an exciting and ambitious project and for all of the support, advice and wonderful opportunities which you have afforded me.

I would also like to thank the rest of our team, Clancy James, Paul Roberts, Dr Chris Phillips, Professor Jaime Alvarez-Muñiz, Professor Ray Protheroe, Justin Bray, Professor Steven Tingay and Dr Ramesh Bhat. I would particularly like to thank Paul for his patience and understanding while explaining new hardware concepts to me (and while I blew up capacitors!) and I would also like to thank Jaime for his helpful discussions on the phenomenology of neutrino-induced particle showers ... and frogs – it is surprising how often those two topics overlap! I am very fortunate to have had the opportunity to work with, and learn from, a team of such diverse expertise, but mostly I would like to thank everyone for making these past four years so enjoyable.

Thank you to Professor Bob Sault for helping me with my lunar polarimetry work. Your expertise and advice were invaluable in helping me to demonstrate a new technique for ionospheric calibration. I am also very grateful to Professor Geoff Taylor, for guidance and supervision during the final stages to my PhD. I must also thank the head of the University of Melbourne Astrophysics Group, Professor Rachel Webster, and the Faculty of Science for providing me with a scholarship during my candidature.

Many thanks go to the friendly staff at the ATCA in Narrabri. A big thank you to the Officer In Charge, Dr Phil Edwards, for always accomodating our many scheduling constraints and for making the resources available for us to coordinate

an experiment of this magnitude. Thank you also to all of the engineers who were always happy to assist us with our enquiries and the logsitics of our experiment.

I would like to thank the students of the University of Melbourne Astrophysics Group. Especially Jhan Srbinovsky, Matthias Vigelius, Alpha Mastrano, Christine Chung and Sal Langford, your support and friendship have been invaluable to me during my PhD. Thank you also to Paul Geil for making the Narrabri Synthesis School even more enjoyable and for helping me to better understand interferometry.

Finally, thank you to my loving husband, Marty, for all of your support and advice during my PhD and for helping me to chase this dream. Thank you also to my cat Jasmin who, after ten wonderful years of companionship and four years sitting diligently beside me as I worked on my thesis, sadly is no longer here to see me submit. I am forever grateful and hope that you may now get to play among the stars.

Contents

List of Figures

CHAPTER 1

Overview

The emerging field of Ultra High Energy (UHE) neutrino astronomy promises to provide an exceptional probe for distant astronomical sources. Neutrinos make ideal messengers since they have extremely small interaction cross-sections and any neutrino flux will be almost unattenuated over cosmological distances. As neutral particles they are also unperturbed by cosmic magnetic fields so their direction of arrival will reveal information about their origin. UHE neutrino production scenarios include acceleration in astrophysical plasmas, which occurs when large scale macroscopic motions (shocks and turbulence flows) are transferred to individual particles such as in Gamma Ray Bursts (GRB) and Active Galactic Nuclei (AGN), or 'top-down' scenarios including topological defects and the decay of super-massive dark matter particles (21). UHE neutrinos are also inextricably linked to the origin of UHE Cosmic Rays (UHECR) through cosmogenic neutrinos which are produced during cosmic ray interactions with photons of the Cosmic Microwave Background (CMB).

1.1 The Relationship between UHE Neutrinos and Cosmic Rays

The origin of UHECR is of great importance to our understanding of the Universe as it impacts on our knowledge of dark matter, gravity and high energy particle interactions (22). The energy spectrum of cosmic rays extends from below 1 GeV up to at least 10^{11} GeV and essentially follows a power law with small breaks known as the *knee* and the *ankle* (see Figure 1.1 and Ref. (6)). At lower energies (10^{7}–10^{10}

eV), events have been attributed to energetic processes in the sun, such as solar flares, coronal mass ejections and shocks in the interplanetary medium. Above this range and to at least 10^{15} eV (roughly the *knee* of the spectrum), events have been attributed to particles being accelerated in the shock fronts of supernova remnants. However, the origin of the highest energy cosmic rays (above $\sim 10^{18}$ eV or the *ankle* of the spectrum) has remained a mystery.

In the rest frame of an UHE cosmic ray proton, the 2.73 K CMB photons are strongly blue-shifted to gamma ray energies and the threshold for Bethe-Heitler pair production and pion photoproduction is reached. UHECR traveling over distances larger than $\sim$80 Mpc therefore lose energy to photo-pion production which leads to a suppression of the cosmic ray spectrum in this regime. This suppression has been confirmed by UHECR observations at the Pierre Auger Observatory (23). The importance of this effect was first noted by Greisen (24) and Zatsepin & Kuzmin (25) and the cut-off they predicted is referred to as the 'GZK cut-off'.

The origin of UHECR is not fully understood. Our local magnetic field is not strong enough to contain the gyromagnetic radius of such accelerated particles and until recently there had been no extragalactic UHECR sources identified within the GZK horizon. However, recent results from the Pierre Auger Observatory (2) show a statistical correlation with the matter distribution in the local Universe as represented by nearby active galactic nuclei (see Figure 1.2). The onset of this anisotropic sky is observed at essentially the same energy as the suppression of the cosmic ray spectrum. These two observations may provide valuable clues to identifying potential UHECR sources within the GZK horizon. However, for extragalactic UHECR originating beyond this horizon, almost all spectral information above the GZK cut-off is lost due to pion photoproduction interactions during propagation. Significant information is preserved in the spectrum of cosmogenic neutrinos as these unstable pions decay (26) and therefore UHE neutrino astronomy will be able to provide more insight into the origin of the UHECR with the possibility of new physics at energies inaccessible to terrestrial particle accelerators.

1.2 UHE Cosmic Ray and Neutrino Detection Experiments

UHECR events have been observed by the Akeno Giant Air Shower Array (AGASA) (27) and the High Resolution Fly's Eye experiment (28) (29) since 1984. These early observations provided conflicting evidence for the suppression of UHECR above the GZK cut-off (30). Then in 2007, this effect was confirmed by the Auger collaboration with UHECR observations which which showed a suppression at the highest energies.

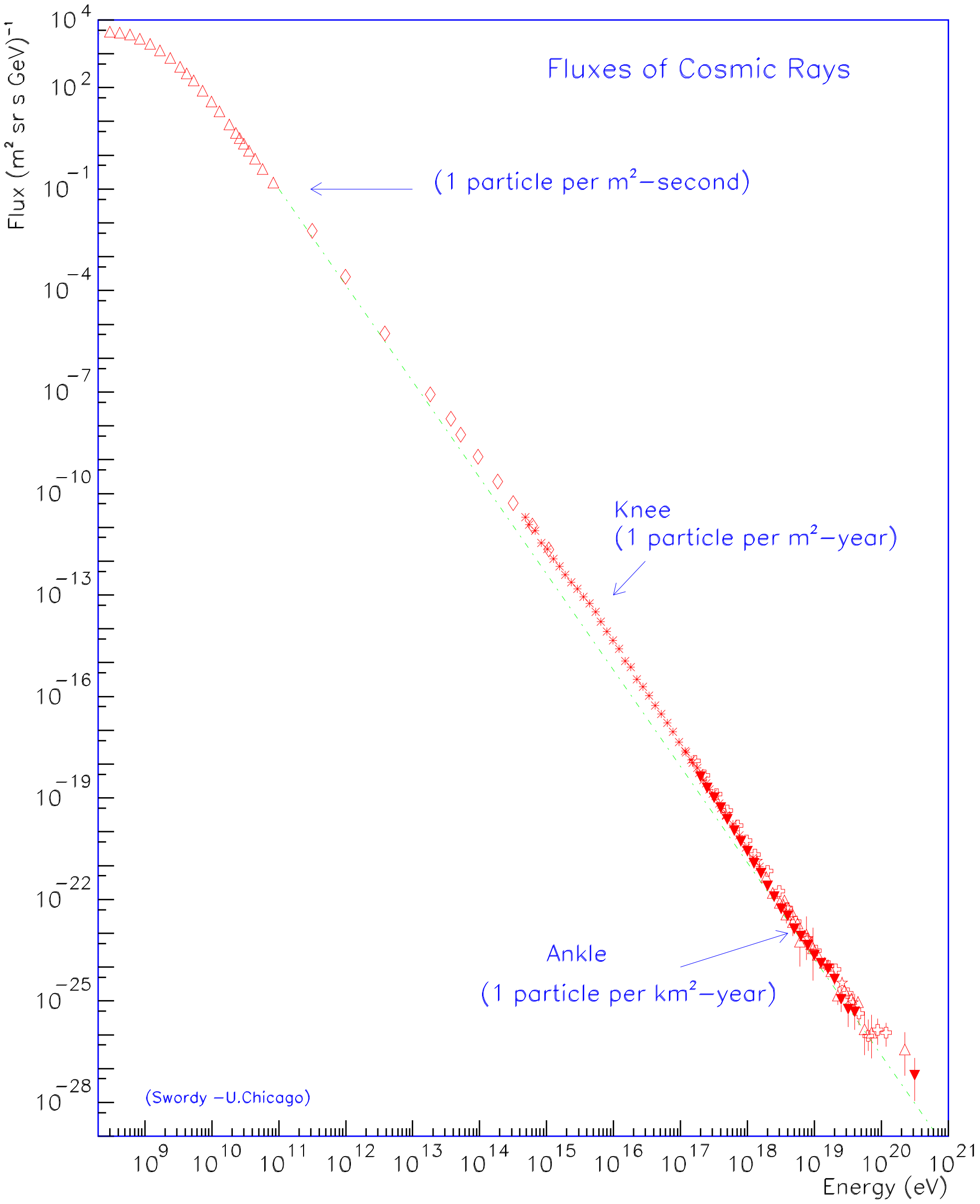

Figure 1.1: Cosmic Ray Spectrum. (6)

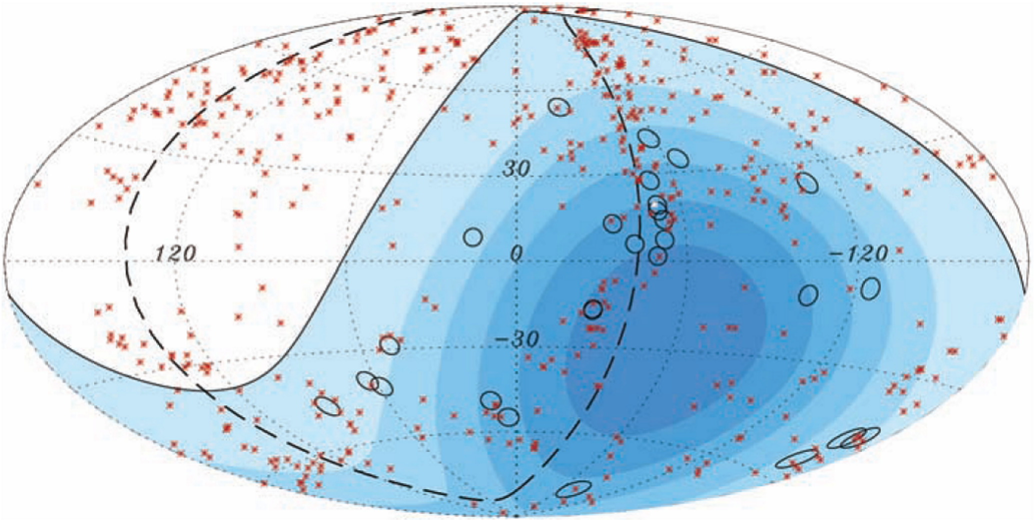

Figure 1.2: An Aitoff projection of the celestial sphere in galactic coordinates which shows the arrival directions of the 27 highest energy cosmic rays detected by Auger. The energies are greater than 57×10^{18} eV (57 EeV). These are shown as circles of radius 3.1°. The positions of 472 AGN within 75 Mpc are shown as red *'s. The blue region defines the field of view of Auger; deeper blue indicates larger exposure. The solid curve marks the boundary of the field of view, where the zenith angle equals 60°. The closest AGN, Centaurus A, is marked as a white $\ast$. Two of the 27 cosmic rays have arrival directions within 3° of this galaxy while 20 of the 27 events are within 3.1° of AGN closer than 71 Mpc. The supergalactic plane is indicated by the dashed curve. This plane delineates a region where large numbers of nearby galaxies, including AGNs, are concentrated (2).

More recently the ANtartic Impulsive Transient Antenna (ANITA) has detected radio pulses which may be interpreted as geosynchrotron emissions from UHECR Extensive Air Showers (EAS) (31). All UHECR production scenarios predict an associated UHE neutrino flux and since the Auger Observatory has measured a suppression in the cosmic ray spectrum consistent with the GZK cut-off (32), the cosmogenic neutrinos, produced in the interaction of UHECR with CMB photons, are guaranteed at some level.

Direct detection of UHE neutrinos is very difficult due to their extremely small interaction cross-sections. Instead, they may be detected indirectly via observation of the Askaryan effect (1) in the lunar regolith (a sandy layer of ejecta covering the Moon to a depth of ∼10 m). Askaryan first predicted coherent Čerenkov emission in dielectric media at radio and microwave frequencies and this has been verified in sand (33), salt (34) and ice (35). Using the Moon as a large volume neutrino detector[1], coherent radio Čerenkov emission from neutrino-induced cascades in the lunar regolith can be observed with ground-based telescopes. This method was first proposed by Dagkesamanskii and Zheleznykh (36) and first applied by Hankins, Ekers and O'Sullivan (37) using the 64-m Parkes radio telescope. Significant limits have been placed on the UHE neutrino flux by the Parkes experiment and subsequent experiments using the Kalyazin 64-m radio telescope (38) and the NASA 70-m Deep Space Network antenna, known as the Goldstone Lunar Ultra high Energy neutrino Experiment (GLUE) (39).

Currently, lunar Čerenkov experiments are being performed at the Australia Telescope Compact Array (ATCA), by the LUNASKA collaboration (3), and at the Westerbork Synthesis Radio Telescope (WSRT), by the NuMoon collaboration (40) (41). Although the next phase of the NuMoon experiment will make use of LOFAR (LOw Frequency ARray) which is currently being comissioned. One of the key differences between the LUNASKA and NuMoon experiments is the choice of observational frequency. The spectrum of coherent Čerenkov emission rises approximately linearly with frequency until a peak value is reached. This peak frequency is determined by de-coherence and/or attenuation in the regolith, and can vary between a few hundred megahertz and approximately 5 GHz. The dependence of the peak on shower geometry makes the choice of an optimum observation frequency non-trivial. NuMoon takes the approach of advocating lower frequency experiments (100–250

---

[1] For this type of experiment, the moon could be considered a *target* for neutrino interactions and the radio telescope array could be considered as the *detector* of resulting Čerenkov emission. However for this thesis, and in keeping with current literature, potential neutrino sources are typically referred to as *targets* (in the context of 'targeted experiments') and the moon or other large volume bodies which are suitable for neutrino interaction are referred to as *detectors*. Where possible these detectors are described as neutrino detectors or planetary detectors to avoid confusion.

MHz) which increase the experimental sensitivity to a range of particle interaction geometries while the current LUNASKA ATCA experiments are being conducted in the GHz range to take advantage of geometrically favorable events.

Significant limits have been placed on an isotropic flux of UHE neutrinos with one scenario for UHECR production already ruled out (the Z-burst scenario) and 'top-down' scenarios strongly disfavored by recent Auger results (42). The current limit has been set by ANITA-lite (43), a preliminary stage of the ANITA experiment, which is a balloon-borne neutrino telescope that aims to detect neutrino-induced showers in the Antartic ice sheet. However, ANITA is only sensitive to neutrinos from the equatorial zone and therefore has no sensitivity in the region of Cen A, a giant radio galaxy which is also our nearest AGN, or the supergalactic plane. Complementary experiments, such as the LUNASKA ATCA experiments, are therefore required to provide sensitivity toward the potential sources identified by the Auger observations. Future experiments will help to determine the origin of UHECR either by providing spectral information, which may eliminate proposed production scenarios, or direction of arrival information which will assist in identifying the source of UHE neutrinos.

1.3 Outline of this Thesis

This thesis explores issues associated with UHE neutrino detection using the lunar Čerenkov technique. It covers a series of experiments performed by the LUNASKA collaboration and the development of new detection techniques which can be applied to the next generation of radio telescope detectors.

Chapter 2 provides an exploration of the basic UHE neutrino detection issues. This chapter begins by considering what makes a good planetary detector and provides a simple comparison of Earth's nearest neighbors; the Moon, Venus and Mars. The second part of this chapter uses an analytical description of the radio Čerenkov spectrum to explore the experimental parameter space for UHE neutrino detection.

Chapter 3 presents an analysis of the dispersive effects of the ionosphere on a radio Čerenkov pulse. Dual-frequency Global Positioning System (GPS) data was used to analyse the variability of the ionosphere's Total Electron Content (TEC) and its relationship to the differential delay imposed across a bandlimited pulse.

Chapter 4 contains details of UHE neutrino detection experiments which were performed at the ATCA. This includes the development of custom-designed pulse detection hardware and pulse generation test equipment and also a brief summary of the experimental outcomes.

Chapter 5 provides an introduction to interferometry and data calibration at the ATCA. It contains concepts which are necessary to understand the method of ionospheric calibration presented in the next chapter.

Chapter 6 presents a novel technique for determining the ionospheric TEC in real time and line-of-sight to the Moon. This is achieved by combining Faraday[2] rotation estimates of polarised emission, from the lunar limb, with geomagnetic field models. This technique also requires exploration of lunar Stokes parameters in the visibility domain, or the far field of the source, to illustrate how lunar position angle measurements can be obtained from a synthesis array without imaging.

---

[2] In this thesis, capitalisation has been retained where a proper noun is used as an adjective to describe a technical effect or method (44).

CHAPTER 2

The UHE Neutrino Detection Problem

Direct detection of UHE neutrinos is very difficult due to their extremely small interaction cross-sections. However, using a planetary body as a large volume detector, coherent radio Čerenkov emission from neutrino-induced cascades in the regolith layers can be observed using ground-based telescopes.

A high energy neutrino interaction produces a cascade of secondary particles. During the development of this cascade, a combination of electron entrainment and positron annihilation causes an excess of relativistic negative charge. Askaryan (1) first described this effect and also noted that, in a dense dielectric medium, it should lead to strong coherent Čerenkov emission at radio and microwave frequencies. The Askaryan effect has been verified in a variety of media (33) (34) (35) and these measurements have been consistent with theoretical predictions (45).

Dagkesamanskii and Zheleznykh (36) proposed that the surface layers of the Moon could be used to observe the Askaryan effect as an indirect means of detecting UHE particles, and this was first attempted by Hankins, Ekers and O'Sullivan (37) using the Parkes radio telescope (see Chapter 1 for a more detailed review of UHE neutrino detection experiments). This chapter explores alternative planetary detector candidates for this technique and provides an analytical characterisation of the predicted radio Čerenkov emission.

2.1 Comparison of Planetary Detector Candidates

Ice planets, potentially among the Saturnian or Jovian moons, have been suggested as alternative planetary bodies for UHE neutrino detection via the Askaryan effect (46). This strategy assumes ice as the optimal medium for neutrino detection though the Askaryan effect has also been confirmed in a variety of media. In this section Earth's nearest neighbors, Mars and Venus, have been considered as potential UHE neutrino detectors. To provide a simple evaluation of these detector candidates, the probability of neutrino interaction and expected signal-to-noise ratio for each detector were considered. The signal-to-noise ratio is a measure of the received Čerenkov pulse amplitude relative to any non-transient contaminating signals, or noise, present in the measured data. In experiments to detect planetary Čerenkov radiation this 'noise' is composed of receiver noise and thermal emission from the planetary detector itself.

Probability of Interception

The probability of a neutrino interaction is proportional to the volume of the candidate detector. Only the outer layers of the detector are transparent to radio frequencies therefore detectable neutrino interactions have been limited to the regolith and outer sub-regolith layers. The volume contained within the regolith shell has been calculated assuming a thickness of 10 m (see (7) for a discussion of interactions occurring in sub-regolith layers). Assuming a perfect spherical shape for the detectors, the shell volume is therefore given by

$$V_{\text{shell}} = \frac{4}{3}\pi r^3 - \frac{4}{3}\pi (r - d_i)^3, \tag{2.1}$$

where r is the planetary radius and d_i is the interaction depth. The resulting detector shell volumes are summarised in Table 2.1

	Radius (km)	Volume (km^3)	Shell Volume (km^3)
Moon	1.74×10^3	2.12×10^{10}	3.80×10^5
Mars	3.40×10^3	1.64×10^{11}	1.45×10^6
Venus	6.05×10^3	9.28×10^{11}	4.60×10^6

Table 2.1: Candidate Detector Shell Volumes.

Signal Strength

The achievable signal-to-noise ratio is limited by the attenuation which occurs during pulse propagation. The main effect of this attenuation is to decrease the electromagnetic radiation intensity by the square of the distance it travels. For neutrino-induced Čerenkov radiation this refers to the distance between the neutrino detector and an Earth-based receiver.

Estimating the amount of attenuation is relatively straightforward when the Moon is being considered as a detector. The Moon is in orbit around the Earth and therefore its distance from any Earth-based receiver remains relatively constant at $d_{\text{Moon}} \sim 3.84 \times 10^5$ km. Čerenkov radiation originating at the Moon will therefore have reduced in intensity by a factor which is proportional to $d^2_{\text{Moon}} \sim 1.47 \times 10^{11}$ by the time it reaches an Earth-based detector. The case for Venus or Mars is complicated by the fact that both planets orbit the Sun and therefore their distance from Earth changes significantly over time.

Mars and Venus Orbital Parameters

Venus is in orbit approximately .72 AU from the Sun and completes an orbit every 224.7 (Earth) days. Its orbit is only slightly elliptical with an eccentricity of less than 1%. Earth and Venus come into inferior conjunction every 584 days. Inferior conjunction describes the position when Venus lies between the Earth and the Sun, it also corresponds to Venus' closest approach to Earth at a distance of ∼ 40 million km.

Mars is in orbit approximately 1.52 AU from the Sun and completes an orbit every 687 (Earth) days. With an eccentricity of ∼ 0.09 Mars' orbit is highly elliptical compared with other planets in the solar system. Earth and Mars come into opposition approximately every 780 days. Opposition describes when Mars is nearest to Earth during each orbit. This distance varies from 55–100 million km due to the changing interaction between the Mars and Earth elliptical orbits.

The best case scenario of minimum detector distance has been considered and the propagation attenuation proportionality factors for each detector are summarised in Table 2.2.

	Attenuation Proportionality Factor
Moon	1.47×10^{11}
Mars	3.02×10^{15}
Venus	1.6×10^{15}

Table 2.2: Propagation Attenuation Factors.

Thermal Noise Contributions

The expected signal-to-noise ratio is also influenced by the level of noise measured on each detector. This noise is characterised by the on-source system temperature which is defined according to the following equation

$$T_{\mathrm{sys}} = T_a + T_r, \tag{2.2}$$

where T_a is an antenna temperature, which relates to the physical temperature of the source, and T_r is the receiver temperature. All three candidate detectors are being compared for the same detection system, therefore the main difference in their noise levels will be due to any contribution from their own thermal emission.

Measurements of the system temperature were taken at the Australia Telescope Compact Array in May 2007. These measurements were taken at 1.4 GHz for both the case of the array pointing on and off the Moon (Table 2.3). The off-Moon system temperature is directly related to the receiver noise, T_r, and combined with the higher on-Moon system temperature can be used to derive an estimate of the noise contribution coming from the Moon's thermal emission, $T_{\mathrm{a(Moon)}}$.

This lunar thermal emission estimate can be scaled to derive estimates of the system temperature contribution from either Mars or Venus. The same observing frequency and bandwidth has been assumed for each detector (the peak of the Čerenkov radiation will be between 1–3 GHz for most angles near the Čerenkov cone (see Section 2.2)) therefore the thermal contribution to system temperature will scale with the detector's angular dimension and also its brightness temperature at radio frequencies.

	Angular Size ($''$)	Physical Temperature (K)	Antenna Temperature (K)	Receiver Temperature (K)	System Temperature (K)
Moon	1800	241	$54_\dagger$	40*	94*
Mars	25	211	$1_\dagger$	40*	$41_\dagger$
Venus	60	700	$5_\dagger$	40*	$45_\dagger$

Table 2.3: Parameters used to estimate the relative noise levels between detector candidates (size and temperature from Kraus (47), * denotes an ATCA measurement and † denotes an derived value).

For the case of Mars and Venus, the system temperature contributions from thermal emission are much lower than the off-source system temperature measurements, in fact they fall roughly within a standard deviation of these measurements, and therefore for these detectors the system temperature will be internally limited (at

$\sim$40° K). For the Moon the system temperature is dominated by thermal emission (at 94° K) and so the noise is worse by a factor of $\sim$2.

Detector Comparison

The probability of making a detection is proportional to the probability of intercepting a neutrino and subsequently the detector shell volume. It is also related to the expected signal-to-noise ratio which is inversely proportional to both the square of the detector distance from Earth and also the on-source system temperature for each detector. A simple comparison of the detectors can be made by considering the figure of merit, F for each detector

$$F = \frac{V_{\text{shell}}}{d^2 T_{\text{sys}}}, \tag{2.3}$$

where V_{shell} is the detector shell volume, d is the distance from the detector to Earth and T_{sys} is the detector's on-source system temperature. The probability of detection is therefore proportional to (normalised to the lunar case):

$$F_{\text{Venus}} = 2.2 \times 10^{-3}, \tag{2.4}$$

$$F_{\text{Moon}} = 1, \tag{2.5}$$

$$F_{\text{Mars}} = 3.71 \times 10^{-4}. \tag{2.6}$$

From these calculations, the best candidate for neutrino detection is the Moon.

Other Considerations

This comparison considers factors which are relatively easily quantified, however, there are also other important considerations for comparing detector candidates.

Firstly, the Earth-detector distances taken for Mars and Venus were best case scenarios which only occur very infrequently. For Venus, inferior conjunction only occurs every 584 days while for Mars opposition only occurs only every 780 days and even then, the closest approach can vary by almost an order of magnitude due to the high eccentricity of Mars' orbit. These large distances make Mars and Venus non-ideal candidates for UHE neutrino detection using Earth-based telescopes. However, new advances in space-based astronomy, such as planetary orbiters, may make these other detectors increasingly attractive options. This is particularly true for Mars which has a similar brightness temperature to the Moon at radio frequencies and therefore will not will not suffer from thermal noise contributions at smaller distances.

Potential planetary detectors also have to be evaluated on their surface composition, particularly with respect to radio absorption and scattering properties. For a smooth planetary surface these properties are characterised by the complex dielectric constant of the surface material which contains terms relating to both the refractive index (see Section 2.2 for an expression relating refractive index of the detector surface to the expected Čerenkov radiation spectrum) and absorption of the material. For a more realistic surface, large scale surface roughness effects (from impact craters and geological formations) and clumping or non-uniform density on a smaller scale can contribute to further scattering of the Čerenkov pulse. An optimal interaction surface consists of a material with low radio absorption properties such as dry rock or ice which make both the Moon and Mars attractive detector candidates.

Čerenkov pulse propagation will also be affected by any planetary atmosphere. In particular, Venus is known for having extremely dense clouds composed of sulfuric acid while Mars has a relatively thin atmosphere (about 1% the surface pressure of Earth) and the Moon is thought to have no atmosphere at all (48). The presence of an atmosphere may cause attenuation as well as distortion to the pulse from frequency dispersion. This effect would be the most significant for Venus, however, with no magnetic field, polarization effects such as Faraday rotation through the Venus atmosphere would not have to be considered. Mars has large magnetic fields although they are not global. This may cause local variations in the properties of the Martian atmosphere making it difficult to predict pulse distortion or optimise detection algorithms.

From this analysis, the Moon has been identified as the best planetary, UHE neutrino detector candidate. However, new advances in space-based instrumentation, such as satellite detectors and planetary probes, may warrant further investigation into alternative planetary detectors. Mars in particular is an attractive option due to its dry surface composition, thin atmosphere and large volume.

2.2 Simulation of Lunar Čerenkov Emission

Designing an optimal detector system for lunar-neutrino interactions requires an understanding of the expected radio Čerenkov emission. This section uses a basic analytical model to describe the spectrum expected from neutrino-induced hadronic showers and explores the effect of experimental parameters such as observing frequency, bandwidth and dedispersion[1] gain. Only hadronic showers, expected from the dominant ν_e charged-current interactions, have been considered (49).

When an UHE neutrino interacts in the lunar regolith, it initiates a cascade of

---

[1] Dedispersion refers to reversal of the dispersion characteristic.

secondary particles which produce an excess of relativistic negative charge. Since the excess charge is traveling faster than the speed of light through the lunar dielectric, coherent Čerenkov radiation is emitted at radio and microwave frequencies. The distribution and spectral properties of this emission are related to the particle shower dimensions. The angular distribution of the emission (see Figure 2.2) can be interpreted as a Fraunhofer diffraction pattern of the longitudinal charge excess in the shower and, for observation angles close to the Čerenkov cone, the position of the spectral peak (see Figure 2.1) is directly related to the transverse shower structure (50).

At sufficiently low frequencies, where the wavelength is comparable to the shower length, the emission is nearly isotropic while at higher frequencies, where the wavelength is comparable to the lateral shower distribution, the emission peak occurs in a narrow cone around the Čerenkov angle, $\theta_c = \cos^{-1}(1/n) = 54.7°$, where $n = 1.73$ is the refractive index of the lunar regolith (7).

On the Čerenkov angle the radiation spectrum rises linearly with frequency until the wavelength becomes much smaller than the lateral distribution of the shower and destructive interference effects start to take place. This occurs at the decoherence frequency, f_0, above which the emission fall-off is characterised by the phenomenological form-factor (51)

$$F(f) = \left(\frac{1}{1 + \left(\frac{f}{f_0}\right)^{\alpha}} \right), \tag{2.7}$$

where α is medium dependent. The electric field strength $\varepsilon_{\mathrm{EM}}(\theta_c, f)(\mathrm{V/m/Hz})$, at a distance $R(m)$, of a hadronic shower with energy E_s, can be parameterised as (7)

$$R|\varepsilon_{\mathrm{EM}}(\theta_c, f, E_s)| = V_0 \times \left(\frac{E_s}{1\mathrm{EeV}}\right) \left(\frac{f}{1\mathrm{GHz}}\right) \left(\frac{1}{1 + \left(\frac{f}{f_0}\right)^{\alpha}} \right) \mathrm{V/MHz}, \tag{2.8}$$

with V_0=0.0845 V/MHz, f_0=2.32 GHz and α=1.23. Away from the Čerenkov angle, decoherence effects over the length and width of the shower track cause a reduction in the Čerenkov emission. This is described by

$$R|\varepsilon_{\mathrm{EM}}(\theta, f)| = \varepsilon(\theta, f) \left(\frac{\sin\theta}{\sin\theta_c}\right) 2^{\frac{-(\theta-\theta_c)^2}{\Delta\theta^2}} \mathrm{V/MHz}, \tag{2.9}$$

where the angular spread, $\Delta\theta$ is given by (8)

$$\Delta\theta_H = C_H \left(\frac{f}{1\mathrm{GHz}}\right)^{-1} \frac{1}{1 + 0.075 \log_{10}(E_s/10\mathrm{EeV})}. \tag{2.10}$$

The angular spread around the Čerenkov cone is inversely proportional to both shower length and frequency. This inverse relationship is consistent with the analogy of the longitudinal shower distribution acting as a diffraction slit to produce the angular form and peak of the Čerenkov emission. At higher frequencies (~1 GHz), the first minima of the interference pattern will occur approximately 5° from θ_c, while at lower frequencies, the $\sin\theta$ term in $\varepsilon_{\mathrm{EM}}(\theta, f)$ becomes significant due to the projection of the particle track onto the observer's celestial sphere of reference (50).

The analytical model was implemented with a primary particle energy of $E_\nu = 10^{20}$ eV and the resulting shower energy given by $E_s = 0.2E_\nu$. The spectrum was evaluated at the Čerenkov angle and then at 5° increments from this angle (see Figure 2.1). As the observational angle moves away from the Čerenkov cone, the onset of deconstructive interference effects occurs at progressively lower frequencies. Essentially this may be seen as moving from a very directional regime, where at high frequencies the radiation forms a narrow cone around the Čerenkov angle, to a nearly isotropic regime at lower frequencies. The angular distribution of the emission has been calculated for both a low (0.2–0.8 GHz) and high (1.2–1.8 GHz) frequency band (see Figure 2.2). The high frequency band was chosen to correspond to the bandwidth available at the Australia Telescope Compact Array (see Chapter 4) and the lower frequency band was chosen as a comparison. The analytical description of the Čerenkov radiation does not produce the expected secondary diffraction peaks in the angular distribution, however, an investigation of these secondary peaks can be found in (50).

2.2.1 Comparison Spectrum

A second parameterisation of the Čerenkov emission (9) was implemented to explore the associated parameter space. The main difference in this parameterisation is the treatment of radiation emitted away from the Čerenkov angle. For these angles, the emission is described by an exponential term, e^{-Z^2}, defined below. The dependence of Z has been determined by comparing analytical predictions with Monte Carlos simulations as described in (9). A different value for the medium dependent parameter, α, in the form-factor has also been assumed.

The energy density, F, of the Čerenkov radiation in a frequency range $\Delta\nu$ around ν, and at an angle θ to the shower axis, from a charged particle shower of total energy E_s, inside the lunar regolith is given by

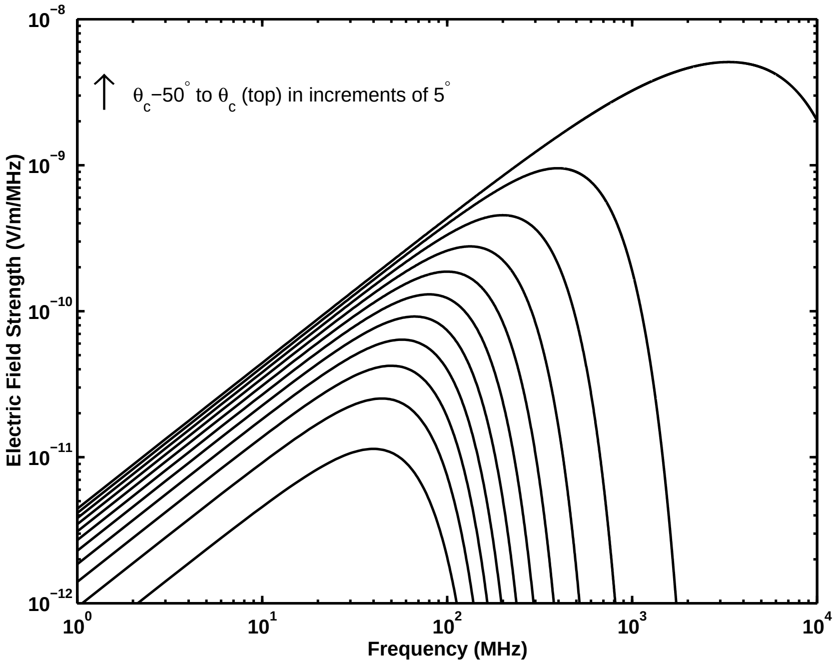

Figure 2.1: Čerenkov Radiation Spectrum.

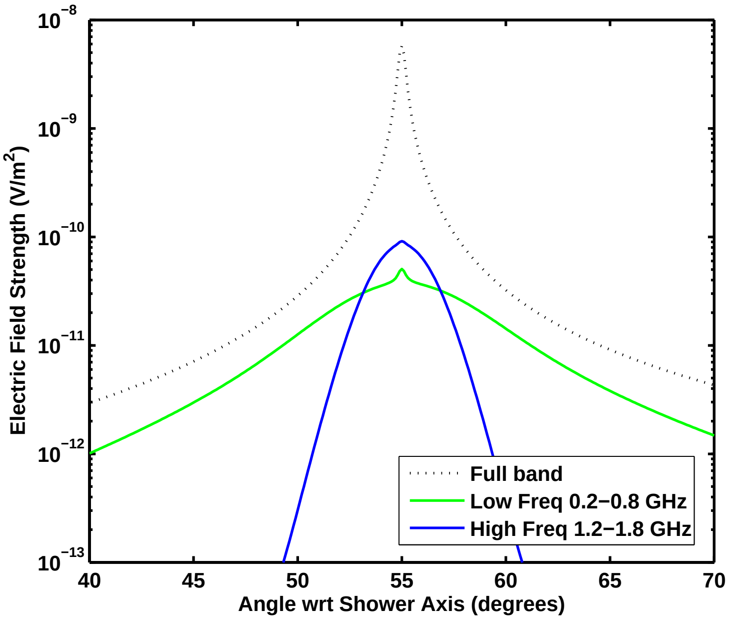

Figure 2.2: Čerenkov Radiation Angular Distribution

$$F(\theta,\nu,E_s) = 1.89{\times}10^9 e^{-Z^2}\left(\frac{\sin\theta}{\sin\theta_{\rm VC}}\right)^2\left(\frac{E_s}{E_0}\right)^2\left(\frac{R_L}{R}\right)^2\left(\frac{\nu}{\nu_0[1+(\nu/\nu_0)^{1.44}]}\right)^2\frac{\Delta\nu}{100{\rm MHz}}, \tag{2.11}$$

where $E_0 = 10^{20}$ eV, $Z = (n\cos\theta - 1)/(\Delta_{\rm VC}\sqrt{n^2-1})$, n is the refractive index of the lunar regolith and ν_0 is the decoherence frequency where the radiation wavelength becomes comparable to the transverse dimension of the shower. R_L is the lunar radius, R is the distance from the emission source to the detector and

$$\Delta_{\rm VC} = 0.0302\frac{\nu}{\nu_0}\frac{L(E_0)}{L(E_s)} \tag{2.12}$$

gives the angular spread around the Čerenkov angle $\theta_{\rm VC}$ where the shower length $L(E_s)$ is given by $L(E_s) = 12.7 + 2/3\log(E_s/E_0)$ in units of radiation length. Again, a neutrino energy of $E_N = 10^{20}$ eV has been assumed and the resulting shower will carry 20% of this energy giving a total shower energy of $E_s = 0.2 \times 10^{20}$ eV.

Both parameterisations have been implemented for angles of θ_c, 66.8° and 90° (see Figure 2.3). These values of θ were chosen to correspond to Monte Carlo simulation results published by Alvarez-Muñiz (10). The main difference between the analytical parameterisations and the published Monte Carlo results can be seen in the structure above the decoherence frequency. These differences arise as the parameterisations are only approximations to a full shower simulation which models all hadron-hadron, hadron-nucleus and nucleus-nucleus interactions.

The spectral peaks obtained from the Monte Carlo simulation are roughly consistent with those obtained using the analytical descriptions, particularly the first parameterisation. When the observation angle θ is aligned with the Čerenkov angle the spectrum peaks in the high gigahertz range. As the observation angle moves away from the Čerenkov angle, the peak is attenuated and occurs at much lower frequencies. For the Monte Carlo simulation and the first analytical parameterisation, these peaks occur at $\sim 2 \times 10^2$ MHz for $\theta = 66.8°$ and ~60 MHz for $\theta = 90°$. The spectral peaks of the second parameterisation are more compact and are concentrated toward the low gigahertz range.

Different parameterisations will introduce uncertainties in the expected Čerenkov spectra. Changes in the distribution of spectral peaks are due to differing treatment of the emission radiated away from the Čerenkov cone. On the Čerenkov cone, variations in the medium dependent parameter, α, also produce changes to the spectrum above the decoherence frequency. The second parameterisation produces a more compact spectrum with geometrically favorable events centred in the low gigahertz range. However, for these investigations, the first analytical parameterisation has been adopted.

2.2.2 Pulse Profiles

Peak Čerenkov emission will occur on the Čerenkov cone. According to the analytical parameterisation, this peak will occur just above 5 GHz for emission precisely on the Čerenkov cone. For a broader range of angles just off the cone, the maximum emission will occur in the 1–3 GHz range (see Figure 2.4). A pulse profile can be obtained by taking an inverse Fourier transform of the spectra and can be seen in Figure 2.4b. The resultant pulse is a nano-second scale pulse with no obvious modulation features.

Ionospheric Dispersion

A Čerenkov pulse originating on the Moon will travel through the ionosphere and experience a frequency dependent time delay resulting in pulse dispersion. This ionospheric dispersion was modeled using a transfer function described by Hankins *et al.* (37):

$$H(\omega) = e^{\frac{-i\omega n(\omega) z}{c}}, \tag{2.13}$$

where ω is frequency, $n(\omega)$ is the refractive index of the ionosphere as a function of frequency, z is the ionospheric thickness and c is the speed of light. This is essentially an all-pass filter with a phase distortion characteristic.

The ionospheric refractive index n, as a function of frequency ω, is given by

$$n^2(\omega) = 1 - \frac{\omega_p^2}{\omega^2}, \tag{2.14}$$

where ω_p is the plasma frequency,

$$\omega_p = \sqrt{\frac{n_e e^2}{m\epsilon_o}}, \tag{2.15}$$

n_e is electron density (related to the TEC, $TEC \sim n_e z$), m is electron mass, ϵ_o is the permittivity of free space and e is the charge on an electron.

The model assumes a relatively simple refractive index which could be improved by including a loss term γ (52) such that

$$n^2 = 1 - \frac{\omega_p^2}{\omega^2 + i\omega\gamma}, \tag{2.16}$$

or by investigating a more complicated expression for the refractive index such as the Appleton-Hartree expression (53). However, the simplification of

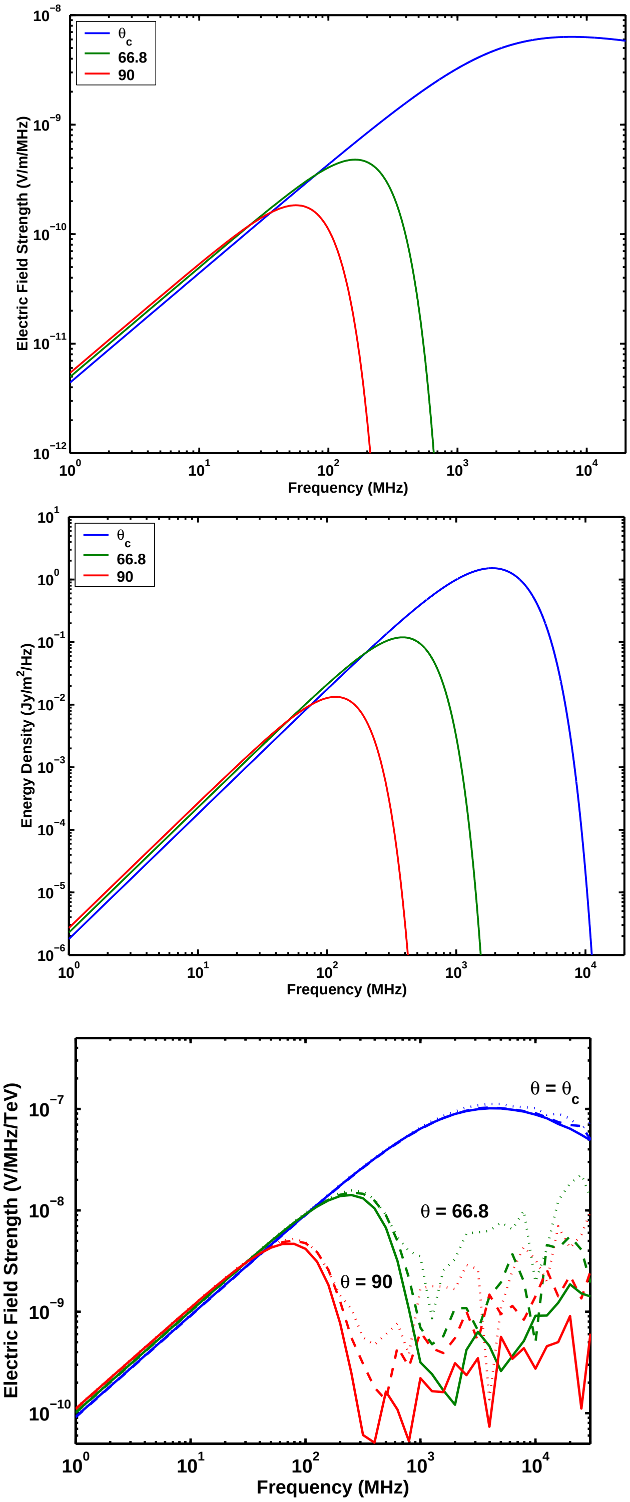

Figure 2.3: Spectrum from (*top*) James (7) and Alvarez-Muñiz (8) parameterisation (*middle*) Scholten parameterisation (9) and (*bottom*) Monte Carlo simulation results published by Alvarez-Muñiz. The Monte Carlo simulations shown are for lower energy showers (dotted lines indicate 1 TeV, dashed 10 TeV and solid 100 TeV). However, at higher energies they will just continue to scale with energy (10). These plots are shown to illustrate the shape of the Čerenkov emission spectra and the distribution of spectral peaks. Therefore the y-axis for each plot has been left in the units of the original publication.

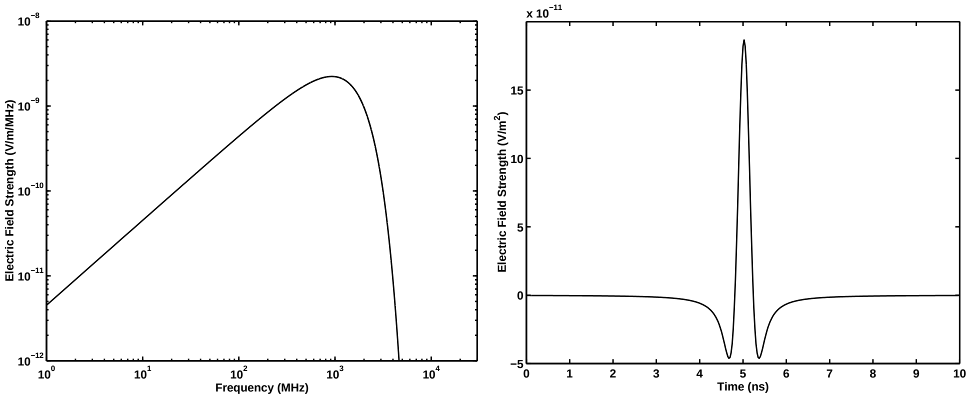

Figure 2.4: (*Left*) The radio Čerenkov spectrum just off the Čerenkov cone (at $\theta = 53°$) and (*right*) the resulting undispersed pulse profile.

$$n = \sqrt{1 - \frac{\omega_\rho^2}{\omega^2}} \tag{2.17}$$

is accurate to better than 1% (54). This model also neglects magnetic effects such as any polarisation effects caused by Faraday rotation and assumes that the radiation travels radially toward the Earth (polarisation and slant angle effects are considered in Chapter 6).

The dispersion characteristic is applied to the incoming pulse by multiplying the pulse spectrum with the ionospheric transfer function

$$F(\omega) \times H(\omega) \tag{2.18}$$

and converting to the time domain via an inverse Fourier transform. Dispersed pulses may be seen in Figure 2.5 for TEC values typical of both solar min (TEC=10 TECU, 1 TECU = 10^{16} electrons per m^2) and solar max (TEC=100 TECU). TEC values were obtained from NASA's JPL (Jet Propulsion Laboratory) (55) and an ionospheric thickness of 600 km was assumed.

The dispersed pulses are broadened with their trailing edge spread out in time. This spreading is consistent with the ionosphere's dispersive characteristic which causes different frequency components to experience different time delays. The dispersed pulses are also reduced in amplitude relative to the undispersed profile. The loss in amplitude is proportional to the ionospheric TEC and occurs as the pulse energy spreads in time.

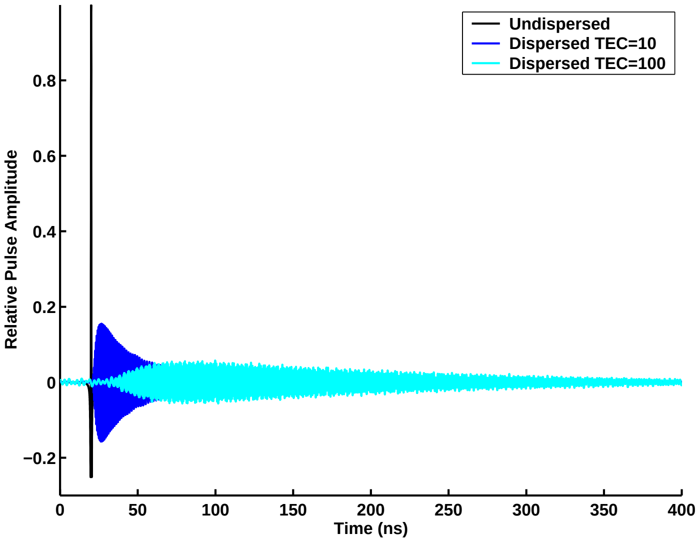

Figure 2.5: Dispersed Pulse Profile

Receiver Bandwidth

A large receiver bandwidth must be used to achieve the required time resolution for sub-nanosecond pulse detection. At the ATCA, 600 MHz (1.2–1.8 GHz) is available from a maintenance point in the antenna vertex (see Chapter 4 for more details on the experimental detector system hardware).

The effects of bandlimiting can be investigated by including a bandpass filtering stage in the simulation. The bandpass filter has been designed using a remez algorithm and implemented in the frequency domain via a multiplication with the filter's frequency response. The main effects of bandlimiting are that the pulse becomes broadened (symmetrically) in time and reduced in amplitude (see Figure 2.6). The reduced amplitude occurs as all of the pulse energy outside of the bandpass has been filtered out. Figure 2.7 provides a comparison of dispersed pulses for typical solar min and solar max TEC values, over both low and high frequency bands.

2.2.3 Experimental Considerations

Pulse profiles can be compared to optimise the experimental parameters of UHE neutrino detection. Lunar Čerenkov pulses received at an Earth-based radio telescope will be dispersed by the ionosphere and further broadened by receiver bandlimiting. The amount of dispersion loss will be affected by the ionospheric TEC, choice of observing frequency and the experimental bandwidth while the choice of observational frequency and bandwidth will also determine which shower geometries the

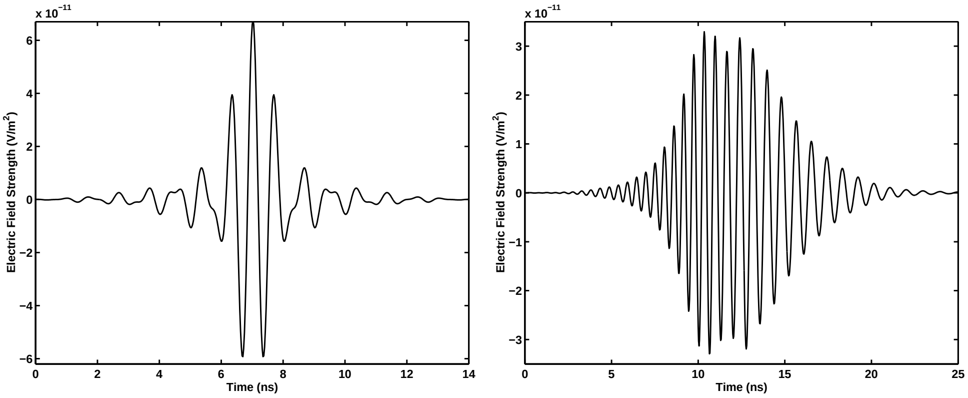

Figure 2.6: Close-up of bandlimited pulse profiles (*left*) undispersed (*right*) dispersed

experiment will be sensitive to.

Dispersion Loss

As described earlier, radio waves propagating through the ionosphere are dispersed by a frequency dependent time delay. This dispersion causes the energy of a pulse to spread out over time resulting in an overall loss of amplitude, or dispersion loss. The amount of loss will be related to the width of the dispersed pulse, which is determined by the differential delay experienced between the lowest and highest frequency terms in the propagating signal. This delay is described by Equation 2.19 and a full derivation of this expression is presented in Chapter 3. While there is a simple analytic expression to describe the differential delay in terms of the frequency and ionospheric TEC, there is no analytic description for the dispersion loss. Therefore the dependencies of this loss have been explored by generating both dispersed and undispersed pulses, and plotting their ratios for a given set of parameters.

$$\Delta t = 0.00134 \times TEC \times (\nu_{\mathrm{lo}}^{-2} - \nu_{\mathrm{hi}}^{-2}), \tag{2.19}$$

where Δt is the differential delay in seconds, TEC is the total electron content in electrons per cm^2 and ν_{lo} and ν_{hi} are the lowest and highest frequency terms respectively, which are in Hz.

An initial investigation of the dispersion parameter space assumed a pulse generated from a flat featureless spectrum, or an impulse. While the spectrum of an impulse is featureless, it does need to be constrained by a bandwidth. To remain consistent with the ATCA experiments, a 600-MHz bandwidth was chosen, and the dispersion loss was calculated over this band for both increasing TEC (see Figure

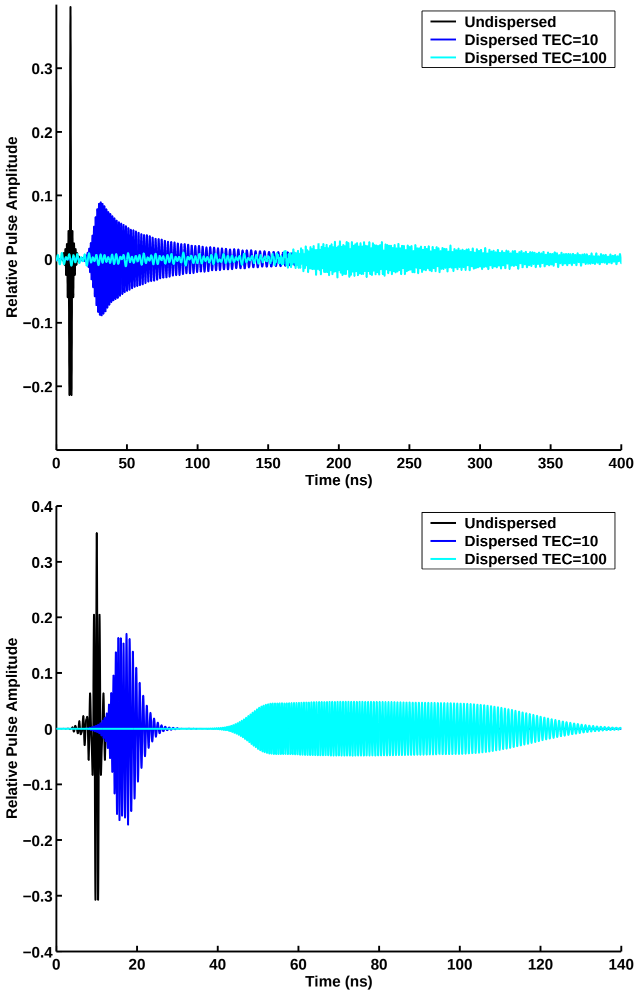

Figure 2.7: Dispersed pulse profiles at (*top*) low frequencies (0.2–0.8 GHz) and (*bottom*) high frequencies (1.2–1.8 GHz)

2.8) and increasing center frequency (see Figure 2.9). This bandwidth is impractical for the lower frequency ranges considered in Figures 2.8 & 2.9, however, it has been kept constant to illustrate the relationship between dispersion loss and frequency without introducing new parameters, such as bandwidth.

The relationship between dispersion loss and TEC has a near linear characteristic, with the main deviation from this trend occurring for low TEC values, while the dependence on center frequency follows an approximate power law. The expected delay due to dispersion has a linear TEC dependence and is proportional to the observing frequency squared. Therefore, while the dispersion loss will not necessarily have the same dependencies as the delay, these trends were not entirely unexpected.

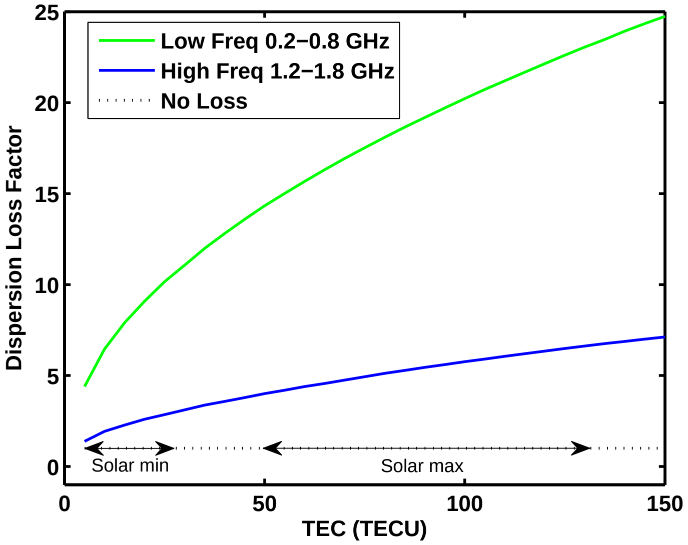

Figure 2.8: Dispersion loss factor as a function of ionospheric TEC. This loss has been calculated over 600-MHz bands of flat spectrum (ie. for an impulse). This band is impractical at lower frequencies, however, it has been kept constant to provide a general exploration of the dispersion loss parameter space.

Pulse dispersion can be corrected using matched filtering techniques. The recovered gain in pulse amplitude is known as the dedispersion gain and full signal recovery requires an accurate knowledge of the ionospheric TEC. For the experimental detector system described in Chapter 4, an analog dedispersion filter was used with a fixed dispersion characteristic. It was designed for a 5-ns differential delay (over 1.2–1.8 GHz) which corresponds to an ionospheric TEC of 9.65 TECU. This specification was based on predictions made using dual-frequency GPS data (a full analysis is presented in Chapter 3). The ionosphere experiences both temporal and spatial fluctuations in TEC and therefore some signal loss is expected with a fixed

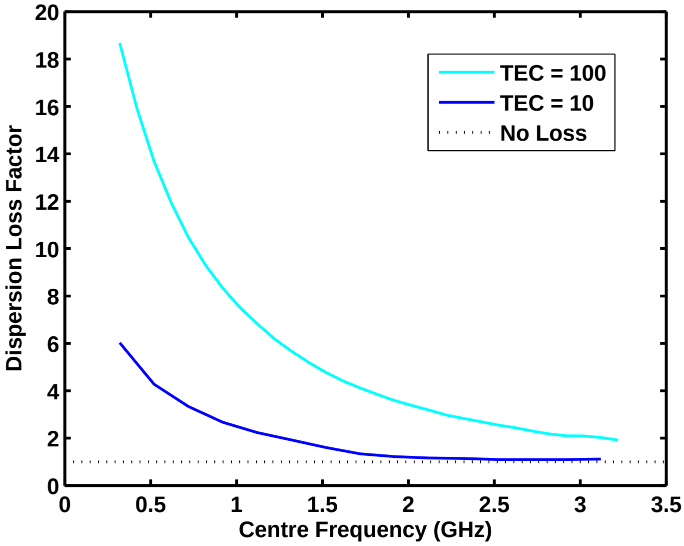

Figure 2.9: Dispersion loss factor as a function of center frequency. This loss has been calculated over a sliding band of 600 MHz. This band is impractical at lower frequencies, however, it has been kept constant to provide a general exploration of the dispersion loss parameter space.

dedispersion filter. The dependence of this loss was investigated by multiplying dispersed pulses (dispersed by a range of TEC values) with a dedispersion filter modeled on the analog hardware filter. For simplicity the simulated filter was designed for a TEC of 10 TECU rather than 9.65 TECU. The resulting loss is symmetric about the filter characteristic (see Figure 2.10) and is only about 5% for values of TEC which are within a standard deviation (∼1.3–1.5 TECU during May-June in solar min) of the predicted value.

While, in general, the dispersion loss is directly related to the ionospheric TEC and observing frequency, the dispersion loss associated with Čerenkov emission is also indirectly related to the shower viewing angle. As the shower is viewed at an increasing angle off the Čerenkov cone, the spectral peak moves lower in frequency. The effect of dispersion is higher at low frequencies and therefore the expected dispersion loss is higher away from the cone (see Figure 2.11). To investigate this effect, both dispersed (100 TECU) and undispersed pulses were generated from the (full) spectrum described in Equation 2.8. To determine the dispersion loss at each viewing angle, the peak of the dispersed pulse was compared to the peak of the undispersed pulse for that viewing geometry. By comparing the two pulses for the same viewing geometry, the intrinsic signal loss due changing viewing geometry is calibrated out. This result shows that, via the chosen frequency band, there is indirectly a

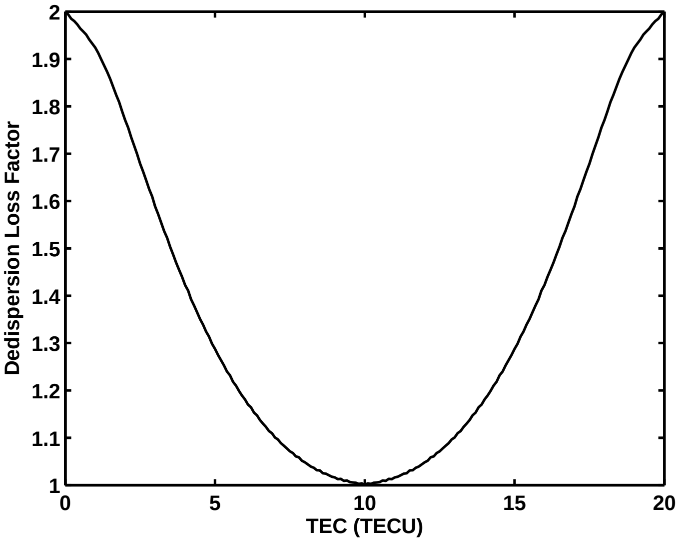

Figure 2.10: Dispersion loss factor using a dedispersion filter with a differential delay corresponding of ~5 ns over 1.2–1.8 GHz, corresponding to 10 TECU (as used in the ATCA detection experiments)

relationship between the interaction geometries being targeted and the importance of dispersion correction.

Effects of Bandlimiting

Bandlimiting also reduces the pulse amplitude as out of band energy is filtered out of the spectrum. For Čerenkov emission, the spectral distribution depends on shower viewing geometry. As the viewing angle moves away from the Čerenkov cone, the spectral distribution moves lower in frequency and there is an intrinsic decrease in the peak of the spectrum. Since the spectral distribution changes with viewing geometry, the amount of signal loss due to bandlimiting has a complicated relationship to the shower viewing angle and varies as the spectral peak moves in and out of the chosen bandwidth.

This effect has been investigated by considering the total electric field strength (Figures 2.12 & 2.13) and the pulse amplitude loss due to bandlimiting (Figures 2.14 & 2.15) over bandwidths associated with existing and planned experiments. To produce these plots, pulses were generated from both full band and bandlimited versions of the spectrum described in Equation 2.8. These pulses were generated for different viewing angles and the electric field strength at each angle was determined from the peak pulse amplitude. To determine the loss incurred from bandlimiting, at

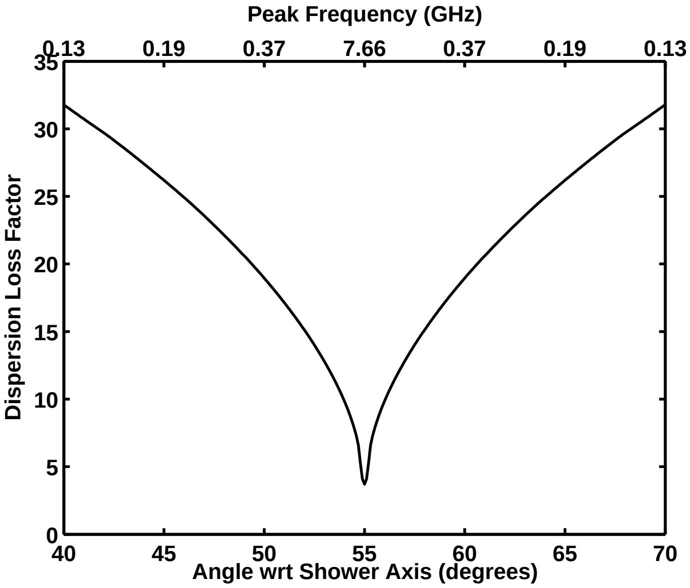

Figure 2.11: Dispersion loss as a function of shower viewing angle. At each viewing angle, the dispersed and undispersed pulses are compared to determine the dispersion loss associated with that viewing angle. The dispersed pulses have been dispersed according to solar maximum conditions (*i. e.* TEC=100 TECU) and no bandlimiting has been applied. The peak frequency of the Čerenkov emission, for the given viewing angle, is given on the top axis.

each viewing angle the peak of the bandlimited pulse was compared to the peak of the full band pulse for that viewing geometry. By comparing the two pulses for the same viewing geometry, the intrinsic loss due changing viewing geometry is calibrated out.

These calculations were performed for both the low and high frequency bands defined earlier (0.2–0.8 GHz and 1.2–1.8 GHz respectively). The high band represents the existing ATCA band and, while the low band has been kept for comparison, it does not represent a practical experimental bandwidth. Therefore frequency bands representative of proposed experiments have also been used. The experimental frequency bands chosen were the LOFAR band, 100–250 MHz (9), and the proposed ATCA Compact Array Broadband (CABB) upgrade, 1–3 GHz. The Čerenkov spectrum covered by these bands is highlighted in Figures 2.16 & 2.17 which emphasise that the higher frequency bands are sensitive to stronger events but only at favorable geometries while the lower frequencies bands are sensitive to all events but at the expense of a higher energy detection threshold.

This is further illustrated by considering the angular distribution of the electric field strength for both sets of frequency bands (see Figure 2.12 & 2.13). Higher frequency bands produce a distribution which is highly directional and forms a strong peak around the Čerenkov angle while lower frequency bands appear increasingly isotropic. The LOFAR and proposed CABB bandwidths provide extreme cases of this phenomenon. Close to the Čerenkov angle, the CABB bandwidth provides two orders of magnitude more sensitivity, however, within $\sim 5°$ of this angle the LOFAR band becomes more sensitive. These cases highlight the trade off which occurs when choosing an observational frequency for Čerenkov detection experiments.

Another way to consider this trade off is to look at the bandlimiting loss which occurs for each bandwidth as a function of the shower viewing angle (see Figures 2.14 & 2.15). These plots can roughly be broken into three regions. The first region describes the peak in bandlimiting loss around the Čerenkov cone which occurs because the spectral peak of the Čerenkov emission is higher in frequency and significantly wider than any of the chosen bandwidths. The CABB bandwidth is optimal in this region as it contains significantly higher parts of the spectrum than any of the other bandwidths considered. The second region describes where the bandlimiting loss is optimally low as the Čerenkov peak has moved into the chosen bandwidth. For the highest frequency bands this occurs a few degrees with either side of the Čerenkov cone, however, for the lower frequency bands, most notably for the LOFAR case, the optimal region occurs progressively further from the Čerenkov angle. The third region describes where the Čerenkov peak begins to move out of each chosen band and to lower frequencies. In this region, which is only visible for the two higher bandwidths, the bandlimiting loss rises again until a maximum is reached when all of the spectral energy is out of band.

As discussed in Section 2.2.1, these results are sensitive to the choice of radio Čerenkov emission parameterisation. The alternative parameterisation produces a more compact spectrum with events from more favorable geometries centered in the low gigahertz range. Therefore it is likely to be even more optimistic in predicting which geometries the high frequency ATCA experiments are sensitive to and estimating the resulting bandlimiting losses.

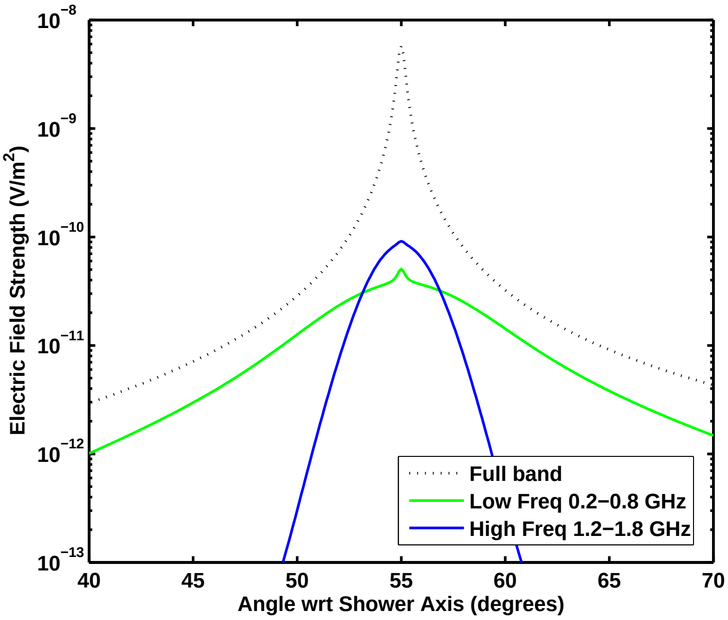

Figure 2.12: Angular distribution for Low and High frequency bands. Pulses were generated from both full band and bandlimited versions of the spectrum described in Equation 2.8 and the electric field strength was determined from the peak pulse amplitude at each viewing angle.

2.3 Conclusions

In this chapter, it was determined that the Moon is the best planetary candidate for UHE neutrino detection using Earth-based telescopes. However, with the advent of space-based instrumentation, other planetary detectors (particularly Mars) may warrant further investigation.

Simulations of the radio Čerenkov emission, expected from lunar-neutrino interactions, were used to identify optimal experimental parameters for UHE neutrino detection. It was shown that the Čerenkov emission is a broadband emission with

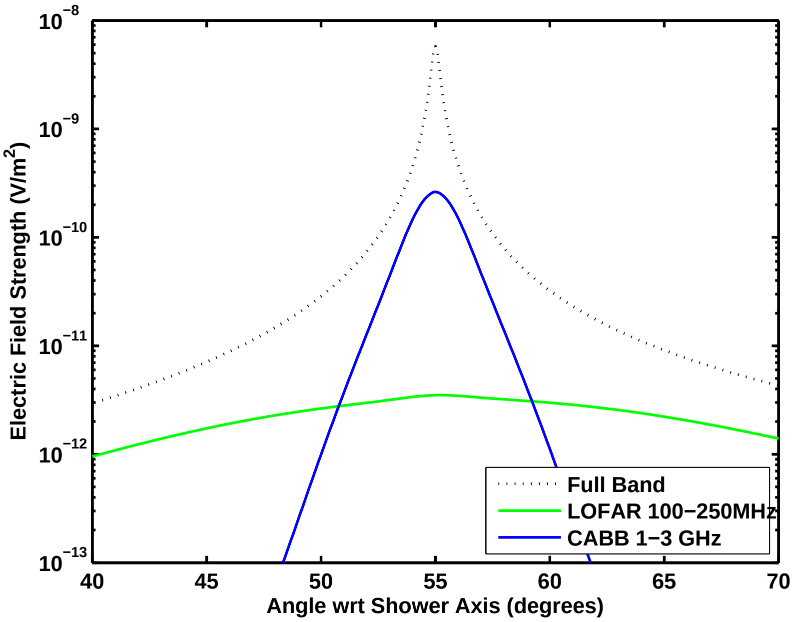

Figure 2.13: Angular distribution for LOFAR and CABB bands. Pulses were generated from both full band and bandlimited versions of the spectrum described in Equation 2.8 and the electric field strength was determined from the peak pulse amplitude at each viewing angle.

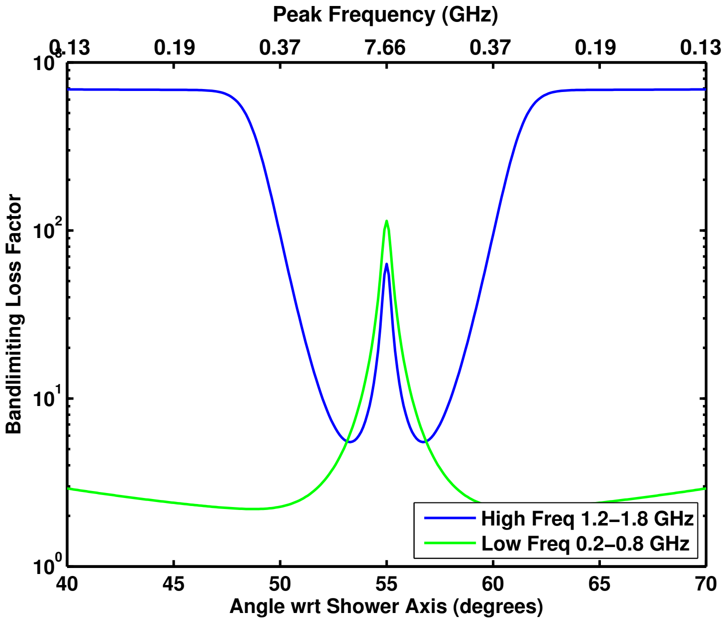

Figure 2.14: Bandlimiting loss for Low and High frequency bands. To determine the loss incurred from bandlimiting, at each viewing angle the peak of the bandlimited pulse was compared to the full band pulse for that viewing geometry. By comparing the two pulses for the same viewing geometry, the intrinsic loss due changing viewing geometry is calibrated out.

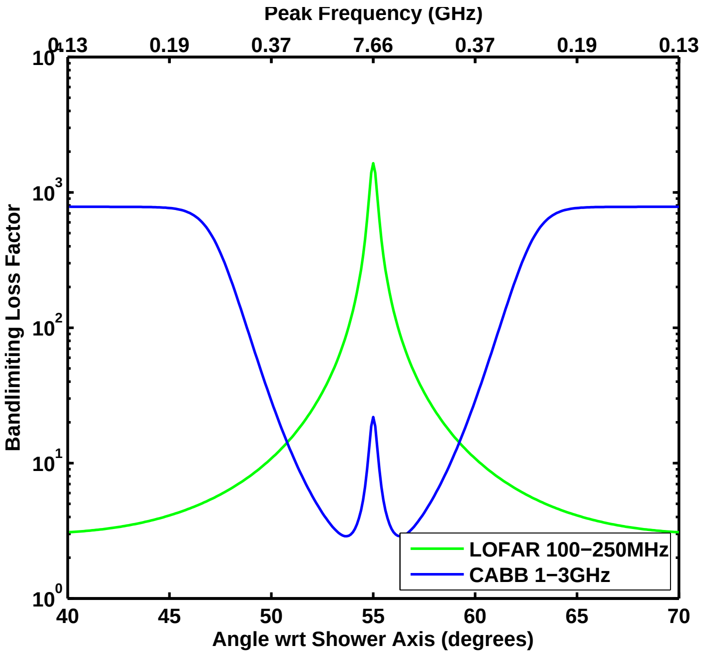

Figure 2.15: Bandlimiting loss for LOFAR and CABB bands. To determine the loss incurred from bandlimiting, at each viewing angle the peak of the bandlimited pulse was compared to the full band pulse for that viewing geometry. By comparing the two pulses for the same viewing geometry, the intrinsic loss due changing viewing geometry is calibrated out.

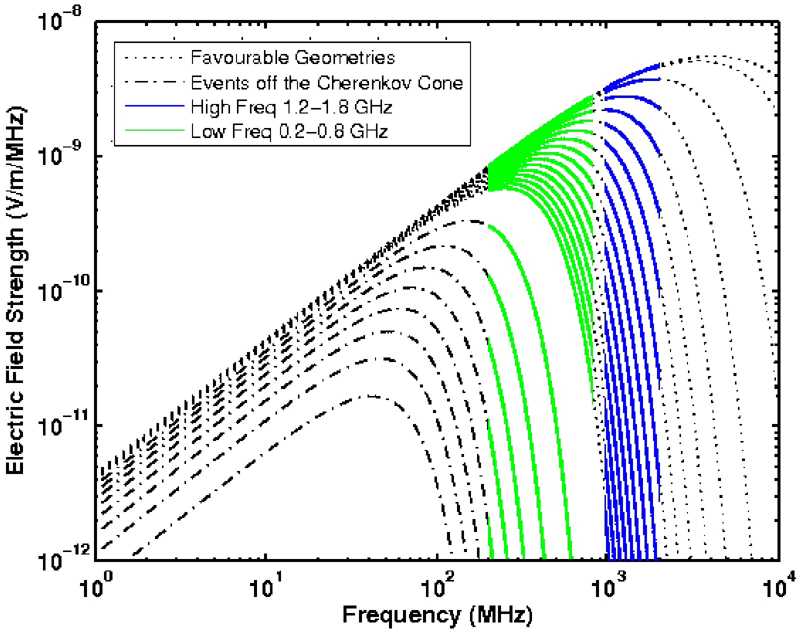

Figure 2.16: Low (0.2–0.8 GHz) and High (1.2–1.8 GHz) regions of the Čerenkov spectrum. Geometrically favorable events are shown as events viewed from 47–55° (at 0.5° increments) and events off the Čerenkov cone have been shown as events viewed at 7–42° (at 5° increments).

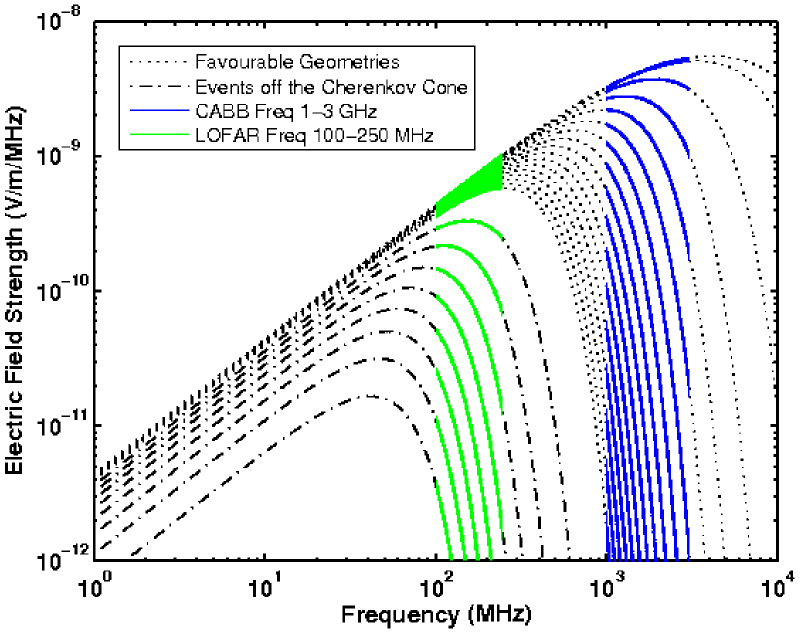

Figure 2.17: LOFAR (100–250 MHz) and CABB (1–3 GHz) regions of the Čerenkov spectrum. Geometrically favorable events are shown as events viewed from 47–55° (at 0.5° increments) and events off the Čerenkov cone have been shown as events viewed at 7–42° (at 5° increments).

a spectral distribution which is determined by the shower viewing geometry. The emission is strongest on the Čerenkov cone and peaks in the high gigahertz range. As the shower is viewed away from the cone, the spectral peak moves lower in frequency and there is an intrinsic loss in signal strength.

The broadband emission produces short pulses and, for events viewed within a few degrees of the Čerenkov cone, these pulses are only a few nanoseconds in duration. When received by an Earth-based telescope, the peak pulse amplitude will be reduced by signal bandlimiting and dispersion which occurs during propagation through the ionosphere. It was shown that the effects of pulse dispersion are more significant at lower frequencies. Over a 0.2–0.8 GHz band, solar minimum conditions (10 TECU) produced a loss factor of $\sim$5 and solar maximum conditions (100 TECU) produced a loss factor of $\sim$18. Over the higher 1.2–1.8 GHz band the loss factors for solar minimum and maximum were $\sim$2 and $\sim$6 respectively.

It was also shown that the choice of observing frequency determines the experimental sensitivity to different shower geometries. At higher frequencies, the Čerenkov emission is strong and highly directional (with the highest frequency emission occurring only on the Čerenkov cone) while for lower frequencies, the emission is produced over increasingly more viewing geometries. Therefore, as long as the effects of ionospheric dispersion can be corrected, an experiment which performs a blind search for anisotropic emission is better at lower frequencies. Meanwhile, searches which specifically target a potential neutrino source (such as Cen A) are optimal at higher frequencies, since observations can be aligned for detections on the peak of the Čerenkov cone.

The ATCA experiments were designed as targeted observations and therefore employed the second strategy. For showers viewed just off the Čerenkov cone, the spectral peak of this emission falls in the 1–3 GHz range. Observing in this range extends the experimental sensitivity to a range of favorable geometries while still maximising the predicted flux, which falls by almost two orders of magnitude $\sim 5^\circ$ off the cone. Under the current solar minimum conditions, a dedispersion gain of 1.6–1.7 is expected over a 1.2–1.8 GHz bandwidth and, by observing during the relative stability of the night ionosphere, within 5% of this gain can be achieved using a fixed analog dedispersion filter. As the solar cycle enters a more active phase, a more significant loss (a factor of $\sim$5–6) will occur from dispersion and accurate pulse dedispersion will become a more important experimental concern. A new method for characterising this dispersion is presented in Chapter 6.

CHAPTER 3

Ionospheric Dispersion of the Čerenkov Pulse

Electromagnetic pulses originating in the lunar surface will be dispersed when they arrive at Earth-based receivers due to their propagation through the ionosphere. Ionospheric dispersion will reduce the peak amplitude of a pulse. However, dedispersion techniques can be used to recover this loss and consequently increase the chances of detection. These techniques require an understanding of the ionospheric dispersion characteristic and its effect on radio-wave propagation.

This chapter provides an analysis of the typical ionospheric conditions during solar minimum, which was used to make predictions for a series of UHE neutrino detection experiments at the ATCA. The ionospheric dispersive characteristic is parameterised by its TEC which is defined as the integrated number of electrons in a vertical column through the ionosphere having a 1-m^2 cross section. TEC values can be derived from GPS dual-frequency signals and are available online from NASA's Crustal Dynamics Data Information System (CDDIS) (55).

A full derivation of the ionospheric dispersion relation is presented which also contains conversions between this relation, the differential path difference due to ionospheric propagation (referred to in telecommunications literature) and the interstellar medium (ISM) dispersion measure (DM) (as it appears in pulsar literature). The work was produced in an attempt to verify the ionospheric dispersion relationship published in (37) for the first lunar Čerenkov detection experiment.

3.1 TEC Variability

The ionosphere is a weakly ionized plasma which is formed by ultraviolet ionizing radiation from the sun. Due to its relationship with the sun, the ionosphere's electron density experiences a strong diurnal cycle and is also dependent on the season of the year, the current phase of the 11-year solar cycle and the geometric latitude of observation.

Figures 3.1–3.6 are world maps of the ionospheric TEC measured on May 01, 2006. The maps were produced, using CDDIS data imported into *Matlab* (see Section 3.2), at 4 hour intervals and show the progression of the ionosphere's TEC over a 24-hour period. Red areas indicate peak values of TEC and correlate with equatorial latitudes and daytime time zones illustrating the ionosphere's relationship to solar activity and in particular the diurnal cycle.

The seasonal variation and 11-year solar cycle dependence may be seen in Figure 3.7 which shows the evolution of the Earth's mean TEC since January 1, 1995. This plot was produced by the Centre for Orbit Determination in Europe (CODE) (56). CODE is a European collaboration which forms one of the seven International GPS Service Analysis centres.

3.2 TEC Predictions for ATCA Experiments

The initial ATCA neutrino detection experiments took place during mid 2007. At this time, the solar cycle was at a minimum and the predicted TEC values (from Figure 3.7) for mid 2007 were similar to those of mid 2006. Existing data from 2006 was therefore analysed to give an indication of the range and variation of TEC values expected during these initial experiments.

The CDDIS publish TEC measurements which are along a vertical line-of-sight through the ionosphere (VTEC). The true TEC, Slant TEC (STEC), depends on the angle of propagation through the ionosphere which is determined by the elevation angle of the source. Since the source elevation will vary, most of the following analysis has been performed for VTEC values. However, the method of converting between vertical and slant TEC is discussed further in Chapter 6.

The CDDIS TEC data is sampled at two hour intervals and is published in IONEX format (57). Rather than use the existing Fortran reader, a *Matlab* reader was developed to enable more convenient extraction and analysis of the data relevant to the detection experiment. The CDDIS data is published in geodetic coordinates and had to be converted to geocentric coordinates before extracting data sets, roughly corresponding to the position of the ATCA at Narrabri, from the global maps. As

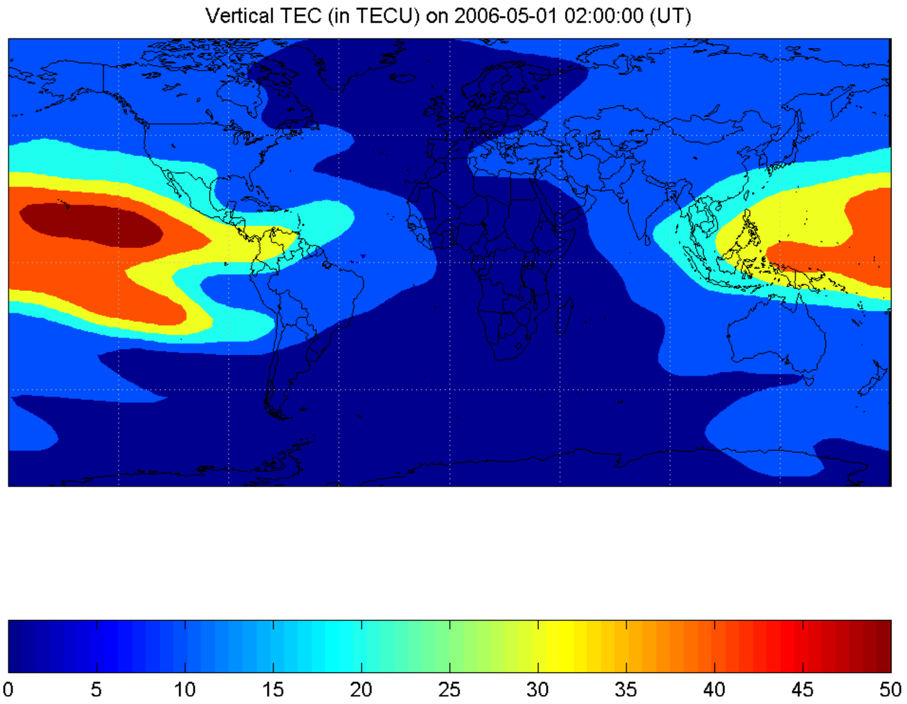

Figure 3.1: Vertical TEC for May 2006 at 02:00 UT

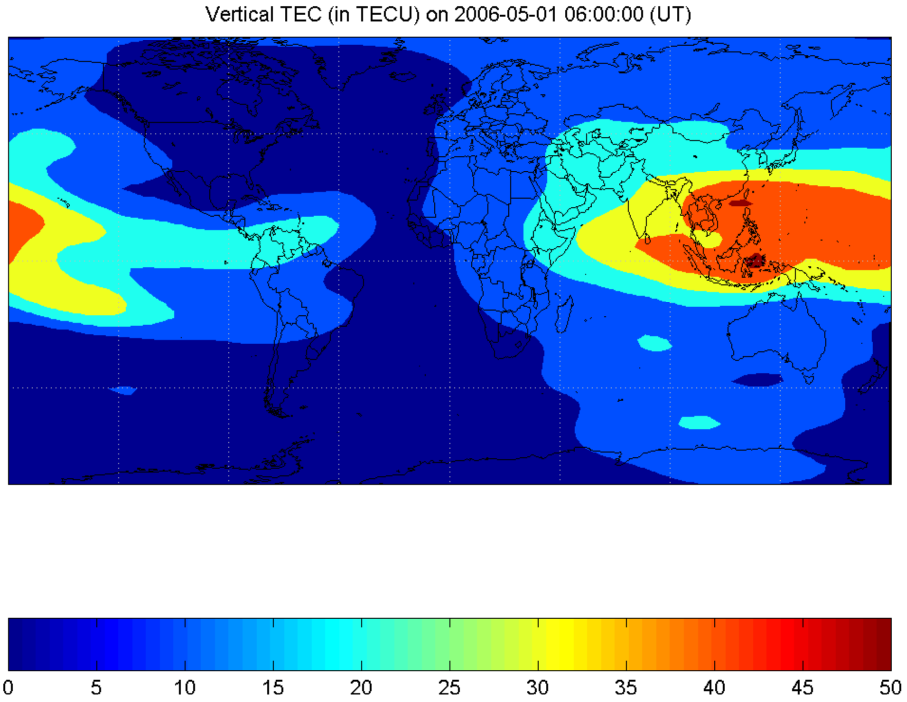

Figure 3.2: Vertical TEC for May 2006 at 06:00 UT

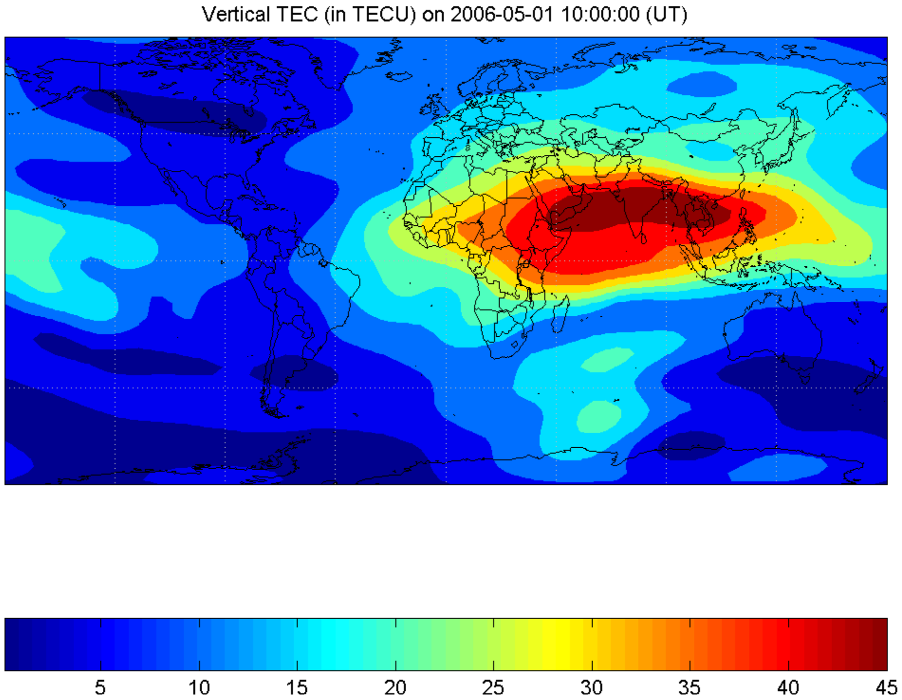

Figure 3.3: Vertical TEC for May 2006 at 10:00 UT

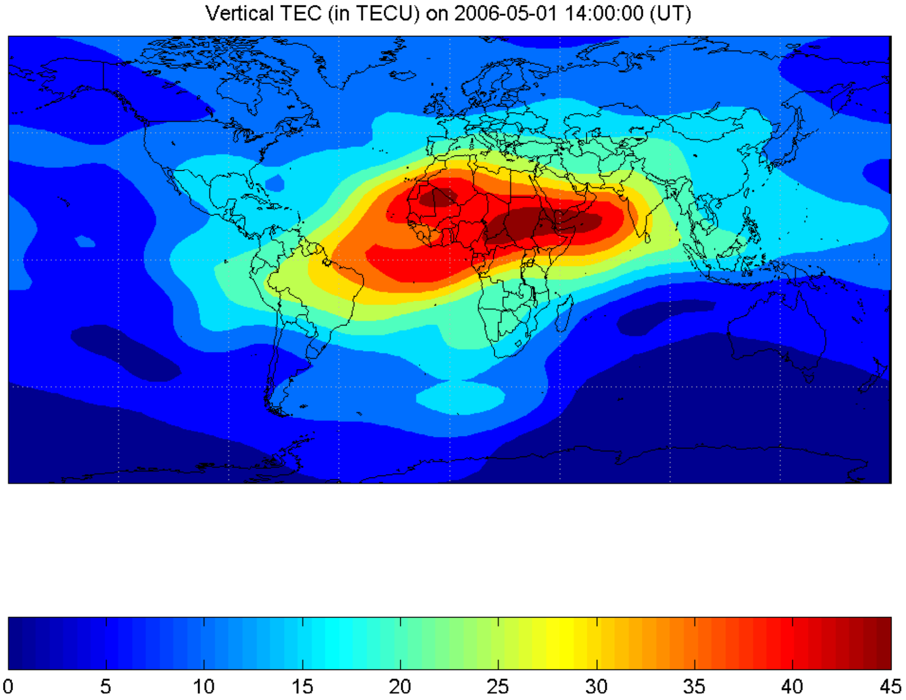

Figure 3.4: Vertical TEC for May 2006 at 14:00 UT

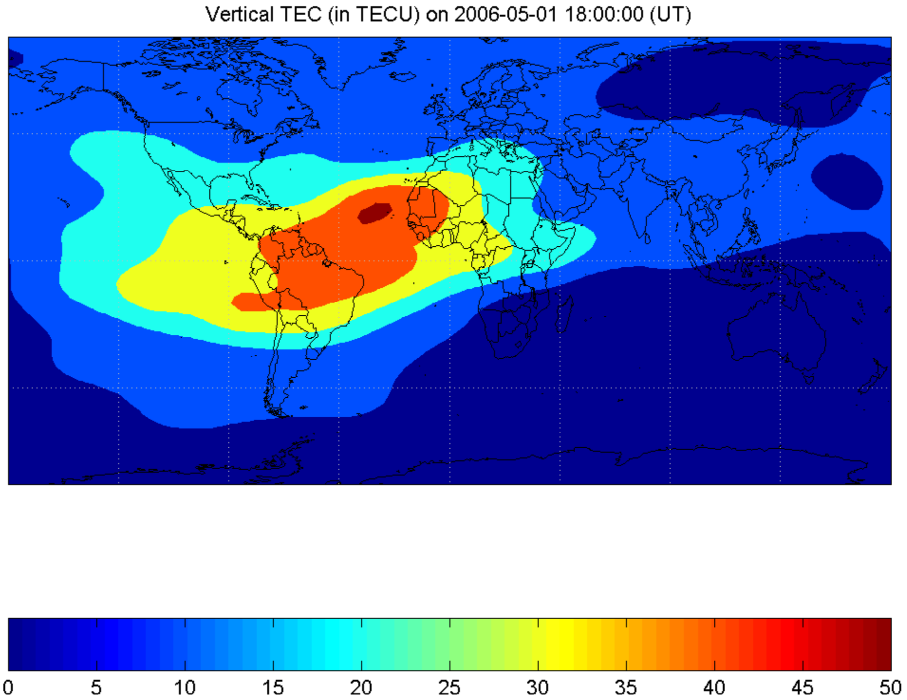

Figure 3.5: Vertical TEC for May 2006 at 18:00 UT

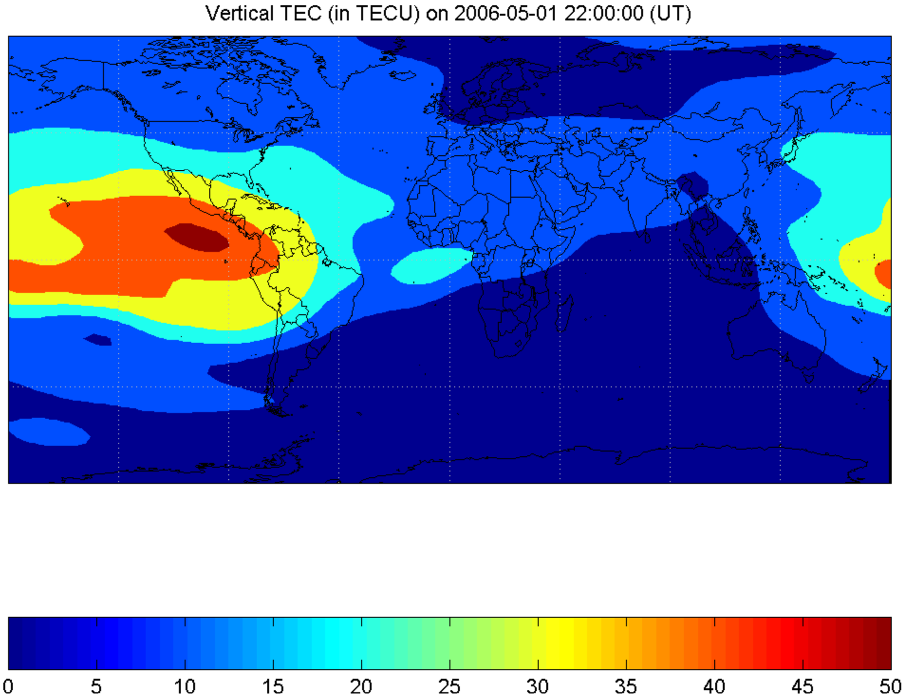

Figure 3.6: Vertical TEC for May 2006 at 22:00 UT

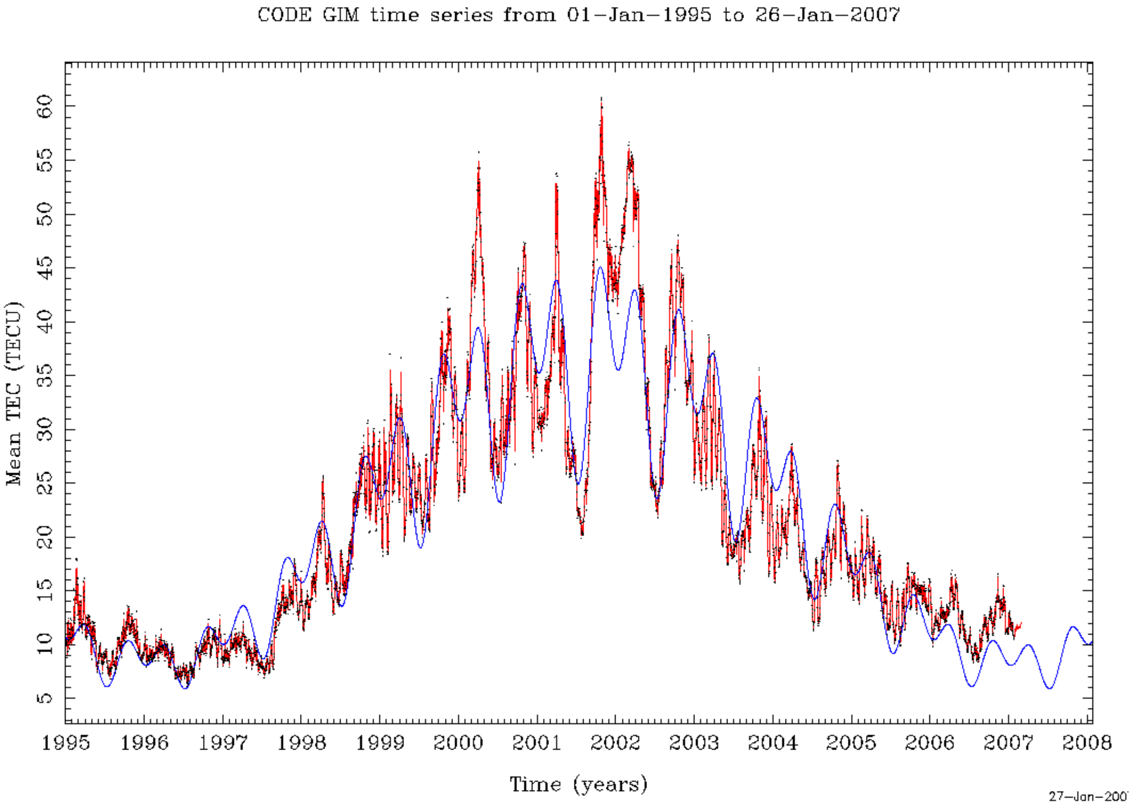

Figure 3.7: Evolution of the Earth's mean VTEC from Jan 1 1995 showing the 11-year solar cycle. Smaller oscillations are due to seasonal effects. The red curve shows the interpolated mean VTEC, the daily averaged mean VTEC values are in black and a seven parameter trend function, extrapolated for one year, is plotted in blue.

this analysis is indicative only, no interpolation algorithms were used and the analysis was performed for a (geodetic) latitude of 150 E and longitude of 30.17 S (Narrabri's true geodetic latitude is 149.8 E and longitude is 30.3 S).

The strong diurnal cycle of the ionospheric TEC can be seen in Figures 3.8 and 3.9 which show the TEC measurements obtained during May and June. Average TEC values and their standard deviation over a 24-hour period follow in Figures 3.10 & 3.11. The ionosphere is most stable during the hours of low solar activity (8pm–6am) with an average TEC of 7.06 ± 1.3 and 6.03 ± 1.5 TECU for May and June respectively.

Figures 3.12 and 3.13 show histograms of the measured TEC values for May and June respectively. Each color represents a different sample time (samples are taken every 2 hours). The darker colors roughly correspond to night-time samples and the

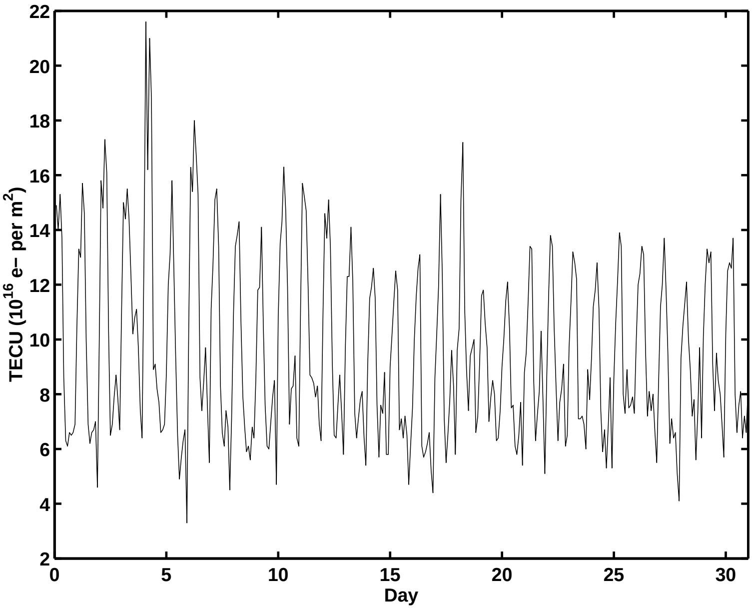

Figure 3.8: Vertical TEC for May 2006

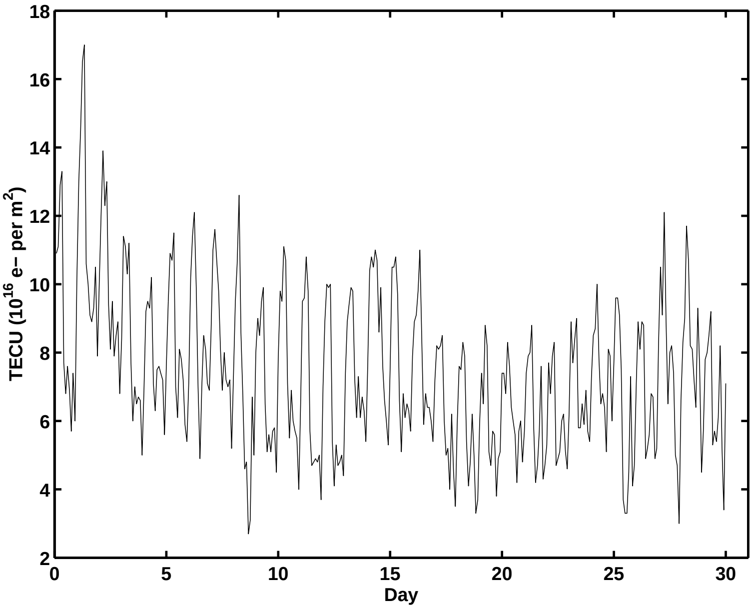

Figure 3.9: Vertical TEC for June 2006

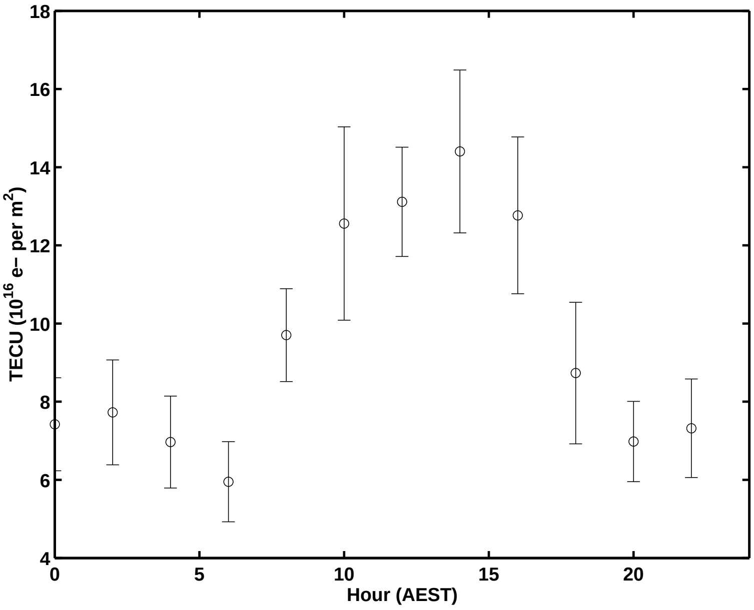

Figure 3.10: Average Vertical TEC for May 2006

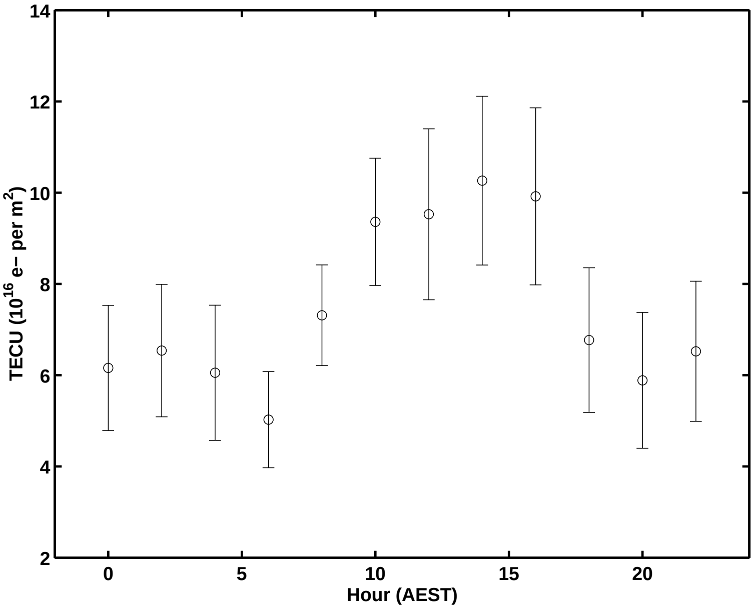

Figure 3.11: Average Vertical TEC for June 2006

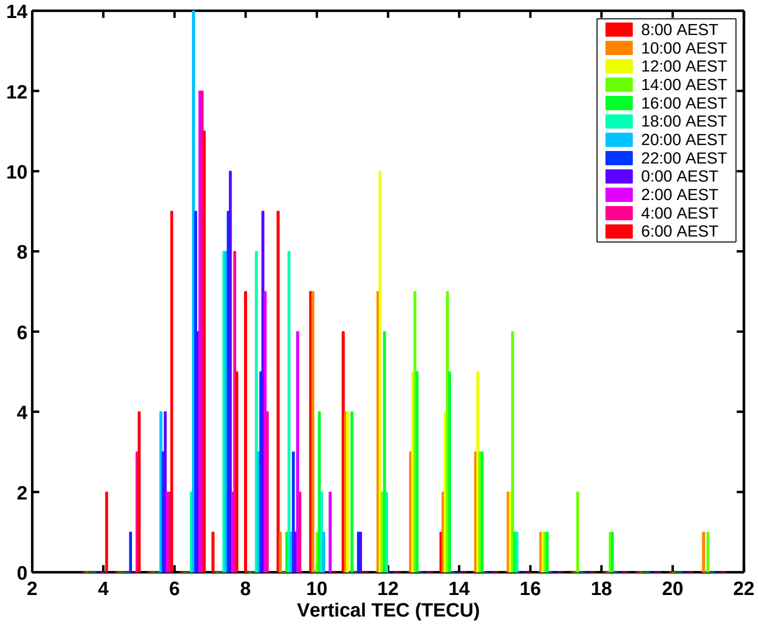

Figure 3.12: Histogram of Vertical TEC for May 2006

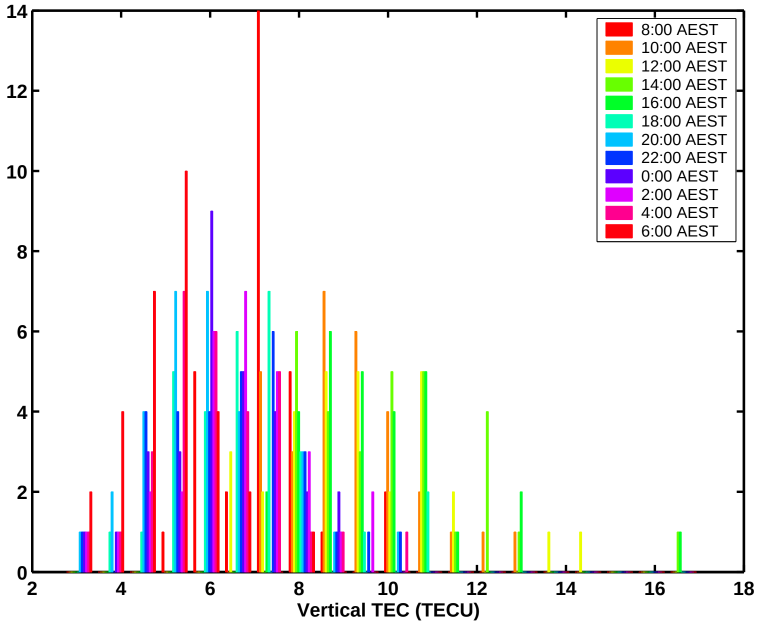

Figure 3.13: Histogram of Vertical TEC for June 2006

brighter colors correspond to daytime samples (refer to diagram legend) so again these figures show higher TEC distributions during the day and lower more stable distributions during the night due to the diurnal cycle of solar activity.

3.3 The Relationship between Ionospheric TEC and Differential Additive Delay

Hankins, Ekers and O'Sullivan (37) first described the relationship between ionospheric TEC and the resulting differential additive delay as

$$\Delta t = 0.012 \times STEC \times \frac{\Delta \nu}{\nu^3}, \tag{3.1}$$

where Δt is the duration of the dispersed pulse in seconds, $STEC$ is the Slant Total Electron Content in electrons per cm^2 and $\Delta\nu$ and ν are the receiver bandwidth and the centre frequency respectively in Hz.

Further investigation into the derivation of this result begins with the dispersion relation for electromagnetic waves propagating through a neutral isotropic plasma,

$$\omega^2 = \omega_p^2 + c^2 k^2 \tag{3.2}$$

where ω is angular frequency, ω_p is the plasma frequency, c is the speed of light and k is the wave number (eg (58), (59) and (60)). The signal group velocity, v_g, is obtained by differentiating this dispersion relation

$$v_g = \frac{d\omega}{dk} = \frac{d}{dk}\{c^2k^2 + \omega_p^2\}^{\frac{1}{2}} \tag{3.3}$$

and with some rearranging this becomes

$$v_g = c\sqrt{1 - \frac{\omega_p^2}{\omega^2}}. \tag{3.4}$$

The time, t, for a signal to propagate through the ionosphere is given by

$$t = \frac{L}{v_g} = \frac{L}{c\sqrt{1 - \frac{\omega_p^2}{\omega^2}}}, \tag{3.5}$$

where L is the distance traveled through the ionosphere. Assuming that $\omega_p \ll \omega$ binomial expansion can be used to obtain

$$t = \frac{L}{c}\left\{1 + \frac{\omega_p^2}{2\omega^2}\right\}. \tag{3.6}$$

The first term in the brackets of Equation 3.6 gives the time delay due to propagation in a vacuum. Therefore the additive delay, Δt, introduced by the ionosphere is given by

$$\Delta t = \frac{L}{c}\left\{\frac{\omega_p^2}{2\omega^2}\right\}. \tag{3.7}$$

Converting the frequency term from angular frequency to hertz and substituting for plasma frequency gives

$$\Delta t = \frac{L}{c(2\pi)^2}\frac{n_e e^2}{m_e \varepsilon_o}\left\{\frac{1}{\nu^2}\right\}, \tag{3.8}$$

where the plasma frequency (with all terms in SI units) is given by

$$\omega_p = \sqrt{\frac{n_e e^2}{m_e \varepsilon_o}}, \tag{3.9}$$

n_e is the electron density, e is the charge on an electron, m_e is the mass of an electron and ε_o is the permittivity of free space.

The equation can be rearranged in terms of the Slant Total Electron Content ($STEC = L \times n_e$) and a differential delay over the frequency band ($\nu_{\mathrm{lo}} - \nu_{\mathrm{hi}}$).

$$\Delta t = \frac{e^2}{c(2\pi)^2 m_e \varepsilon_o} \times STEC \times \left\{\frac{1}{\nu_{\mathrm{lo}}^2} - \frac{1}{\nu_{\mathrm{hi}}^2}\right\} \tag{3.10}$$

Using $e = 1.6 \times 10^{-19}$, $m_e = 9.1 \times 10^{-31}$ and $\varepsilon_o = 8.85 \times 10^{-12}$, all in SI units, this evaluates to

$$\Delta t = 1.34 \times 10^{-7} \times STEC \times (\nu_{\mathrm{lo}}^{-2} - \nu_{\mathrm{hi}}^{-2}), \tag{3.11}$$

where Δt is in seconds, $STEC$ is in electrons per m^2 and the frequency terms are in Hz. The leading constant becomes 0.00134 if the TEC is in electrons per cm^2. In terms of a signal bandwidth and centre frequency, this becomes

$$\Delta t = 2.68 \times 10^{-7} \times STEC \times \frac{\Delta\nu}{\nu^3} \tag{3.12}$$

and the leading constant becomes 0.00268 if the TEC is in electrons per cm^2. This is inconsistent with Equation 3.1 as published in (37). Therefore, further checks were carried out on the derivation of this relation.

3.4 Comparison of Plasma Dispersion Relations

References to plasma dispersion relations can be found in both pulsar literature and ionospheric literature written for telecommunications applications. In pulsar literature, this relation refers to the dispersion which occurs during propagation through the interstellar medium. Due to the cosmic distances involved the units used to describe this dispersion, usually electrons per cm^{3}pc, are much larger than those used to describe ionospheric dispersion. This results in a different value for the leading constant in the equation. In the telecommunications industry, ionospheric dispersion is characterised by a differential path difference over a given bandwidth rather than a differential time delay. While the conversion between these relations requires only simple calculations, each step has been explicitly stated in an attempt to clearly identify which of the previous dispersion relations is correct.

3.4.1 The ISM Dispersion Measure from Pulsar Literature

There are two main forms of the plasma dispersion equation commonly found in pulsar literature (*e. g.* (61))

$$\Delta t = 4.15 \times 10^6 \times DM \times (\nu_{\mathrm{lo}}^{-2} - \nu_{\mathrm{hi}}^{-2}) \tag{3.13}$$

$$\Delta t = 8.3 \times 10^6 \times DM \times \frac{\Delta\nu}{\nu^3}, \tag{3.14}$$

where for both equations Δt is the duration of the dispersed pulse in milliseconds, DM is the dispersion measure in electrons per cm^3 pc and $\Delta\nu$, ν_{lo}, ν_{hi} and ν are the receiver bandwidth, low and high and edges of the band and the centre frequency respectively in MHz.

Equation 3.14 is in the same form as Equation 3.1 and therefore the two can be compared via some simple unit conversions on the leading constant. The unit conversions performed on the leading constant of Equation 3.14 are as follows:

1. Time delay term from ms to s

   $8.3 \times 10^6 \times 10^{-3} = 8.3 \times 10^3$.

2. Frequency terms from MHz to Hz

   $\frac{MHz}{MHz^3} = \frac{1}{MHz^2} = \frac{1}{10^{12}}\frac{1}{Hz^2}$

   therefore the leading constant becomes

   $8.3 \times 10^3 \times 10^{12} = 8.3 \times 10^{15}$.

3. Electron density term from $\mathrm{cm}^{-3}\mathrm{pc}$ to cm^{-2}

   $1\mathrm{pc} = 3.085 \times 10^{18}$ cm

   so the leading constant becomes

   $8.3 \times 10^{15} \times \frac{1}{3.085\times10^{18}} = 0.0027$

and the final equation is

$$\Delta t = 0.0027 \times STEC \times \frac{\Delta\nu}{\nu^3}. \tag{3.15}$$

The same process can be used for the non-bandwidth dependent pulsar equation to get

$$\Delta t = 0.00134 \times STEC \times (\nu_{\mathrm{lo}}^{-2} - \nu_{\mathrm{hi}}^{-2}), \tag{3.16}$$

where both equations are now in the same units as Equation 3.1 *i. e.* Δt is in seconds, $STEC$ is in electrons per cm^2 and the frequency terms are in Hz.

These equations are not consistent with the published Equation 3.1, however, they are consistent with the rederived Equation 3.12.

3.4.2 Ionospheric References in Telecommunications Literature

The ionospheric references in telecommunications literature deal mainly with the ionospheric effects on GPS applications, in particular the differential dispersion experienced between GPS L band frequencies (L_1 is 1575.42 MHz and L_2 is 1227.6 MHz). The main dispersion relation in this literature (for *e. g.* (54)) is in terms of the path difference due to the effect of dispersion in the ionosphere

$$\Delta pd = 40.3 \times STEC \times (\nu_{\mathrm{lo}}^{-2} - \nu_{\mathrm{hi}}^{-2}), \tag{3.17}$$

where Δpd is the differential path difference in meters, $STEC$ is the total electron content in electrons per m^2 and ν_{lo} and ν_{hi} are the low and high band edges of the frequency band respectively in Hz. This equation can be converted to an additive time delay in the same units as Equation 3.1 via a series of simple unit conversions applied to the leading constant.

1. Convert the path difference to a time delay

   $\Delta t = \frac{\Delta pd}{c} = \frac{40.3}{3\times10^8} \times STEC \times (\nu_{\mathrm{lo}}^{-2} - \nu_{\mathrm{hi}}^{-2})$

   $\Delta t = 1.34 \times 10^{-7} \times STEC \times (\nu_{\mathrm{lo}}^{-2} - \nu_{\mathrm{hi}}^{-2})$.

2. Convert the electron density term from electrons per m^2 to electrons per cm^2

$\frac{1}{m^2} = \frac{1}{cm^2} \times \frac{1}{100^2}$

therefore the leading constant becomes
$1.34 \times 10^{-7} \times 100^2 = 1.34 \times 10^{-3} = 0.00134$
and the final equation is

$$\Delta t = 0.00134 \times STEC \times (\nu_{\mathrm{lo}}^{-2} - \nu_{\mathrm{hi}}^{-2}), \tag{3.18}$$

where this is now in the same units as Equation 3.1 *i. e.* Δt is in seconds, $STEC$ is in electrons per cm^2 and the frequency terms are in Hz. This equation is consistent with the dispersion equations derived from the pulsar literature, *i. e.* Equations 3.15 and 3.16, and the rederived Equation 3.12.

Published figures are also available on the relationship between TEC and differential dispersion at L band (for GPS L_1 is 1575.42 MHz and L_2 is 1227.6 MHz). Mannucci from NASA's JPL (62) states that every 1 ns of differential delay across this band corresponds to 2.85 TECU (1 TECU = 10^{12} electrons per cm^2 or 10^{16} electrons per m^2). These figures are also consistent with the derived equations (Equations 3.12, 3.15, 3.16 and 3.18). Therefore all derived equations are self consistent but not consistent with the original equation (3.1). The rederived equation, Equation 3.12, was therefore adopted for further ionospheric differential delay analysis.

3.5 Differential Additive Delay Statistics

Equation 3.12 was used to obtain statistics on differential delays expected for the ATCA UHE neutrino detection experiments. These delays were calculated using TEC data from Section 3.1 and over a bandwidth of 1.2–1.8 GHz. The average expected delay values and their standard deviation over a 24-hour period, for both May and June, can be seen in Figures 3.14 & 3.15. Differential delay statistics for the hours of low solar activity (8pm–6am) are summarised in Table 3.1.

	May	June
Mode	3.28	3.13
Median	3.57	3.05
Mean	3.65	3.12
Std Dev	0.68	0.78

Table 3.1: Differential Delay Statistics (ns)

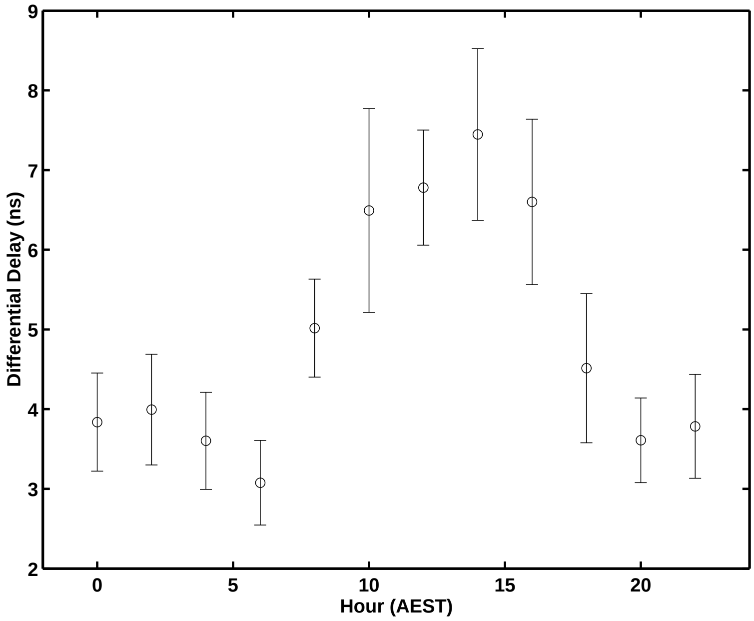

Figure 3.14: Average Differential Delay for May 2006

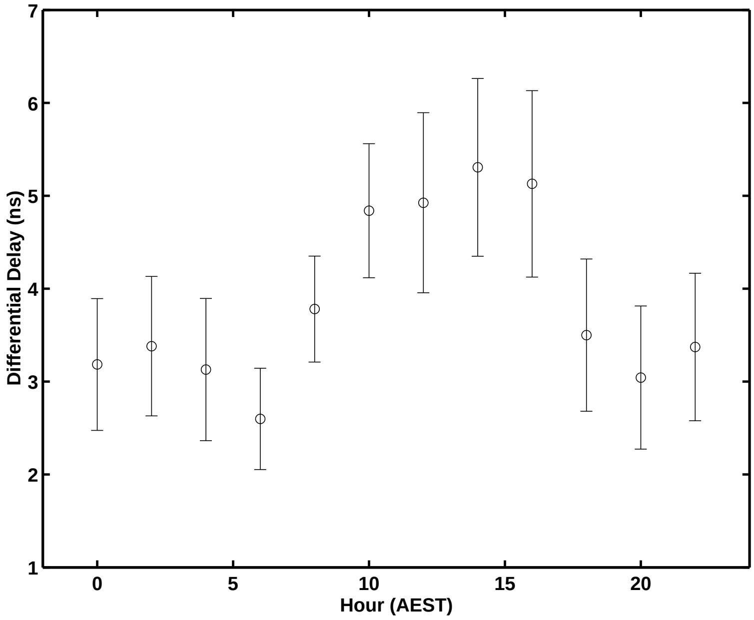

Figure 3.15: Average Differential Delay for June 2006

3.6 Conclusions

An analysis was performed of ionospheric TEC data obtained from dual frequency GPS measurements. The analysis covered typical solar minimum conditions and showed that the ionosphere was most stable during the hours of low solar activity (*i. e.* at night). The ionospheric dispersion relation previously published by Hankins, Ekers and O'Sullivan (37) was found to have an incorrect coefficient and therefore a new form of the equation, verified against the plasma dispersion relations found in both pulsar and telecommunications literature, was adopted. The new plasma dispersion relation was applied to the TEC data analysis to obtain estimates of the differential delays expected during the ATCA UHE neutrino detection experiments. Based on this data, 3.5 ns was chosen to be an appropriate differential delay for the design of an ionospheric dedispersion filter (described in Chapter 4) over 1.2–1.8 GHz and, corrected for slant angle, this became a 5-ns differential delay.

CHAPTER 4

Detector System Design and Test Pulse Generation

This chapter describes a series of UHE neutrino detection experiments performed with the Australia Telescope Compact Array. The ATCA is a radio telescope array located at the Paul Wild Observatory near Narrabri, 550 km northwest of Sydney, Australia (see Figure 4.1). It consists of six 22-m radio antennas stationed over a six kilometer track. The neutrino detection experiments used custom-designed hardware and advances in signal processing technology to take advantage of a 600-MHz (1.2–1.8 GHz) output available from the ATCA receivers. This wideband output provides the high time resolution required to detect dispersed sub-nanosecond pulses and, combined with array elements which are optimally sized to cover the entire Moon with their primary beam, make the ATCA attractive for UHE neutrino detection experiments using the lunar Čerenkov technique.

4.1 Lunar Čerenkov Detection Issues

The lunar Čerenkov technique is a promising method for the detection of UHE neutrinos. This technique uses Earth-based radio telescopes to detect the coherent Čerenkov radiation emitted when a UHE neutrino interacts in the outer layers of the Moon. Detection of UHE neutrinos is extremely difficult due to their low predicted flux (2 per km^2 per day per steradian for the standard GZK model) and low interaction probability (0.2% per km of water). For reasonable rates of detection, a detector volume of order 1000 km^3 sr is required (13). The lunar Čerenkov technique makes use of the lunar regolith as a detector which has a far greater volume than

Figure 4.1: The Australia Telescope Compact Array. Photo taken by R. McFadden during May 2008 lunar observations.

current ground-based detectors. However, the challenges presented by this technique involve achieving a high time resolution to detect extremely narrow pulses, maximising antenna sensitivity while maintaining Moon coverage, recovering full sensitivity by correcting for ionospheric pulse dispersion and combining the array elements with nanosecond timing.

4.1.1 Bandwidth and Data Rate Requirements

As discussed in Chapter 2, coherent Čerenkov radiation is a linearly polarised broadband emission (see Figure 4.2). The spectrum of Čerenkov emission rises approximately linearly with frequency until a peak value is reached. The peak frequency is determined by de-coherence and/or attenuation in the regolith, and can vary between a few hundred megahertz (for events viewed off the Čerenkov cone) and approximately 5 GHz (for events viewed on the Čerenkov cone). For skimming events, viewed just off the Čerenkov cone, the spectral peak falls in the 1–3 GHz range. Therefore observations in this range are sensitive to favorable geometries. At lower frequencies, the Čerenkov cone is broader, and these observations are sensitive to events with a wider range of interaction geometries. However, they also require a higher energy detection threshold.

The broadband Čerenkov emission produces a sub-nanosecond pulse and therefore detection requires gigahertz bandwidths to achieve a high time resolution. Due to excessive data storage requirements, the only way to exploit such high data rates is to implement real-time dedispersion and detection algorithms and to store potential events at full bandwidth for later processing. This requires innovations in hardware design to perform the necessary signal processing with nanosecond timing accuracy. Wideband circuits must also be designed carefully to avoid unwanted reflections in the system.

4.1.2 The Advantages of using a Radio Telescope Array

There are three possible types of interaction which may occur in the lunar regolith: ‘upward-going’, where the primary particle has penetrated through most of the Moon prior to interaction, ‘down-going’, where the primary interacts traveling toward the Moon and ‘Moon-skimming’ where the primary only penetrates through a small portion of the lunar limb and interacts traveling nearly parallel to the surface (see Figure 4.3) (12). Gorham *et al.* (63) found that that the ‘upward-going’ events are effectively ruled out as, at the highest energies, the neutrino mean free path is considerably less than the lunar diameter. For the remaining cases (‘down-going’ geometries in particular) radiation at or near the Čerenkov angle will be totally internally reflected by the lunar surface boundary leaving only weaker radiation, far off the Čerenkov cone, to escape. Moon-skimming and near Moon-skimming interactions will therefore be the main detectable events and most detectable signals will originate from the limb of the Moon (12). Detector volume and subsequent chances of detection can therefore be maximised by choosing antennas which are small enough to contain the whole Moon in their primary beam. However, the total collecting area must also be maximised to achieve the required antenna sensitivity.

In the gigahertz frequency range, an antenna with a diameter less than ∼20 m will be small enough to cover the entire Moon with its primary beam. Above this size, a trade-off occurs between antenna sensitivity and Moon coverage for a single dish aperture. While in principal a larger dish offers an increase in sensitivity, this gain is off-set by a decrease in Moon coverage due to the smaller beam size, and thus a reduced detector volume (see Figure 4.4). Using multiple smaller dishes allows an increase in sensitivity without the loss of coverage, provided that their separation is such that the thermal lunar emission – which dominates the system temperature – is incoherent between antennas. Using an array, signals can also be added coherently to form multiple beams around the limb of the Moon, where the event rate is maximised, and the array geometry can be exploited for Radio Frequency Interference (RFI) discrimination based on the signal direction of arrival. An array

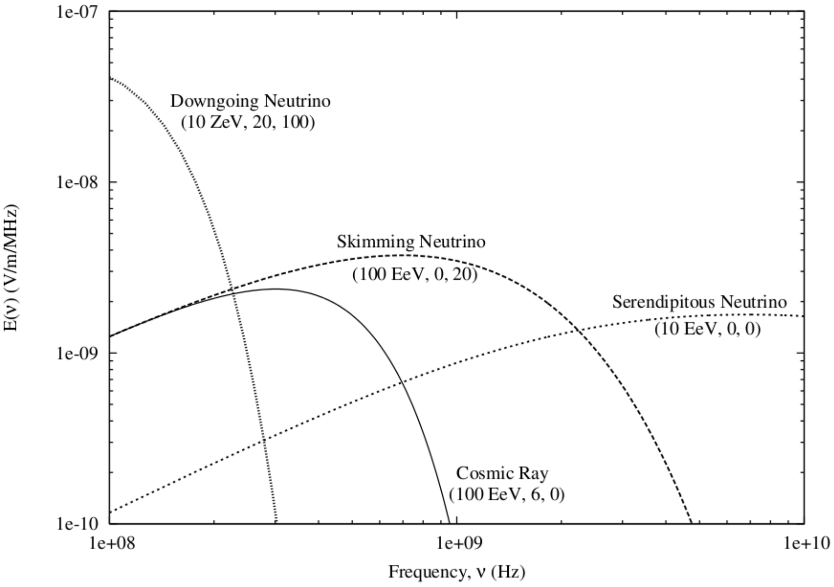

Figure 4.2: Simulated spectra of four different particle interactions as viewed from Earth. The three parameters (E, d, θ) give interaction energy, depth (m), and viewing angle for the Čerenkov angle respectively. (11)

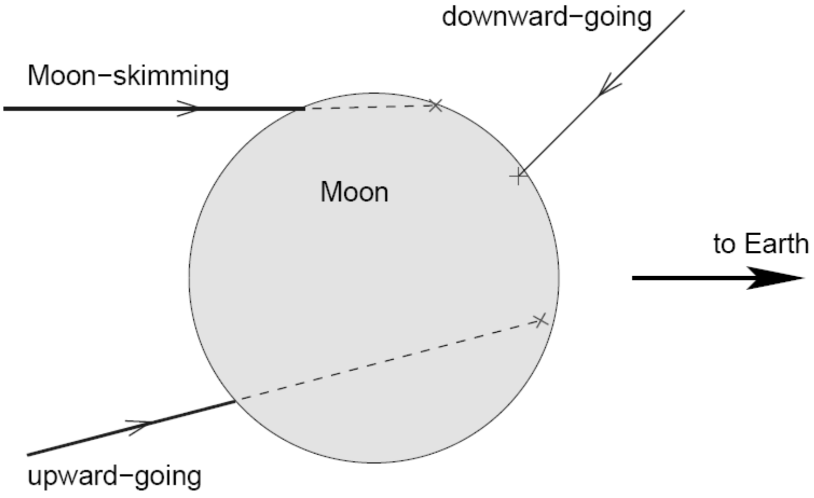

Figure 4.3: Neutrino Interaction Geometries. (12)

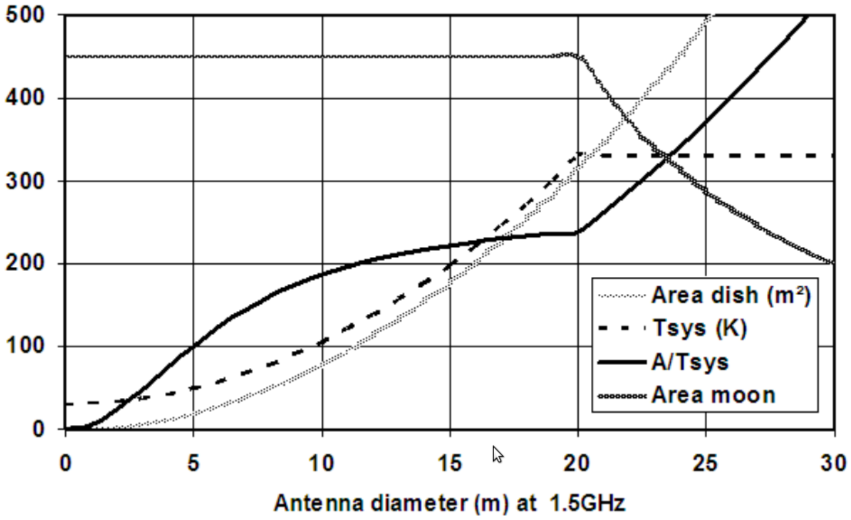

Figure 4.4: Telescope collecting area (m^2), T$_{\rm sys}$(K), A/T$_{\rm sys}$ and area of Moon in beam (arbitrary units) vs. antenna diameter (m) at 1.5 GHz. At this frequency, the primary beam of a 20 m diameter antenna will just cover the Moon. Antennas smaller than this will still cover the whole Moon. However, their sensitivity ($\propto$A/T$_{\rm sys}$) will not scale directly with aperture size as the system temperature will increase as the Moon fills more of the primary beam. For antennas larger than ~20 m, the Moon will fill the primary beam and the system temperature will remain independent of dish size. In this regime, increases in antenna sensitivity will be offset with a decreases in Moon coverage. (13)

of small dishes (~20 m in diameter) is therefore the optimum radio instrument for this experiment. The Compact Array consists of six 22-m dishes, and at 1.4 GHz the primary beam of a Compact Array antenna can illuminate the entire Moon, which makes it an ideal instrument for UHE neutrino detection experiments using the lunar Čerenkov technique.

4.1.3 Correcting for Pulse Dispersion in the Ionosphere

Lunar Čerenkov emission produces an extremely narrow pulse which travels through the Earth's ionosphere and experiences a frequency dependent time delay. This results in pulse dispersion similar to the dispersion experienced by pulsar pulses traveling through the interstellar medium. Lunar Čerenkov pulses received on an Earth-based radio telescope will therefore be dispersed by the ionosphere and further broadened by receiver bandlimiting.

The amount of ionospheric pulse dispersion must be known in real time to maximise the received signal-to-noise ratio and subsequent chances of pulse detection. Coherent pulse dedispersion requires an accurate knowledge of the ionospheric dis-

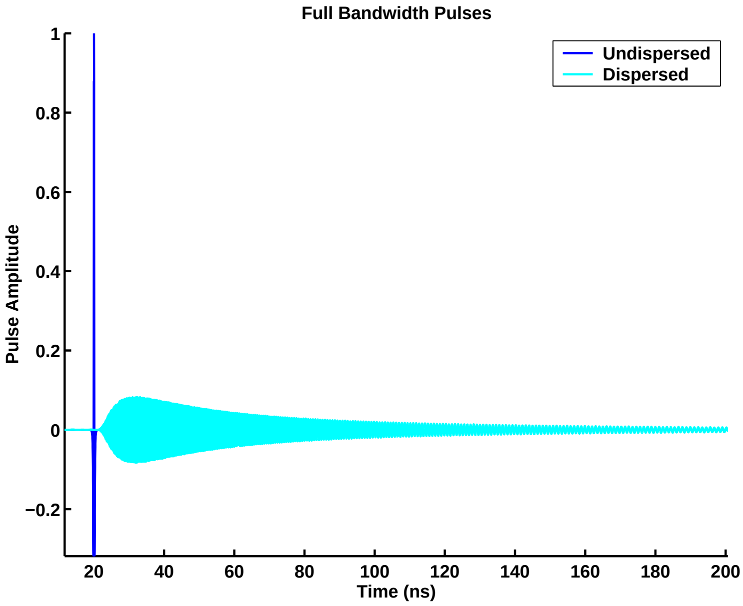

Figure 4.5: Pulse dispersion from ionospheric electron content of 100 TECU (corresponding to solar maximum). The dispersed pulse has a peak amplitude which is approximately 10% of the original pulse.

persion characteristic which can be parameterised by the instantaneous ionospheric TEC. The TEC produces a frequency dependent delay in the received signal via

$$\Delta t = 1.34 \times 10^{-7} \times TEC \times \nu^{-2}, \tag{4.1}$$

where Δt is in seconds, TEC is in electrons per m^2 and frequency is in Hz. Measurements of the ionospheric TEC can be derived from dual-frequency GPS signals and are available online from NASA's CDDIS (55) (see Chapter 3). However, these values are not available in real time nor directly line-of-sight to the Moon and instead rely on spatial interpolation algorithms. Therefore the author has developed a technique to use Faraday rotation measurements of the polarised thermal radio emission from the lunar limb combined with geomagnetic field models to obtain estimates of the ionospheric TEC which are both instantaneous and line-of-sight to the Moon (this method is presented in Chapter 6). Once TEC estimates have been obtained, pulse dispersion can be corrected using either analog or digital technology.

4.1.4 Investigation of Digital Dedispersion Techniques

A promising digital solution lies in the use of high speed Field Programmable Gate Arrays (FPGAs). An FPGA implementation allows the dedispersion characteristic to be tuned in real time to reflect temporal changes in the ionospheric TEC. Dedispersion can be performed in a filterbank structure which consists of a series of narrowband filters. Using this approach, an inverse ionospheric frequency characteristic can be applied to each frequency sub-band. In a traditional post-detection filter bank implementation, the detected output from each sub-band is delayed appropriately to compensate for dispersion delay. This method is not coherent and leaves a residual time smearing across the sub-bands which incurs a signal-to-noise ratio (SNR) penalty. The final time resolution is also limited to the reciprocal sub-band width. A fully coherent or predetection dedispsersion method was pioneered by Hankins and Rickett (64) (65) which completely eliminates the effect of dispersive smearing. This is achieved by passing the predetected signal through an inverse ionosphere filter which can be implemented in either the time or frequency domain.

The original frequency domain approach used an FFT (Fast Fourier Transform) architecture followed by a filter matched to the ionospheric dispersion characteristic. However, coherent dedispersion can also be implemented in a polyphase filterbank which consists of a polyphase FIR (Finite Impulse Response) pre-filtering stage that feeds into an FFT structure (66). The advantage of the pre-filtering stage is that the bandpass response for each channel can be specifically designed as opposed to FFT based methods which can only have a sinc function response. Polyphase filtering is a branch of multi-rate digital signal processing (67). In a polyphase filter, the data stream is distributed over n filter branches, each of which operates at a lower sampling rate ($1/n \times F_s$) than the original data. The signal on each branch is therefore aliased down to the same band, however, the relative phase between them is different. This information is preserved and can be exploited to reconstruct a signal at the original data rate after processing in the frequency domain (68). Using this architecture, signal phase information is preserved and therefore coherent dedispersion is possible. The polyphase structure provides additional efficiency since computations can be shared among the decimated filterbank channels. However, for the relatively small amount of dispersion produced by the ionosphere, a frequency domain implementation will require significantly more overhead than a more straightforward time domain FIR filter implementation. The frequency domain implementation is a more attractive ionospheric dedispersion option for hardware with a pre-existing filterbank architecture, such as hardware which has been optimised for beamforming, or when a longer FIR filter is required due to increased dispersion (*i. e.* during solar maximum).

For the ATCA experiments, the hardware available for digital dedispersion consisted of a single Xilinx Vertex 4 FPGA on a 2 GHz Analog to Digital Converter (ADC) board (see Section 4.2.3). For this hardware a time domain implementation was considered which involves using an FIR filter matched to the ionospheric characteristic. As the Xilinx Vertex 4 operates at a maximum of 512 MHz (latching on both clock edges), a parallel implementation such as polyphase filter decomposition is required. This describes the process of decomposing a fast data stream (*e. g.* 2 GHz) into several smaller data streams (*e. g.* 4 x 512 MHz) for processing data in parallel. As with other polyphase schemes, each stream at the lower data rate has a relative phase offset to each other which can be exploited later for signal reconstruction.

An FIR filter is essentially a weighted tapped delay line filter which produces each output sample from a weighted sum of previous inputs. The number of previous inputs which contribute to each output sample is referred to as the filter length. For an inverse ionosphere characteristic, the filter length is determined by the maximum delay introduced by the dispersion *i. e.* if the dispersed pulse is spread out over m samples, to correct for the effects of dispersion, each output sample must be composed of the correct weighted sum of m input samples and therefore the filter must be of length m. This means that the required filter length increases with ionospheric TEC and/or signal bandwidth. Preliminary calculations of the required filter length for ionospheric dedispersion raised concern that a single FPGA may not be sufficient to handle the subsequent number of floating point operations (in part due to an error in the dispersion relation which was used for the initial calculations, see Section 3.3). This was particularly a concern for daytime observations and later experiments which would occur outside of solar minimum. It was therefore decided to restrict ATCA experiments to night-time observations (when the ionosphere is most stable and has its lowest TEC) and to make use of analog technology with a fixed dedispersion characteristic (see Section 4.2.1).

4.2 ATCA Experimental Detection System Design

The UHE neutrino detection experiments made use of the ATCA, an Earth Rotation Aperture Synthesis Array located in northern NSW. The array consists of six 22-m dish antennas, three of which have been fitted with custom-designed hardware for the neutrino detection experiments. These experiments make use of a 600-MHz bandwidth signal (1.2–1.8 GHz) available from monitor points at the receiver in each antenna. Since the monitor points are not usually used for data capture, obtaining this bandwidth required the development of customised detection hardware, which had to operate with nanosecond timing accuracy, and using an alternative signal path back to the computers in the site control room. For these experiments, analog dedispersion filters and a FPGA-based trigger system were developed to detect events in real time and transmit event data to the control room via an ethernet link. The full signal path at each antenna is shown in Figure 4.6.

The compact array L-S band feed horn is sensitive to frequencies in the 1.2–2.5 GHz range. As part of the standard ATCA receiving system, this wideband signal is split into its L and S band counterparts, centred at 1.5 and 2.3 GHz respectively, and each of these bands is further split into dual linear polarisations. The split polarisations are amplified using low noise amplifiers (LNAs) and pass through various splitter modules before reaching an RF monitor point. For the neutrino detection experiments, the 600-MHz signal was taken from the L-band monitor point and connected directly to custom-made analog dedispersion filters.

4.2.1 Analog Dedispersion Filter Design

Ionospheric pulse dispersion must be corrected in real time to maximise the received signal-to-noise ratio for threshold detection (37). For these experiments, pulse dedispersion was achieved through the use of innovative new analog dedispersion filters which employ a method of planar microwave filter design based on inverse scattering (69). These filters were developed by Paul Roberts at the Australia Telescope National Facility (ATNF).

Inverse scattering describes the process of reconstructing the physical properties of a scatterer, such as its shape or density, based on its scattering data. Techniques based on this process can therefore be used to design microwave transmission structures with complex scattering properties that realise a particular frequency response. For lunar Čerenkov detection experiments, a matched filter with an inverse ionospheric characteristic is required to recover full pulse sensitivity. Therefore the desired filter response has a group delay which is quadratically chirped according to (the inverse of) Equation 4.1. This is essentially an all pass filter with a non-linear phase response. Inverse scattering techniques have been used to realise this design in microstrip lines which have a continuously changing impedance profile (see Figure 4.7). Changes in the impendence profile correspond to width modulations on the microstrip line and cause cascades of frequency dependent reflections which sum to produce the desired inverse ionosphere frequency response. A mask of the microstrip profile can be seen in Figure 4.8 and the resulting frequency response in Figure 4.9.

The filters consist of 1 m of tapered microstrip line which were coiled into a spiral pattern for easy storage (see Figure 4.10). Signals enter and exit the filter through the same point, having undergone reflections through the length of the microstrip line, therefore an isolator module is required to direct the signal flow into and out of the filter (see Figure 4.11).

As the microwave dedispersion filters have a fixed dedispersion characteristic, an

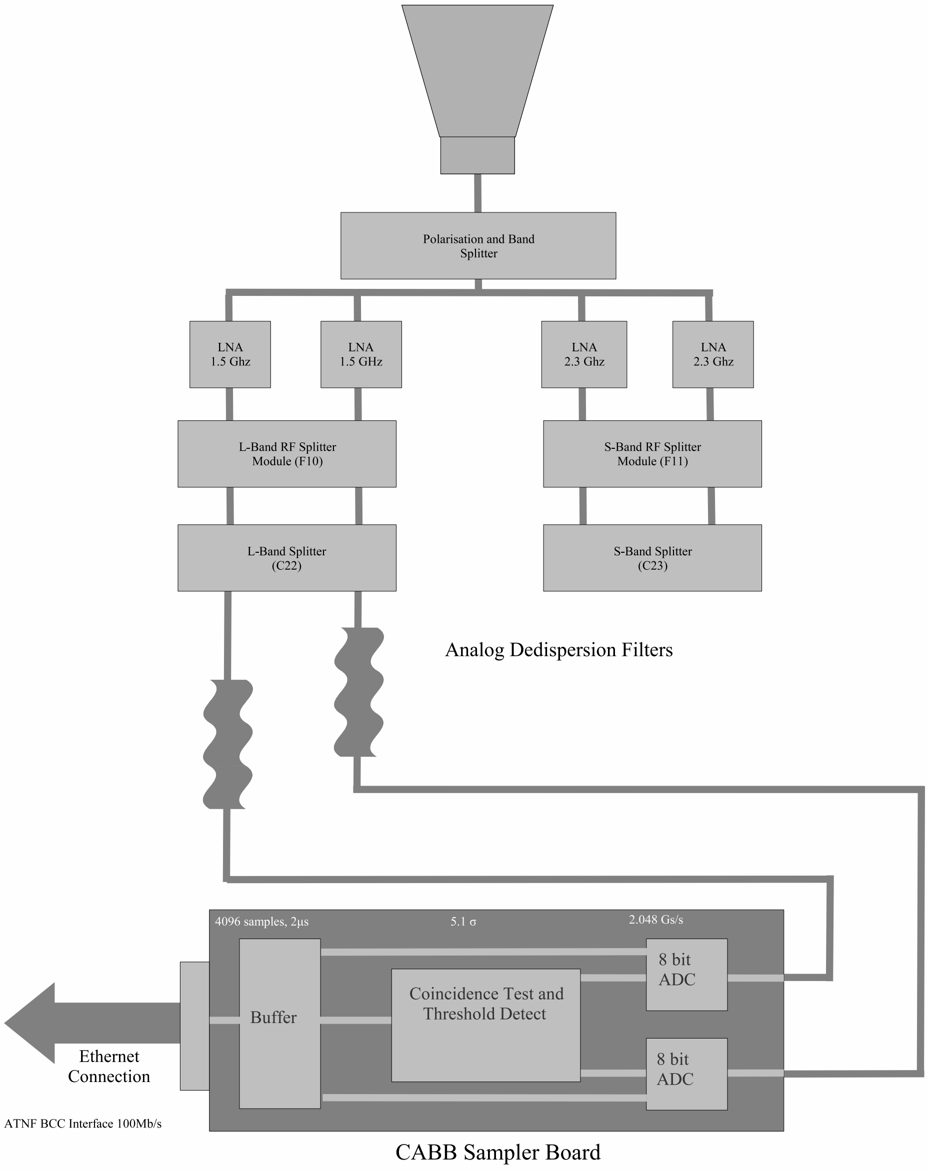

Figure 4.6: Diagram of the signal path at each antenna. The modules down to and including the L-Band splitter module represent the standard ATCA signal path, the customised hardware is shown from the dedispersion filters onwards.

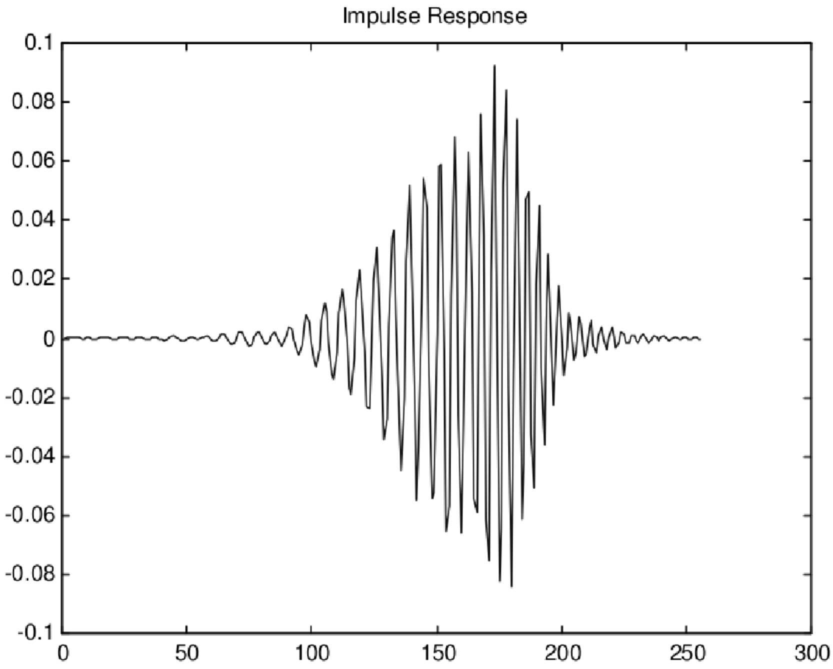

Figure 4.7: Impedance profile (vs. distance) along the dedispersion filter. (14)

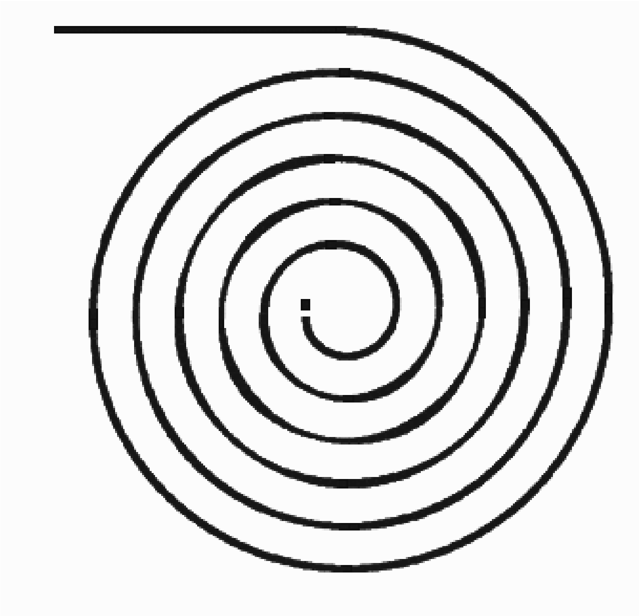

Figure 4.8: Dedispersion filter mask pattern. (14)

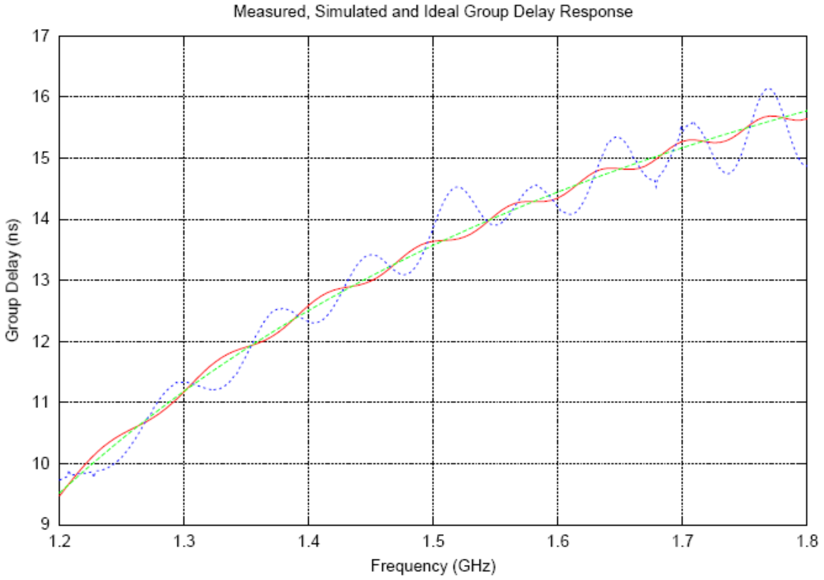

Figure 4.9: Filter group delay: measured (*blue*), simulated (*red*) and ideal (*green*). (14)

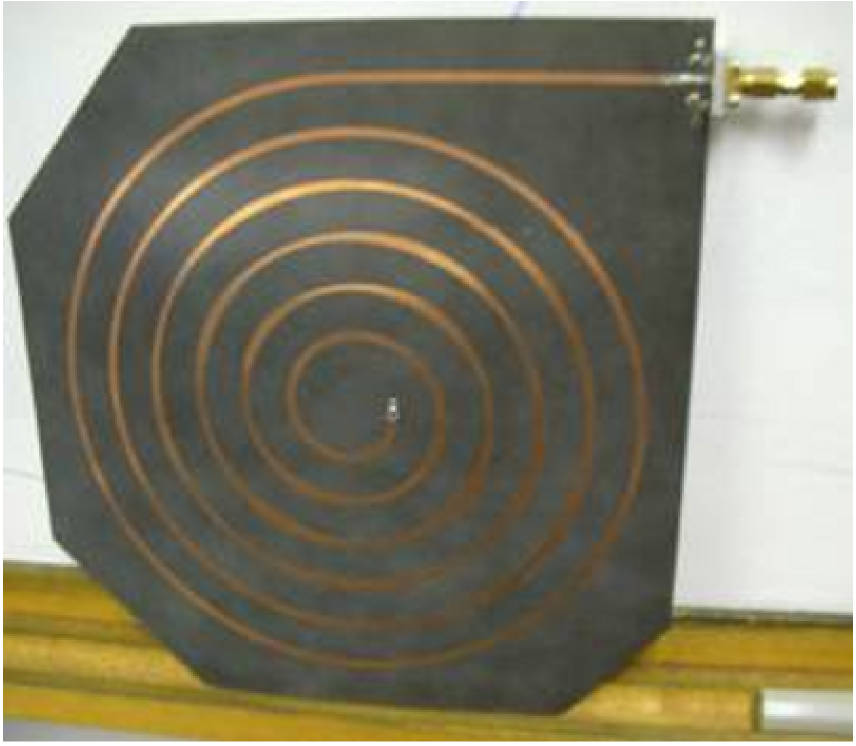

Figure 4.10: Prototype dedispersion filter. Photo by P. Roberts, ATNF.

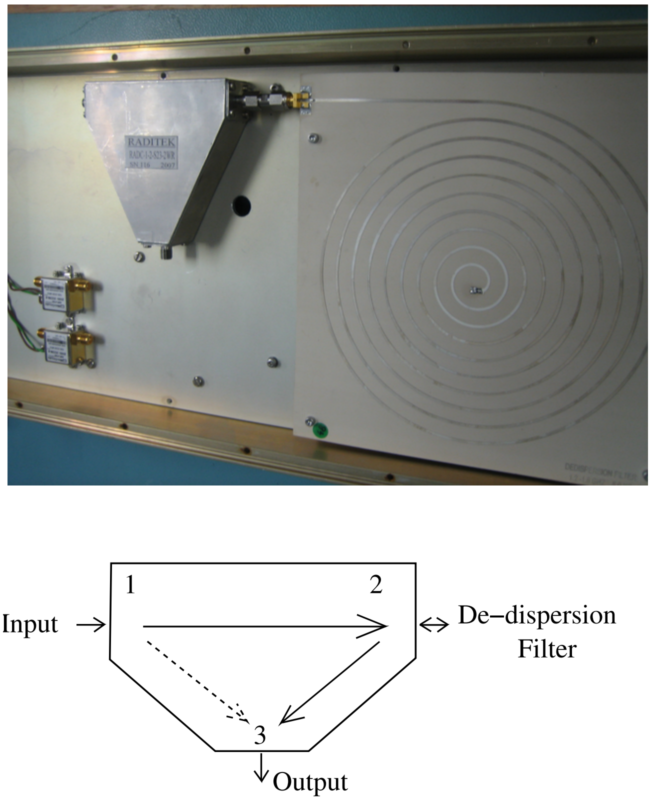

Figure 4.11: (*Top*) Rack-mounted dedispersion filter. The triangular box to the top left is the isolator module which directs signal flow in and out of the filter. (*Bottom*) Signal flow through the isolator module. Photo taken by R. McFadden before Feb 2008 observations.

estimate had to be obtained for the TEC which would minimise errors introduced by temporal ionospheric fluctuations. The ATCA detection experiments were performed in 2007 and 2008 during solar minimum and therefore relatively stable ionospheric conditions. Initial observations were during the nights of May 5, 6 and 7, 2007 and these dates were chosen to ensure that the Moon was at high elevation (particularly during the night-time hours of ionospheric stability) and positioned such that the ATCA would be sensitive to UHE particles from the galactic center. The author obtained CDDIS measurements for the month of May 2006 which gave an average Vertical TEC (VTEC) of 7.06 TECU over night-time hours (10pm–8am) with a standard deviation of 1.3 TECU. The filter design therefore assumed a differential delay of 5 ns across the 1.2–1.8 GHz bandwidth, which was based on the average VTEC value, corrected for slant angle through the ionosphere, and converted to a differential time delay (see Chapter 3 for more details). GPS data available post experiment revealed that the average VTEC for these initial nights of observation was actually 7.01 TECU which gave an average differential delay of 4.39 ns, with a standard deviation of 1.52 ns, corrected for slant angle.

4.2.2 Comparison of Analog and Digital Technologies

In 2009, the LUNASKA collaboration started a series of UHE neutrino detection experiments using the 64-m Parkes radio telescope. Details of the Parkes experiments have not been included in this thesis, however, one interesting development was the implementation of a digital dedispersion filter. The digital filter implementation was possible for these experiments since only a 300 MHz bandwidth was available (compared to 600 MHz at the ATCA). The specifications for this digital filter and the analog dedispersion filter, employed in the ATCA system, can both be found in Table 4.1.

Analog filters are very inexpensive to produce however there are two main drawbacks to this approach. These are a high insertion loss and a fixed delay characteristic. The insertion loss scales with differential delay due to multiple reflections which occur in the filter's extra physical length. The maximum practical differential delay is therefore determined by the filter length at which the insertion loss becomes greater than the dedispersion gain. However, the filter design methods are not analytic and this length must be empirically derived.

As the required filter length increases a cascade of shorter filters will perform better than one long filter since the effects of multiple reflections are minimised. A suite of shorter filters can also be used to 'tune' the dedispersion characteristic. However, dedispersion tuning requires a range of filters to match the time-varying

	Insertion Loss	Maximum Clock Rate	Data Rate /Bandwidth	Differential Delay (max.)
Analog Filter	3 dB (over 1 GHz)	NA	1.2–1.8 GHz	designed for 5 ns*
Digital Filter	0.1 dB	256 MHz	1.024 GS/s	0–8 ns (1ns steps)
Digital Pulse Generator	NA	256 MHz	2.048 GS/s	0–500 ns (0.5ns steps)

Table 4.1: Design specifications for the analog and digital filters and the digital pulse generator. High data rates are achieved using a parallel implementation. (*) The analog dedsipersion filter does not have a definite maximum achievable differential delay and therefore this is the value of delay which the filter was designed for. The filter length can be increased to produce longer delays at the cost of an increase in insertion loss. The maximum practical differential delay is therefore determined by the filter length at which the insertion loss becomes greater than the dedispersion gain. However, the filter design methods are not analytic and this length must be empirically derived.

ionospheric TEC and this would be significantly more complex and expensive than implementing a single design.

The insertion loss of a digital dedispersion filter is almost negligible. Therefore a digital implementation is likely to be the best option as long as the filter architecture can handle the number of operations associated with the required differential delay. For the Parkes experiments, the digital dedispersion filter was implemented on a Vertex 4 FPGA. The maximum FIR filter length which can implemented is determined by the number of hardware multiplier blocks and the speed at which they can be used. The Vertex 4 has a maximum clock speed of 256 MHz, therefore signal processing had to be done in parallel to achieve a higher data rate. A 4:1 parallelism was used on its 32-bit multipliers to produce an 8-tap FIR filter at four times the original data rate, 1.024 gigasamples per second (GS/s). At this data rate, an 8-tap FIR filter can theoretically correct for a maximum of 8 ns of delay (equivalent to 8 samples). However, in practise a number of degrees of freedom are used up in obtaining the correct shape in the filter's response and minimising the group delay error. Therefore in reality, the maximum differential delay which can be corrected for using a Vertex 4 is $\sim$4 ns. This sort of delay is typical for solar minimum conditions (see Table 4.2). However, as the next solar maximum approaches, digital dedispersion at these data rates will require a more complex implementation.

4.2.3 FPGA Based Event Detection Boards

The ATCA experiment made use of FPGA based ADC boards for event triggering. These boards were designed as part of a broadband upgrade planned for the Compact

	Typical TEC (TECU)	Differential Delay (over 1.2–1.8 GHz)
Solar Min.	10	5 ns
Solar Max.	100	52 ns

Table 4.2: Typical solar minimum and solar maximum values for a mid-latitude region such as the ATCA.

Array which will eventually extend its bandwidth capability to 2 GHz bandwidth, over 1–3 GHz. FPGAs are reprogrammable semiconductor devices, composed of Configurable Logic Blocks (CLBs), which can perform simple logic tasks as well as more complicated mathematical and signal processing algorithms. Their reconfigurable logic blocks also provide the ability to optimise hardware interconnections for each specific algorithm implemented. Modern FPGAs can operate at clock frequencies of around 500 MHz and have signal processing capabilities that far exceed anything previously available for optimised real-time operation. This high speed operation and optimised processing power make FPGAs an ideal technology to perform real-time signal processing and pulse detection.

One of the main challenges of the CABB upgrade was to develop an ADC board capable of supporting the 4.096 GS/s rate required for processing 2 GHz of bandwidth (see Figure 4.12). To overcome this challenge, the ATNF developed an ADC subsystem which is composed of two commercial 2 GS/s 10-bit ADC chips and can be operated in an interleaved fashion. For normal CABB operation, the same input is distributed over the two converters with their sampling times in precise anti-phase, to give an equivalent 4 GS/s 10-bit converter. The subsystem can also be used as two independent 1-GHz bandwidth ADCs and was employed in this configuration for the Parkes Radio Telescope 1-GHz pulsar digital filter bank correlator.

The independent input configuration was also used for the ATCA neutrino detection experiments. The two 2.048 GS/s inputs were used to import the two linear orthogonal polarisations of the 600-MHz RF signal. Inside the board, the sampled inputs were then multiplexed into parallel 512-MHz data streams for input into a Xilinx Virtex 4 FPGA to perform pulse detection (see Figure 4.13). The Xilinx Virtex 4 only has a 256-MHz processor, however, its data rate can effectively be doubled by latching data on both the rising and falling clock edges. Detection was performed via an adjustable threshold on both polarisation streams. The sampled data was buffered for 125 ns (256 samples) so that data surrounding candidate events could be sent back and recorded in the case of a detection.

For these experiments at the ATCA, the full 600-MHz bandwidth could not be

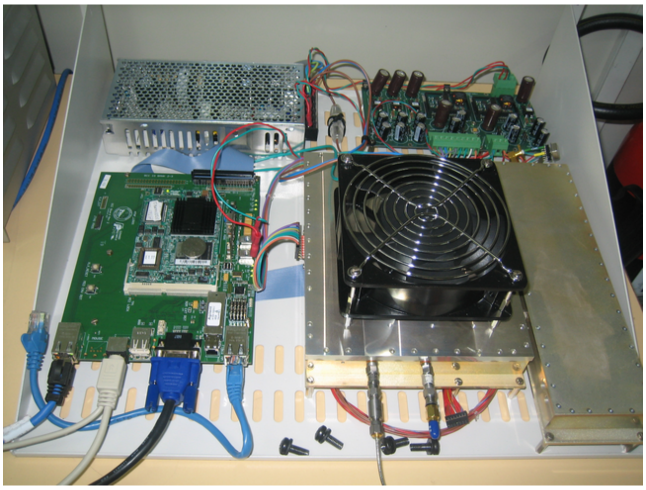

Figure 4.12: Pulse detection equipment rack. The board in the lower left corner is the onboard PC which controls data flow back to the control room. PC interrupts are generated by the CABB digitiser board (hidden by the large fan on the bottom right). The back of the rack contains power supply circuitry. Photo taken by R. McFadden before May 2007 observations.

returned to the central processing site for coincident triggering. Instead events triggered independently on each antenna, and this sent an interrupt to an on-board computer to capture the event data. The data was then returned asynchronously to a central processing site via a gigabit ethernet connection for off-line processing. The dedipsersion filters and CABB ADC boards were installed on three antennas so that coincidence testing and direction of arrival discrimination could be performed during off-line processing. As each antenna triggered independently, trigger timing information and nanosecond synchronisation was essential for both of these processing stages.

4.3 Test Pulse Generation

Lunar Čerenkov pulses are much shorter in duration than any signals normally encountered in radio astronomy. Therefore pulse generators, which could produce nanosecond scale pulses, were required to test the operation and timing accuracy of the custom-designed pulse detection hardware. There are two main strategies for nanosecond test pulse generation. An analog pulse generator is much simpler to implement, however, there is little flexibility to modulate the pulse with any specific features such as spectral shape or dispersion characteristic. The second option is to program a digital pulse generator which provides much greater flexibility in pulse

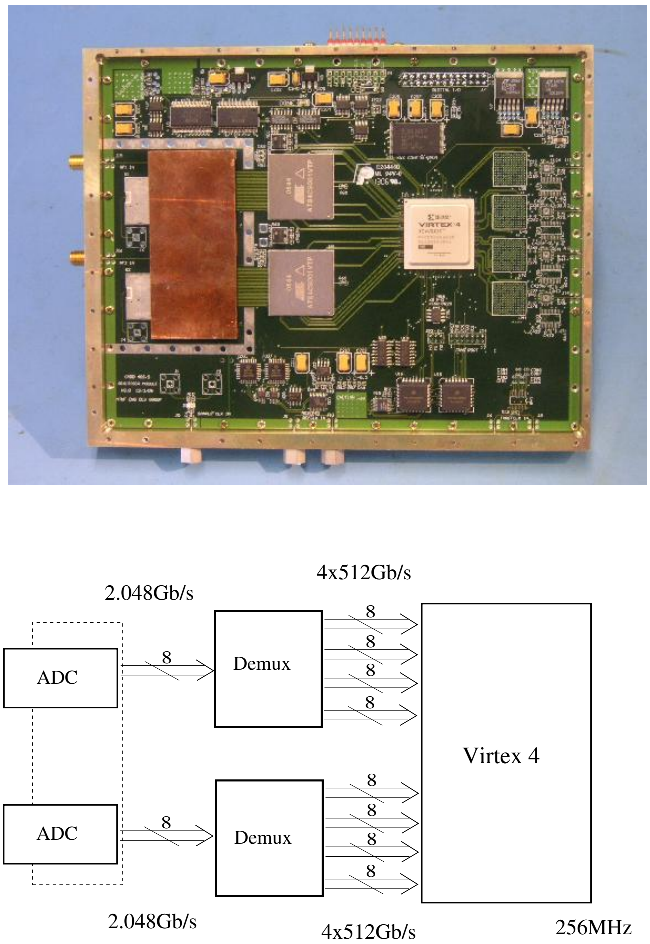

Figure 4.13: CABB ADC board. (*Top*) Photo by P. Roberts (*bottom*) Block diagram of ADC board. (*From left to right*) The two digitisers (one for each polarisation stream) feed into demultiplexers which split each polarisation stream into lower data rate substreams for input into the Virtex 4 FPGA.

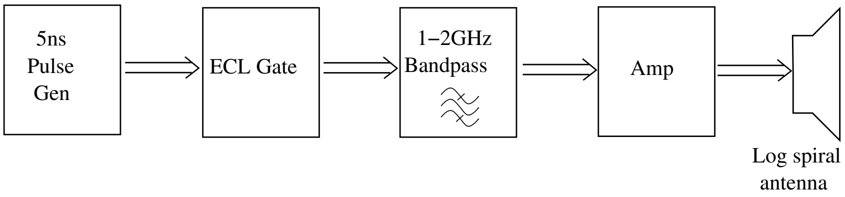

Figure 4.14: Analog pulse generator.

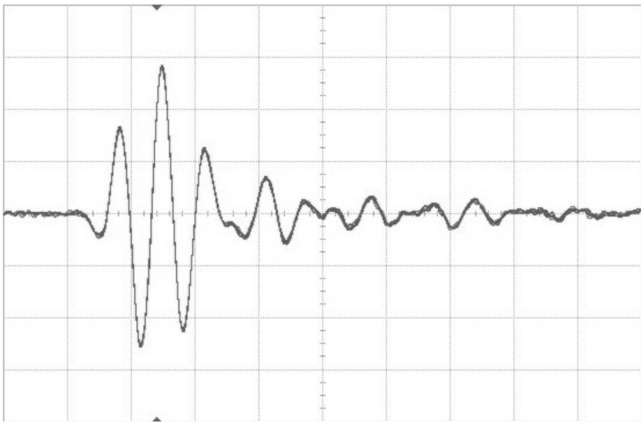

Figure 4.15: Test pulse generated by the analog pulse generation equipment. Horizontal scale is 1 ns per division and vertical scale is 200 mV per division.

characteristics. However, this is at the cost of greater complexity in implementation and programming. Both methods of test pulse generation were employed for the ATCA neutrino detection experiments.

4.3.1 Analog Pulse Generator

To generate nanosecond test pulses from analog hardware, a commercial wave generator was used (see Figure 4.14). The wave generator was set to produce a square wave with a period of approximately 5 ns. This was used as a seed to trigger an ECL (Emitter Coupled Logic) gate with a 300 ps rise time output. The fast rise time of this gate replicates the original waveform with extremely sharp edges which produce a flat spectrum. When one of these edges passes through a 1–2 GHz bandpass filter and amplifier a sub-nanosecond pulse is produced. These pulses have a 600 mV/(+8 dBm) peak voltage/(power) as seen in Figure 4.15. This basic pulse generator was connected to a log periodic spiral antenna that covers the 1–2 GHz band and assembled on the roof of the ATCA site control building (see Figure 4.16) for transmission toward the array.

Figure 4.16: Analog pulse generator set up on the roof of the ATCA control building. (*From back to front*) The waveform generator (grey box) drives the ECL gate (on the green board). The output of the ECL gate passes through a 1–2 GHz bandpass filter (silver rectangle) and a signal amplifier (small square box). The large white box to the left is the power supply.

Test pulses generated by this analog system were transmitted horizontally toward the array and captured by the custom pulse detection hardware installed at each antenna (see Figure 4.17). Since the array has a minimum elevation limit of 12°, it was not possible to point the antennas directly at the pulse generator and the transmitted pulses therefore entered the system through the antenna side lobes. The captured pulses were broadened over a few hundred samples (corresponding to roughly 100 ns) and contained highly complex structure. The increased complexity in the pulse structure was caused by reflections of the pulse entering the receiving system through multiple paths. These reflections may have been delayed and/or attenuated with respect to the original pulse by reflecting off structures before entering the feed horn or entering the receiving system through components other than the feed horn.

Wideband systems can also generate reflections internally. The isolator module attached to the dedispersion filters produces such internal reflections. They are caused by leakage from the input to the output of the isolator which bypasses the intended signal flow through the filter. Reflections associated with the isolator were detected by looking at the effects of this module on a pulse generated within the ATCA receiving system.

The ATCA has a noise calibration diode which switches a calibrated noise source, located in each antenna, on and off at a rate of 8 Hz (70). Switching this diode on couples the calibrated noise source into the receiver's RF path before the low noise

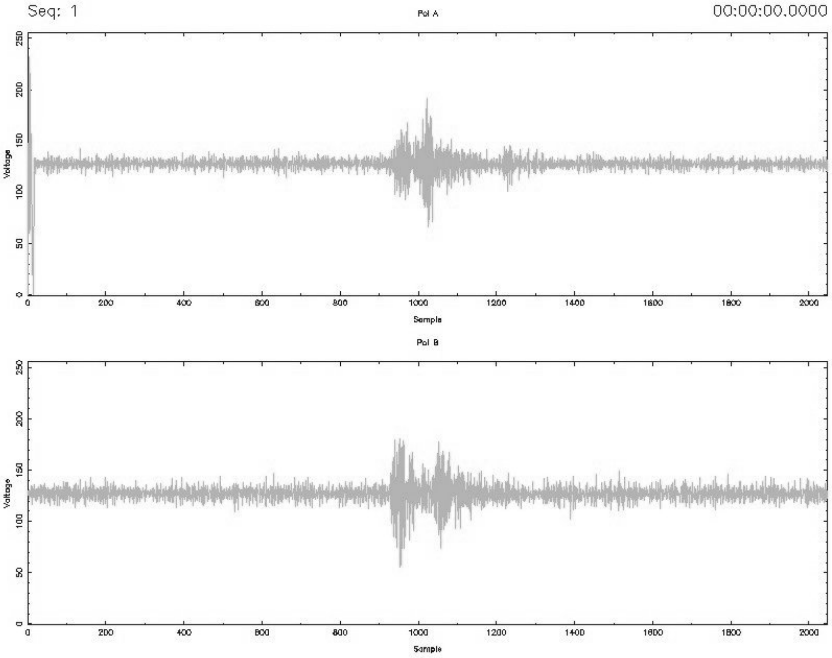

Figure 4.17: Test pulses generated by the analog pulse generation equipment and captured through the pulse detection hardware installed on the ATCA. Vertical axis is in mV.

amplifiers so that the level of multiplicative noise in the system can be measured. This process is used to monitor the gain and system temperature in each antenna. When the noise calibration diode is switched off, the circuit driving the diode generates a nanosecond scale pulse. This nanosecond scale pulse, generated by the diode circuitry, was a serendipitous discovery made using the UHE neutrino fast pulse detection equipment.

The noise calibration diode was switched off during detection experiments to avoid saturating the pulse detection equipment trigger rates. These pulses occur asynchronously in each antenna, due to differing transmission delays, and therefore were not ideal for testing the pulse detection equipment. However, they provided a simple way to trigger all buffers for the quasar calibration (see Section 4.5) and they also provided an insight into how pulses can be reflected internally within the system.

To investigate these reflections, the diode was set switching and one polarisation stream was allowed to bypass the dedispersion filter rack and subsequently the isolator module. A pulse captured during this investigation can be seen in Figure 4.18. The plot shows both the polarisation stream which bypassed the filter rack (*top*) and the stream which took the usual path through the pulse detection system including the filter rack (*bottom*). The pulse which passed through the rack is delayed and shows some broadening due to the effects of the dedispersion filter (the filter will disperse a pulse which enters it undispersed) and a pre-pulse can be seen approximately 35 samples or 18 ns before the main pulse. The pre-pulse occurs at precisely the same time as the pulse in the other polarisation stream (which did not pass through the filter) confirming that it is likely to be a reflection of the main pulse that has leaked through the isolator and bypassed the dedispersion filter. This pre-pulse does not show the broadening associated with the dedispersion filter and is also heavily attenuated (by approximately a factor of five with respect to the main pulse) which is also consistent with it being caused by leakage through the isolator.

Therefore while the analog pulse generator was successful in generating pulses which were captured by the custom-designed pulse detection equipment, the captured pulses were distorted by multipath reflections through the receiving system. A further example of this multipath reflection effect was found by investigating reflections of a nanosecond scale pulse generated internally within the ATCA.

4.3.2 Digital Pulse Generator

The use of a digital pulse generator allows the possibility of programming features such as spectral shape and pulse dispersion characteristics into a test pulse. It was

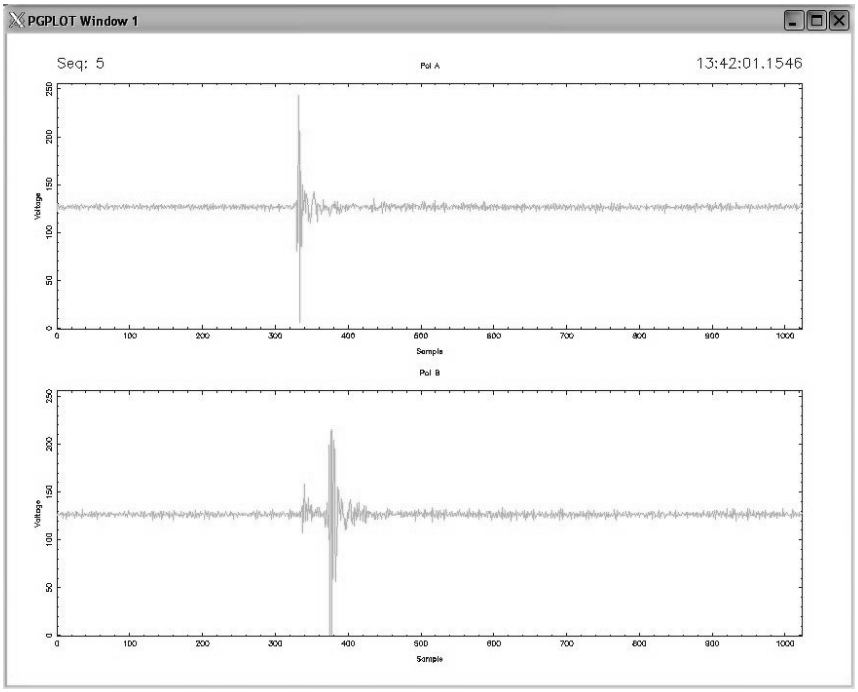

Figure 4.18: Noise calibration pulse captured by the pulse detection hardware. (*Top*) Polarisation stream which bypassed the dedispersion filter rack. (*Bottom*) The stream which took the usual path through the pulse detection system including the filter rack. Vertical axis is in mV.

implemented on a 2 GHz digital to analog converter which takes its input from a firmware memory block in a Xilinx Virtex 4 FPGA. The test pulse can be programmed directly into the memory block as a digital binary signal and this is converted to an analog waveform via an MD653CI (see Appendix A) 10-bit Digital to Analog Converter (DAC).

The logic blocks within an FPGA can be reconfigured to optimise their performance for a particular algorithm. The behavior of these blocks is defined by a Hardware Description Language (HDL) which is translated to a series of logic interconnections in the FGPA architecture via an electronic design automation tool (Xilinx ISE). The schematic design of the digital pulse generator can be seen in Figure 4.19. The *memb* structure is a memory block which stores the 10-bit samples of the digital pulse being generated. The input to this memory block is taken as a text file which can be specified using the Xilinx ISE tool. The contents of the text file are then uploaded into the firmware memory bock during programming of the FGPA.

The samples leaving the *memb* block are latched on both edges of the clock signal. This effectively doubles the output data rate of the Virtex 4 from 256 MB/s to 512 MB/s. Samples are also distributed across a data bus so that forty bits are output at once. The forty bits are composed of four samples in time, each consisting of ten bits, and this effectively increases the output data rate again by a factor of four to achieve the required 2 GB/s sampling rate. The output samples go through differential input/output buffers (denoted by gates labeled *OBUFDS* on the schematic) to produce the differential pairs required for input to the DAC.

The MD653CI takes as its input four, 10-bit differential pair data streams at 512 MB/s each (see Figure 4.20). These streams are multiplexed together to form the full 2 GB/s data stream which is latched and encoded to drive the digital to analog converter. The DAC uses a complementary interpolation format (see Figure 4.21). Like a return-to-zero format, complementary interpolation makes signal images in the second and third Nyquist zones usable and extends the available frequency range up to 3 GHz *i. e.* the third Nyquist zone with a 2 GHz clock (see Figure 4.22). The advantage of complementary interpolation over a return-to-zero format is that it avoids the reduction of output signal power that is introduced by the zero-valued samples in a return-to-zero scheme. This makes complementary interpolation an ideal interpolation scheme for wideband or high frequency digital to analog conversions.

The required pulse should occupy the 1.2–1.8 GHz band (to match the specifications of the pulse detection hardware). Using standard interpolation methods, *i. e.* operating in the first Nyquist zone only, this would require a 4 GHz clock signal and introduce increased complexity in hardware design. However, using the complementary interpolation method allows a 2 GHz clock signal to be used by making available

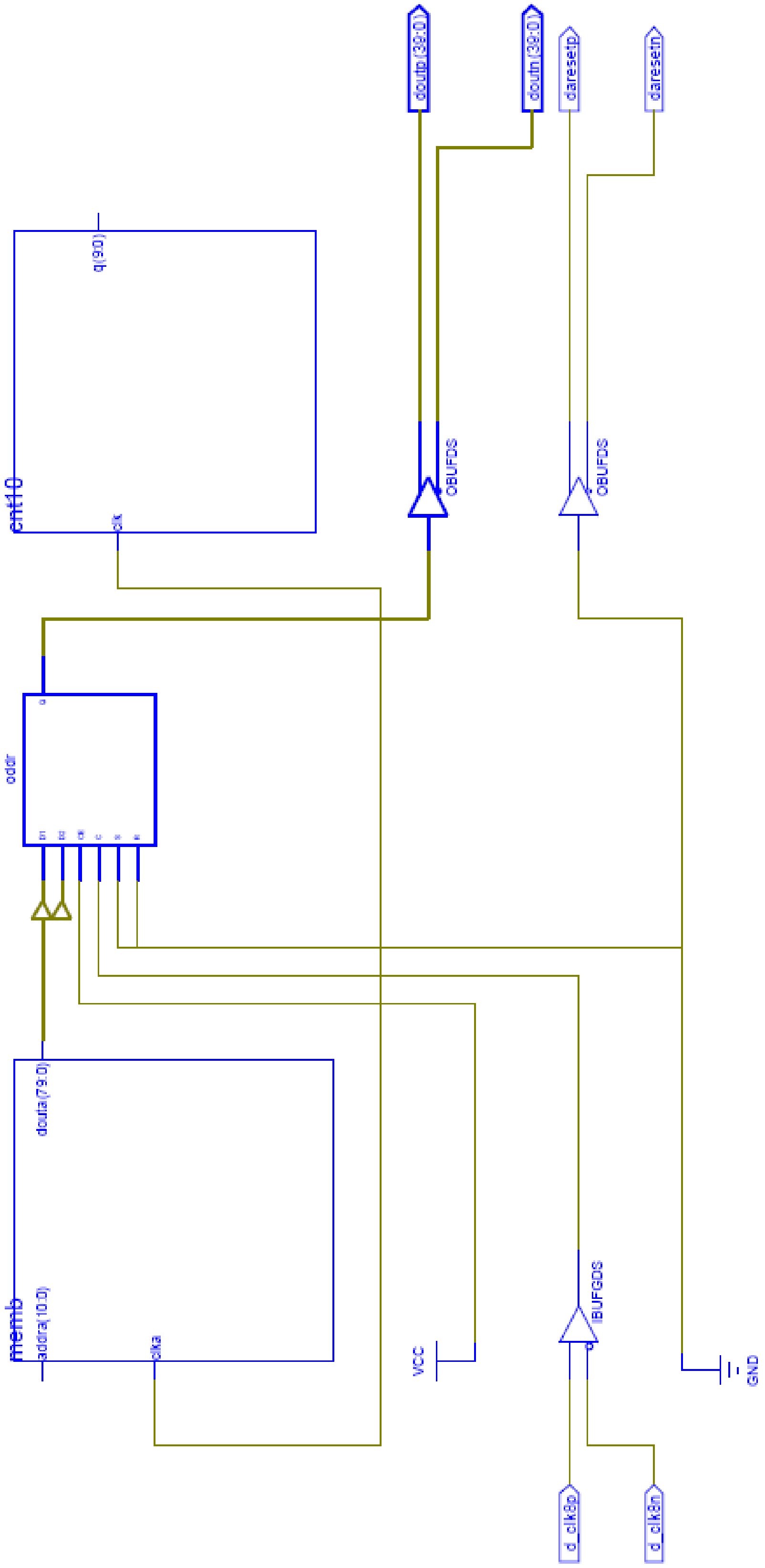

Figure 4.19: Schematic design of the digital pulse generator FPGA firmware.

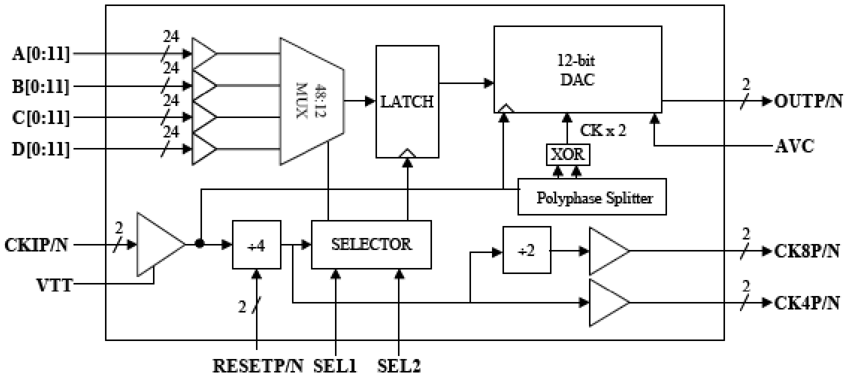

Figure 4.20: Block diagram of the MD653CI high speed 2 GHz multiplexer digital to analog converter.

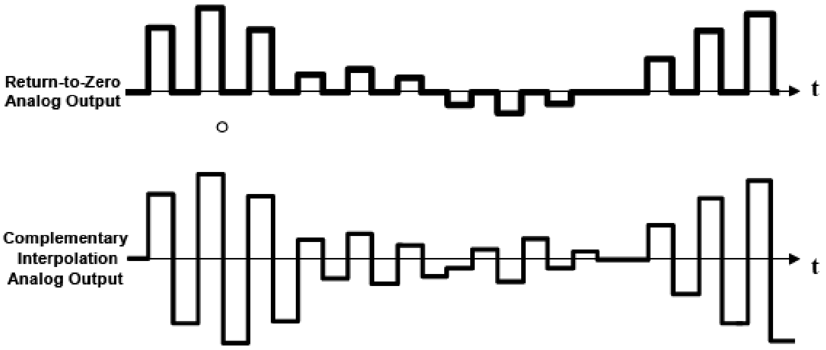

Figure 4.21: Comparison of return to zero and complementary interpolation output waveforms in the time domain.

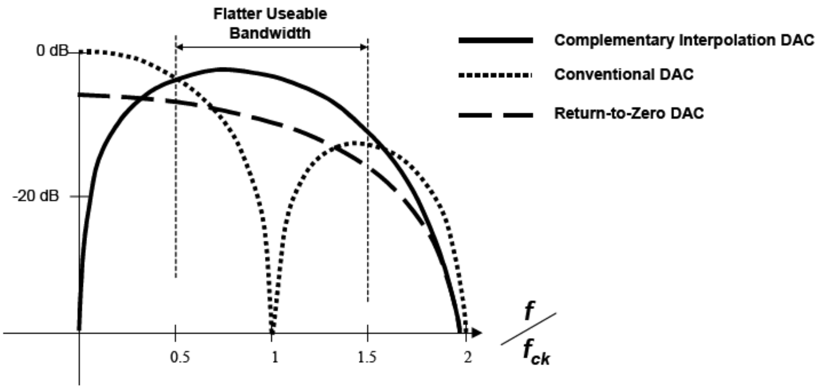

Figure 4.22: Comparison of spectral envelope between conventional non-return-to-zero, return-to-zero and complementary interpolation outputs.

the signal image in the second Nyquist zone. Therefore, to produce the correct image in the second Nyqist zone (1–2 GHz), the required 1.2–1.8 GHz signal must first be mirrored into the first Nyquist zone (0–1 GHz) before programming into the FPGA memory block (see Figure 4.23). As the signal is sampled, this spectrum will be mirrored back into subsequent Nyquist zones and complementary interpolation in the DAC will ensure a usable response in these second and third zones.

The author generated the required digital pulse samples in *Matlab*. These samples were produced as a continuation of the simulation work described in Chapter 2. They were generated with a dispersion characteristic consistent with solar minimum conditions. However, the memory block is programmed with 1000 samples which, at a data rate of 2.048 GS/s, could contain a pulse with a maximum differential delay of 500 ns (see Table 4.1). Therefore this could also easily accommodate the delays associated with solar maximum (see Table 4.2). The dispersed pulses developed in this chapter had to be conditioned for use in the digital pulse generator hardware. The first step in this conditioning was to mirror the signal into the first Nyquist zone. This was achieved by flipping the pulse spectrum according to Figure 4.23. Care had to be taken during this process to ensure that the spectral symmetries were preserved so the signal remained real in the time domain. For a real signal, this requires that the spectral amplitude is symmetric and the spectral phase is anti-symmetric. Once the pulse was correctly conditioned for the complementary interpolation scheme, it was normalised, quantised and formatted into a text file of 10-bit binary samples. The digital pulse text file could then be uploaded to the FPGA using the Xilinx ISE tool and was ready for testing.

The test set up for the digital pulse generator is shown in Figure 4.24. The output of the pulse generator board was connected to a 1–2 GHz bandpass filter and this was then passed through an analog dedispersion filter (to test the correct operation of the pulse dispersion characteristic) before connecting to a spectrum analyser. The output was captured at each point along the testing chain. Figure 4.25 shows the output from the digital pulse generator before any, bandpass or dedispersion, filtering was performed. As this stage, the pulse is dispersed (*top*) and its spectrum is replicated in the first three Nyquist zones (*bottom*) as expected with a complementary interpolation scheme. The peaks appearing at multiples of 2 GHz are harmonics of the clock signal. The next output captured (see Figure 4.26) is at the output of the bandpass filter. At this stage the pulse is still dispersed, however, signal images have been removed from all but the second Nyquist zone. The final output captured (see Figure 4.27) is from the output of the dedispersion filter. This pulse has been compressed in time (from the dedispersion filter) although little amplitude has been recovered from this process as the isolator and dedispersion filter loss is

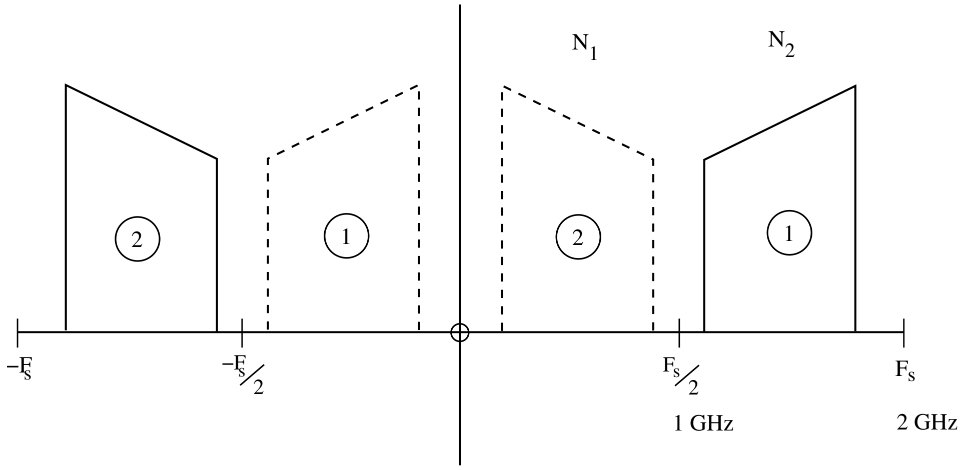

Figure 4.23: First and second Nyquist zones. The solid lines indicate the usable signal images in the second Nyquist zone and the broken lines indicate the corresponding first Nyquist zone signals which must be passed into the DAC to produce these signal images.

comparable to the dedispersion gain expected during solar minimum. This test scenario introduces very little noise into the signal path. However, a pulse received through an array antenna will contain receiver noise and a pulse of lunar origin will also have a component of thermal emission from the Moon. These noise contributions will also be attenuated by the isolator and dedispersion filter loss, however, they will not recover any amplitude from the dedispersion process resulting in a lower noise floor. This means that even during solar minimum the dedispersion filter should provide an overall increase in signal-to-noise ratio under realistic, noisy conditions. To further verify the operation of the digital pulse generator, the pulse programmed into the FPGA was given an inverse-ionosphere dispersion characteristic to match the dedispersion filter. When such a pulse enters the dedispersion filter, it should come out further dispersed (by a factor of two) rather than dedispersed. The output of this test can be seen in Figure 4.28. As predicted, this pulse came out of the dedispersion filter further dispersed and there was also a significant loss in amplitude relative to the output pulse which had the correct ionospheric dispersion characteristic.

Therefore the digital pulse generator could be used to generate nanosecond scale pulses with spectral features and a dispersion characteristics. Initial testing of this pulse generation system was able to verify the correct implementation of these features.

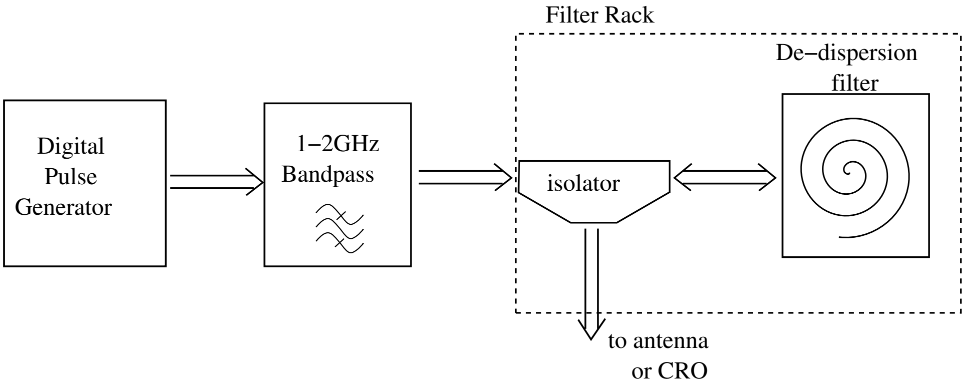

Figure 4.24: Block diagram of the digital pulse generator test setup.

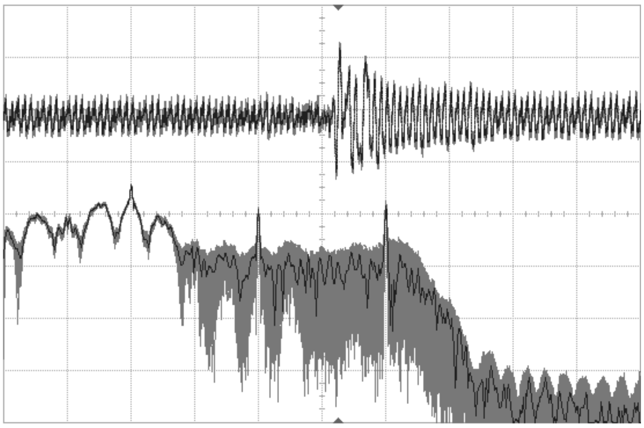

Figure 4.25: Test pulse captured at the output of the digital pulse generator. The horizontal scale is 5 ns per division and the vertical scale is 100 mV per division (*top*). For the spectrum (*bottom*), the horizontal scale is 1 GHz per division and the vertical scale is 30 dB per division.

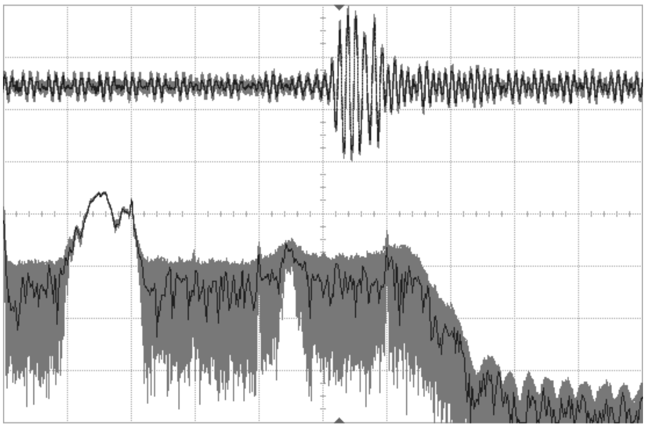

Figure 4.26: Test pulse captured at the output of the band pass filter. The horizontal scale is 5 ns per division and the vertical scale is 50 mV per division (*top*). For the spectrum (*bottom*), the horizontal scale is 1 GHz per division and the vertical scale is 30 dB per division.

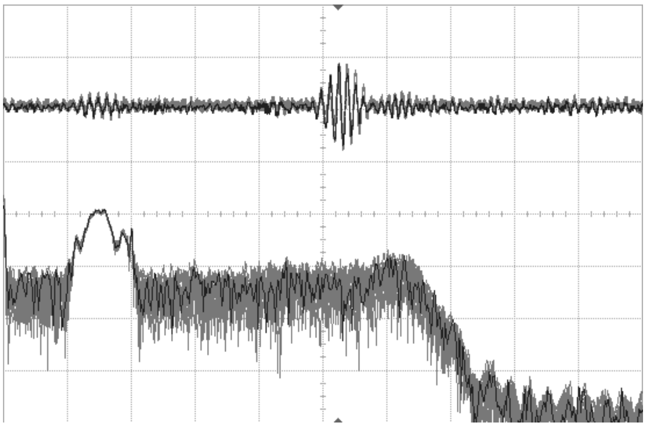

Figure 4.27: Test pulse captured at the output of the dedispersion filter. The horizontal scale is 5 ns per division and the vertical scale is 50 mV per division (*top*). For the spectrum (*bottom*), the horizontal scale is 1 GHz per division and the vertical scale is 30 dB per division.

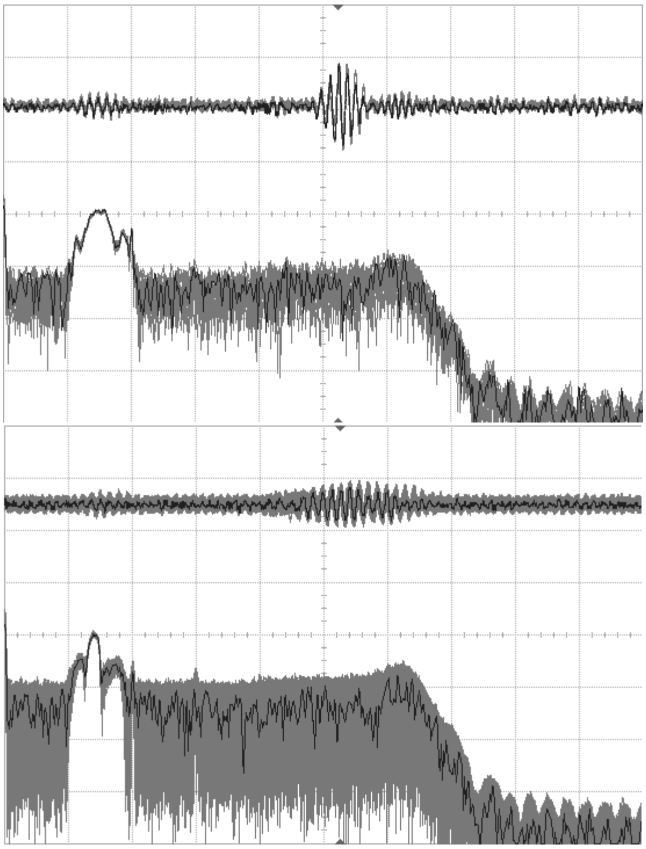

Figure 4.28: Comparison of two different test pulses, captured at the output of the dedispersion filter. Test pulse with (*top*) the correct ionospheric dispersion characteristic (*i. e.* inverse phase characteristic to the filter) and (*bottom*) an inverse-ionosphere dispersion characteristic (*i. e.* phase characteristic matched to the filter). Within each plot, the horizontal scale is 5 ns per division and the vertical scale is 50 mV per division (*top*). For the spectrum (*bottom*), the horizontal scale is 1 GHz per division and the vertical scale is 30 dB per division.

4.4 Detection Experiments with the ATCA

During experiments at the ATCA, 36.5 hours of lunar observations were collected using the custom pulse detection hardware. This data came from three observing runs which included a trial period in May 2007 and two main observing runs in February and May 2008 (Table 4.3). The earlier runs (May 2007 and Feb 2008) were scheduled to target a broad region surrounding the galactic centre. This region was chosen as it harbors the closest super massive black hole and potential accelerator of UHECR. Scheduling of the May 2008 experiment was influenced by results published by the Pierre Auger Observatory in late 2007, which showed a statistical correlation between observations of the highest energy CR and the matter distribution in the local universe as represented by nearby active galactic nuclei (2). This experiment was therefore designed to target Centaurus A (Cen A), a nearby active radio galaxy which could potentially account for two of the events detected by Auger. Regardless of their source, this result suggests the likelihood of an accompanying excess of UHE neutrinos in this region.

The ATCA is sensitive to a region which covers 30 degrees either side of the ecliptic (see Figure 4.29). Within this region, specific objects can be targeted by selecting dates which provide the correct geometry to align them with the Moon, as seen from the ATCA. While targeting the galactic centre, the antenna were pointed towards the centre of the Moon, to maximise limb coverage. However, during the targeted Cen A observation, the antenna were pointed to the limb closest to Cen A to maximise sensitivity to particles interacting in this region. As well as targeting considerations, observing dates were also influenced by the requirement for ionospheric stability which occurs at night. Observations were nominally between the hours of 10pm and 6am local time although some of this time was spent fine tuning the experimental system. Therefore observational dates were chosen carefully to ensure that the Moon was at high elevation (particularly during the night-time hours of ionospheric stability) and the geometry was such that potential pulses from the Moon lined up with specific targets, such as Cen A or the galactic centre.

For all observing runs, baselines of a few hundred metres were requested to keep the level of lunar correlation low between antennas (Table 4.3) and the custom hardware was installed on three of the six ATCA antennas (CA01, CA03 and CA05). Since the experiments were performed during an upgrade to the array, hardware improvements became available incrementally during the course of the experiments. During 2007, data capture was performed by prototype ADC boards. By 2008 the final CABB ADC boards had been completed and rack mounted in the antennas. These boards were well screened and therefore offered a significant improvement

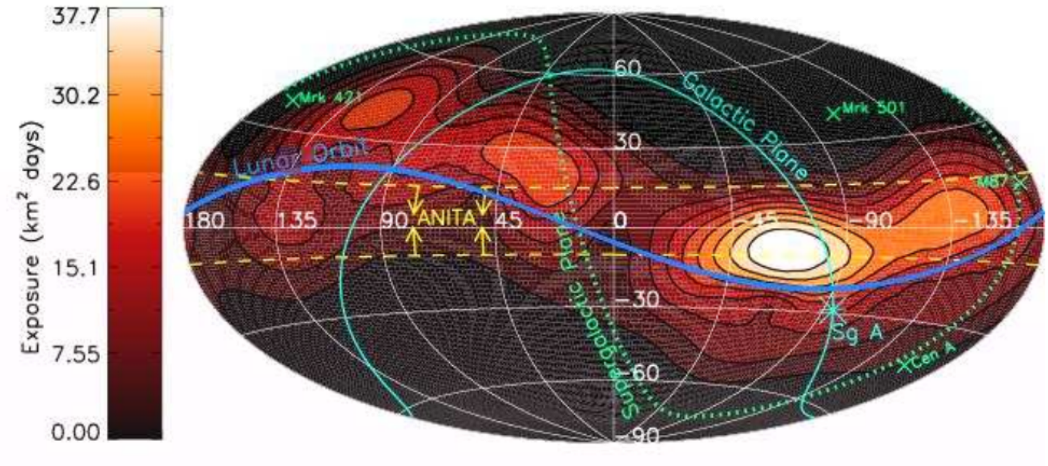

Figure 4.29: Combined exposure of the GLUE and Parkes Experiments to 10^{22} eV neutrinos as a function of celestial coordinates. Also shown is the ATCA range (within ∼30° of the lunar orbit) and the ANITA $-10° < \delta < +15°$ declination range. (12)

in RFI characteristics. There were also significant changes to the process of time stamping triggered events during the course of the experiments. Initially nanosecond timing was not available and for the 2007 experiment, PC clocks with a timing accuracy of ±1 ms were used. With the installation of the CABB ADC boards, a 32 MHz common reference signal, distributed to all antennas, became available. This signal is multiplied up (by a factor of 64) within the boards to produce a 2 GHz signal to drive the ADC boards. Therefore for the 2008 experiments the ADC boards were synchronized but had a timing offset, due to differing transmission delays, which had to be calibrated. Timing calibration methods are discussed further in the next section.

Day	May 2007 7th	Feb 2008 26th 27th 28th	May 2008 17th 18th	May 2008 19th
Observing Time (mins)	210	275 330 255	320 370	435
Array	1.5C	750B	750A	352
Baseline Range (m)	337–1485*	230–765	352–735	107–352

Table 4.3: Summary of observations. (*) For these initial observations, hardware was installed on CA02, CA03 and CA04.

4.5 Data Analysis

Off-line processing involved searching through candidate event data to identify pulses which exhibit three-fold coincidence with timing, duration, dispersion characteristic and linear polarisation consistent with Čerenkov pulses originating from the Moon. The timing constraint was found to be both the most reliable and the easiest constraint to automate. Once timing based discrimination had been performed, remaining events could be checked against the other criteria manually.

At the time of the ATCA experiments, the CABB ADC boards did not have their time stamping capability enabled with high accuracy and so alternative methods of time stamping were investigated. For the May 2007 experiment, PC clocks with only ±1 ms accuracy were used. This was not sufficient to accept events as having lunar origin but it was powerful enough to reject all but 4 out of an initial 150 000 candidates for each antenna. It was predicted that there would be ~6 random events from purely thermal noise therefore it was concluded that it was unlikely any of the 4 remaining candidates were of lunar origin (4). For the 2008 experiments a 32 MHz common reference signal was available at each antenna which locked the digitiser's clock synthesisers and kept the digitised data absolutely fixed relative to 32 MHz signal edge. This signal could be used to synchronise the operation of the ADC boards with an absolute timing offset, due to transmission delays, which had to be calibrated. Observations of bright quasar 3C273 were used to calibrate this timing offset.

To perform the timing calibration, the noise calibration diode was set switching to trigger the pulse detection hardware. Captured buffers were then cross correlated between antennas to determine the relative time differences between them. The buffers were resized to the longest possible buffer size (8 μs) to ensure that they contained signals which overlapped in time, even over the longest baselines. The cross correlation process required averaging over approximately 200 buffers before the correlation peak could be seen above the noise floor (see Figure 4.30) and the associated time delays had to be corrected for known positional delays before they could be used to calibrate the hardware timing offsets. This was achieved using Very Long Baseline Interferometry (VLBI) software. Once these corrections had been applied, the resulting timing offsets were expected to remain constant throughout the observations, however, it was found that they varied by hundreds of nanoseconds over the course of the observations (see Figure 4.31). By folding the timing data into one 24-hour plot (see Figure 4.32), the author determined that the unexpected variations in timing offsets occurred in discrete jumps between observations of 3C273 and that these jumps were in integer increments of approximately 96 ns. Once these

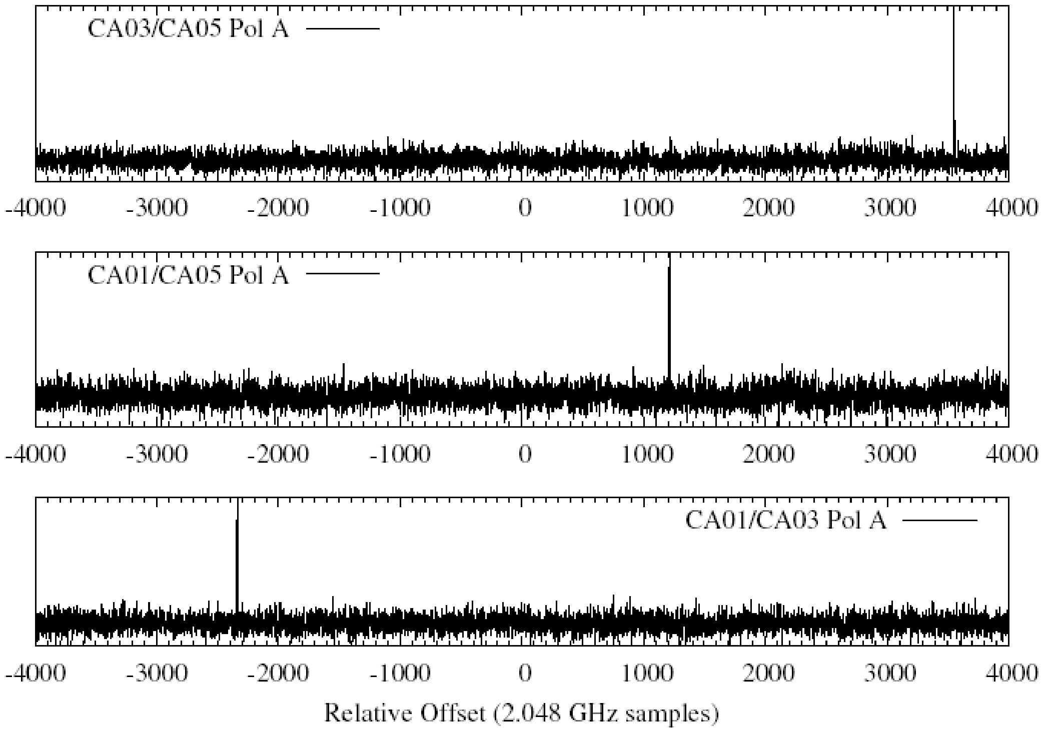

Figure 4.30: Cross correlations of buffers from antennas CA01, CA03 and CA05, triggered near-simultaneously while pointing at the bright quasar 3C273. The cross correlations have been averaged over 200 buffers and corrected for the quasar position.

jumps had been adjusted in the timing offset data, a small slope was still evident (see Figure 4.33). This slope was attributed to a positional error between the VLBI position for 3C273 and the position of the most dominant feature (an active jet) at the resolution of the ATCA. The 96 ns jumps were eventually traced to a fault in the ADC board hardware. It was discovered that each time the event buffers were resized (going between 3C273 for timing calibration and the Moon for pulse detection), re-intialising the hardware caused a clock cycle to be dropped which subsequently increased the relative delay between the antenna being re-initialised and the other antennas. Due to a combination of human error and tests being performed between observations, it was not known, post experiment, how many times the hardware on each antenna had been re-initialised. However, RFI events which were common to all antennas could be used to correct the data alignment and determine the absolute timing offsets between the antennas to an accuracy of ±1 ns.

Analysis of the data revealed that most of the candidate events could be attributed to terrestrial RFI and no candidates events are suspected to be lunar

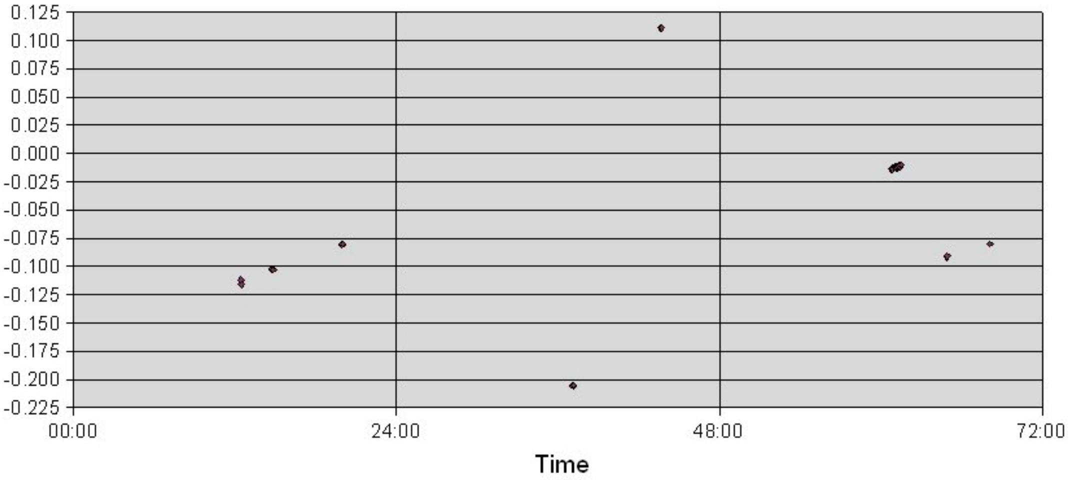

Figure 4.31: Timing offsets between antennas CA01 and CA03 over a 3 day period (vertical scale is in ms).

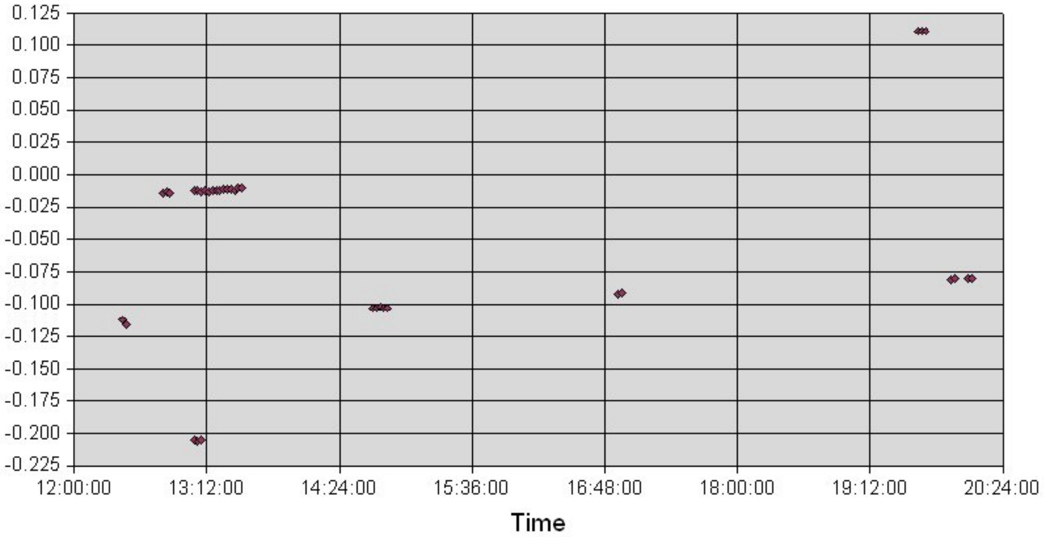

Figure 4.32: Timing offsets between antennas CA01 and CA03 wrapped into one 24-hour period (vertical scale is in ms).

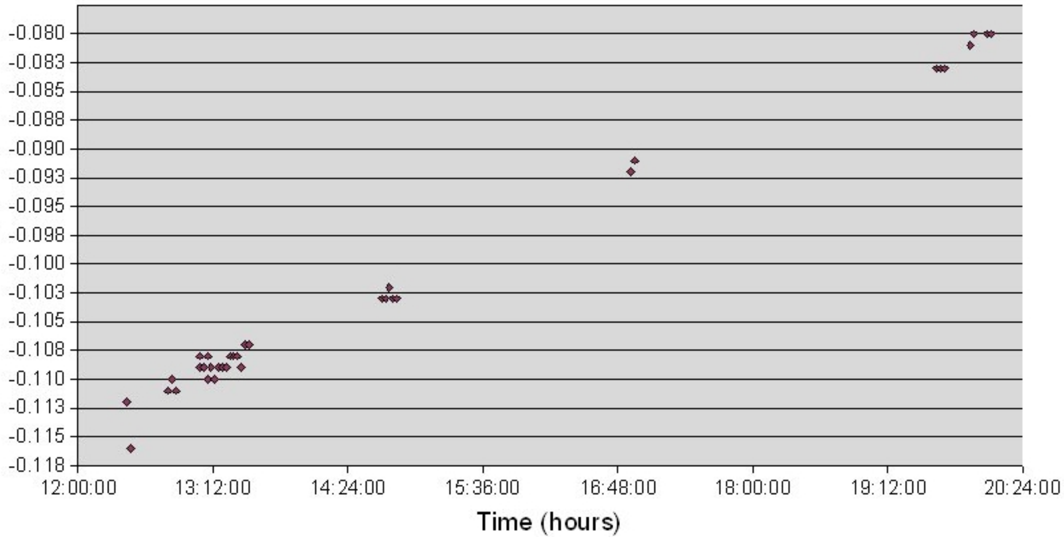

Figure 4.33: Timing offsets between antennas CA01 and CA03 wrapped into one 24-hour period and corrected for lost clock cycles (vertical scale is in ms).

Čerenkov pulses. The isotropic flux limits from these experiments are not expected to be competitive with current limits from ANITA (see Chapter 1), however, as targeted experiments, they offer an increase in exposure in the regions of Sagittarius A* (Sgr A*) and Centaurus A (Cen A) (Table 4.4), (4).

	Parkes and GLUE			LUNASKA		
Energy (eV)	10^{21}	10^{22}	10^{23}	10^{21}	10^{22}	10^{23}
Sgr A*	0.5	14	175	3.7	75	565
Cen A	0.015	2.1	43	9.3	145	970

Table 4.4: Accumulated exposure (km^{2}days) to Cen A and Sgr A* for the Parkes (37), GLUE (63) and ATCA (2007) (3) experiments.

4.6 Candidate Events

This section provides a summary of the candidate events and RFI features detected during experiments at the ATCA. It is based on analysis performed by Clancy James at the University of Adelaide. Further information can be found in (15) and (71).

The number of two-fold and three-fold coincidences for each night of observations are summarised in Table 4.5. They represent the number of event triggers, which occurred on multiple antennas, within a timing window consistent with propagation from a physically real location. For purely random events, it was anticipated that the the three-fold rate would account for approximately 2% of the two-fold rates, at 1.6 Hz and 70 Hz respectively (15). There were some times during the observations that the ratio of observed coincidences matched this expectation. However, there were also periods of time where the three-fold coincidence rate significantly exceeded this expectation. It was concluded that these statistics indicated the presence of a strong source of RFI.

Date	CA01/03	CA01/05	CA03/05	CA01/03/05
Feb 26	6445	1286	1533	449
Feb 27	68894	39898	43224	30051
Feb 28	23296	8590	11072	6781
May 17	2344	1925	1994	96
May 18	21774	19445	20635	3437
May 19	114383	74311	71313	57493

Table 4.5: Number of two-fold and three-fold coincidences, within a 4 μs window each night of observations (15).

In Figure 4.34, all two-fold coincidences have been plotted showing time and direction of arrival information. The angle of arrival, θ, was defined as the angle between the east direction and the direction of arrival determined by event timing. The cosine of this angle has been plotted against time. The lunar position is shown as a dotted line and candidate neutrino events, exhibiting timing information consistent with lunar origin, are marked as crosses along this line (an example of this type of event can be seen in Figure 4.35). Coincidences occurring away from this line are considered to be RFI and can be classified according to their directional and timing information. Vertical features extending over the the full range of $\cos\theta$ indicate a lowering to the effective threshold by an increase in background noise. This is most likely caused by very narrow-band RFI which exhibits random timing information, possibly as different antennas trigger off different parts of the signal's broad time structure. Vertical features extending over part of the $\cos\theta$ range may indicate a combination of a random signal component, which effectively lowers the trigger threshold, and/or an extended source of RFI which adds a directional component. While horizontal features indicate an on-going source of RFI from a specific physical location, such as on-site buildings, nearby towns or the local television station. There also appears to be some very interesting RFI features on February 27. These feature occur at approximately 17:00–19:00 UT and slope across time and direction at an anti-sidereal rate. These features remain largely unexplained, however, timing information has revealed that they occurred in the near field and were strong enough to give a high rate of triple coincidences.

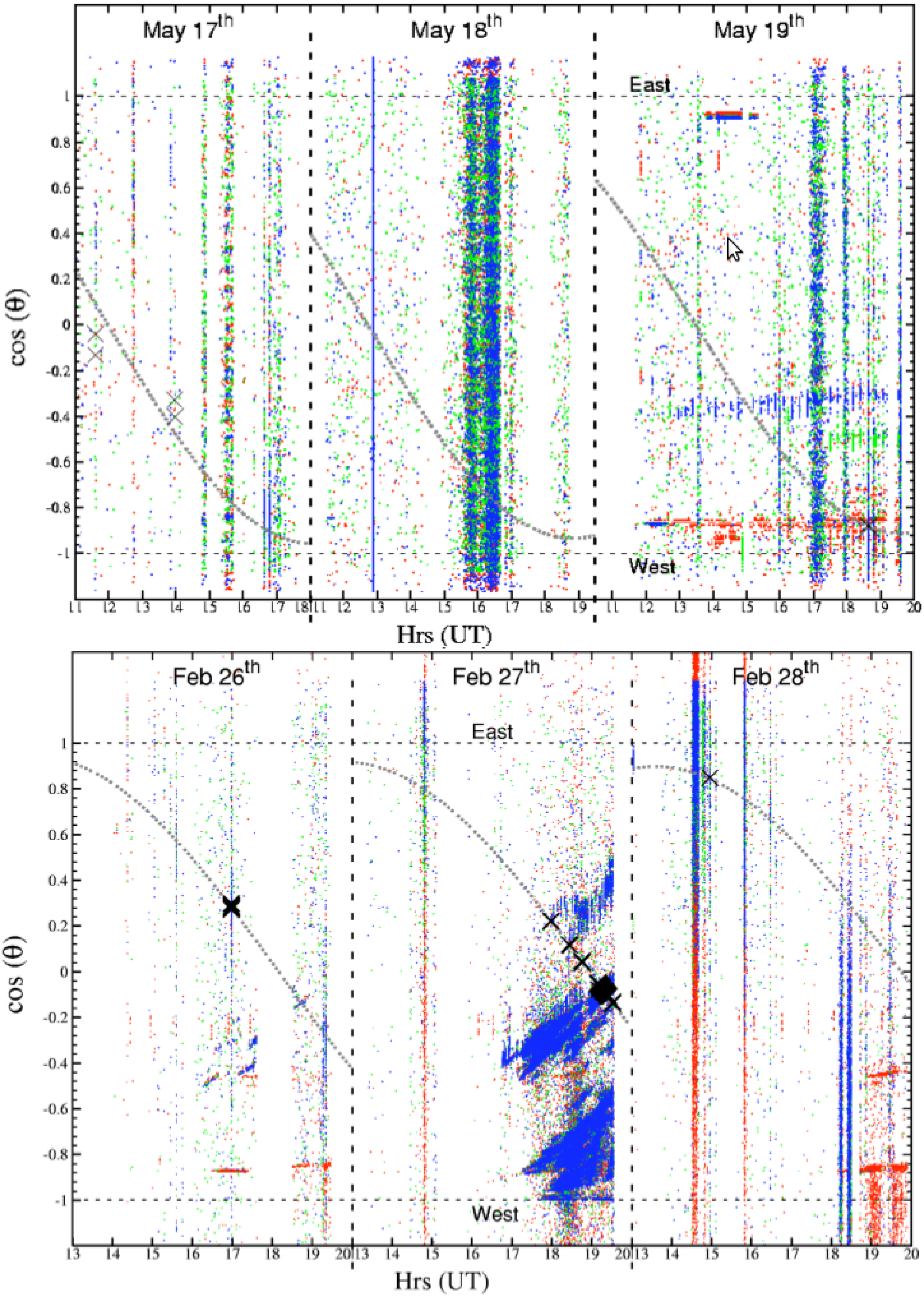

Figure 4.34: For each two-fold coincident event the angle, θ, between the east direction and the direction of propagation of a plane wave fitting the arrival times at the two relevant antennas is calculated, and $\cos\theta$ is plotted (dots) against the time of the occurrence of each event for February (*top*) and May(*bottom*). Red dots represent coincidences between antennas CA01 and CA03, green dots for CA01 and CA05, and blue dots for CA03 and CA05. In dot-dense regions, only blue points show, since they are plotted last. The lunar direction (grey dotted line) is also potted, and positions of candidate events (crosses) are marked (15).

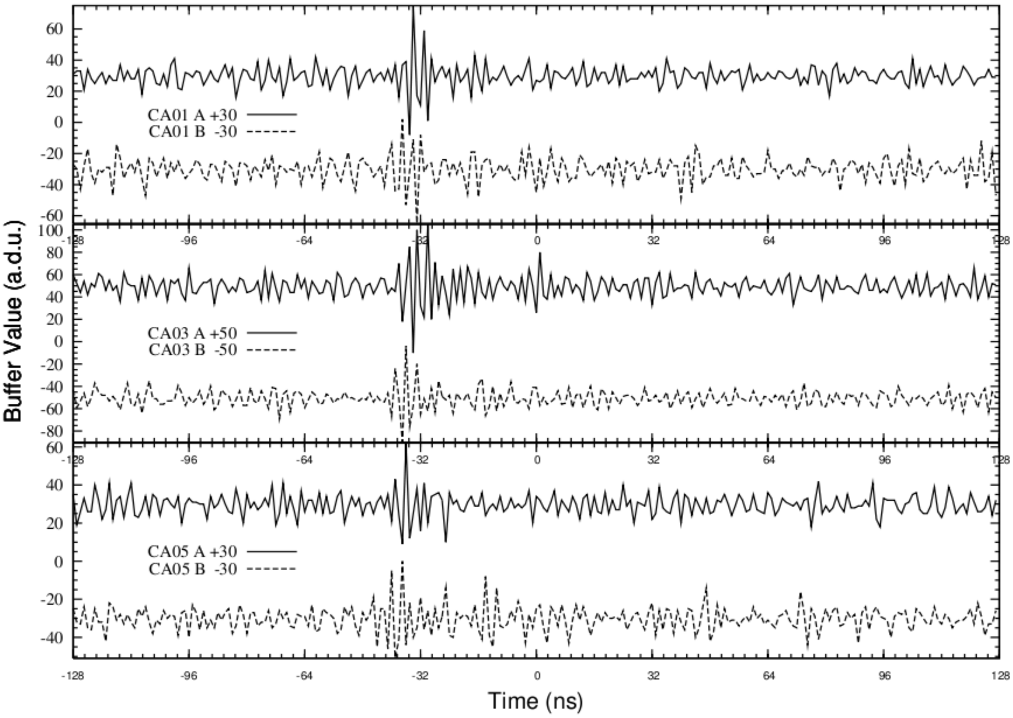

Figure 4.35: A narrow time structure event from February 27. Note that the signal has been displaced vertically by ±30 as indicated for display purposes (15).

4.7 Detection Experiments with the SKA

The ATCA experiments provide a framework for UHE neutrino detection experiments with the next generation of radio instruments, such as the Square Kilometre Array (SKA). The SKA will provide huge advances in collecting area and one hundred times more sensitivity than the best present day instruments. Current proposed designs consist of large numbers ($\sim 10^4$) of small dishes (10–15 m). This will achieve a square kilometre of collecting area in the 0.1–3 GHz range which is critical for UHE neutrino experiments. For these experiments dishes should not exceed 15 m in diameter. This will ensure that the moon is covered by the primary beam at low gigahertz frequencies. Dishes smaller than 15 m will still meet this criteria, however, additional electronics will be required to maintain the same sensitivity. To gain the full advantage of the large number of small dishes offered by the proposed SKA designs, signals will have to be coherently combined and analysed with nanosecond timing accuracy.

Special purpose beamforming hardware may be required to form phased array beams in real time and there will have to be enough beams to cover the visible surface of the Moon (or at least the whole limb of the Moon) over the entire frequency range. Due to the increasing complexity of the SKA it will remain impractical to record the full time resolution output of each antenna, over the large bandwidths required for UHE neutrino detection, despite predicted increases in digital recording speeds. Therefore a trigger algorithm will still be required to detect candidate events in real time. Before triggering, the signal from each beam needs to be filtered to compensate for the dispersive effects of the ionosphere. An FPGA architecture is ideal for this filter implementation due to its low loss and reprogrammable nature. The ability to be reprogrammed is important as the filter characteristic needs to be updated during observations to follow changes in the ionospheric TEC. The exact implementation of these filters depends on the output of the beamforming hardware with filterbank-structured outputs likely to favor a frequency domain implementation. As discussed in Section 4.1.4, a filterbank implementation is likely to be more efficient than an FIR filter during periods of increased solar activity. However, either of these implementations will require a more complex solution than the single FPGA architecture used during the solar minimum conditions of the ATCA experiments.

The optimal processing path should allow for a hierarchical trigger so that initial event triggering can occur within compact sub-arrays of the inner SKA core before producing a global trigger across longer baselines. The advantage of a hierarchical structure is that it allows for faster triggering and a reduced buffer length within the inner core while a secondary global trigger ensures that information from longer baselines is retained. If the inner sub-arrays are limited to baselines of a few hundred metres, then buffers can be kept to less than 1 μs and still cover the geometric delay associated with a pulse of lunar origin. Employing a low angular resolution primary trigger will reduce the initial event rate and trigger 'dead time' associated with longer buffer lengths. On longer baselines, a buffer length of 1 ms (plus processing time) would be required for the global trigger and these baselines would provide higher angular resolution information on the location of any Čerenkov events. Using these methods, it is expected that the SKA sensitivity will reach the level at which a flux of UHE neutrinos will be detected (7).

4.8 Conclusions

The ATCA experiments were successful at increasing exposure in the regions of Cen A and Sgr A* although they did not result in any potential lunar Čerenkov events. Future improvements to the ATCA UHE neutrino detection experiment include using 5 antennas, performing coherent signal combination in real time to enable coincidence testing and an increase to 2 GHz bandwidth when the CABB upgrade is complete. This upgrade will include the installation of powerful new FPGA based back-end receiver hardware which will allow the implementation of real-time dedispersion algorithms. The ATCA experiments provide a framework for UHE neutrino detection experiments with the next generation of radio instruments such as the SKA, which is expected to reach a level of sensitivity at which a flux of UHE neutrinos will be detected (7).

CHAPTER 5

Interferometry and Data Reduction at the ATCA

This chapter provides an introduction to interferometry and data calibration at the ATCA . The ATCA is a radio telescope array located at the Paul Wild Observatory ($149^\circ\ 32'\ 56''$, $-30^\circ\ 18'\ 52''$) near Narrabri, 550 km northwest of Sydney, Australia. It consists of a six kilometer linear east-west array of six 22-m radio antennas (with a small north-south spur) which are used in pairs to form two element interferometers. An interferometer samples the spatial coherence of a source by comparing the electric field measured between antenna pairs or baselines. A 2-dimensional Fourier transform of the coherence samples can be used to produce an image of the source which will have the same angular resolution as a single antenna the size of the largest antenna baseline spacing. Incomplete sampling of the spatial coherence function will lead to artifacts in the resulting image, therefore, to maximise the 2-dimensional sampling, data is collected over a long period of time and for a large range of antenna spacings. Since the ATCA is aligned in the east-west direction, there is good resolution in this direction. However, to obtain better resolution in the north-south direction, a technique known as 'Earth Rotation Aperture Synthesis' is used. This synthesis technique exploits the projection of an east-west baseline onto the sky and uses its change in orientation, due to the Earth's rotation, to increase the 2-dimensional sampling of the spatial coherence function. The array can also take full polarimetric observations by simultaneously measuring two orthogonal linear polarisations.

5.1 Fundamentals of Radio Interferometry

A radio telescope samples the incoming electric field and converts detected radio waves to a voltage signal. It consists of a large parabolic antenna which reflects and focuses radio waves onto the focal point of the receiver (see Figure 5.1). A plane wave incident on this aperture will reach the focal point nearly in phase only if it arrives from an angle less than λ/d to the aperture plane (where λ is the signal wavelength and d is telescope diameter). The telescope's angular resolution, θ, is defined by this diffraction limit and is therefore inversely proportional to the telescope's diameter (see Equation 5.1 (16)). This means that there is a limit to the finest angular resolution that is practically achievable with a single dish telescope.

$$\theta = 1.22\frac{\lambda}{D} \tag{5.1}$$

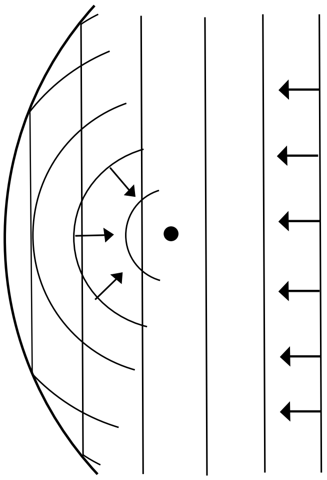

Figure 5.1: Wavefronts reflecting off a parabolic reflector toward the antenna focal point. (16)

Interferometric techniques can be used to obtain better angular resolution. An interferometer maps the brightness distribution of a source by employing the Van Cittert-Zernike theorem which states that the measured spatial coherence function of a source is the Fourier transform its source brightness distribution (as described in (72)). Therefore, once measurements of the coherence function have been obtained, the source brightness distribution can be obtained through Fourier inversion.

An interferometer samples the spatial coherence of a source by considering the correlation of the electric field at two spatially separated antennas which define a baseline. An incoming wavefront, originating from a single location, arrives at each antenna with a relative phase offset due to the geometric path difference between them (see Figure 5.2). If the phase offset is an integer number of wavelengths then the measured correlation will produce constructive interference while destructive interference will occur for phase offsets which are an integer number of wavelengths plus a half. Regions of the sky which produce constructive or destructive interference, for a particular baseline, form stripes, commonly known as *fringes*.

Mathematically, fringes can be explained by considering the signal processing stages of a simple interferometer. These consist of bandpass amplifiers followed by a multiplier and integrator as shown in Figure 5.2. The output of the multiplier in response to a single frequency, ν is proportional to: (17)

$$\begin{aligned} F &= 2\sin(2\pi\nu t)\sin 2\pi\nu(t-\tau_g) && (5.2)\\ &= \cos 2\pi\nu\tau_g - \cos(4\pi\nu t)\cos(2\pi\nu\tau_g) - \sin(4\pi\nu t)\sin(2\pi\nu\tau_g), && (5.3) \end{aligned}$$

where $\tau_g = (D/c)\sin\theta$ is the geometric time delay between signals arriving at each antenna, D is the distance between the antenna, known as the *baseline*, and λ is the signal wavelength. The more rapidly varying terms are easily filtered out leaving the fringe function

$$F = \cos 2\pi\nu\tau_g = \cos\left(\frac{2\pi Dl}{\lambda}\right), \tag{5.4}$$

where $l = \sin\theta$. This describes a cosine which is a function of the path difference between the two antennas.

The correlator can be thought of as casting this sinusoidal fringe pattern across the sky. From an engineering perspective, this is analogous to projecting the array beam pattern of the two antennas. The fringes have an angular scale of λ/D and their orientation is set by the baseline geometry. For astronomical observations an Earth-based array will be in the far field of the source, which defines a region where the angular field distribution is independent upon distance from the source. In this regime, the actual baseline location is unimportant and the level of correlation sampled by each baseline is determined by the baseline length.

The interferometer multiplies the fringe pattern with the source brightness distribution and integrates this result across the sky. As a source moves through the fringe pattern, it produces an oscillating output signal from the interferometer. The effectiveness of the interferometer in obtaining information about the source depends on the scale of the source relative to the fringe half-spacing, $\lambda/(2D)$. If the source is very small compared to the fringe half-spacing, the output signal is just the fringe pattern and the source structure can not be determined. In this instance, the source

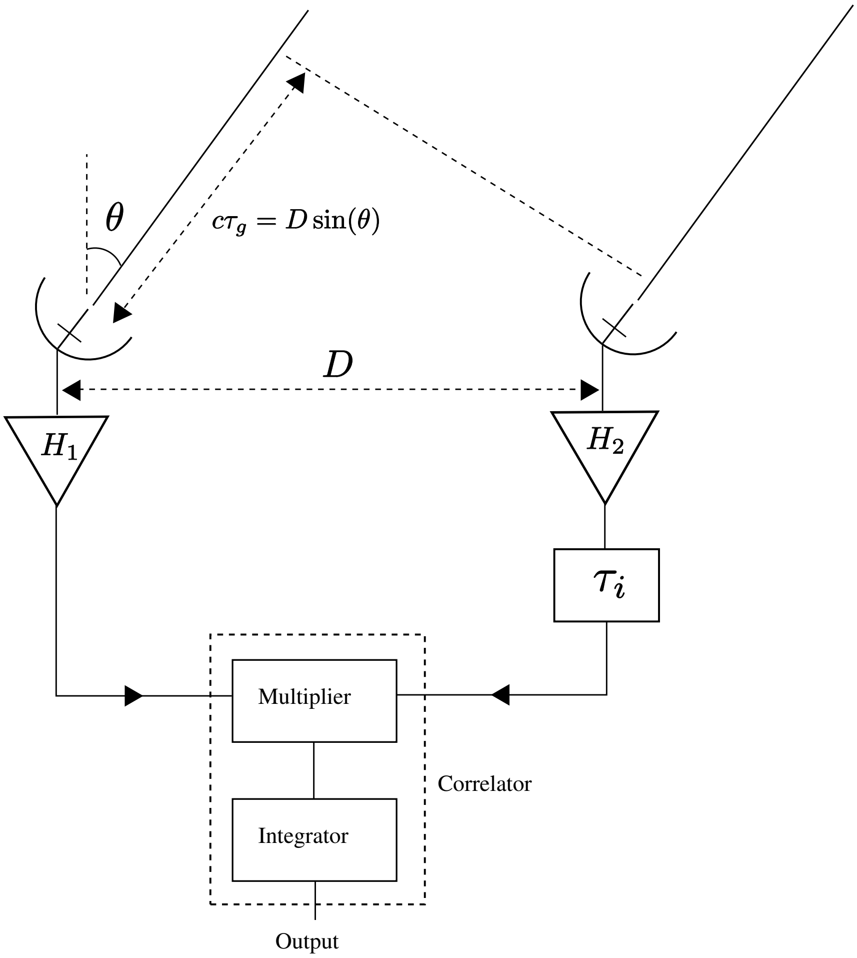

Figure 5.2: Elementary interferometer showing bandpass amplifiers H_1 and H_2, the geometric time delay τ_g, the instrumental time delay τ_i, baseline D and the correlator consisting of a multiplier and an integrator. (17)

is said to be *unresolved* and can only be used as a calibrator (details on calibration strategies follow later in this chapter). Ideally, the source should be comparable to the fringe half spacing, then the output signal is given by the fringe pattern smoothed by the finite size of the source and contains information about the source distribution. However, if the source is large enough to span both a peak and a trough in the fringe pattern, the output signal is nearly constant, the source is said to be *resolved out* and its structure poorly determined. At 1.4 GHz the Moon can be considered to be resolved out over baselines which are longer than a few hundred meters. Essentially, the angular scale that can be resolved by an interferometer is determined by the width of the fringes projected by each baseline, and these are inversely proportional to the baseline length.

Measurements taken of the spatial coherence in the far field of a source are known as *visibilities*. Generally, the brightness distribution of a radio source is not symmetric therefore its Fourier transform or visibility function will be complex. The complex visibility function is measured using a complex correlator which is essentially the combination of a cosine and sine correlator. The complex visibility function, $V(b)$, is given by Equation 5.5 (17) where b is a spatial frequency parameter. This function is obtained by multiplying the source distribution function, $I_\nu(s)$, by both cosine and sine fringes (through the exponential term) and integrating this over a region of sky, $d\Omega$.

$$V(b) \equiv |V|e^{i\nu\phi} = \int\int I_\nu(s)e^{-2i\pi\nu b\cdot s/\lambda}d\Omega \tag{5.5}$$

5.2 Earth Rotation Aperture Synthesis

Fourier synthesis imaging is based on measurements of the complex visibility as a function of antenna spacing. The antennas are in the far field of the source, which is known as the *uv* plane. An Earth Rotation Aperture Synthesis Interferometer uses the Earth's rotation to increase the number of baseline orientations included in an observation. As the Earth rotates, each baseline traces out an ellipse through the *uv* plane (see Figure 5.4). The projected baseline can be specified using *uv* coordinates where u gives the east-west component and v gives the north-south component of the baseline. Including more baseline orientations gives a more complete coverage of the *uv* plane and provides more samples to produce the source distribution through Fourier inversion.

If a source were placed at a celestial pole, it would observe a perfectly rotating east-west baseline which would map out a circle in the *uv* plane. This may be seen by considering Figure 5.3 which shows a series of east-west cuts and how they would project onto a plane perpendicular to the South Celestial Pole. However, as the source position increases in declination, baseline projection occurs and the circles become compacted to form ellipses. This may be seen in Figure 5.4 along with the resulting samplings of the *uv* plane.

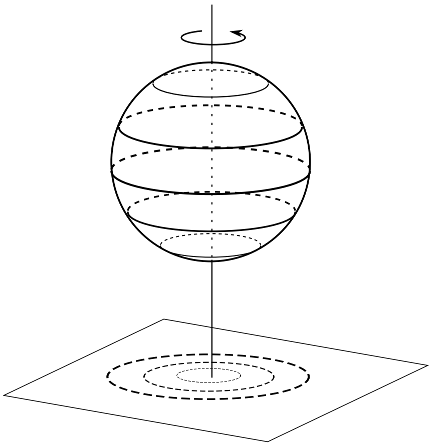

Figure 5.3: As the Earth rotates, east-west baselines project as perfect circles onto a plane perpendicular to the South Celestial Pole.

5.3 An Example of the Imaging Process

As the Earth rotates, antenna baselines trace out a pattern of concentric circles or ellipses in *uv* space (see Figure 5.4). If not enough baselines are used incomplete sampling of the *uv* plane will lead to artifacts in the image plane. This produces a 'dirty' image which can be 'cleaned' using deconvolution algorithms. Essentially, the measured visibilities can be considered as the continuous distribution of the true source visibilities multiplied (or masked) by the *uv* plane sampling pattern. In the image plane, this multiplication is equivalent to a convolution (by the Fourier theorem) and therefore the effects of the sampling pattern mask can be removed by deconvolving the 'dirty' image with the Fourier transform of the known visibility sampling pattern. An example of a 'dirty' and 'clean' image can be seen in Figure 5.5. The image is of a ring of closely spaced point sources which represent the Moon's polarised intensity. Further details on the Moon's polarisation distribution and the development of this model are presented in Chapter 6.

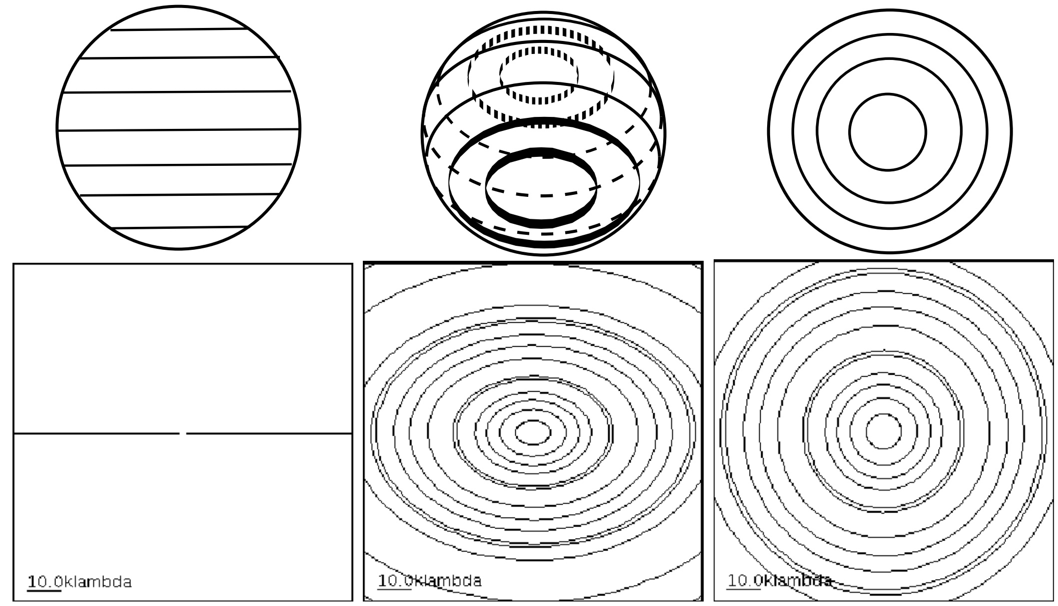

Figure 5.4: East-west baseline projection as the declination decreases from 0° through to $-90°$ (*left to right*) and the resulting *uv* plane sampling. The *uv* plane images were generated using the ATNF's Virtual Radio Interferometer (18) with 6A as the array configuration.

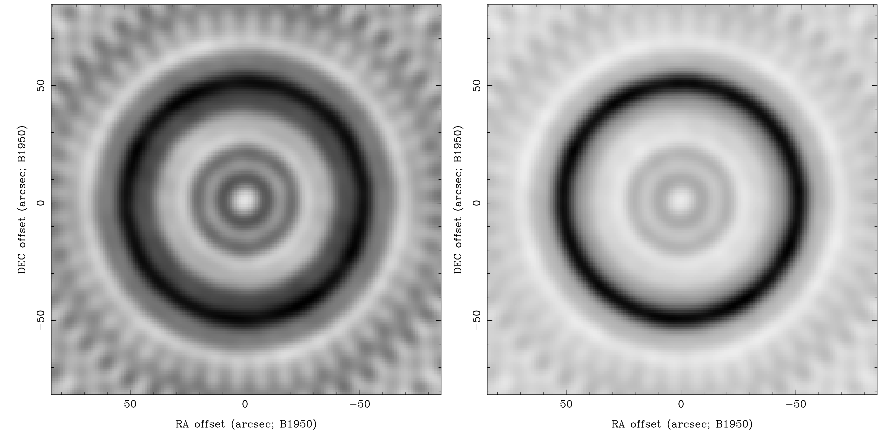

Figure 5.5: Model image of the Moon's polarised intensity (*left*) 'dirty' image produced directly from the raw visibilities (*right*) after applying deconvolution algorithms to the image.

5.4 Polarimetry at the ATCA

The ATCA antennas each measure two orthogonal linear polarisations (X and Y) simultaneously. Raw polarisation measurements are taken with respect to the orientation of the antenna feeds. However, the Earth is a moving frame of reference for the raw polarisation measurements and as it rotates the antenna feeds will rotate with respect to the source. This rotation is characterised by the source parallactic angle, χ.

The two linear polarisations can be combined to obtain the four Stokes parameters I,Q,U, and V. Stokes conversions must contain a correction term to account for the antenna feed rotation.

$$I = \frac{1}{2}(XX + YY) \tag{5.6}$$

$$Q = \frac{1}{2}[(XX - YY)\cos(2\chi) - (XY + YX)\sin(2\chi)] \tag{5.7}$$

$$U = \frac{1}{2}[(XX - YY)\sin(2\chi) + (XY + YX)\cos(2\chi)] \tag{5.8}$$

$$V = \frac{1}{2}i(YX + XY) \tag{5.9}$$

I corresponds to the total flux density, V corresponds to the circularly polarised component and the linearly polarised component is described by vectors Q and U, oriented north and north-east respectively. These vectors are oriented at 45° to each to other, not 90°, as they are directionless and only contain information about the orientation of the polarisation vector. The linear polarisation can be characterised by its flux density, P, as well as its vector orientation, known as the position angle, ψ.

$$P = \sqrt{Q^2 + U^2} \tag{5.10}$$

$$\psi = \frac{1}{2}\arctan\frac{U}{Q} \tag{5.11}$$

The position angle is defined with respect to north through east. The factor of 1/2 in Equation 5.11 is due to the polarisation vectors being directionless. This creates a two-fold redundancy around the vector plane, where 0 to π is meaningful and there is redundancy from π to 2π. Mathematically, this means that the usual four trigonometric quadrants can be considered as being compressed into 0 to π.

5.5 Lunar Polarisation Observations at the ATCA

Lunar polarisation data was taken at the ATCA, on 19 September 2008, to verify a new ionospheric calibration technique (outlined in Chapter 6). Observations were made at center frequencies of 1.4 and 2.3 GHz, with most of the analysis carried out on the 1.4 GHz data set to take advantage of the stronger ionospheric dispersion effects at lower frequencies. Full polarisation measurements were taken and 128 MHz bands were used around both center frequencies.

A hybrid array configuration was used (H168C) with the baselines shown in Table 5.1. The hybrid array makes use of a small north-south spur and was chosen as it contains instantaneous 2-dimensional *uv* coverage to allow for the use of traditional planetary imaging techniques, if required, while also offering short east-west baselines. East-west baselines are preferable for working in the visibility domain as they simplify the relationship between *uv* angle and time (the ionospheric calibration technique outlined in Chapter 6 is visibility-domain based). Baselines 1–4 (61 m), 4–5 (107 m) and 1–5 (168 m) were used extensively during the analysis as these were the shortest east-west baselines and therefore contained the highest degree of lunar correlation. Since the Moon has such a large angular extent ($\sim 0.5°$), it tends to be resolved out on longer baselines.

	CA02	CA03	CA04	CA05	Ca06
CA01	141	192	61	168	4469
CA02		61	111	132	4379
CA03			171	185	4381
CA04				107	4408
CA05					4301

Table 5.1: Baselines (m) available using Compact Array configuration H168C. In this configuration, antennas 1, 4, 5 and 6 are on the east-west track while Antennas 2 and 3 are on a small north-south spur.

Observations were taken over an 8 hour period with approximately 7 hours of lunar data recorded and the rest of the time spent looking at calibrators. The flux density scale was calculated using the primary calibrator PKS 1934−638, while secondary calibrators were used to determine the time-varying gains, bandpass function and instrumental polarisation as well as to provide an independent method of verifying the lunar polarisation results.

Two secondary calibrators were chosen from the ATCA calibrator catalogue, both with known linear polarisation. Properties of the calibrators are summarised in Table 5.2. Since the Moon is a solar system object and experiences its own rotation with respect to Earth, its position does not remain constant in Right Ascension (RA) and Declination (Dec). During the observations, the Moon rose to the ATCA elevation limit at approximately RA $03^h\ 11^m\ 19^s$, Dec $23^h\ 58^m\ 43^s$ (13:23:15 UT) and set at RA $03^h\ 27^m\ 16^s$, Dec $24^h\ 35^m\ 52^s$ (21:06:29 UT). The secondary calibrators were chosen to transit in the center of this range. Observations of these calibrators were taken for a few minutes each hour with extra observations taken during transit to ensure good parallactic angle coverage for the instrumental polarisation calibration (particularly since 0139−273 is at a similar declination to the latitude of the array and therefore experiences little change in parallactic angle until rapid change occurs around transit).

	Flux at 1.4 GHz (Jy)	linear polarisation (%)
0159−117	2.63	3.5
0139−273	1.5	7.1

Table 5.2: Properties of the secondary calibrators used during lunar polarisation observations on 19 Sep 2008.

5.6 Calibration of ATCA Lunar Polarisation Data

The software package that was used to calibrate the lunar polarisation data taken at the ATCA is called *Miriad.* Further analysis of the data was performed in *Matlab* and will be described in the next chapter.

Visibility data taken at the ATCA is recorded in RPFITS format. Data in this format can be imported into the *Miriad* data reduction package using the command *atlod.* This command imports all data from an observation into a single dataset according to *Miriad's* internal format. A *Miriad* visibility dataset contains several kinds of data or 'items' including the source name, observing frequency, *uv* coordinates, baseline number, calibration tables and actual measured correlations. Since *Miriad* imports all data from an observation into a single dataset, it is often practical to split this data into smaller sets according to source and/or frequency. This can be achieved using the *Miriad* task *uvsplit.*

Before the observations can be calibrated, it is necessary to check for bad regions of data. This can be achieved using the *Miriad* task *blflag* which is an interactive flagging tool, or *uvflag* which uses 'select' keywords and can flag bad data according to parameters such as day, time or antenna. Narrowband interference is common at 1.4 GHz and 2.3 GHz and anomalous data is best removed using an interactive tool such as *blflag.* This tool can also be used to view calibrator data in a scatter plot (real vs. imaginary components) and flag points which are not behaving like a point source. A point source should remain unresolved at the frequency of observation. Therefore no internal structure should be measurable on different baseline scales and the scatter plots should form four concentrations of points in the complex plane – one for I at the flux density of the source and the others for Q, U and V near zero (19). Scatter plots for the primary and secondary calibrators can be seen in Figure 5.6. The secondaries both suffer from source confusion and therefore have larger scatters, particularly in I. This is caused by choosing polarised secondary calibrators, which lead to a trade-off in source flux density. 0159−117 is the least confused and therefore was used in the calibration process. 0139−273 is a particularly weak source but has a strong linearly polarised component and these linear components (U and Q) experience significantly less confusion than its total flux density, I. Therefore, 0139−273 was used as a means of independently verifying the polarisation results obtained in Chapter 6.

Lunar visibility data, measured as a function of time, appears as fragments of Bessel functions. Therefore bad regions of data can be identified by looking for points which deviate from the smooth, continuous nature of these curves. The lunar dataset can be seen, before and after flagging, in Figure 5.7 which contains all baselines except those containing antenna 6. The baselines containing antenna 6 were too long to contain significant lunar correlation and were removed using *uvflag*.

The Bessel function nature of the lunar visibilities arises from the fact that they are samples taken in the Fourier plane of the Moon which is a circular structure. This is more clearly seen by considering the visibilities as a function of baseline (see Figures 5.9 & 5.8). Each individual baseline only contributes a small fragment of this function as it projects with the Earth's rotation. Further discussion of this phenomenon can be found in Chapter 6.

Calibration of the data was performed to determine the flux density scale and the antenna gains and bandpass as a function of time. For full polarisation measurements, instrumental polarisation and the polarisation of the secondary calibrator must also be determined. The preferred calibration strategy uses the primary calibrator to determine absolute flux density scale and derives all other quantities from the secondary. It requires good parallactic angle coverage of the secondary so that its polarisation can be distinguished from the instrumental polarisation. This calibration strategy is outlined in Figure 5.10. It starts with calibration of the primary calibrator using the task *mfcal*, which calculates the antenna gains and bandpass assuming that the calibrator is unpolarised and that there are no polarisation leakage terms. These assumptions can be corrected using *gpcal* which determines the instrumental polarisation and the recalculates the antenna gains. *Gpcal* does not

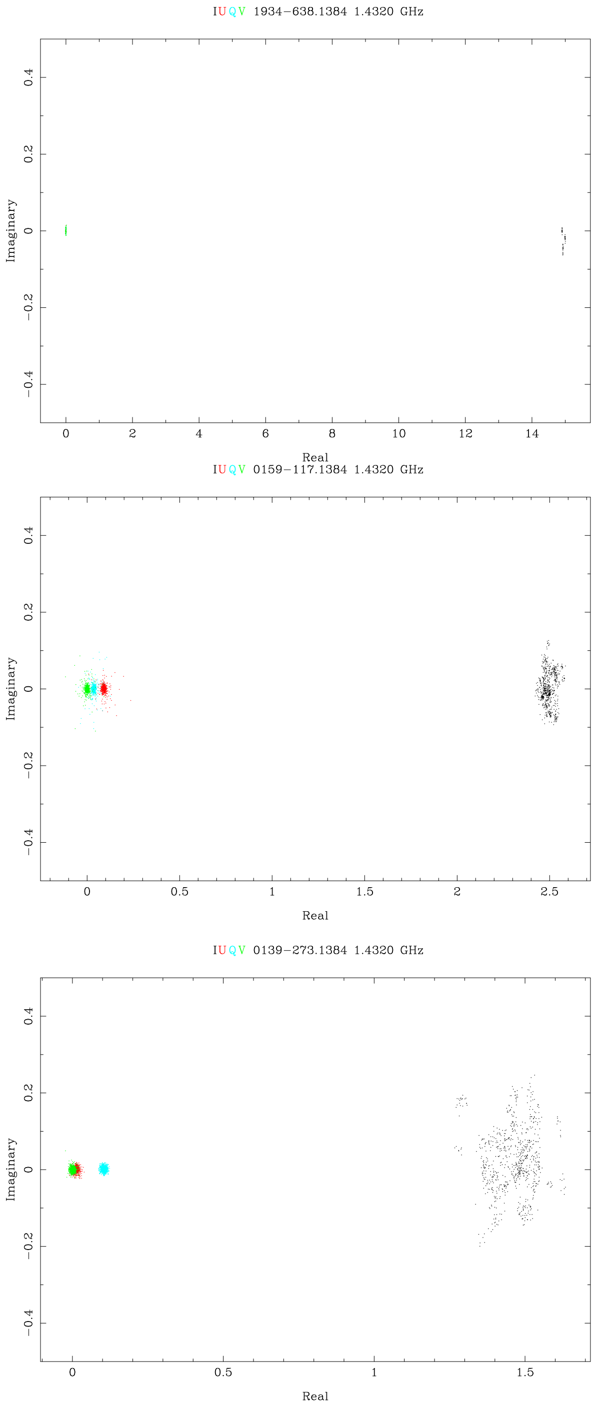

Figure 5.6: Scatter plots for the primary calibrator (1934−638) and the two secondaries (0159−117, 0139−273).

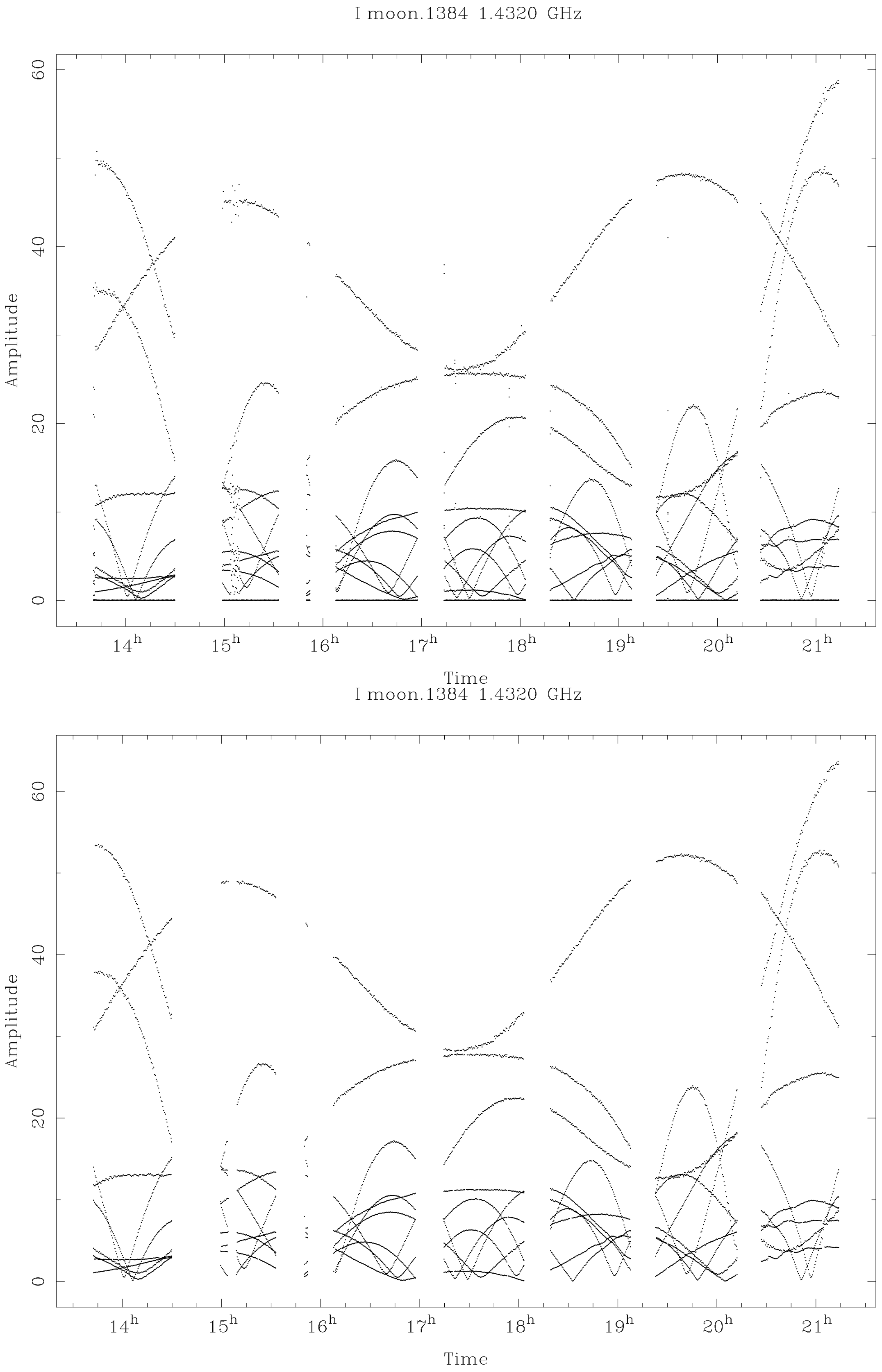

Figure 5.7: Lunar visibilities (I) measured on 19 September 2008 (*top*) before data flagging (*bottom*) after data flagging. All baselines are plotted except those containing Antenna 6 as the Moon is resolved out on longer baselines.

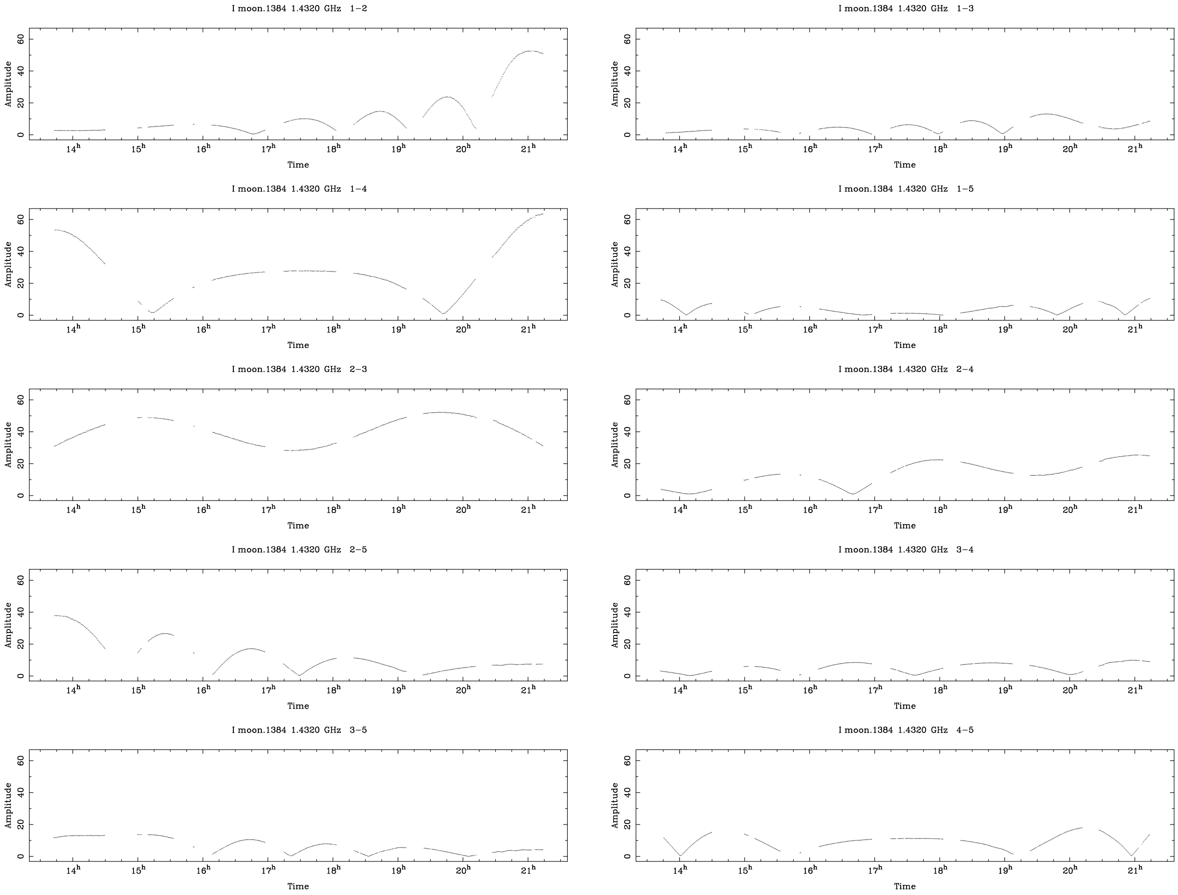

Figure 5.8: Flagged lunar visibilities (I) measured on 19 September 2008 with baselines plotted separately.

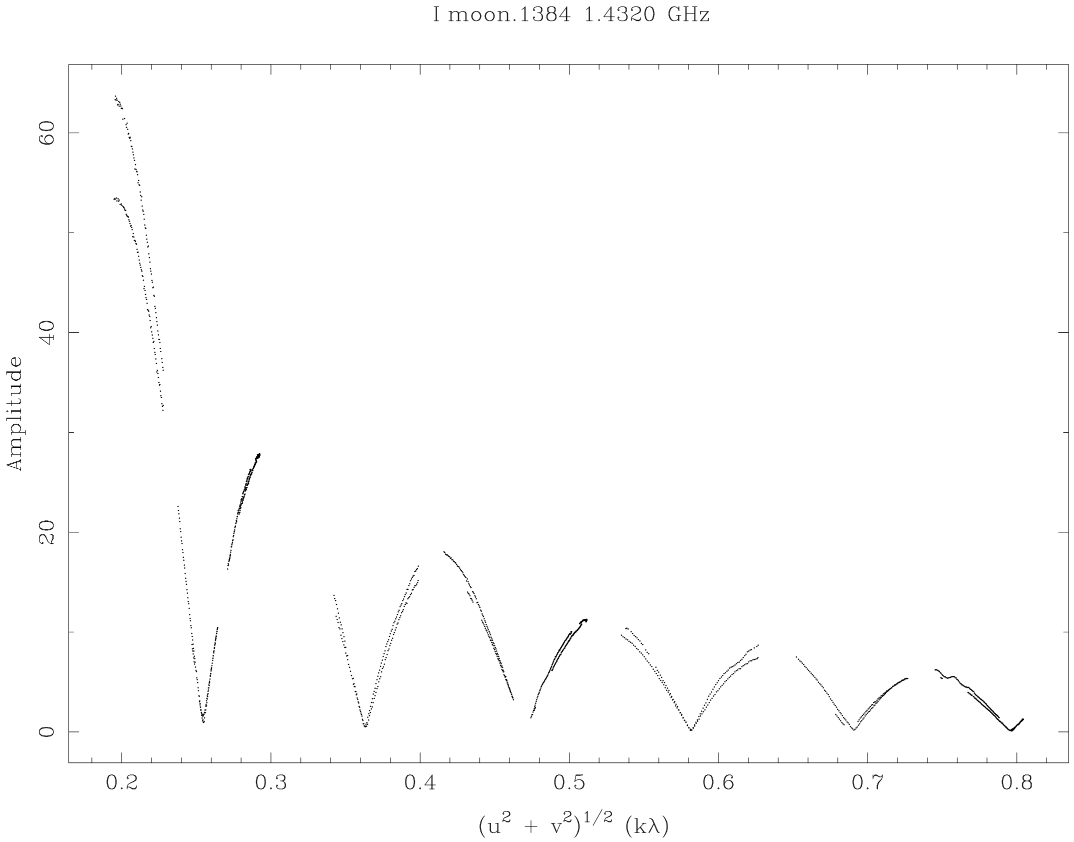

Figure 5.9: Lunar visibilities as a function of *uv* distance or baseline length. This plot shows the amplitude of the flux density, I, and therefore will resemble a squared Bessel function.

calculate a bandpass function therefore it makes use of the bandpass determined by *mfcal*. It is used with an *xy-vary* option which solves for the xy-phases as a function of time rather than assuming that they are constant throughout the observation.

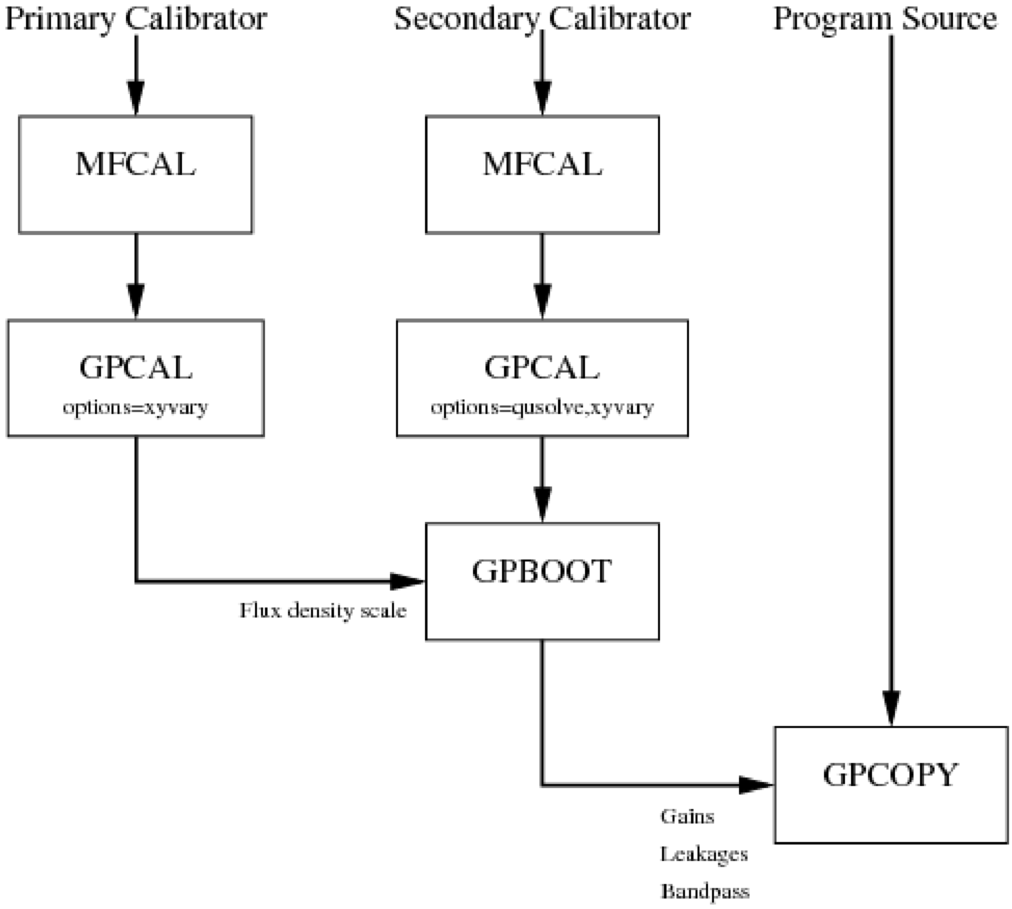

Figure 5.10: Preferred calibration strategy from the *Miriad* manual. (19)

The secondary is calibrated using the same method as the primary with the tasks, *mfcal* and *gpcal*. In this instance, *gpcal* is used with the additional option *qusolve* to solve for the U and Q flux densities of the calibrator. Then the task *gpboot* is applied to the primary and secondary to correct the flux density scale in the calibration gain table. The *Miriad* manual suggests several tests for verifying the quality of the both the primary and secondary calibration solutions including the scatter plots shown in Figure 5.6 which should appear as concentrations of points (as described earlier). Once the calibration solutions obtained using this strategy were confirmed to be valid, the corrected calibration tables (bandpass, leakage and gains) were applied to the source data using the *gpcopy* command.

5.7 Summary

Approximately 7 hours of lunar data were taken at 1.4 GHz using the polarimetric facility of the ATCA. The lunar data set was flagged by looking for deviations from the smooth continuous Bessel type visibility functions expected from circular object such as the Moon. Calibration was performed using the primary calibrator PKS 1934−638 and 0159−117 as a secondary. Further analysis on the calibrated data set is explained in Chapter 6.

CHAPTER 6

A New Method to Calibrate Ionospheric Dispersion Effects using Lunar Polarisation Observations

This chapter introduces a new technique to calibrate ionospheric pulse dispersion effects using lunar polarisation observations. This work not only has the potential for planetary and atmospheric science results but also has particular application to the detection of UHE neutrinos using the lunar Čerenkov technique.

As described in earlier chapters, lunar Čerenkov emission produces an extremely narrow pulse (Chapter 2). As a Čerenkov pulse travels to Earth it will pass through the ionosphere and experience a frequency dependent time delay resulting in pulse dispersion (Chapter 3). Broadband technology is needed to achieve the time resolution required for pulse detection and, due to data storage restrictions, signal dedispersion and detection must be performed in real time. The ionospheric pulse dispersion characteristic must therefore be known in real time to maximise the received signal-to-noise ratio and subsequent chances of pulse detection (Chapter 4).

The author has formulated a technique for obtaining measurements of the ionospheric TEC which are both instantaneous and line-of-sight to the Moon. The ionospheric TEC can be deduced from Faraday rotation measurements of a polarised source combined with geomagnetic field models, which are more stable than ionospheric models (the CCDIS (55) states that ionospheric TEC values are accurate to $\sim$20% while the IGRF (73) magnetic field values are accurate to better than 0.01%). Lunar thermal emission can be used as the polarised source since Brewster angle effects produce a nett polarisation excess in the emission from the lunar limb. This provides a method for calibrating the ionosphere directly line-of-sight to the Moon and makes the lunar Čerenkov technique extremely attractive for UHE cosmic ray and neutrino astronomy as it allows the characteristic dispersion to be used as a powerful discriminant against terrestrial RFI whilst removing the need to search in dispersion-space.

6.1 Development of the Ionospheric Calibration Technique

This chapter follows the development of the ionospheric calibration technique and begins by considering the different requirements for an UHE neutrino detection experiment using the lunar Čerenkov technique and the polarimetry imaging techniques traditionally required for obtaining Faraday rotation estimates from a synthesis array. Conflicts between the optimal array configurations for these two techniques made it necessary to explore the possibility of obtaining Faraday rotation estimates in the visibility domain. An initial investigation into the lunar polarisation distribution revealed radial symmetries in this emission and motivated the idea that an interferometer baseline will act like a rotating spatial filter, sampling only the polarisation measurement from the central fringe for any given *uv* angle. The spatial filtering concept removes the need for imaging as it provides a way for a radially symmetric distribution to become spatially resolved in the visibility domain.

The work presented in this chapter was developed to further understand the rotating spatial filter concept and to demonstrate the ionospheric calibration technique. This began with an investigation into the distribution of polarised lunar emission including Brewster angle theory and the geometry which causes a polarisation excess around the lunar limb. Existing polarimetry measurements of the Moon were used to develop a lunar model which could generate Stokes visibilities. To further understand how these visibilites are sampled by an interferometer, 2-dimensional visualisations of the Stokes parameter visibility distributions were produced. The spatial filtering technique was applied to the modeled lunar visibilities and it was verified that this technique could be used to produce meaningful position angle measurements in the visibility domain. Once verified, the technique was also applied to real lunar data taken with the ATCA (see Chapter 5) so that real Faraday rotation estimates could be determined from the position angle measurements. The Faraday rotation estimates were combined with magnetic field models to obtain values for the ionospheric TEC. To evaluate the effectiveness of this technique, these results were compared against Faraday rotation measurements derived from a polarised source and ionospheric TEC estimates derived from dual-frequency GPS data. Details of each of these stages is presented in the following sections.

6.2 Lunar Polarisation Observations and the Neutrino Detection Experiment

The unique constraints of an UHE neutrino detection experiment using the lunar Čerenkov technique conflict with traditional methods of planetary synthesis imaging and polarimetry. Therefore to apply this method of ionospheric calibration to a detection experiment, innovations are required in the analysis of lunar polarisation observations. In particular, a method of obtaining lunar Faraday rotation estimates in the visibility domain had to be developed. This method requires an understanding of the interferometric process (outlined in Chapter 5) and exploits symmetries in the lunar polarisation distribution.

An array of small dishes is the optimum radio instrument for a non-targeted UHE neutrino detection experiment using the lunar Čerenkov technique (this was discussed in Chapter 4). An array is advantageous as it avoids the trade-off between antenna sensitivity and Moon coverage which occurs for a single dish aperture of increasing size. Using multiple smaller dishes allows an increase in sensitivity without loss of coverage, provided that the dish separation is large enough to ensure the thermal lunar emission – which dominates the system temperature – is incoherent between antennas. An array configuration with long baselines will ensure that there is only a low degree of lunar correlation between antennas and is therefore optimal for UHE neutrino detection, however, this is non-ideal for lunar polarimetry observations. Synthesis imaging is traditionally the first stage in obtaining polarimetry measurements from a radio array and planetary imaging requires a compact configuration to ensure that the source is not too resolved out. This is particularly important for lunar imaging due to the Moon's large angular extent.

Traditionally, the imaging stage of synthesis array polarimetry is required to spatially resolve the distribution of polarised emission. Imaging requires good coverage of the *uv* plane which can be achieved by taking several hours of data from a large number of baselines. Planetary imaging in particular requires that these baselines be kept small (<100 m). Inverse Fourier transform techniques are used to convert measured Stokes visibilities into the image plane. Once they have been spatially resolved, position angle measurements, ψ, can be calculated for each point in space from the resulting Stokes U and Q images via $\psi = 1/2 \arctan(U/Q)$. Multi-frequency observations can then be used to place a constraint on the observed rotation measures. This is achieved by fitting the equation $\psi = \psi_0 + RM\lambda^2$ to a series of position angle images at different frequencies. For a linear array, synthesis imaging requires 12 hours of data (this reduces to ∼8 hours for the ATCA's hybrid configuration), therefore rotation measures obtained via this technique are not available in real time and are averaged over the observation period. This type of polarmetric synthesis imaging is typically used to determine interstellar rotation measures which remain constant with time. The implicit averaging that occurs through imaging makes it less useful for ionospheric Faraday rotation measurements due to the time varying nature of the ionospheric electron content (see Chapter 3 for an analysis of the expected ionospheric TEC). Obtaining rotation measures using traditional imaging techniques therefore introduces an undesirable time averaging effect and the requirement for good *uv* coverage conflicts with the long baseline requirements of the detection experiment.

To overcome these limitations, the author has developed a technique to obtain position angle measurements directly in the visibility domain. Working in the visibility domain removes the requirement for a compact array configuration and allows measurements to obtained in real time. This technique makes use of the angular symmetry in planetary polarisation distribution. The intrinsic thermal radiation of a planetary object appears increasingly polarised toward the limb, when viewed from a distant point such as Earth. The polarised emission is radially aligned and is due to the changing angle of the planetary surface toward the limb combined with Brewster angle effects. The angular symmetry of this distribution can be exploited by an interferometer so that an angular spatial filtering technique may be used to obtain real-time position angle measurements directly in the visibility domain.

The measured position angles are uniquely related to the corresponding *uv* angle at the time of the observation. Comparison with the expected radial position angles, given the current *uv* angle of the observation, gives an estimate of the Faraday rotation induced on the Moon's polarised emission. Faraday rotation estimates can be combined with geomagnetic field models to determine the associated ionospheric TEC and subsequently provide a method of calibrating the current atmospheric effects on potential Čerenkov pulses. This method not only has the advantage of obtaining estimates which are line-of-sight to the Moon but also allows for instantaneous estimates to be obtained. Further discussion of lunar polarisation properties and this new technique for ionospheric calibration is presented in the following sections.

6.3 Distribution of Lunar Polarisation

The distribution of polarised planetary emission was first described by Heiles and Drake and lunar polarisation measurements have been obtained by Heiles and Drake (74) and also the Sky Polarisation Observatory (SPOrt) collaboration (20). These studies have shown that the distribution of polarised emission from a planetary body is radially symmetric with polarisation vectors oriented radially and the polarised intensity increasing toward the limb. This distribution arises from a combination of

Brewster angle effects and a change in viewing angle from the center to the limb of the body.

Toward the limb, the received emission comes from an increasing angle of refraction (see Figure 6.1) and subsequently an increasing angle of incidence at the lunar dielectric boundary. Passage of an electromagnetic wave through such a boundary polarises the initially unpolarised thermal radiation and this occurs more dramatically for an increasing angle of incidence. This is because components of the polarised emission which are parallel and perpendicular to the plane of incidence (which is formed between the surface normal and the line-of-sight) have different Fresnel reflection coefficients. The parallel $R_{\|}$ and perpendicular $R_{\perp}$ Fresnel coefficients are given by

$$R_{\|}(\theta_i) = \left[\frac{tan(\theta_r - \theta_i)}{tan(\theta_r + \theta_i)}\right]^2 \tag{6.1}$$

$$R_{\perp}(\theta_i) = \left[\frac{\sin(\theta_r - \theta_i)}{\sin(\theta_r + \theta_i)}\right]^2, \tag{6.2}$$

where (θ_i) and (θ_r) are the angles of incidence and refraction respectively, related by Snell's law. The amount of radiation which is refracted by the surface is related to the emissivity coefficients which are complementary to these reflection coefficients *i. e.*

$$E_{\|}(\theta_i) = 1 - R_{\|}(\theta_i) \tag{6.3}$$

$$E_{\perp}(\theta_i) = 1 - R_{\perp}(\theta_i). \tag{6.4}$$

At the center of the body, the angles of incidence and refraction are both equal to 0° and the Fresnel coefficients are equal so there is no polarisation excess. Toward the limb the angle of incidence required to refract radiation toward a distant point of observation, such as Earth, approaches the Brewster angle. Approaching this angle, the perpendicular component experiences more internal reflection resulting in an excess of polarised emission parallel to the surface normal (see Figure 6.2).

The SPOrt collaboration (20) performed measurements of polarised emission from the Moon at 8.3 GHz using the polarimetric facility of the Medicina 32-m Radio telescope. They performed right ascension scans, repeated at different declinations, which showed that the polarised emission drops off very sharply toward the center of the Moon (see Figure 6.3). A map of the lunar polarisation distribution may be seen in Figure 6.4.

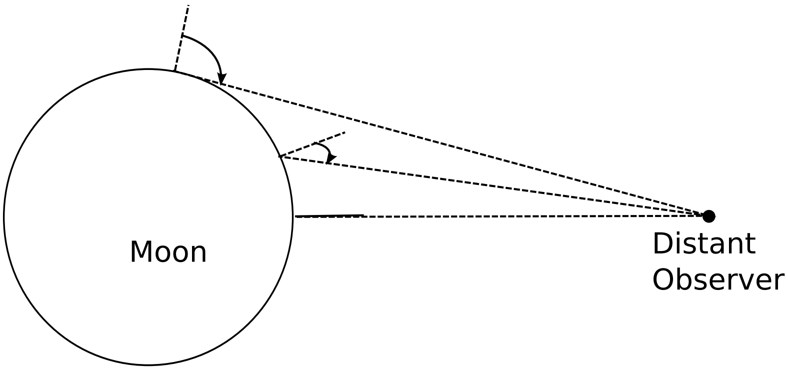

Figure 6.1: The Moon refracts its intrinsic thermal radiation in all directions. The component of this radiation seen by a distant observer comes from an angle of refraction which increases toward the limb of the Moon.

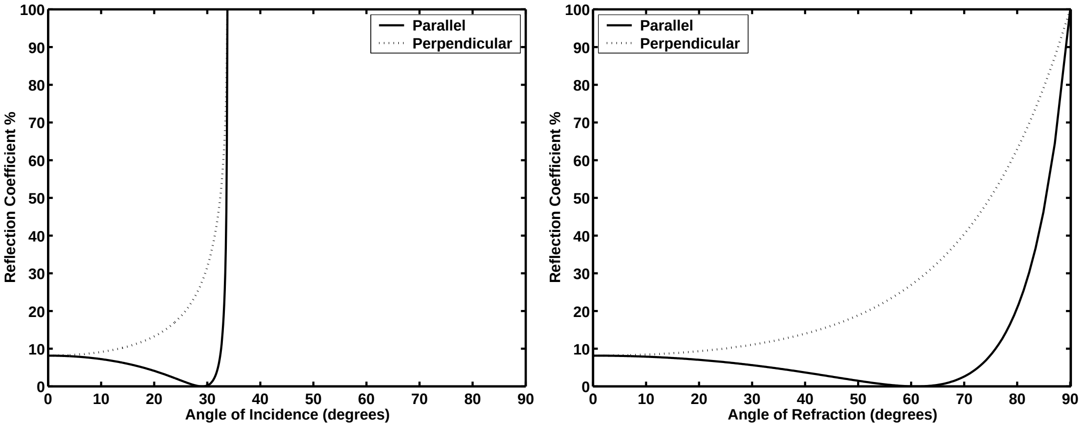

Figure 6.2: Parallel and perpendicular reflection coefficients as a function of angle of incidence and refraction. As the angles of incidence and refraction, related by Snell's law, increase they approach the Brewster angle where the parallel reflection coefficient goes to zero. This results in total emission of the parallel component of radiation and a net excess over the perpendicular component. Refractive indices of 1.8 and 1.0 have been used at the lunar dielectric boundary.

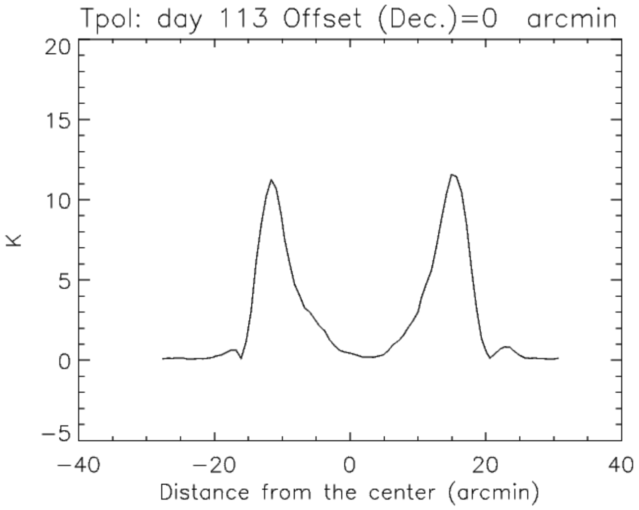

Figure 6.3: Right ascension scan of lunar polarised brightness temperature. The scan was made at 8.3 GHz (FWHM = 4.8′) by the SPOrt collaboration using the polarmetric facility of the 32-m Medicina Radiotelescope (20).

6.4 Development of a Lunar Polarisation Model

To investigate how this polarisation distribution affects the Stokes visibility measurments, a lunar polarisation model was developed in *Miriad* using the *uvgen* task which computes visibilities for a model source. The model source generated consisted of a ring of points and each was given 3% linear polarisation with the position angle aligned radially according to its position in the ring.

For N points, the Position Angle (ψ), Right Ascension (RA) and Declination (Dec) of each point was given by

$$\psi_n = \frac{n}{N} \times 360^\circ \tag{6.5}$$

$$RA_n = \frac{size}{2}\sin(\psi_n) \tag{6.6}$$

$$Dec_n = \frac{size}{2}\cos(\psi_n), \tag{6.7}$$

where $size$ is the diameter of the ring. These points were generated using a *Matlab* script and imported into a text document for use with *uvgen*. Typical system parameters for the ATCA were obtained from a built-in *Miriad* catalogue using the command *source $MIRCAT/uvgen.def.atca*. Antenna configuration 1.5C was used

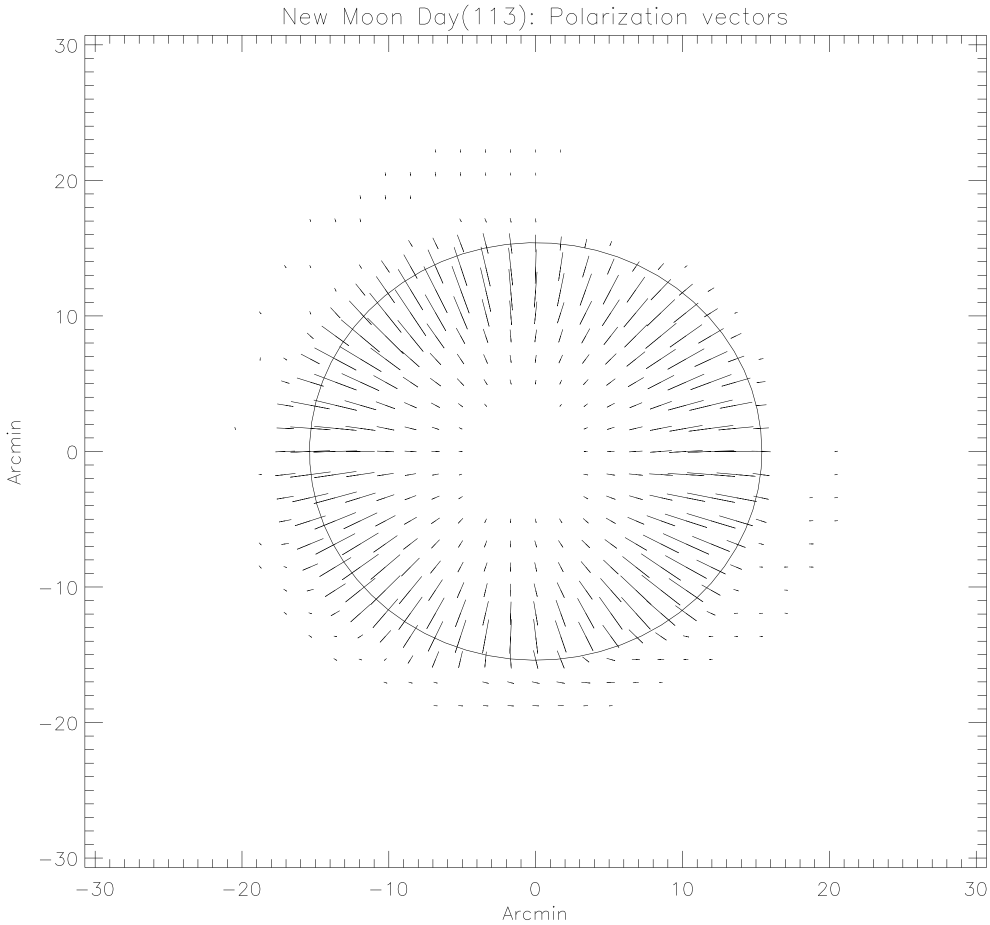

Figure 6.4: Lunar polarisation vector distribution. This map was made from observations at 8.3 GHz (FWHM=4.8′) by the SPOrt collaboration using the polarmetric facility of the 32-m Medicina Radiotelescope (20).

to coincide with the array configuration used during initial test observations. This configuration also had the advantage of being an east-west array which simplifies the relationship between the expected position angle measurement and the corresponding *uv* angle of the observation. The polarisation leakage and system temperature were both set to zero to remove noise from the generated model polarisation measurements and, for most of the simulations, the cycle was reset to its default values to ensure a 100% on-source duty cycle.

The number of points around the ring was chosen to avoid any aliasing effects of the visibility function. This was achieved by over-sampling the Nyquist interval in the image plane. Baseline length can be related to angular resolution via

$$R_{\text{rad}} = \frac{\lambda}{B}, \tag{6.8}$$

where R_{rad} is the angular resolution in radians, λ is the wavelength and B is the baseline. At 1.4 GHz, and for a maximum baseline of 300 m, the minimum angular resolution achievable will be $\sim 2.3'$. Two samples are required in this spatial interval to avoid aliasing in visibility space. Therefore the Moon must be sampled approximately every $1.15'$ and, assuming an angular diameter, D, of $\sim 30'$, the number of points required is

$$N = \frac{\pi D}{1.15'} \approx 82. \tag{6.9}$$

To verify the model, firstly a 5% scaled version was produced for imaging (see Chapter 5 for a description of interferometry and the imaging process). An additional parameter was added to the model to rotate the polarisation vectors in the same manner as Faraday rotation. This simple model assumes that any Faraday rotation will be constant across the Moon's footprint on the ionosphere. An image of both the original model and a model with 20° Faraday rotation applied may be seen in Figure 6.5. Figure 6.6 also shows the U and Q Stokes parameter components of the original model. These images have been produced by inversion of the *uvgen* visibility data and therefore contain sampling artifacts from the *uv* coverage of the simulated array configuration. Some of these artifacts have been removed by applying a threshold, particularly in the polarised intensity image. However, they are still clearly evident in the Stokes U and Q distributions.

6.5 Lunar Stokes Parameters in the Visibility Domain

Once the lunar polarisation model had been verified through imaging, the Stokes parameter visibilites could be investigated. The structure of lunar Stokes visibilities

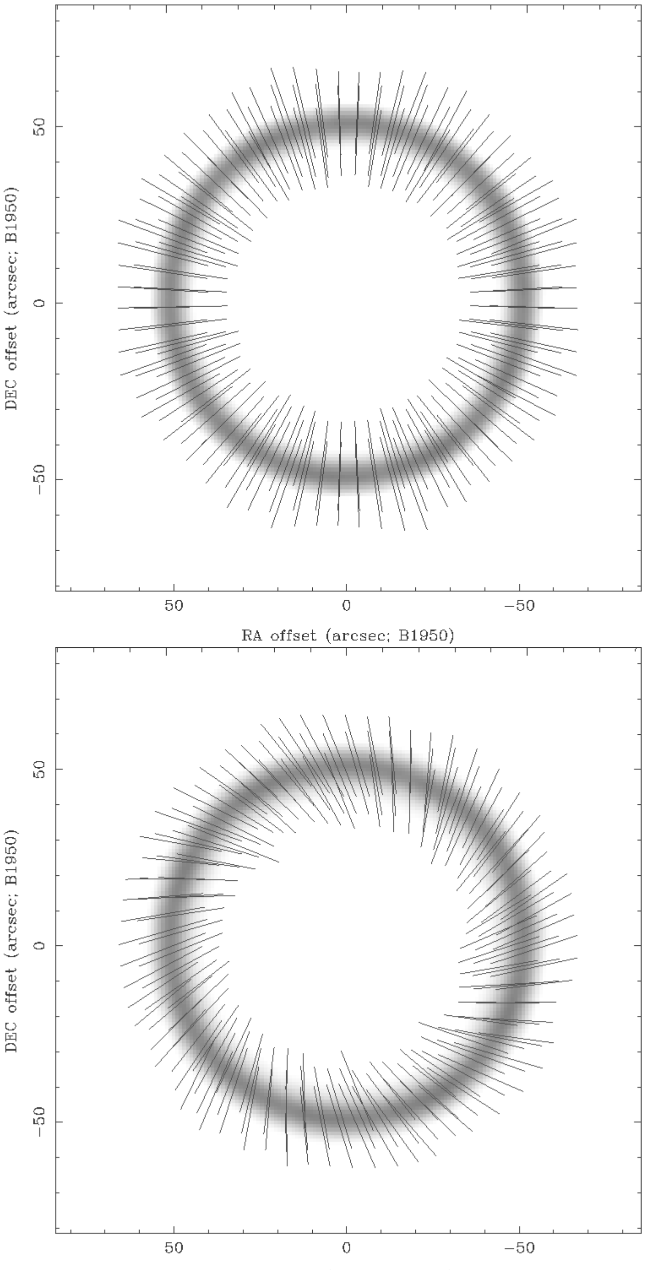

Figure 6.5: The lunar polarisation model developed in *Miriad*. (*Top*) no Faraday rotation applied and (*bottom*) 20° Faraday rotation applied. In both cases, the grey scale indicates the level of polarised intensity and the vectors indicate the position angle.

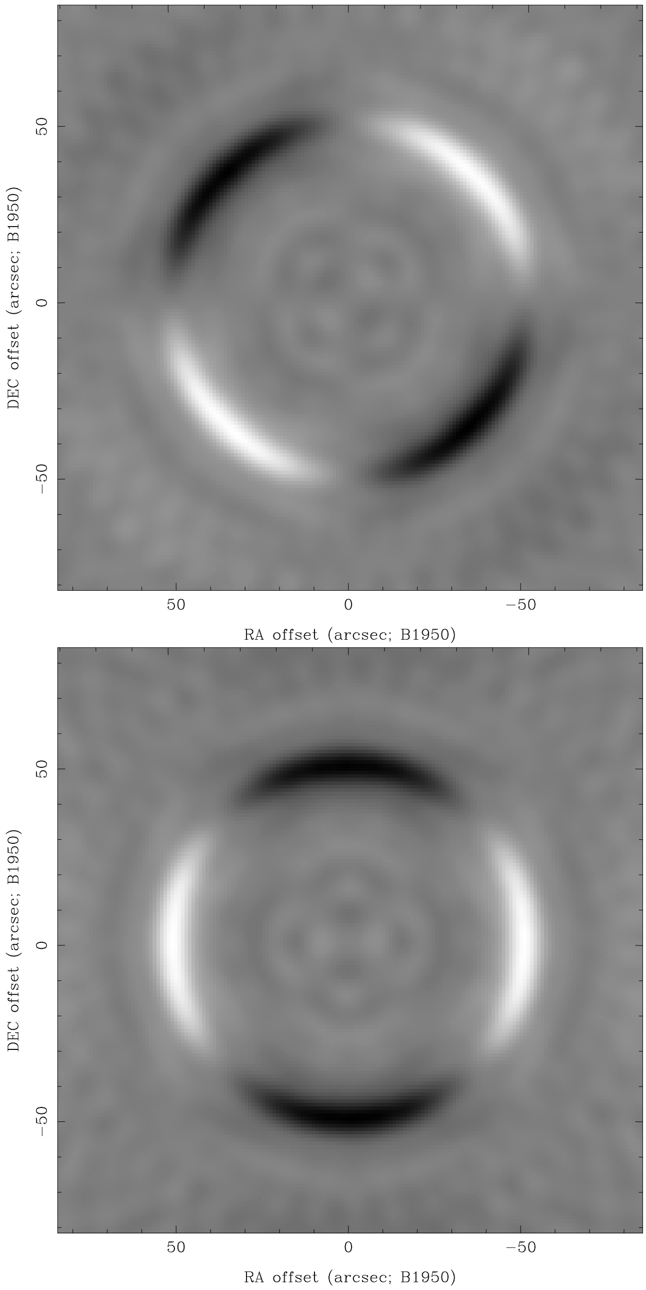

Figure 6.6: U and Q Stokes parameter distributions produced from the lunar polarisation model developed in *Miriad* (no Faraday rotation applied).

is influenced by the angular structure of the U and Q distributions and modulated by the level of spatial correlation that is sampled by each baseline. To understand this phenomenon, it helps to consider each effect separately. Therefore the model was placed at the South Celestial Pole to generate model visibilities without baseline projection effects. It was actually slightly offset from the South Celestial Pole as the offsets in right ascension and declination required to specify the model's point source positions would no longer produce a ring if centered exactly at the Pole. Placing a ring exactly on the South Pole can be achieved using a different, and much simpler, co-ordinate system. However, this would not provide an accurate test of the co-ordinate system which was required to place the model at more realistic declinations.

As the Earth rotates, orientation of the interferometer fringes rotate on the Moon which sample a rotating radial cut of the lunar polarisation distribution. The radial cut being sampled corresponds to the polarisation measurement contribution from the central fringe. This occurs as polarisation vectors corresponding to other radial cuts average to produce the same result as the central fringe. The nett polarisation measured will therefore correspond to the orientation of the averaged polarisation vectors in the central fringe. This is best understood by considering the 2-dimensional Stokes parameters visibility distributions as presented in Section 6.6.

As the central fringe rotates it will act like a rotating spatial filter. If it rotates on a radially symmetric object there will be no structure in the resulting visibility functions. However, while the polarisation vector distribution is radially symmetric, the underlying Stokes U and Q distributions are not (see Figure 6.6). Therefore structure emerges in the Stokes U and Q visibility measurements as the rotating fringes sample their angular distribution. This produces visibilities which are sinusoidal in nature and can be seen in Figure 6.7.

The amplitude of these sinusoidal curves depends on the baseline length, as each baseline samples a different point on the spatial correlation function. Since baseline effects have been minimised by 'placing' the model at the South Pole these modeled visibilities are only influenced by the angular structure of the Stokes U and Q distributions. The next step in understanding the lunar Stokes visibilities is to consider the spatial coherence function and associated baseline projection effects that occur at a more realistic declination.

Baseline projection refers to the shortening of effective baseline length due to changing geometry that occurs with the Earth's rotation (see Section 5.2). Source declination determines the baseline's path through uv space and the degree of baseline projection that will occur. Placing the model at a higher declination causes array baselines to trace out elliptical patterns in uv space and introduces a higher

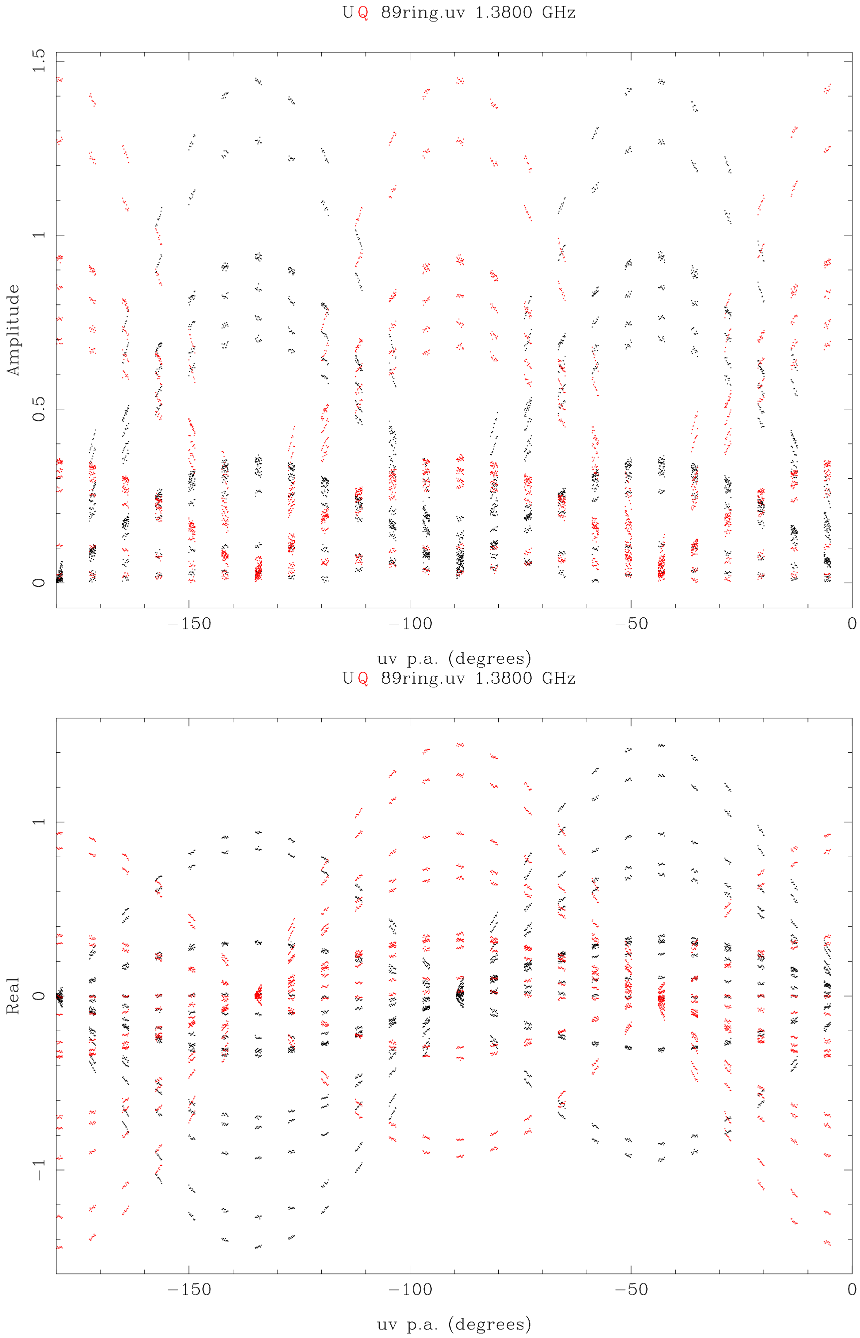

Figure 6.7: The amplitude (*top*) and real part (*bottom*) of the Stokes visibilities (U in black and Q in red) produced by the lunar polarisation model developed in *Miriad*. All baselines are plotted together and each baseline function has a different amplitude due to the different level of lunar correlation it samples.

degree of projection. The effect of this projection is determined by the spatial coherence function and it can be isolated from other effects by considering the polarised intensity distribution (see Figure 6.8) which contains no angular structure *i. e.* it is radially symmetric.

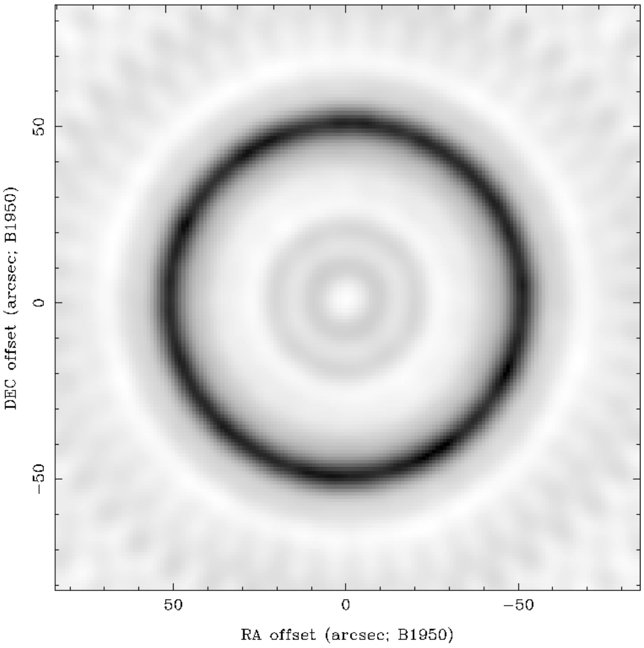

Figure 6.8: Polarised intensity image produced by the lunar polarisation model developed in *Miriad*.

For a radially symmetric object, the 2-dimensional Fourier transform relationship between the sky brightness distribution and the spatial coherence (visibility) function reduces to a 1-dimensional Hankel transform with a Bessel function kernel (75). In particular, for the case of a uniformly illuminated disk ($I(\rho) = I_0$), of radius R, this becomes

$$V(\beta) = 2\pi R^2 \int_0^1 I(\rho) J_0(2\pi\rho\beta)\rho d\rho \qquad (6.10)$$

$$= I_0 \pi R^2 J_1(2\pi\beta)/\pi\beta, \qquad (6.11)$$

where ρ is the normalised radial image coordinate and β is the radial *uv* plane coordinate.

As discussed in Section 6.3, the distribution of polarised emission from a planetary object appears as a well with maxima aligned around the object's limb and this arises due to differences in the Fresnel transmission coefficients. The polarised visibility function can be calculated from these coefficients and is given by a Hankel transform with an order 2 Bessel function kernel (see Ref. (76)).

$$V_p(\beta) = \int_0^1 (R_{\|} - R_{\perp}) J_2(2\pi\rho\beta)\rho d\rho \tag{6.12}$$

This transform has no analytical solution and must be numerically integrated (see Ref. (77) for the expected polarised response). However, the function will be zero at $\beta = 0$ due to the order two Bessel kernel. Physically this represents the integrated polarised emission canceling at zero spacing.

The visibility functions for an unpolarised ring and an unpolarised well distribution are given by a first order Bessel function and a sinc function respectively. These Hankel transforms are plotted in Figure 6.9 and are useful for understanding the *uv* plane distributions of a planetary object's Stokes U and Q which are discussed later.

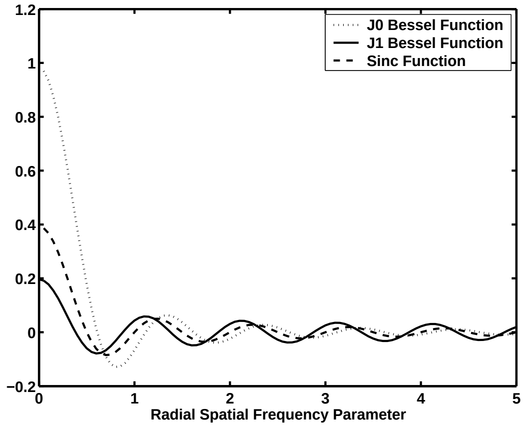

Figure 6.9: Hankel Transforms: $J_0(\beta)/\beta$ Bessel function for a disk, $J_1(\beta)$ Bessel function for a ring, and $sinc(\beta)$ function for a well.

Baseline projection slides the spatial coherence sample along the visibility function. This effect is most easily observed by considering a source with constant angular structure, such as the lunar polarisation intensity which maps out portions of the spatial coherence function when measured in the visibility domain (this was illustrated in Chapter 5). Therefore Stokes visibilities affected by baseline projection are essentially measuring the angular U and Q structure modulated by a time varying level of spatial correlation. At a realistic declination, there are two effects contributing to the measured Stokes U and Q visibilities (see Figure 6.10). Firstly the actual angular distribution of U and Q which is sampled by fringe rotation (see Figure 6.11, *Top*) and secondly an amplitude modulation of this distribution that occurs as the baselines move through the spatial coherence function (see Figure 6.11, *Middle*).

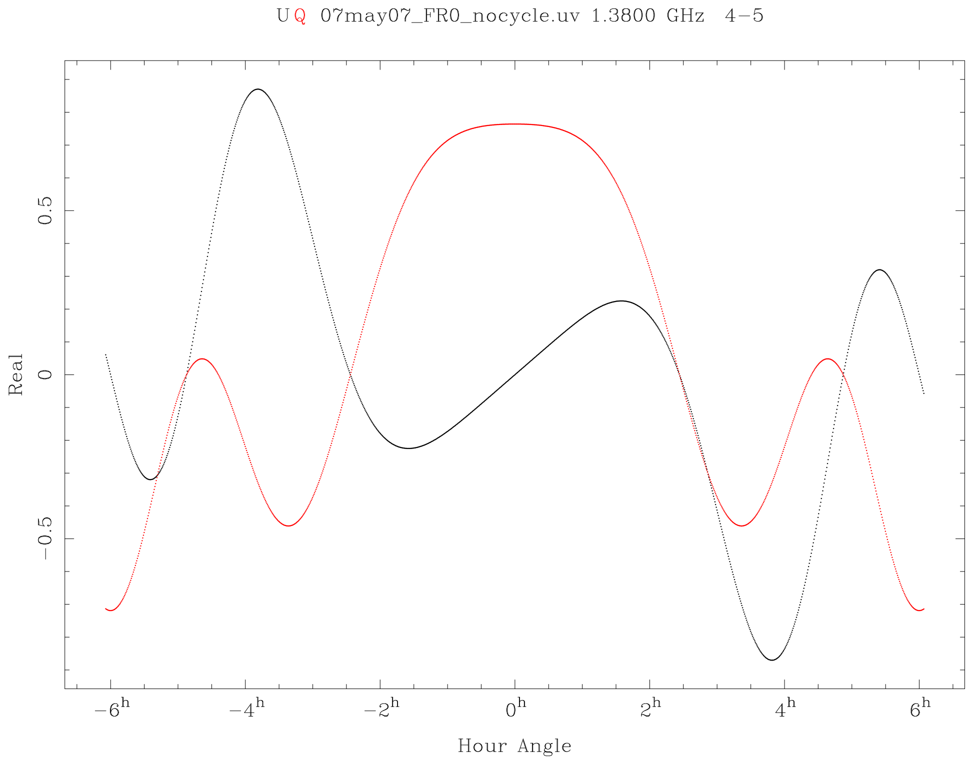

Figure 6.10: Stokes visibilities generated from the lunar polarisation model, developed in *Miriad*, with a realistic scale (∼2000″) and placed at a realistic declination (∼ −30°). This illustrates the two competing effects which influence the structure of lunar Stokes U and Q visibilites, namely the angular structure of the U and Q distributions and the modulation effect of baseline projection.

However, as the Stokes U and Q distributions are not radially symmetric their spatial coherence function will vary with uv angle (see Figure 6.11, *Bottom*). To fully understand the interaction of these effects, it is best to look at the two dimensional distributions of Stokes U and Q in uv space.

6.6 2-Dimensional Visualisation of Lunar Stokes Visibilities and the Angular Filtering Technique

To visualise the lunar Stokes visibilities in 2 dimensions, the author developed a second lunar model in *Matlab*. This was necessary as *Miriad* is not designed for visibility imaging. The angular structure of this model was developed by setting up a fine grid of spatial coordinates (x, y) and describing the lunar polarisation distribution mathematically as an exponential in the angular co-ordinate, θ, such that $x + iy = re^{i\theta}$. The position angle was then be defined as 2θ. This produced

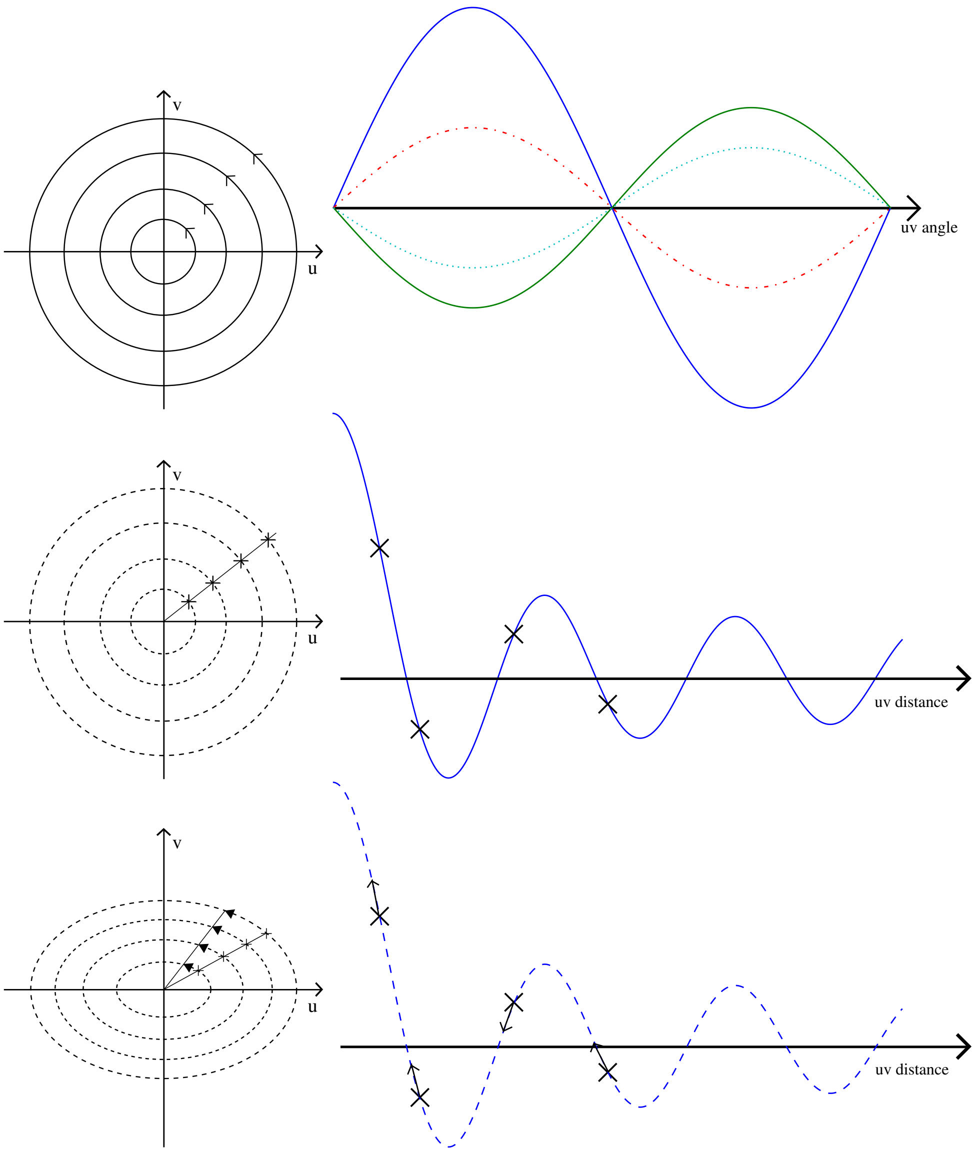

Figure 6.11: (*Top*) When the model is placed at the South Celestial Pole the uv plane is sampled in concentric circles. This measures the angular structure of the lunar U and Q distributions and produces visibilities that are sinusoidal in nature. (*Middle*) When the uv plane is sampled along a radial cut, by baselines of increasing length, the source spatial coherence function is being sampled. These levels of spatial coherence are responsible for the variations in peak amplitude seen between baselines in the top plot. (*Bottom*) At a realistic lunar declination baseline projection causes the uv plane to be sampled in elliptical patterns and therefore the spatial correlation function is sampled in a time varying way.

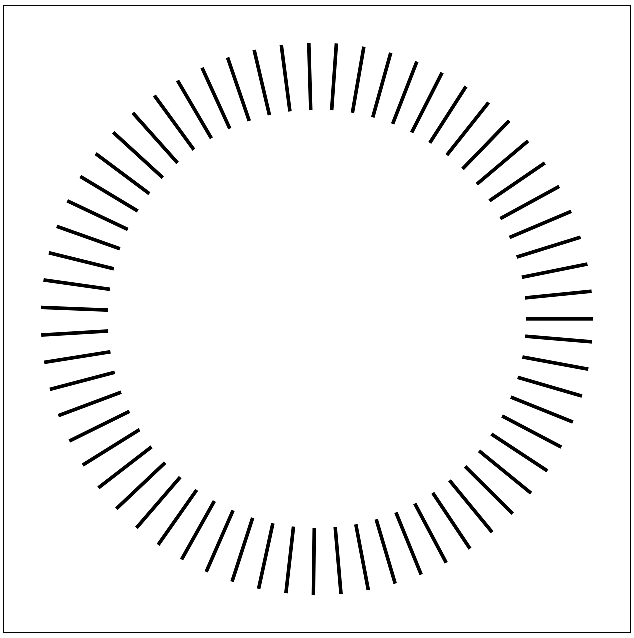

Figure 6.12: Position angle distribution produced by the lunar polarisation model developed in *Matlab*.

a vector field with the correct angular structure to represent the lunar polarisation distribution.

The sky brightness distribution of polarised planetary emission is a steep well and was approximated by a ring around the lunar limb. This ring represents where the well maxima would occur and was used to mask the position angle vector field. The resulting Position Angle sky distribution and associated Stokes U and Q distributions may be seen in Figures 6.12 and 6.13 respectively.

The distribution of Stokes U and Q visibilities was obtained by taking the Fourier transform of the U and Q sky distributions and these are shown in Figure 6.14. On a track of constant uv distance both U and Q vary smoothly and the angular polarisation structure of the image plane distributions is preserved, although rotated by $\pi/2$ for some bands. In the radial direction, these distributions appear to be modulated by a spatial correlation function, causing alternating bands, with the same structure as the visibility functions described above for a ring or well.

In positive bands of the spatial correlation function the image plane angular structure will be rotated by $\pi/2$ (in accordance with the Fourier scaling theorem). While in negative bands, the change in sign of Stokes U and Q will result in an additional rotation of $-\pi/2$ and restore the original angular structure of the image plane. The amplitude of the apparent modulating spatial correlation function varies

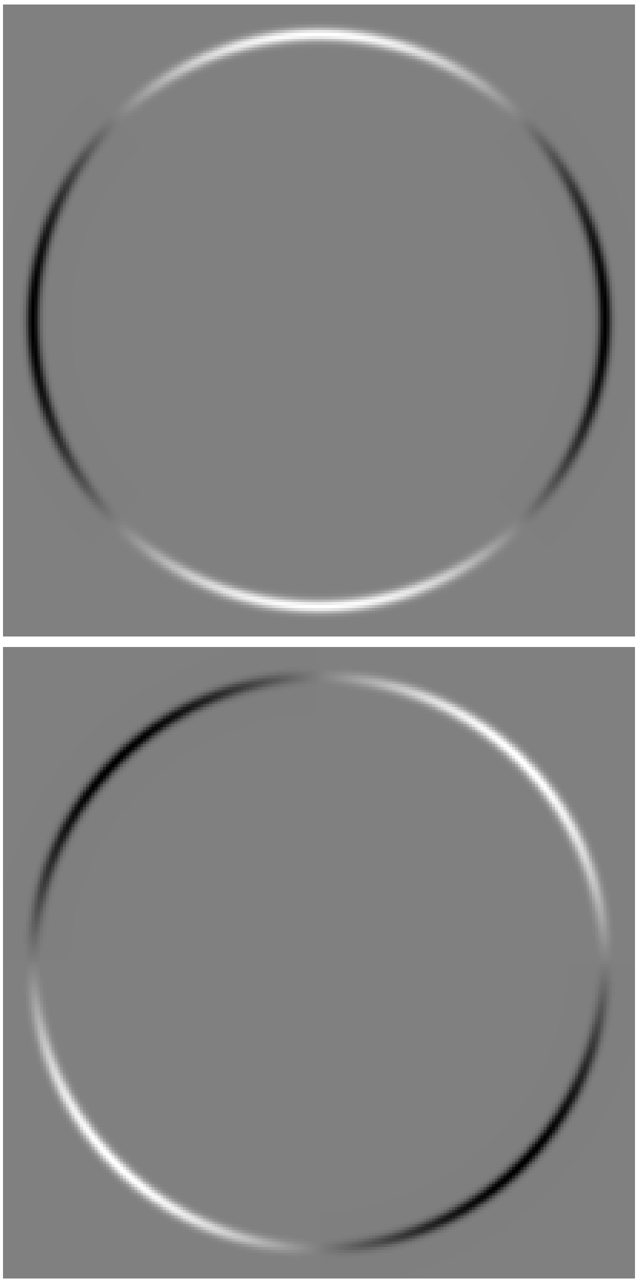

Figure 6.13: Stokes Q and U sky distributions produced by the lunar polarisation model developed in *Matlab*.

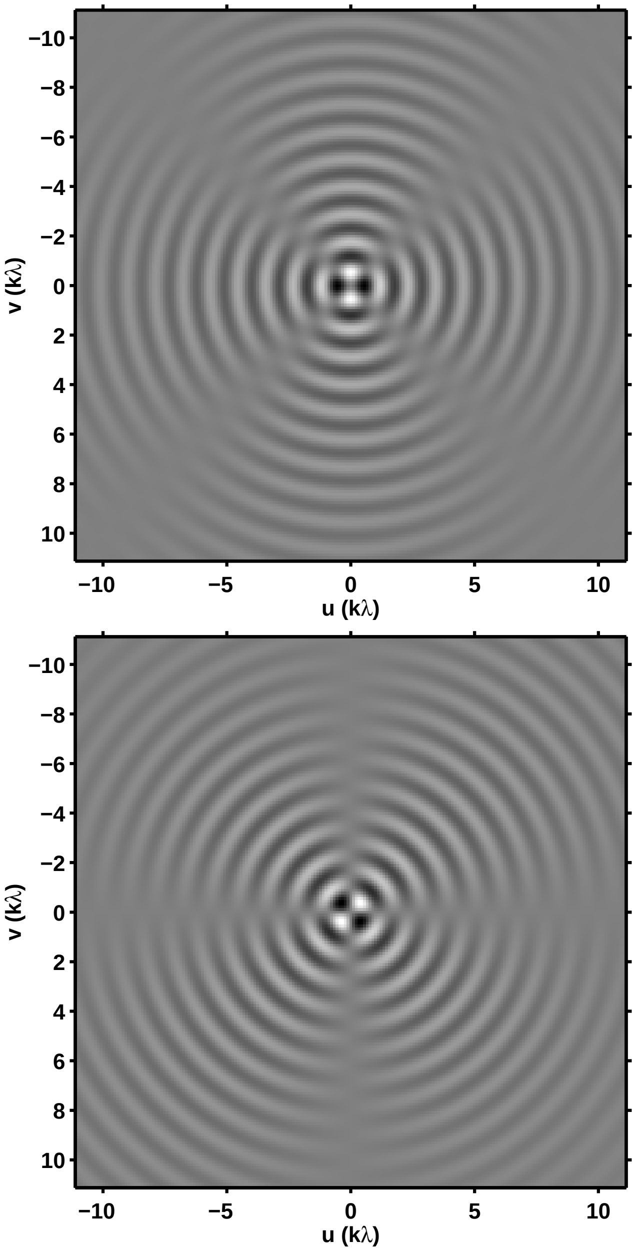

Figure 6.14: Stokes Q and U uv plane distributions produced by the lunar polarisation model developed in *Matlab*.

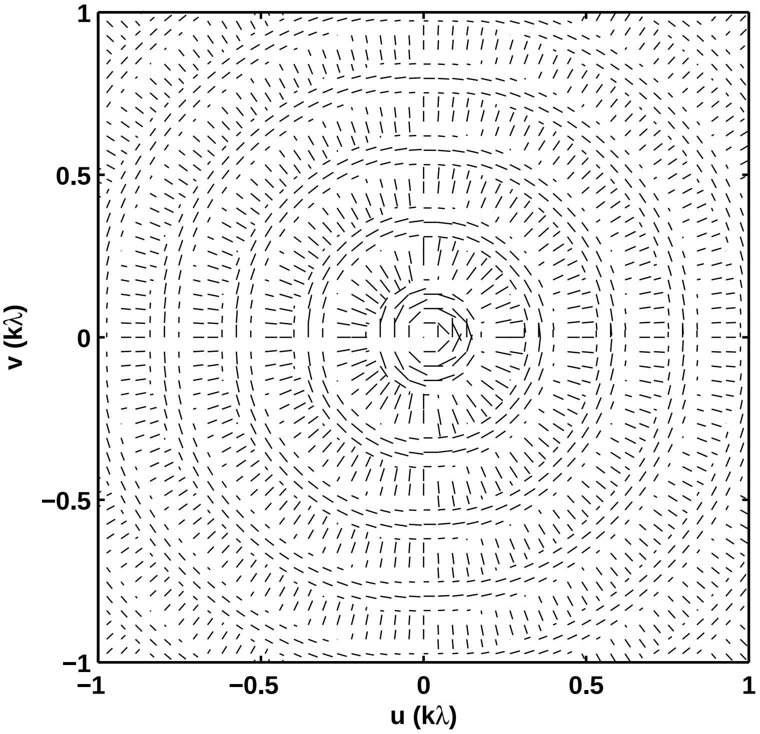

Figure 6.15: Position angle distribution in the *uv* plane produced by the lunar polarisation model developed in *Matlab*.

with *uv* angle. The lack of radial symmetry in this function is due to the asymmetry of the U and Q distributions in the image plane.

Since the angular structure of both distributions is preserved, and the lunar position angle distribution has only angular dependence, position angle measurements can be taken directly from the Stokes U and Q visibilities via

$$\psi = \frac{1}{2}\arctan(\frac{U}{Q}). \tag{6.13}$$

The resulting position angle distribution can be seen in Fig 6.15. This distribution alternates between bands of radial and circular orientation as U and Q change signs and induce $\pi/2$ rotations. Each measurement at a particular *uv* angle will correspond to the position angle measurement of a radial cut in the image plane. In this way each baseline acts like a rotating spatial filter as it sweeps through different *uv* angles. These measurements will only be meaningful for the case of an object with angular symmetry in its position angle distribution, such as the case with a planetary body.

6.7 Analytic Treatment of the Angular Filtering Technique

It was noted in the last section that the angular distribution of planetary position angle measurements is preserved in the visibility domain. This can be described analytically by considering the position angle as a phase term between U and Q.

If we define spatial coordinates such that $x + iy = re^{i\theta}$, we can represent the position angle distribution as $R(r)e^{i\psi}$ where $R(r)$ describes the distribution's radial dependence (for a planetary body this should only be a step function to indicate the planetary boundary) and ψ is the position angle. For a planetary object the position angle is also equal to the spatial angle but this can be generalised to any linear function of the spatial angle ($\psi = n\theta$) and the analytic solution will still hold.

If u and v are spatial coordinates in the visibility domain such that $u+iv = qe^{i\phi}$, then the 2-dimensional Fourier transform is defined as

$$g(u, v) = \int_{-\infty}^{\infty} \int_{-\infty}^{\infty} f(x, y)e^{-2\pi i(ux+vy)}dxdy \tag{6.14}$$

$$\begin{aligned} g(q, \phi) &= \int_{0}^{2\pi} \int_{0}^{\infty} f(r, \theta)e^{-2\pi irq(\cos\phi\cos\theta+\sin\phi\sin\theta)}rdrd\theta && (6.15) \\ &= \int_{0}^{2\pi} \int_{0}^{\infty} R(r)e^{in\theta}e^{-2\pi irq\cos(\theta-\phi)}rdrd\theta. && (6.16) \end{aligned}$$

Introduce a new integration variable $\varphi = \theta - \phi$

$$\begin{aligned} &\int_{-\phi}^{2\pi-\phi} \int_{0}^{\infty} R(r)e^{in\varphi+\phi}e^{-2\pi irq\cos\varphi}rdrd\varphi && (6.17) \\ &= e^{in\phi} \int_{0}^{\infty} R(r)r \int_{0}^{2\pi} e^{-2\pi irq\cos\varphi-n\theta}d\varphi dr. && (6.18) \end{aligned}$$

Let $\varphi = -(\tau + \frac{\pi}{2})$ so $\tau = -(\theta + \frac{\pi}{2})$ and $d\theta = -d\tau$

$$\begin{aligned} &e^{in\phi} \int_{0}^{\infty} R(r)r \int_{-\frac{\pi}{2}}^{-\frac{3\pi}{2}} e^{-i(2\pi rq\cos(-(\tau+\frac{\pi}{2}))+n\tau+n\frac{\pi}{2})} - d\tau dr && (6.19) \\ &= e^{in\phi} \int_{0}^{\infty} -R(r)r2\pi e^{-in\frac{\pi}{2}} \int_{-\pi}^{\pi} e^{-i(-2\pi rq\sin\tau+n\tau)}d\tau dr && (6.20) \\ &= -2\pi e^{in(\phi-\frac{\pi}{2})} \int_{0}^{\infty} R(r)e^{-in}J_n(2\pi rq)rdr. && (6.21) \end{aligned}$$

The exponential term shows that the position angle distribution has been preserved in the visibility domain, in terms of the new spatial angle ϕ, except for a $\pi/2$ rotation (ie $\psi = n(\phi - \pi/2)$). The expression in the integral describes the radial dependence of the position angle distribution. This is a Hankel transform with a Bessel kernel of order n and this function is responsible for the bands of sign change in U and Q which cause $\pi/2$ rotations in the position angle measurements.

6.8 Obtaining Lunar Position Angle Estimates

The preceding sections have explored lunar Stokes parameter distributions in the *uv* plane. This exploration has shown that the angular structure of lunar Stokes U and Q sky distributions is preserved in the *uv* plane and that each baseline acts like a rotating spatial filter as it sweeps through different *uv* angles. This means that meaningful position angle measurements can be calculated directly in the visibility domain.

Each interferometer baseline will track an elliptical path through *uv* space with the degree of ellipticity determined by the object's declination with respect to the interferometer (except for the case of an object aligned with the Celestial Pole which will trace a circular path). Any elliptical path will cross through positive and negative bands of the Stokes U and Q visibility functions causing 90° jumps in the position angle measurement to occur after each null in polarised intensity.

This can be seen in Figure 6.16 which shows the Position Angle measurements both before and after correction for the 90° jumps. These measurements were obtained from visibilities generated by the *Miriad* lunar model and using antenna configuration H168C to match the observational data (as described in Chapter 5). The final plot in the this figure shows the difference measured when comparing the ψ measurement to the *uv* angle with a 90° offset. For the generated data, the difference in this relationship is generally limited by the accuracy of the simulation although this increases sharply to a few degrees when the polarised intensity goes through a null.

In observational data, the difference measured in this relationship will represent any change in polarisation vector orientation due to Faraday rotation. To illustrate this principle, a *Miriad* lunar model was generated with the polarisation vectors offset by 10°. The position angle measurements obtained from the visibilities of this model may be seen in Figure 6.17. The difference in the relationship between these measured position angles and their corresponding *uv* angle is offset by 10° (relative to Figure 6.16) which represents the Faraday rotation term applied to the model. Therefore, the angular spatial filtering technique is successful in determining meaningful position angle estimates in the visibility domain and identifying deviations in the expected relationship between these estimates and the instantaneous *uv* angle.

6.9 Obtaining Lunar Faraday Rotation Estimates from Observational Data

Observations of the Moon were taken using the 22-m telescopes of the Australia Telescope Compact Array with a center frequency of 1384 MHz (see Chapter 5 for more details of these observations). At this frequency the Moon is in the near field of the array, however, investigation of the Fresnel factor in polar coordinates showed that it has no dependence on the spatial parameter, θ (defined above), which determines the polarisation distribution of a planetary body.

Using the angular spatial filtering technique, position angle estimates were calculated directly in the visibility domain of the lunar observational data. Figure 6.18 shows the position angle estimates (both as raw values and corrected for the 90° jumps described earlier), the polarised intensity and the relationship between the *uv* angle and expected position angle measurement. This relationship is near linear and deviations from linear are assumed to be from Faraday rotation.

The deviations are investigated more thoroughly in Figure 6.19 which contains Faraday rotation estimates, for the Moon and the polarised source 0139−263, averaged over the three shortest east-west baselines (1–4 (61 m), 4–5 (107 m) and 1–5 (168 m)) of antenna configuration H168C. The Faraday rotation estimates were obtained by calculating position angles directly in the visibility domain and comparing these angles to the expected position angle, for the polarised source, or instantaneous *uv* angle for the lunar case. The resultant Faraday rotation estimates were averaged over small time increments to smooth out noise-like fluctuations. For the polarised source, averaging was performed over each period of observation (approximately 5 minutes each hour). While for the lunar data, averaging was performed over increments of 6 minutes. Since the polarised lunar emission received on each baseline varied in intensity over time (see Section 6.5 and Figures 6.16 – 6.18), there were nulls during which the obtained position angle information was not meaningful. A threshold was applied to remove position angle measurements taken during these periods of low polarised intensity, P, and baseline averaging was considered necessary as the results on each baseline were slightly different and each affected differently by nulls in P.

The Faraday rotation estimates obtained from the Moon and the polarised source are quite different in both shape and amplitude. This is partly due to the different elevation angle of each source (at any given time) and the resulting differences in magnetic field and slant angle through the ionosphere. These effects are explored

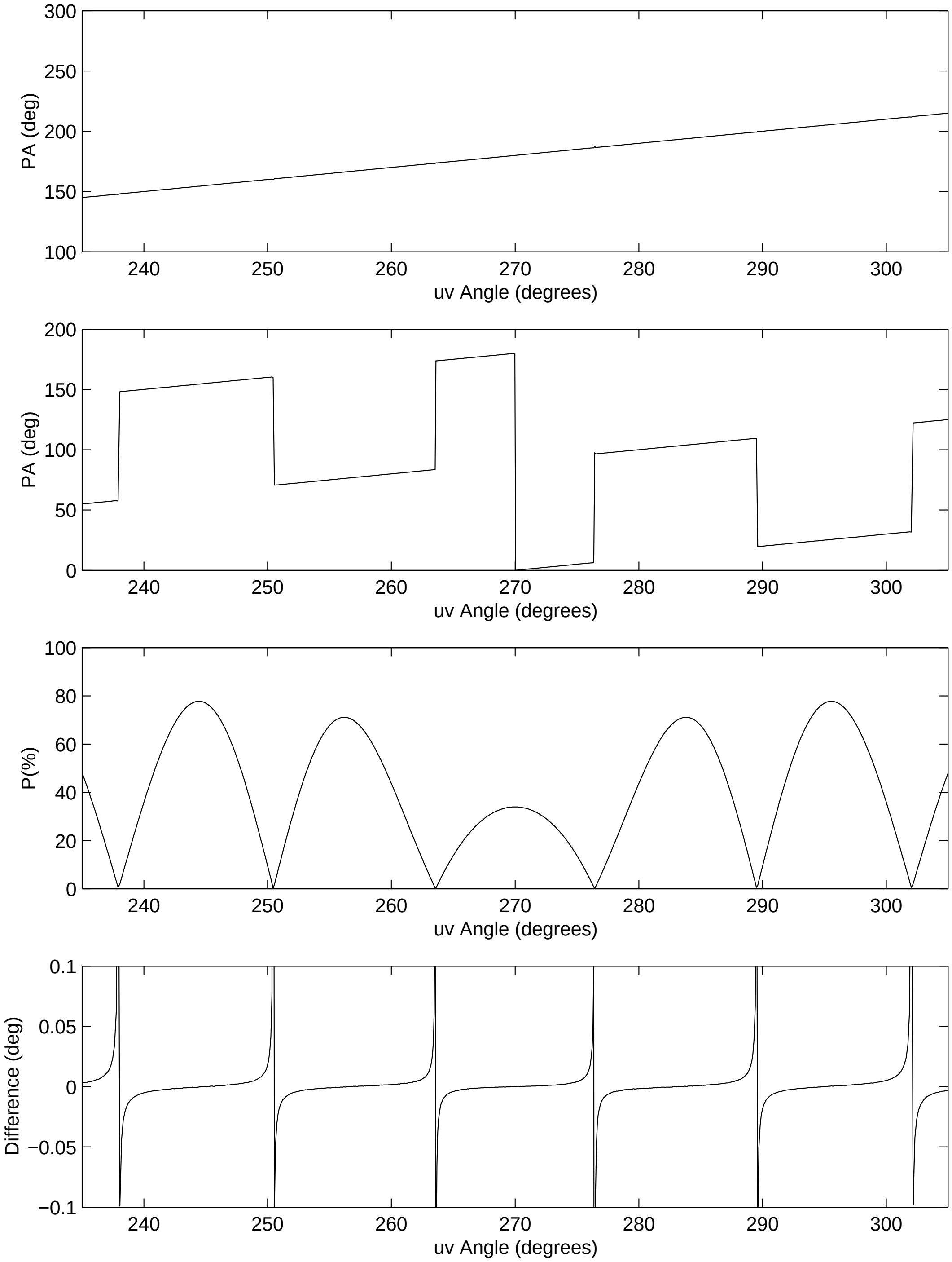

Figure 6.16: This figure shows (*from top*) the position angle measurements corrected for 90° jumps, the uncorrected position angle measurements, polarised intensity and the difference in the relationship between *uv* angle and position angle. These plots were all generated using the *Miriad* model described in Section 6.5 and baseline 1–5 (168 m) of antenna configuration H168C.

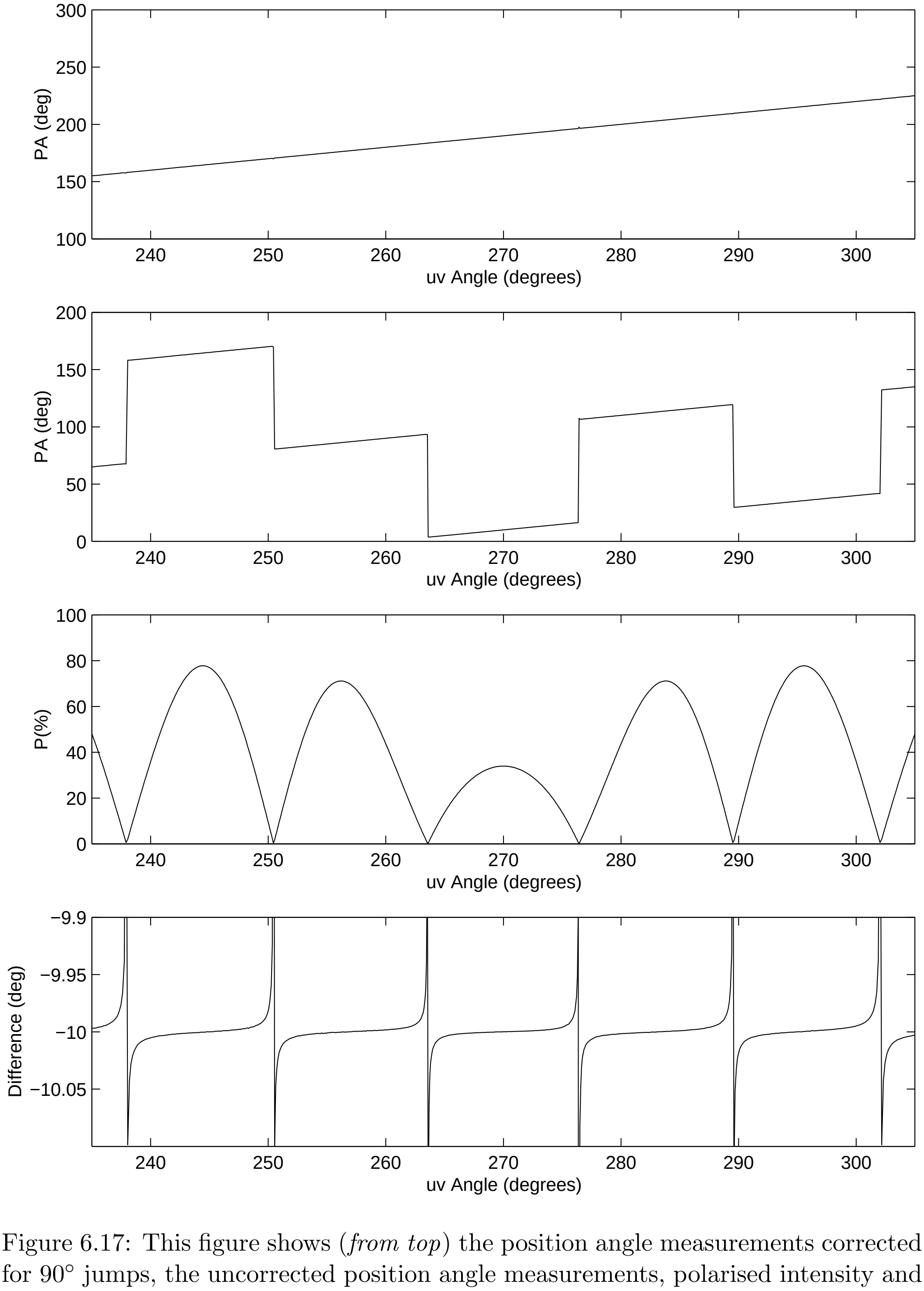

Figure 6.17: This figure shows (*from top*) the position angle measurements corrected for 90° jumps, the uncorrected position angle measurements, polarised intensity and the difference in the relationship between *uv* angle and position angle this time containing a 10° Faraday rotation term applied to the model. These plots were all generated using the *Miriad* model described in Section 6.5 and baseline 1–5 (168 m) of antenna configuration H168C.

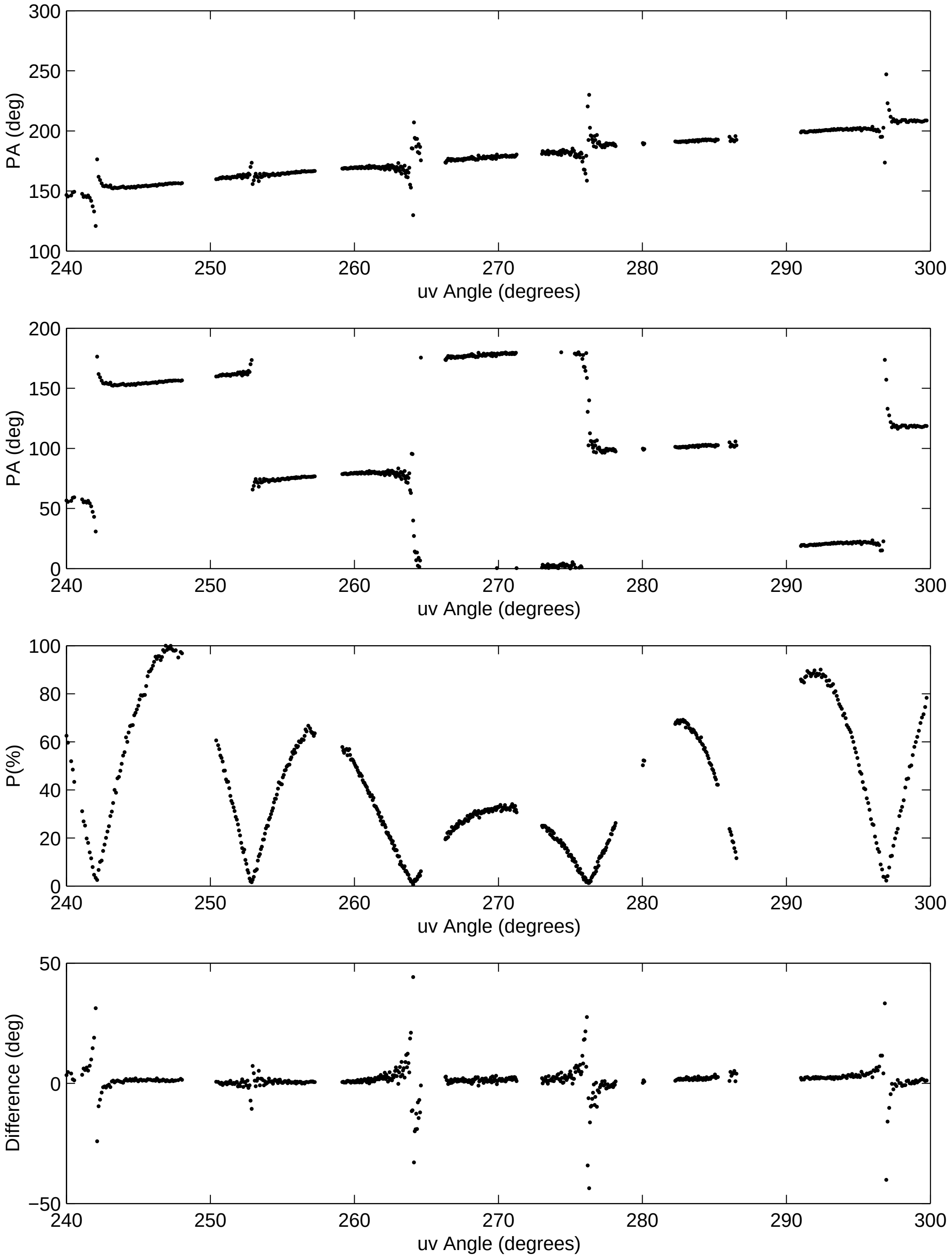

Figure 6.18: This figure shows (*from top*) the position angle measurements corrected for 90° jumps, the uncorrected position angle measurements, polarised intensity and the difference in the relationship between the *uv* angle and position angle. These plots were all generated using data from lunar observations made with the ATCA (see Chapter 5) using baseline 1–5 (168 m) of configuration H168C. Differences between this data and the modeled data (Figure 6.16) can be attributed to minor fluctuations in the actual angular extent of the Moon and also the use of a ring approximation to the polarisation intensity well distribution in the model. In particular this has caused variations to the peaks of the polarisation intensity and also the distribution of nulls against *uv* angle.

further in subsequent sections.

6.10 Conversion to Ionospheric Total Electron Content

Faraday rotation estimates can be converted to estimates of ionospheric TEC which characterise the ionosphere's dispersive effect on radio wave propagation. The Faraday rotation induced in a radio wave is related to the ionospheric TEC via Equation 6.22.

$$\Omega = 2.36 \times 10^4 \nu^{-2} \int_{\mathrm{path}} N(s) B(s) \cos\theta ds, \tag{6.22}$$

where Ω is the rotation angle in radians, f is the signal frequency in Hz, N is the electron density in m^3, B is the geomagnetic field strength in T, θ is the angle between the direction of propagation and the magnetic field vector and ds is a path element in m.

This relation can be used to convert the lunar Faraday rotation estimates to values of ionospheric TEC. To perform this conversion, the ionosphere was modeled as a Single Layer Model (SLM) which assumes that all free electrons are concentrated in an infinitesimally thin shell (78) and removes the need for integration in Equation 6.22. Values for the magnetic field were obtained using the 10^{th} generation International Geomagnetic Reference Field (73). The magnetic field is composed of a north component B_N, an east component B_E and an upward component B_U (oriented radially out from the Earth). These components are summarised in Table 6.1 and are related to the total magnetic field, in the direction of each source, via Equation 6.23.

$$B = B_N \times \cos(Az) + B_E \times \sin(Az) + B_U \times \sin(El), \tag{6.23}$$

where Az is the source azimuth angle and El is the source elevation angle.

B_N	21237 nT
B_E	3988 nT
B_U	38966 nT

Table 6.1: Magnetic field components.

The resulting TEC estimates for both the Moon and the polarised source can be seen in Figure 6.20. The TEC data obtained from the Moon has a fairly symmetric distribution around the Moon's transit at ∼17:30 UT. While the TEC data obtained from the polarised source, which transits earlier in the observations, rises rapidly toward the end of the observations. The rapid rise in TEC values may be caused by

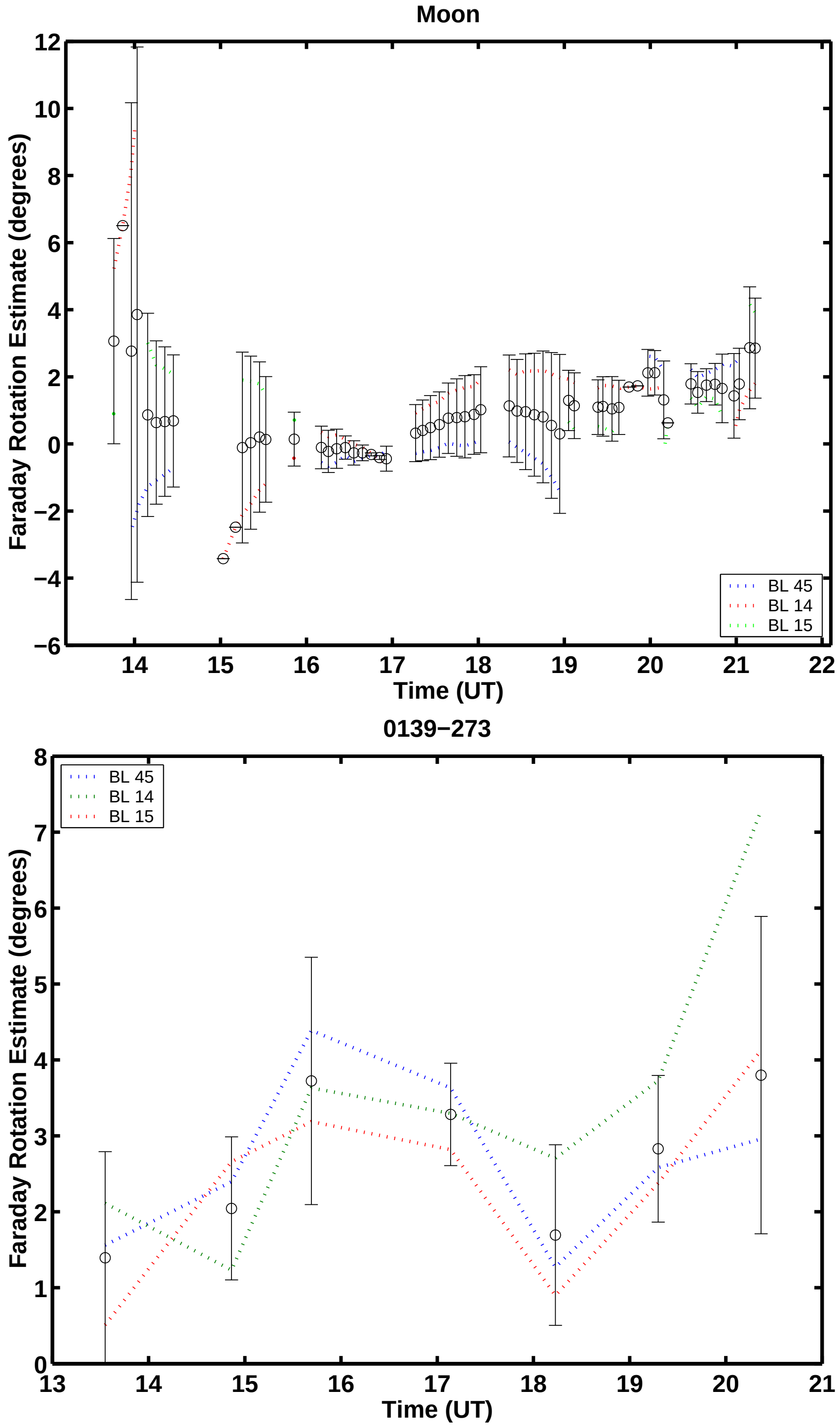

Figure 6.19: Faraday rotation estimates obtained for (*top*) the Moon and (*bottom*) polarised source 0139−273. These plots were generated from ATCA observations (see Chapter 5) using array configuration H168C. The observations cover approximately 14:00–21:00 UT which corresponds to 10pm–8am local time or lunar *uv* angle 300°–240°. The colored lines represent data from each of the shortest east-west baselines and the black points show these baselines averaged together with a one standard deviation error bar.

the low elevation of the polarised source or an increase in TEC caused by sunrise.

6.11 Comparison to GPS Derived Ionospheric TEC Estimates

Ionospheric TEC estimates can be derived from dual-frequency GPS signals. The dual-frequency capability allows comparative delay measurements to be converted to estimates of ionospheric TEC. These estimates are available online from NASA's CDDIS (55) (see Chapter 3). They are published as vertical TEC (VTEC) estimates which must be converted to Slant TEC (STEC), the total electron content through the slant angle line-of-sight to the source, before comparison with the ATCA data.

To perform this conversion, the ionosphere was modeled as an SLM. Slant and vertical TEC can then be related via

$$STEC = F(z)VTEC. \tag{6.24}$$

where $F(z)$ is a slant angle factor defined as

$$\begin{aligned} F(z) &= \frac{1}{\cos z'} && (6.25) \\ &= \frac{1}{\sqrt{1 - \left(\frac{R_e}{R_e + H}\sin(z)\right)^2}}, && (6.26) \end{aligned}$$

R_e is the radius of the Earth, z is the zenith angle to the source and H is the height of the idealised layer above the Earth's surface (see Figure 6.22). The CDDIS (55) also use an SLM ionosphere for GPS interpolation algorithms and assume a mean ionospheric height of 450 km. Therefore 450 km has also been adopted, as the height of the idealised ionospheric shell, for these calculations.

GPS VTEC data was obtained for 19 September 2008, the date of the ATCA lunar polarisation observations. The VTEC data was corrected for slant angle, using a time-varying elevation angle for both the Moon and the polarised source. During the observations the Moon varied slowly in right ascension and declination (from RA 03^h 11^m 19^s, Dec 23^h 58^m 43^s (13:23:15 UT) to RA 03^h 27^m 16^s, Dec 24^h 35^m 52^s (21:06:29 UT)) while the polarised source 0139−263 remained fixed. Therefore different azimuth and elevation angles were required for each source and their respective signals propagated through the ionosphere at different slant angles. The path length through the ionosphere is characterised by the slant angle factor (defined in Equation 6.24) which is normalised to the purely vertical case (90° elevation angle).

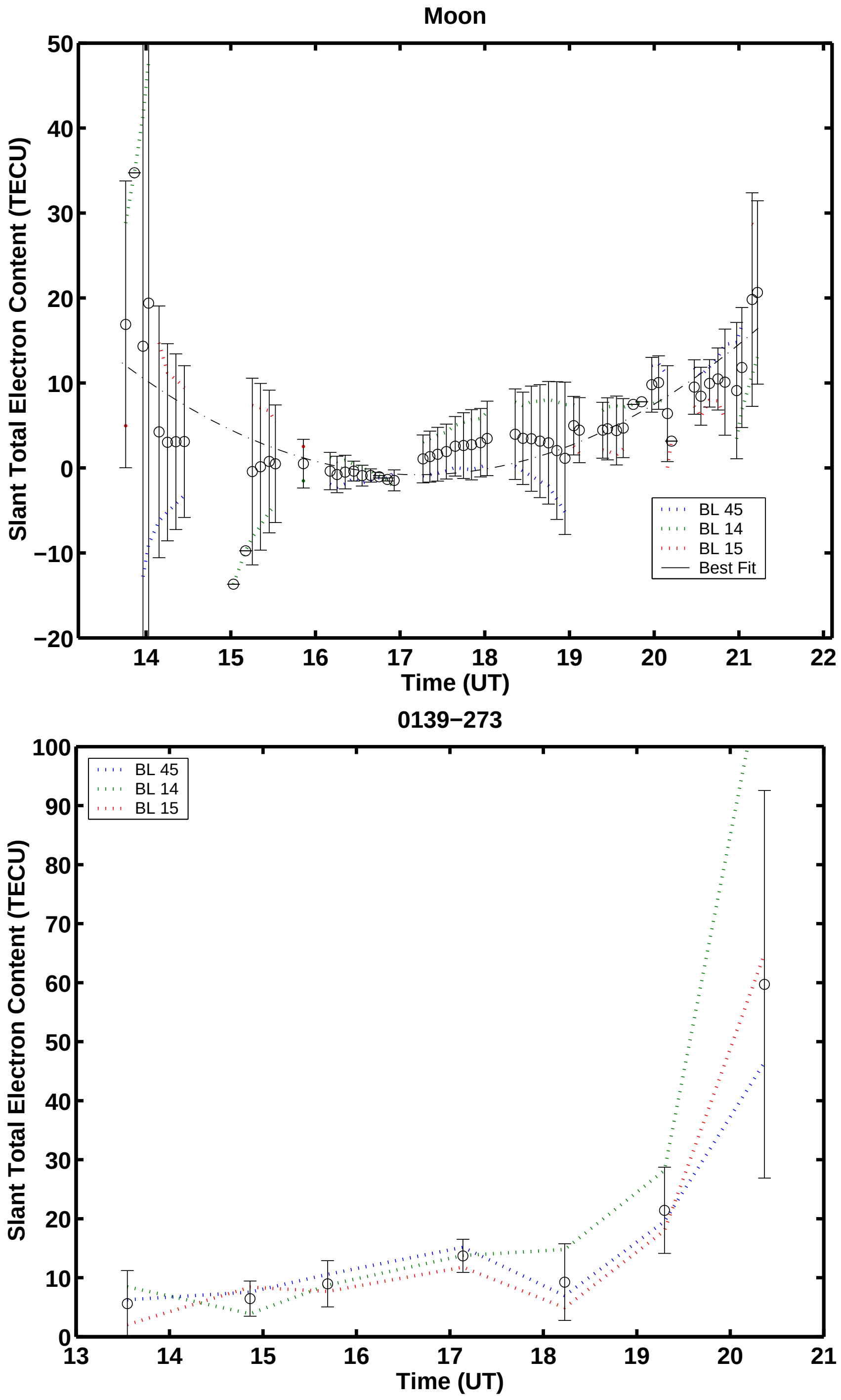

Figure 6.20: Ionospheric STEC estimates obtained from (*top*) the Moon and (*bottom*) polarised source 0139−273. These plots were generated from ATCA observations (see Chapter 5) using array configuration H168C. The observations cover approximately 14:00–21:00 UT which corresponds to 10pm–8am local time or lunar *uv* angle 300°–240°. The colored lines represent data from each of the shortest east-west baselines and the black points show these baselines averaged together with a one standard deviation error bar. For clarity, error bars for each individual baseline are shown in a separate plot (see Figure 6.21).

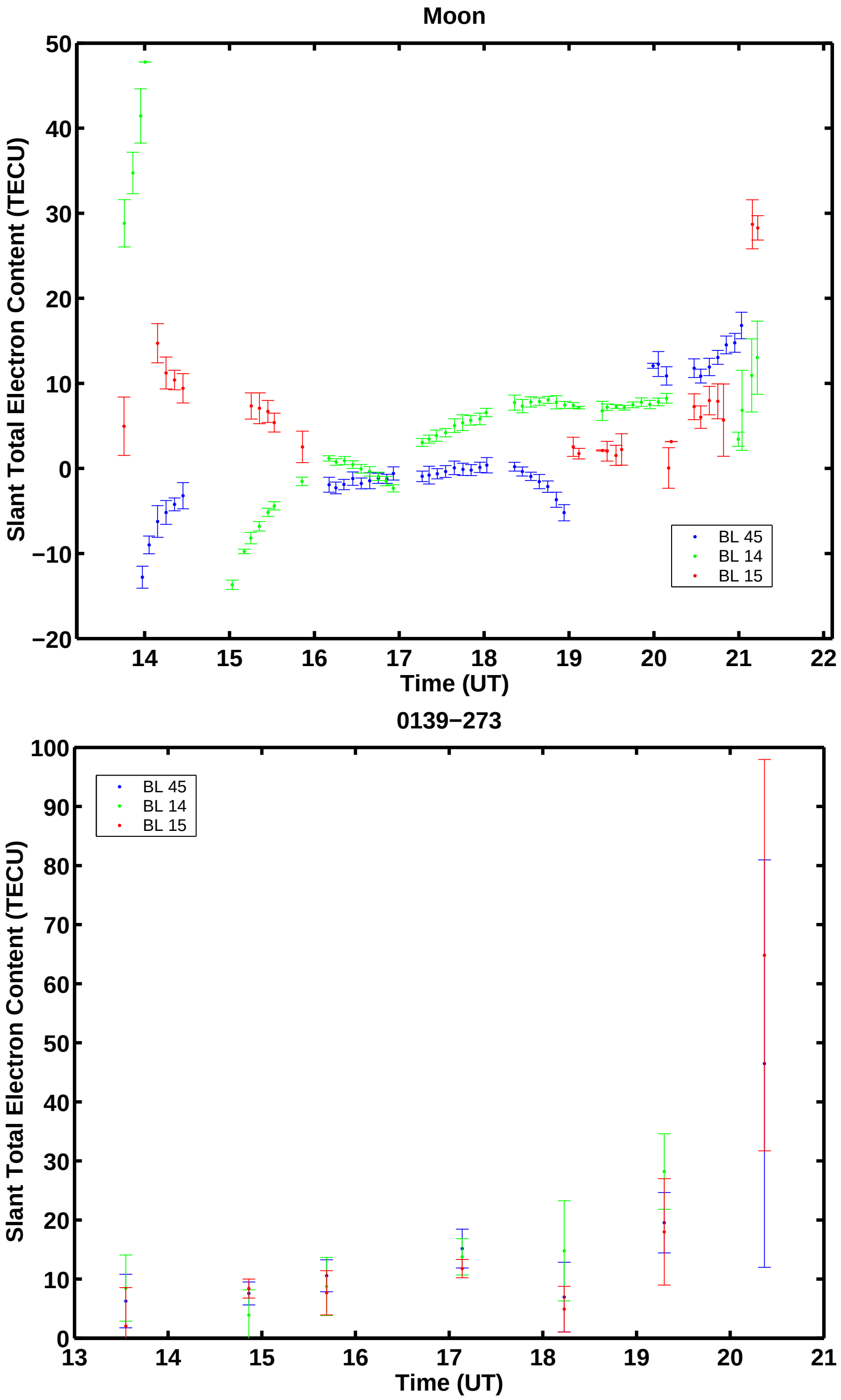

Figure 6.21: Ionospheric STEC estimates obtained from (*top*) the Moon and (*bottom*) polarised source 0139−273. These plots were generated from ATCA observations (see Chapter 5) and using array configuration H168C. The observations cover approximately 14:00–21:00 UT which corresponds to 10pm–8am local time or lunar uv angle 300°–240°. The colored points show one standard deviation errorbars for each baseline.

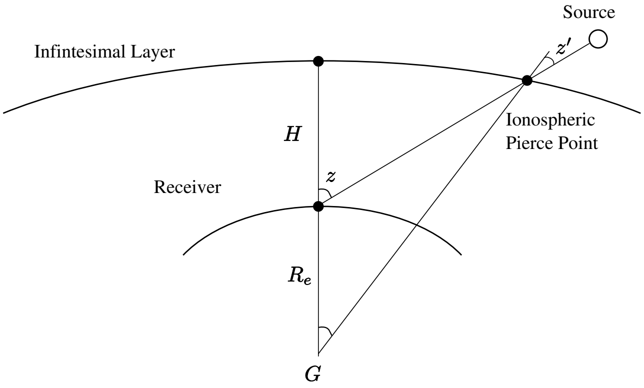

Figure 6.22: Parameters of the Ionospheric Single Layer Model.

High elevation angles correspond to shorter paths through the ionosphere, as signal propagation approaches a purely vertical path at 90°. While at low elevation angles, signals propagate through the ionosphere at an increased slant angle and subsequently experience a greater path length. The polarised source is at a similar declination to the ATCA's latitude and was observed at high elevation angles, particularly around transit, which produced relatively short paths through the ionosphere. The Moon was at more northern declinations and was therefore observed at lower elevation angles which produced longer ionospheric paths (see Figure 6.23).

Slant angle factors were used to convert the GPS VTEC estimates to STEC toward both the Moon and the polarised source for comparison with the ATCA data (see Figure 6.24). For the lunar STEC estimates, both data sets exhibited a similar general trend of symmetry around the Moon's transit. However, the ATCA data often underestimated the GPS data, particularly around 14:30–17:00 UT where the ATCA TEC estimates may have been influenced by bad data from the shorter baselines (see Figure 6.21). For the polarised source both data sets also exhibited a similar trend. However, their amplitude was not consistent particularly towards the end of the observations. Therefore the STEC estimates obtained from the observational data and dual-frequency GPS data exhibited similar features, which can be attributed to ionospheric events. However, more observations are required to investigate this technique further.

The lunar STEC values were also related to a differential delay (Figure 6.25) via

$$\Delta t = 1.34 \times 10^{-7} \times TEC \times (\nu_{\mathrm{lo}}^{-2} - \nu_{\mathrm{hi}}^{-2}), \tag{6.27}$$

where Δt is in seconds, TEC is in electrons per m^2 and the frequency terms are in Hz. Frequency parameters were chosen to illustrate the dispersion associated with

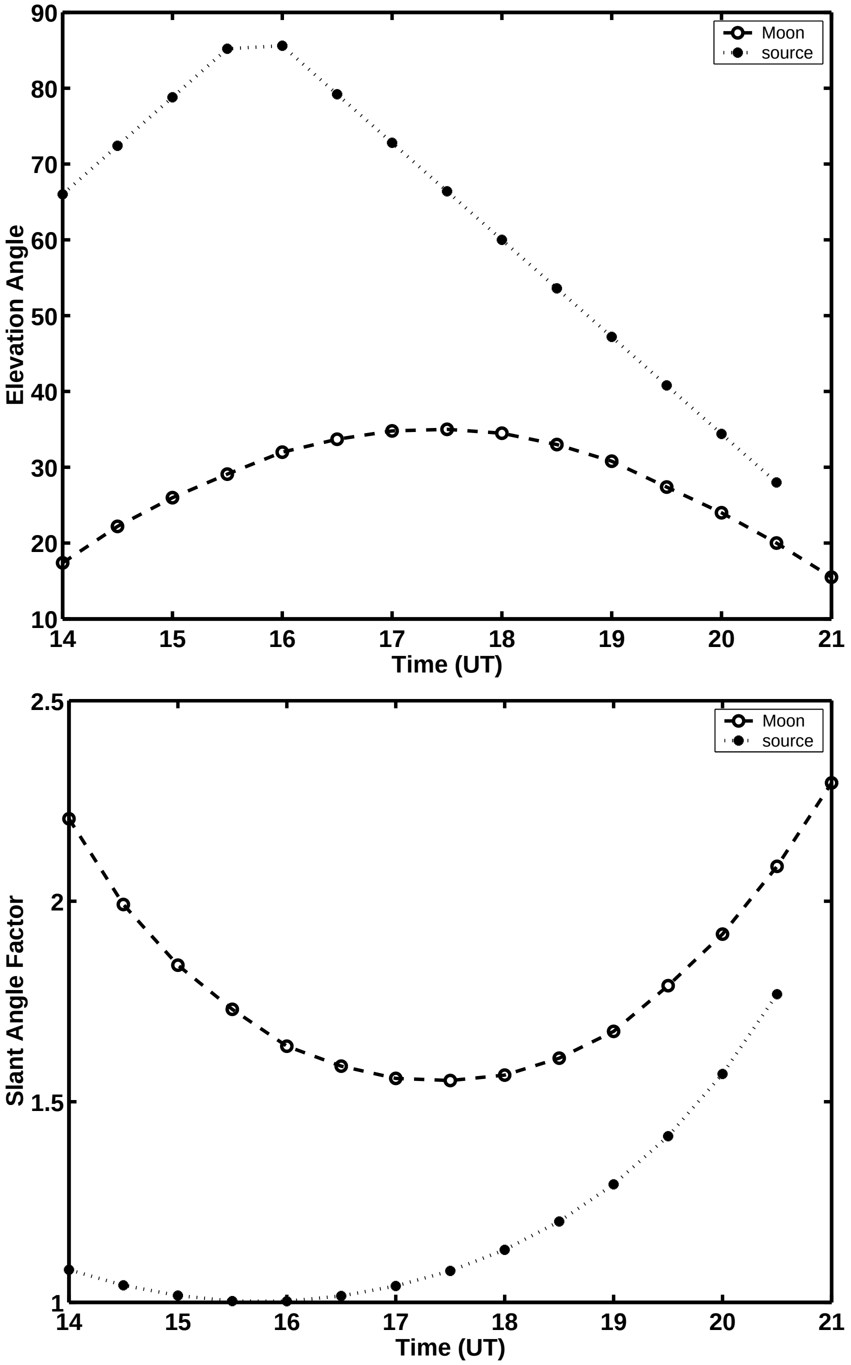

Figure 6.23: (*Top*) Elevation angle from the ATCA to the Moon and the polarised source, 0139−273, during the observations and (*bottom*) the resulting slant angle factors through the ionosphere (with respect to a purely vertical path).

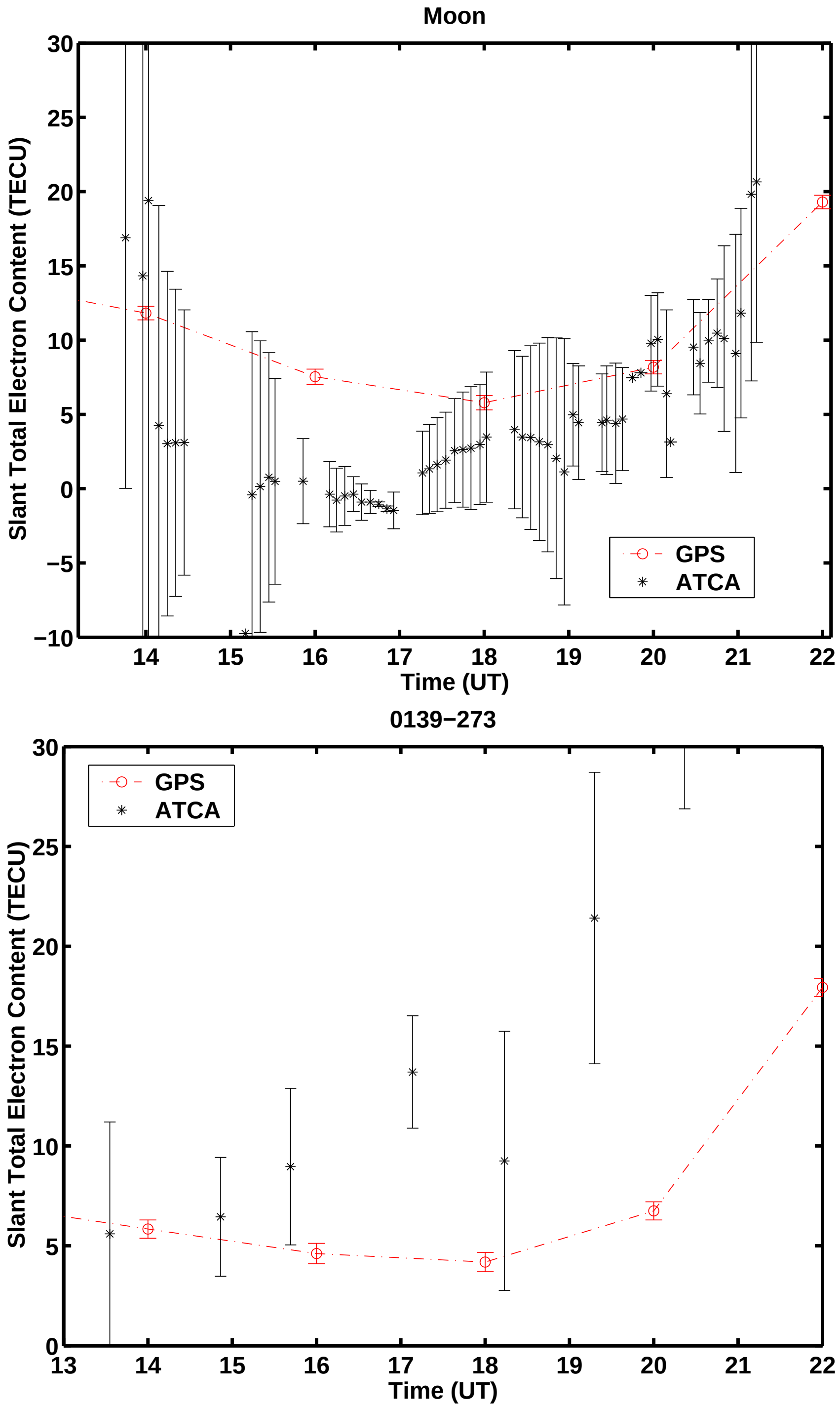

Figure 6.24: A comparison of ionospheric STEC estimates obtained for (*top*) the Moon and (*bottom*) the polarised source 0139−273 using ATCA observations and GPS dual-frequency data (which is only published in 2 hour samples). For the observations, the circles represent averaged data points with one standard deviation error bars. For the GPS data, the circles represent individual data points with a dashed connecting line.

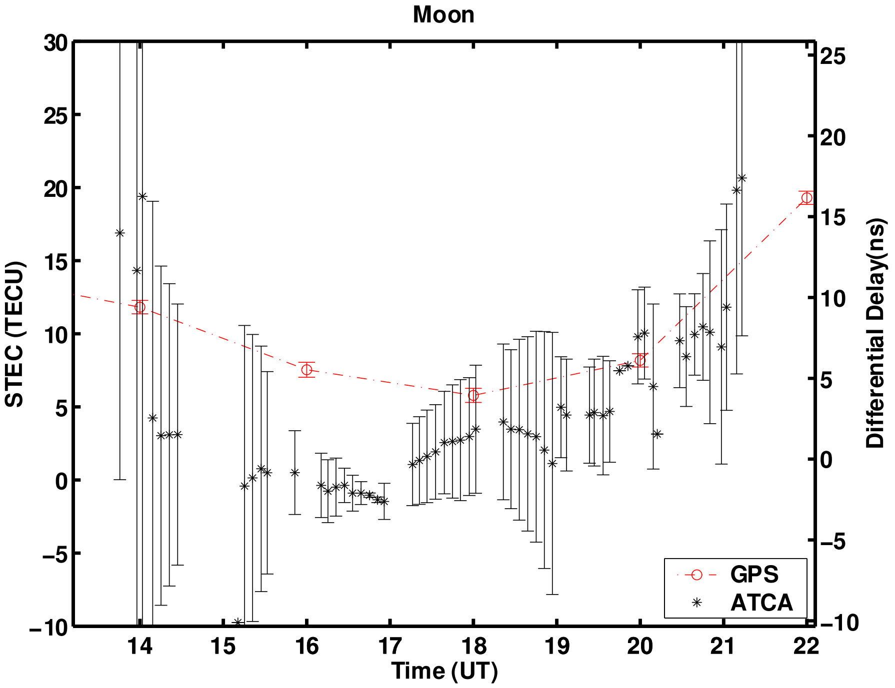

Figure 6.25: Lunar Faraday rotation estimates converted to (*left*) ionospheric TEC values and (*right*) the differential delay across 1.2–1.8 GHz.

the neutrino detection experiment outlined in Chapter 4 *i. e.* 1.2–1.8 GHz.

The effect of the differential delay is to spread out the energy of a pulse over time and reduce its overall amplitude. This occurs because different frequency components are experiencing different time delays. Therefore, if the ionospheric TEC is known, these components can be realigned to recover the maximum pulse amplitude and increase the chances of pulse detection.

6.12 Future Observations

A preliminary investigation of the new ionospheric calibration technique, using polarised emission from the moon, looks promising for UHE neutrino detection. However, more observations are required to further verify and refine this technique. In particular, further investigation is required into discrepancies between the ATCA and GPS lunar STEC estimates. These discrepancies may be caused by inaccuracies in either the ATCA or GPS data.

GPS TEC measurements are originally published as vertical TEC estimates. These values are derived from slant TEC measurements obtained for a network of

GPS satellites and along a line of sight to nearby ground-based receiving stations. Conversion to a global VTEC map requires ionospheric modeling and spatial interpolation techniques. For comparison against the lunar ATCA data, a further slant angle conversion is required to obtain estimates of the STEC along a line of sight to the moon. The approximations assumed during any of these modeling and conversion processes may therefore introduce inaccuracies into the GPS lunar STEC estimates.

Inaccuracies in the ATCA data could be caused by an instrumental error such as polarisation defects or asymmetries in the antenna beam pattern. Such defects would have a large impact on lunar polarisation measurements as the Moon's polarised emission is concentrated around the limb which, at 1.4 GHz, falls around the half-power point of the main beam. These effects could be calibrated by scanning around an object such that it passed through a full revolution of the main beam's half power point. However, the largest discrepancies in the ATCA and GPS data sets occur for the polarised source, 0139−273. The polarised source was observed in the center of the primary beam and therefore large discrepancies in this data set disfavor polarisation defects as the major source of inaccuracies.

Calibration errors in the instrumental polarisation are a more likely candidate for the source of the data discrepancies. For lunar observations, the choice of secondary calibrators is limited by the position of the Moon (which constantly changes in RA and Dec). However, future observations could be scheduled such that the Moon is near a very strong secondary calibrator to improve calibration of the instrumental polarisation. The choice of a different radio telescope array for future observations could also help to identify or eliminate any errors relating to the instrumental polarisation or calibration.

A larger data set would be useful for identifying anomalies in the data. In particular, observations using more baselines would help to identify any data quality issues relating to baseline length and allow a more thorough investigation of the optimal way to threshold and combine data from different baselines. Future observations could also be scheduled such that ionospheric events, such as sunrise or sunset, occur when the moon is at high elevation so that the effects of ionospheric activity can be separated from any changes in slant angle factor and magnetic field which occur for low elevation angles. Observations at lower frequencies, during the day or during solar maximum are also desirable as they will maximise any detectable Faraday rotation. Solar maximum and day-time observations have the added advantage of an increase in TEC which would allow an investigation into how TEC errors scale with absolute value.

6.13 Conclusions

The author has formulated a technique for obtaining measurements of the ionospheric TEC which are both instantaneous and line-of-sight to the lunar Čerenkov detection experiments. The ionospheric TEC can be deduced from Faraday rotation measurements of a polarised source combined with geomagnetic field models, which are more stable than ionospheric models. The author's novel approach is to use this technique with the polarised thermal radio emission from the lunar limb as the polarised source, to obtain instantaneous TEC measurements along a line of sight to the moon. Accurate knowledge of the ionospheric TEC can be used to correct for pulse dispersion and aid in the detection of UHE neutrinos using the lunar Čerenkov technique.

The UHE neutrino detection experiment requires long baselines to keep the levels of lunar correlation between antennas low. This is non-ideal for rotation measure imaging techniques, which require a compact configuration. Therefore Faraday rotation estimation techniques have been developed in the visibility domain. An interferometer baseline may be used as an angular spatial filter to exploit the radial symmetry of a planetary object's position angle distribution and obtain instantaneous position angle measurements directly in the visibility domain. The method of obtaining Faraday rotation estimates exploits the unique relationship between the measured position angle at any time (calculated from the total integrated U and Q) and the uv angle of the observation. Using this method, position angles can be read directly from the visibility data and compared with the expected radial position angles to determine a Faraday rotation estimate which can be combined with geomagnetic field models to determine the associated ionospheric TEC.

These measurements were taken during the reduced ionospheric activity of solar minimum and under night-time conditions. Future experiments will be performed approaching solar maximum and will need to incorporate day-time observing. Under these conditions, the effect of ionospheric dispersion will be greater and subsequently both more important to correct and easier to measure. Further lunar polarimetry observations, particularly at lower frequencies and at times of higher TEC, are required to investigate this technique further. However, preliminary analysis, using both model and observational lunar data, suggests that this is a promising new technique for determining instantaneous lunar STEC estimates for ionospheric calibration.

CHAPTER 7

Conclusions and Further Work

UHE neutrinos may hold the key to one of the most puzzling mysteries in modern astrophysics, understanding the origin of UHECR. This could have a great impact on our understanding of dark matter, gravity and high energy particle interactions. However, direct detection of UHE neutrinos is difficult due to their extremely small interaction cross section and therefore large volume detectors are required. This thesis explored the experimental challenges associated with the lunar Čerenkov detection technique, a method of UHE neutrino detection which uses Earth-based telescopes to look for radio Čerenkov emission from lunar-neutrino interactions.

7.1 UHE Neutrino Detection Issues

Chapter 2 presented a preliminary investigation into the issues of UHE neutrino detection. Alternative planetary detectors were considered and a simple comparison showed that the Moon is currently the best candidate for UHE neutrino detection. However, with advances in space-based instrumentation, such as satellite detectors and planetary probes, alternative planetary detectors may warrant further investigation for future experiments.

The radio Čerenkov emission expected from lunar neutrino interactions was described analytically and used to explore the experimental parameter space for UHE neutrino detection. It was shown that coherent Čerenkov radiation is a broadband emission with a spectrum that rises approximately linearly with frequency until a peak value is reached. The peak frequency is determined by de-coherence and/or attenuation in the regolith, and can vary between a few hundred megahertz and approximately 5 GHz. The dependence of the peak frequency on shower geometry makes the choice of an optimum observation frequency non-trivial. For events viewed just off the Čerenkov cone, the spectral peak falls in the 1–3 GHz range. Observing in this range extends the experimental sensitivity to a range of favorable geometries while still maximising the predicted flux which falls by more than an order of magnitude $\sim 5°$ off the cone.

Broadband lunar Čerenkov emission produces an extremely narrow pulse (subnanosecond duration). These pulses travel through the ionosphere and experience a frequency dependent time delay resulting in pulse dispersion similar to the dispersion experienced by pulsar pulses traveling through the interstellar medium. Therefore lunar Čerenkov pulses received on an Earth based radio telescope will be dispersed by the ionosphere and further broadened by receiver bandlimiting. Both of these effects will result in a loss of pulse amplitude. This is correctable for the case of ionospheric dispersion using dedispersion methods. Broadband technology is needed to achieve the time resolution required for pulse detection and, due to data storage restrictions, signal dedispersion and detection must be performed in real time. Therefore, to maximise the received signal-to-noise ratio and subsequent chance of pulse detection, the ionospheric pulse dispersion must be known in real time.

Chapter 3 investigated predicted values of the ionospheric TEC derived from dual-frequency GPS data. A full derivation of the relationship between the ionospheric TEC and the differential delay imposed across a bandlimited signal was also presented. Under the current solar minimum conditions it was determined that a dedispersion gain of 1.6–1.7 can be expected over a 1.2–1.8 GHz bandwidth. By restricting observations to the relatively stable night-time ionospheric conditions, gain variation of less than 5% can be achieved using a fixed analog dedispersion filter with a 5 ns differential delay.

7.2 Neutrino Detection Experiments at the ATCA

Chapter 4 described a series of UHE neutrino detection experiments performed using the ATCA. These experiments made use of a 600-MHz RF signal which was available from monitor points in each antenna. Obtaining this bandwidth required the development of custom designed detection hardware which could operate with nanosecond timing accuracy. Ionospheric pulse dispersion also had to be corrected in real time to maximise the received signal-to-noise ratio for threshold detection. Both digital and analog solutions were considered for the dedispersion implementation, however, for these experiments, dedispersion was performed in fixed analog filters. An FPGA-based trigger system was used to detect events in real time and transmit event data to the site control room via an ethernet link. The high speed operation and optimised processing power of FPGAs make them an ideal technology to perform the real-time signal processing and pulse detection required for UHE neutrino detection using the lunar Čerenkov technique.

During experiments at the ATCA, the custom pulse detection hardware was used to collect 36.5 hours of lunar observations over three observing runs. Earlier runs were scheduled to target a broad region surrounding the galactic centre, which was chosen as it harbors the closest super massive black hole and potential accelerator of UHECR. Scheduling of the final ATCA experiment in May 2008 was influenced by results published by the Pierre Auger Observatory in late 2007, which showed a statistical correlation between observations of the highest energy CR and the matter distribution in the local universe as represented by nearby AGN (2). The final ATCA experiment was therefore designed to target the giant radio galaxy Centaurus A which is also the nearest AGN. These experiments were successful at increasing exposure in the regions of Centaurus A and Sagittarius A*. However, they did not result in any potential lunar Čerenkov events.

7.3 A New Method for Calibrating Ionospheric TEC

As the solar cycle enters a more active phase, a more significant loss will occur from dispersion and accurate pulse dedispersion will become a more important experimental concern for UHE neutrino detection. A new method to calibrate the dispersive effect of the ionosphere was presented in Chapter 6. This new method is particularly attractive for the lunar Čerenkov technique as it can be used in real time to give values of the ionospheric TEC which are line-of-sight to the Moon.

The distribution of polarised planetary emission was investigated and shown to be radially symmetric. The intrinsic thermal radiation of the Moon appears increasingly polarised toward the limb, when viewed from a distant point such as Earth. The polarised emission is radially aligned. This is due to the changing angle of the lunar surface toward the limb combined with Brewster angle effects.

The author developed a technique to obtain real-time Faraday rotation estimates in the visibility domain, using interferometeric observations. This method exploits the radial symmetry of polarised planetary emission and uses the interferometric response as an angular spatial filter to obtain meaningful position angle measurements in the visibility domain. The expected position angle measurements were shown to have a unique relationship to the *uv* angle of the observation and variations in this relationship could be attributed to Faraday rotation.

Faraday rotation estimates were combined with geomagnetic field models to give continuous estimates of the ionospheric TEC along the line-of-sight to the Moon. The technique of obtaining lunar position angle measurements in the visibility domain was described analytically and the process of obtaining position angle measurements, Faraday rotation estimates and values of ionospheric TEC was demonstrated using both simulated and real lunar data. To demonstrate this technique, approximately 7 hours of lunar data were taken at 1.4 GHz using the polarimetric facility of the ATCA (the calibration of this data and a basic introduction to interferometry were presented in Chapter 5). The TEC values obtained were verified against dual-frequency GPS values and a preliminary analysis, with both modeled and observational lunar data, suggested that this is a promising new technique for obtaining instantaneous lunar STEC estimates.

7.4 Future Work

These experiments provide a framework for UHE neutrino detection experiments with the next generation of radio instruments, such as the SKA, which will have huge increases in collecting area and advances in technology for UHE neutrino detection using the lunar Čerenkov technique.

Investigation into the properties of radio Čerenkov emission and the effect of lunar surface characteristics on pulse propagation is continuing (see Chapter 2 for a sample of the literature on this work) and, as the development of space-based instrumentation continues, this investigation should be extended to include the propagation of radio Čerenkov emission in the surface of other potential planetary detectors. While the analytical description presented in Chapter 2 provides a good preliminary description of this emission, the treatment of surface properties, particularly surface roughness, requires detailed simulations. These effects are difficult to characterise and previous lunar models have produced overly optimistic estimates of the expected Čerenkov pulse strength (7).

Ionospheric analysis performed for the ATCA experiments assumed solar minimum conditions. Future neutrino detection experiments will be performed at future periods including solar maximum and will need to incorporate day-time observing. Under these conditions, the effect of ionospheric dispersion will be greater and subsequently both more important to correct and easier to measure. To further verify the ionospheric calibration technique outlined in Chapter 6 more lunar polarimetry observations, particularly at lower frequencies and at times of higher TEC, are required and the effects of potential instrumental or calibration errors should be investigated further.

The LUNASKA collaboration is involved in continuing UHE neutrino detection experiments. Future improvements to the ATCA experiment include using 5 antennas, performing coherent signal combination in real time to enable coincidence testing and an increase to 2 GHz bandwidth. Real-time coherent signal addition at this bandwidth is difficult to achieve as it requires sub-nanosecond timing accuracy between signal paths. Therefore wide-band data is commonly channelised into smaller frequency bands to perform beamforming, with signal reconstruction occuring post processing. This type of architecture will be implemented for the CABB upgrade and poses a problem for UHE neutrino detection since real-time analysis of the full wide-band signal is required for pulse dedispersion and detection. The CABB upgrade will also include installation of powerful new FPGA based back-end receiver hardware which could be used to implement real-time dedispersion algorithms including the new technique for obtaining real-time measurements of the ionospheric TEC outlined in Chapter 6. However, significant amounts of new hardware would have to be developed to create a new signal path for beamforming before channelisation.

The SKA is a new generation radio telescope array which will be one hundred times more sensitive than the best present day instruments. Current designs proposed for the SKA consist of large numbers ($\sim 10^3$–10^4) of small dishes (10–15 m) to achieve a square kilometre of collecting area in the 0.1–3 GHz range which is critical for UHE neutrino experiments. To gain the advantage of the large number of small dishes offered by the proposed SKA designs, signals will have to be combined coherently and analysed with nanosecond timing accuracy. This may require forming phased array beams in real time using special purpose beamforming hardware. Future work is planned to refine the experimental procedure for UHE neutrino detection using the lunar Čerenkov technique. However, it is expected that the SKA sensitivity will reach the level at which a flux of the cosmogenic UHE neutrinos will be detected (7).

Bibliography

[1] Askaryan, G. A. *Journal of the Physical Society of Japan Supplement* **17**, C257 (1962).

[2] The Pierre Auger Collaboration, Abraham, J., et al. *Science* **318**, 938 (2007).

[3] McFadden, R. A., Bhat, N. D. R., Ekers, R. D., James, C. W., Jones, D., Tingay, S. J., Roberts, P. P., Phillips, C. J., and Protheroe, R. J. In *Proceedings of the 30th International Cosmic Ray Conference,* Caballero, R., D'Olivo, J., Medina-Tanco, G., Nellen, L., Sanchez, F., and Valdes-Galicia, J., editors, (2008).

[4] James, C. W., Ekers, R. D., Philips, C. J., Protheroe, R. J., Roberts, P., Robinson, R. A., Alvarez-Muñiz, J., and Bray, J. D. *ArXiv e-prints* (2009).

[5] Sault, R. J., Teuben, P. J., and Wright, M. C. H. In *Astronomical Data Analysis Software and Systems IV,* Shaw, R. A., Payne, H. E., and Hayes, J. J. E., editors, volume 77 of *Astronomical Society of the Pacific Conference Series*, 433, (1995).

[6] Swordy, S. P. *Space Science Reviews* **99**, 85 (2001).

[7] James, C. W. and Protheroe, R. J. *APh* **30**, 318 (2008).

[8] Alvarez-Muñiz, J. and Zas, E. *Phys. Lett. B* **434**, 396 (1998).

[9] Scholten, O., Bacelar, J., Braun, R., de Bruyn, A. G., Falcke, H., Stappers, B., and Strom, R. G. *APh* **26**, 219 (2006).

[10] Alvarez-Muniz, J. and Zas, E. In *AIP Conf. Proc. 579: Radio Detection of High Energy Particles,* Saltzberg, D. and Gorham, P., editors, 117, (2001).

[11] James, C. W., Ekers, R. D., McFadden, R. A., and et al. In *Proceedings of the 30th International Cosmic Ray Conference,* Caballero, R., D'Olivo, J., Medina-Tanco, G., Nellen, L., Sanchez, F., and Valdes-Galicia, J., editors, (2008).

[12] James, C. W. and Protheroe, R. J. *Nucl. Instrum. & Methods* **604**, 222 (2009).

[13] Ekers, R. D., James, C. W., Protheroe, R. J., and McFadden, R. A. *Nucl. Instrum. & Methods* **604**, S106 (2009).

[14] Roberts, P. In *Workshop on App. of Radio Sci. (WARS)*, (2008).

[15] James, C. W., Ekers, R. D., Alvarez-Muñiz, J., Bray, J. D., McFadden, R. A., Phillips, C. J., Protheroe, R. J., and Roberts, P. *Phys. Rev. D, in press* (2010).

[16] Burke, B. F. and Graham-Smith, F. *An Introduction to Radio Astronomy: Second Edition.* Cambridge University Press, (2002).

[17] Thompson, A. R., Moran, J. M., and Swenson, G. W. *Interferometry and synthesis in radio astronomy.* Malabar, (1991).

[18] Australia Telescope National Facility. `http://www.narrabri.atnf.csiro.au/astronomy/vri.html`.

[19] Australia Telescope National Facility. `http://www.atnf.csiro.au/computing/software/miriad/userguide/userhtml.html`.

[20] Poppi, S., Carretti, E., Cortiglioni, S., Krotikov, V. D., and Vinyajkin, E. N. In *Astrophysical Polarized Backgrounds,* Cecchini, S., Cortiglioni, S., Sault, R., and Sbarra, C., editors, volume 609 of *American Institute of Physics Conference Series*, 187, (2002).

[21] Protheroe, R. J. and Clay, R. W. *PASA* **21**, 1 (2004).

[22] Turner, M. et al. Committee on the Physics of the Universe, Board on Physics and Astronomy, Division on Engineering and Physical Sciences, National Research Council of the National Academies, (2003).

[23] The Pierre Auger Collaboration, Abraham, J., et al. *Phys. Rev. Lett.* **101**(6), 061101 (2008).

[24] Greisen, K. *Phys. Rev. Lett.* **16**, 748 (1966).

[25] Kuzmin, V. A. and Zatsepin, G. T. *Canadian Journal of Physics. Proceedings of the 10th International Conference on Cosmic Rays, Calgary, Alberto, June 19-30, 1967, Vol. 46., p.617* **46**, 617 (1968).

[26] Protheroe, R. J. *APh* **21**, 415 (2004).

[27] Takeda, M., Sakaki, N., Honda, K., Chikawa, M., Fukushima, M., Hayashida, N., Inoue, N., Kadota, K., Kakimoto, F., Kamata, K., Kawaguchi, S., Kawakami, S., Kawasaki, Y., Kawasumi, N., Mahrous, A. M., Mase, K., Mizobuchi, S., Morizane, Y., Nagano, M., Ohoka, H., Osone, S., Sasaki, M., Sasano, M., Shimizu, H. M., Shinozaki, K., Teshima, M., Torii, R., Tsushima, I., Uchihori, Y., Yamamoto, T., Yoshida, S., and Yoshii, H. *APh* **19**, 447 (2003).

[28] Bird, D. J., Corbato, S. C., Dai, H. Y., Elbert, J. W., Green, K. D., Huang, M. A., Kieda, D. B., Ko, S., Larsen, C. G., Loh, E. C., Luo, M. Z., Salamon, M. H., Smith, J. D., Sokolsky, P., Sommers, P., Tang, J. K. K., and Thomas, S. B. *ApJ* **441**, 144 (1995).

[29] Abbasi, R. U., Abu-Zayyad, T., Amman, J. F., Archbold, G. C., Bellido, J. A., Belov, K., Belz, J. W., Bergman, D. R., Cao, Z., Clay, R. W., Cooper, M. D., Dai, H., Dawson, B. R., Everett, A. A., Girard, J. H. V., Gray, R. C., Hanlon, W. F., Hoffman, C. M., Holzscheiter, M. H., Hüntemeyer, P., Jones, B. F., Jui, C. C. H., Kieda, D. B., Kim, K., Kirn, M. A., Loh, E. C., Manago, N., Marek, L. J., Martens, K., Martin, G., Manago, N., Matthews, J. A. J., Matthews, J. N., Meyer, J. R., Moore, S. A., Morrison, P., Moosman, A. N., Mumford, J. R., Munro, M. W., Painter, C. A., Perera, L., Reil, K., Riehle, R., Roberts, M., Sarracino, J. S., Schnetzer, S., Shen, P., Simpson, K. M., Sinnis, G., Smith, J. D., Sokolsky, P., Song, C., Springer, R. W., Stokes, B. T., Thomas, S. B., Thompson, T. N., Thomson, G. B., Tupa, D., Westerhoff, S., Wiencke, L. R., Vanderveen, T. D., Zech, A., and Zhang, X. *APh* **23**, 157–174 (2005).

[30] Connolly, B. M., Benzvi, S. Y., Finley, C. B., O'Neill, A. C., and Westerhoff, S. *Phys. Rev. D* **74**(4), 043001 (2006).

[31] Nam, J. In *Proceedings of the 31st International Cosmic Ray Conference*, (2009).

[32] The Pierre Auger Collaboration, Yamamoto, T., et al. In *Proceedings of the 30th International Cosmic Ray Conference,* Caballero, R., D'Olivo, J., Medina-Tanco, G., Nellen, L., Sanchez, F., and Valdes-Galicia, J., editors, (2008).

[33] Saltzberg, D., Gorham, P., Walz, D., Field, C., Iverson, R., Odian, A., Resch, G., Schoessow, P., and Williams, D. *Phys. Rev. Lett.* **86**, 2802 (2001).

[34] Gorham, P. W., Saltzberg, D., Field, R. C., Guillian, E., Milinčić, R., Miočinović, P., Walz, D., and Williams, D. *Phys. Rev. D* **72**(2), 023002 (2005).

[35] Gorham, P. W., Barwick, S. W., Beatty, J. J., Besson, D. Z., Binns, W. R., Chen, C., Chen, P., Clem, J. M., Connolly, A., Dowkontt, P. F., Duvernois, M. A., Field, R. C., Goldstein, D., Goodhue, A., Hast, C., Hebert, C. L., Hoover, S., Israel, M. H., Kowalski, J., Learned, J. G., Liewer, K. M., Link, J. T., Lusczek, E., Matsuno, S., Mercurio, B., Miki, C., Miočinović, P., Nam, J., Naudet, C. J., Ng, J., Nichol, R., Palladino, K., Reil, K., Romero-Wolf, A., Rosen, M., Ruckman, L., Saltzberg, D., Seckel, D., Varner, G. S., Walz, D., and Wu, F. *Phys. Rev. Lett.* **99**(17), 171101 (2007).

[36] Dagkesamanskii, R. D. and Zheleznykh, I. M. *PAZh* **50**, 233 (1989).

[37] Hankins, T. H., Ekers, R. D., and O'Sullivan, J. D. *MNRAS* **283**, 1027 (1996).

[38] Beresnyak, A. R., Dagkesamanskii, R. D., Zheleznykh, I. M., Kovalenko, A. V., and Oreshko, V. V. *Astronomy Reports* **49**, 127 (2005).

[39] Gorham, P. W., Hebert, C. L., Liewer, K. M., Naudet, C. J., Saltzberg, D., and Williams, D. *Phys. Rev. Lett.* **93**(4), 041101 (2004).

[40] Buitink, S., Bacelar, J., Braun, R., de Bruyn, G., Falcke, H., Scholten, O., Singh, K., Stappers, B., Strom, R., and Yahyaoui, R. a. *ArXiv e-prints* (2008).

[41] Scholten, O., Buitink, S., Bacelar, J., Braun, R., de Bruyn, A. G., Falcke, H., Singh, K., Stappers, B., Strom, R. G., and Yahyaoui, R. a. *ArXiv e-prints* (2008).

[42] The Pierre Auger Collaboration, Roulet, E., et al. *Journal of Physics Conference Series* **136**(2), 022051 (2008).

[43] Barwick, S. W., Beatty, J. J., Besson, D. Z., Binns, W. R., Cai, B., Clem, J. M., Connolly, A., Cowen, D. F., Dowkontt, P. F., Duvernois, M. A., Evenson, P. A., Goldstein, D., Gorham, P. W., Hebert, C. L., Israel, M. H., Learned, J. G., Liewer, K. M., Link, J. T., Matsuno, S., Miočinović, P., Nam, J., Naudet, C. J., Nichol, R., Palladino, K., Rosen, M., Saltzberg, D., Seckel, D., Silvestri, A., Stokes, B. T., Varner, G. S., and Wu, F. *Phys. Rev. Lett.* **96**(17), 171101 (2006).

[44] Taggart, C. and Wines, J. *My Grammar & I... Or Should That Be "me"*. Penguin Group USA, (2009).

[45] Alvarez-Muñiz, J., Marqués, E., Vázquez, R. A., and Zas, E. *Phys. Rev. D* **68**(4), 043001 (2003).

[46] Gorham, P. W. *ArXiv e-prints* (2004).

[47] Kraus, J. D. *Radio astronomy.* Powell, (1986).

[48] Shu, F. *The Physical Universe: an introduction to astronomy.* University Science Books, (1982).

[49] Alvarez-Muñiz, J., Marqués, E., Vázquez, R. A., and Zas, E. *Phys. Rev. D* **74**(2), 023007 (2006).

[50] Zas, E., Halzen, F., and Stanev, T. *Phys. Rev. D* **45**, 362 (1992).

[51] Alvarez-Muñiz, J., Vázquez, R. A., and Zas, E. *Phys. Rev. D* **62**(6), 063001 (2000).

[52] Pedrotti, F. and Pedrotti, L. *Introduction to Optics.* Prentice-Hall, (1987).

[53] Budden, K. *The Propagation of Radio Waves.* Cambridge University Press, (2003).

[54] Klobuchar, J. A. *Progress in Astronautics and Aeronautics* **163**, 485 (1996).

[55] NASA. `http://cddisa.gsfc.nasa.gov/gnss_datasum.html`.

[56] CODE. `http://www.aiub.unibe.ch/ionosphere/`.

[57] Schaer, S. and Gurtner, W. In *Proceedings of the IGS AC Workshop*, (1998).

[58] Chen, F. F. *Introduction to Plasma Physics.* Plenum Press, (1974).

[59] Jackson, J. *Classical Electrodynamics.* John Wiley and Sons, (1975).

[60] Lorimer, D. and Kramer, M. *Handbook of Pulsar Astronomy.* Cambridge University Press, (2005).

[61] Lorimer, D. R. *ArXiv e-prints* (1998).

[62] Wilson, B. and Mannucci, A. *Proceedings of the Institute of Navigation GPS* , 1343 (1993).

[63] Gorham, P., Liewer, K., Naudet, C., Saltzberg, D., and Williams, D. *ArXiv e-prints* (2001).

[64] Hankins, T. H. *ApJ* **169**, 487 (1971).

[65] Hankins, T. H. and Rickett, B. J. In *Methods in Computational Physics. Volume 14 - Radio astronomy*, volume 14, 55, (1975).

[66] Mitra, S. *Digital Signal Procesing.* McGraw Hill, (2001).

[67] Harris, F. *Multirate signal processing for communication systems.* Prentice Hall, (2004).

[68] Crochiere, R. and Rabiner, L. *Multirate digital signal Processing.* Prentice Hall, (1983).

[69] Roberts, P. and Town, G. *IEEE Transactions on Microwave Theory and Techniques* **43**(4 Part 1), 739 (1995).

[70] Australia Telescope National Facility. `http://www.narrabri.atnf.csiro.au/observing/users_guide/html/atug.html`.

[71] James, C. W. *Ultra-High Energy Particle Detection with the Lunar Cherenkov Technique.* PhD thesis, Univ. of Adelaide, Australia., (2009).

[72] Born, M. and Wolf, E. *Principles of Optics.* Cambridge University Press, (1999).

[73] Survey, B. G. `http://www.geomag.bgs.ac.uk/gifs/igrf.html`.

[74] Heiles, C. E. and Drake, F. D. *Icarus* **2**, 281 (1963).

[75] Bracewell, R. N. *The Fourier transform and its applications.* McGraw Hill, (2000).

[76] Rudy, D. J. *Mars: High resolution VLA observations at wavelengths of 2 and 6 CM and derived properties.* PhD thesis, California Inst. of Tech., Pasadena., (1987).

[77] Butler, B. J. and Bastian, T. S. In *Synthesis Imaging in Radio Astronomy II,* Taylor, G., Carilli, C., and Perley, R., editors, volume 180 of *Astronomical Society of the Pacific Conference Series*, 625, (1999).

[78] Todorova, S., Hobiger, T., and Schuh, H. *Advances in Space Research* **42**, 727–736 (2008).

APPENDIX A

MD653CI Digital to Analog Converter Data Sheets

Euvis

MD653*CI* Data Sheet

Email: Sales@euvis.com
Tel: (805) 557-0725 Sales Department
Fax: (805) 557-0752

Document name: MD653CI_DS_Ver00
Release date: 3/02/2006
Related document:
Version: Original: Version O
Revision: Version 00
Note: None

MD653*CI* : *High-Speed 2 GHz Complementary Interpolation MUXDAC*

48:12 Input Multiplexer
12-bit 2-GSPS Complementary Interpolation DAC
Up to 3 GHz Usable Analog Outputs

PRODUCT DESCRIPTION

The **MD653*CI*** is a high-speed 12-bit Digital to Analog Converter (DAC) integrated with a 48:12 (12 channels of 4:1) input multiplexer. The on-chip DAC has Complementary Interpolation output format which makes the signal images in the 2nd and 3rd Nyquist band be useful. Effectively Sine waves up to near 3 GHz (i.e. 3rd Nyquist band with a 2.0-GHz clock rate) can be generated. The differential digital data input interfaces are LVDS compatible. After the 48 pairs of differential data inputs were multiplexed up to 4 times of speed, the 12 high speed data bits are latched and encoded to drive DAC output stage. A clock source with two times the externally supplied clock frequency was generated internally with polyphase splitter and exclusive OR gates. This frequency doubled clock source was used to toggle the DAC current switch inputs between the complementary digital codes to generated complementary interpolated analog output waveforms. To minimize the glitch energy and to achieve high linearity, the DAC is based on a 4-bit segmented with 8-bit R-2R architecture. Complementary outputs are available with 50-Ω output back terminations. Divided-by-4 clock outputs and sampling phase selection (SEL1 and SEL2) are provided to ease the alignment of sampling phase relative to the input data. Divided-by-8 clock outputs are also provided. A RESET function is provided for system applications which need to synchronize the outputs from multiple **MD653*CI***'s.

KEY FEATURES

- 48:12 input multiplexer
- 12-bit resolution DAC with 2-GSPS rate and Complementary Interpolation output format
- Complementary outputs with 50-Ω back terminations
- Both complementary divided-by-4 and divided-by-8 clock outputs are provided for data synchronization
- 3.0 W power consumption
- Variable 400~800 mV_{PP} single-ended output swing
- On-chip 100 ohm termination between each differential input data and RESET pair

BLOCK DIAGRAM

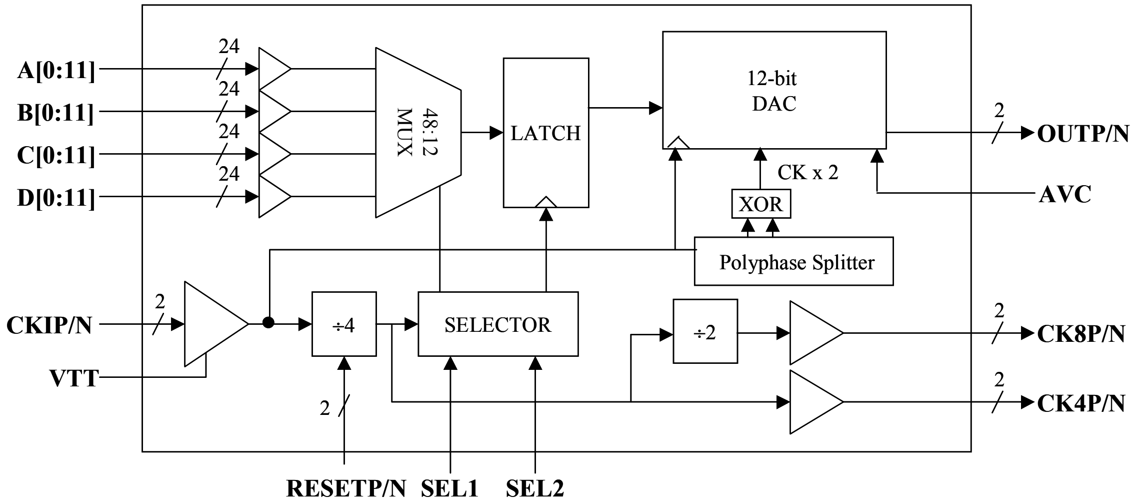

ABSOLUTE MAXIMUM RATINGS

Parameter	Symbol	Typical	Unit
Ambient Temperature	T_A	–40~85	°C
Storage Temperature	T_{STR}	–65~150	°C
Data and Reset Input	V_{DMAX}	–4 ~ 4	V
CKIP, CKIN	V_{CKMAX}	–4 ~ 4	V
Positive Power Supply Voltage	V_{CCP}	+5	V
Negative Power Supply Voltage	$V_{EE}/V_{EEA}/V_{EED}$	-8	V

TYPICAL OPERATION CONDITIONS

Parameter	Symbol	Min	Typ	Max	Unit
Negative Power Supply Voltage	$V_{EE}/V_{EEA}/V_{EED}$	-4.9	-5.2	-5.5	V
Positive Power Supply Voltage	V_{CC}	2.9	3.3	3.7	V
Total Negative Supply Current	$I_{EE}+I_{EEA}+I_{EED}$	570	590	630	mA
Total Positive Supply Current	I_{CC}	55	65	75	mA
Input Data Level	V_{DATA}	400		1000	mV_{PP}
Input Clock Level	V_{CKI}	400		1000	mV_{PP}
Output Clock Level (LVDS)	V_{CKO}	300	400	500	mV_{PP}
Output Swing Control[1]	AVC	0.5		2.5	V
Input Clock Coupling		DC or AC coupled			
Input Data Coupling		DC coupled			
Output Analog Coupling		DC coupled			

[1] AVC pin can be left open as default and the corresponding output swing is 600 mV_{PP}.

ELECTRICAL SPECIFICATIONS

Testing Condition: Power Supplies of –5.2 and 3.3 V, and $R_L = 50\ \Omega$ (for **OUTP/N)**

Parameter	Symbol	Min	Typical	Max	Unit
Operating Temperature	T_o	–40	25	85	°C
Integral Non-linearity Error	*INL*	-2		2	LSB
Full Spectrum SFDR	*SFDR*	40	50 ~ 60		dBc
Full Scale Output Range	V_{FSRS}	400	600	800	mV
Full Scale Current Range	I_{FSRS}	8	12	16	mA
Clock Rate	f_{ck}	0.1	2	TBD	GHz
Clock Input Termination[1]	*VTT*	-0.5		2.0	V
Clock Input Resistance (to VTT)	R_{ck}	45	50	55	Ω
Adjustable Analog Output Range	V_{swing}	400	600	800	mV_{PP}
Output Clock Swing (LVDS)	V_{ck4_swing}	300	400	500	mV_{PP}

---

[1] When clock input is AC coupled, VTT should be grounded. When the clock input is DC coupled, VTT should be terminated with common mode voltage of input clock or left open to provide 100 ohm differential termination for LVDS clock input.

THEORY OF OPERATION

The **MD653D_*CI*** operation can be divided into two parts: the multiplexing unit and the digital-to-analog converter. The multiplexing unit takes the 48 pairs of differential data inputs and 2 DC select pins, **SEL1** and **SEL2**, and a data reset differential pins, **RESET(P/N)**. The select pins are CMOS or TTL compatible. There are four data input groups labeled **A[0:11]**, **B[0:11]**, **C[0:11]**, and **D[0:11]**. The 48 pairs of differential digital data inputs are latched simultaneously into the input registers once every four clock cycles. Internally divided-by-4 clocks are generated and used to control the data sampling of the multiplexing unit. Given a sample once every four cycles, four possible sample phases exist, phase 0, 1, 2, and 3 out of the divided-by-4 circuits. The data-sampling phase is selected with pins **SEL1** and **SEL2**. A pair of differential divided-by-4 output clocks, **CK4P/N** and **CK8P/N** are generated, from the selected data-sampling phase, to aid synchronization of digital data inputs. The **RESET** pin is active low, and when applied will reset the multiplexer timing to phase 0. The selected sample phase will be unaffected. The **RESET** function can be used to synchronize the outputs of multiple **MD653*CI***'s for system applications. After sampling, the latched data are multiplexed to 12-bit high speed data according to the input clock and fed to the following digital-to-analog converter. When in reset mode the latched data is held constant and so is the analog output.

The digital-to-analog converter employs decoding and segmentation techniques to improve linearity and reduce output glitches. It accepts offset binary input format which means all 12-bit with “0” coding has minimal analog outputs and all 12-bit inputs with “1” has maximal analog output. The middle of analog output correspond to coding of “011111111111”. The 12-bit data are respectively segmented and decoded to control 23 current switches to produce the outputs. The current switches are all differential to produce a complementary pair of Complementary Interpolation analog output signals.

Fig.1 shows the difference between Return-to-Zero and Complementary Interpolation outputs in time domain. As shown in Fig.2, the conventional DAC non-return-to-zero (Non-RZ) output format has the sinc(x) (sin(x)/x) frequency response which has notches at the multiples of the clock frequencies. The first notch at the clock frequency makes the images of signals in the 2nd Nyquist band attenuate dramatically to be useful. With the Return-to-Zero DAC output format (**MD653*RZ***) and Complementary Interpolation output format (**MD653*CI***) the notches of the frequency response will happen at multiples of twice the clock rate, assuming the duty cycle of return-to-zero is 50%. The push-out of the notches to higher frequencies makes the signals in the 2nd or even the third Nyquist band available for ultra-wideband and high frequency applications. The images of signals in the 4th Nyquist band will start to attenuate dramatically and couldn’t be used unless the duty-cycle of return-to-zero less than 50% is used, as shown in Fig.2 with an example of 1:3 Return-to-Zero ratio. The drawback of Return-to-Zero output format is the reduction of signal output power because the total power is constant and it is distributed over a much wider bandwidth. Complementary interpolation has output power optimized in the 2nd and 3rd Nyquist band only and suitable for applications need high frequencies between the 2nd and 3rd Nyquist bands. For applications need ultra-wideband including all 1st, 2nd and 3rd Nyquist bands, then **MD653***RZ* should be used.

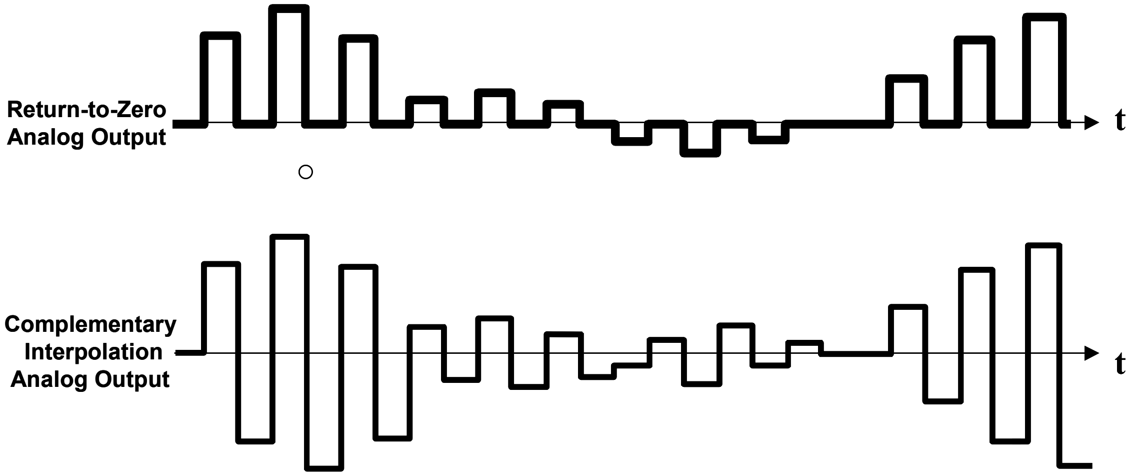

Fig. 1. Comparison of Return-to-Zero (**MD653***RZ*) and Complementary Interpolation (**MD653***CI*) output waveform in time domain.

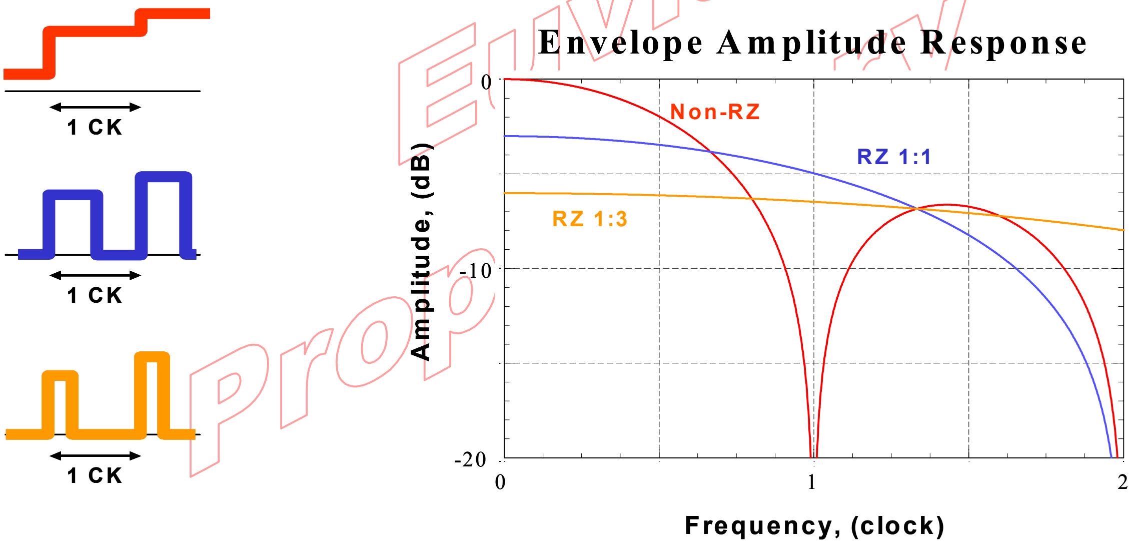

Fig.2. Return-to-Zero DAC output format to extend usable output frequency range to 3rd Nyquist band and beyond.

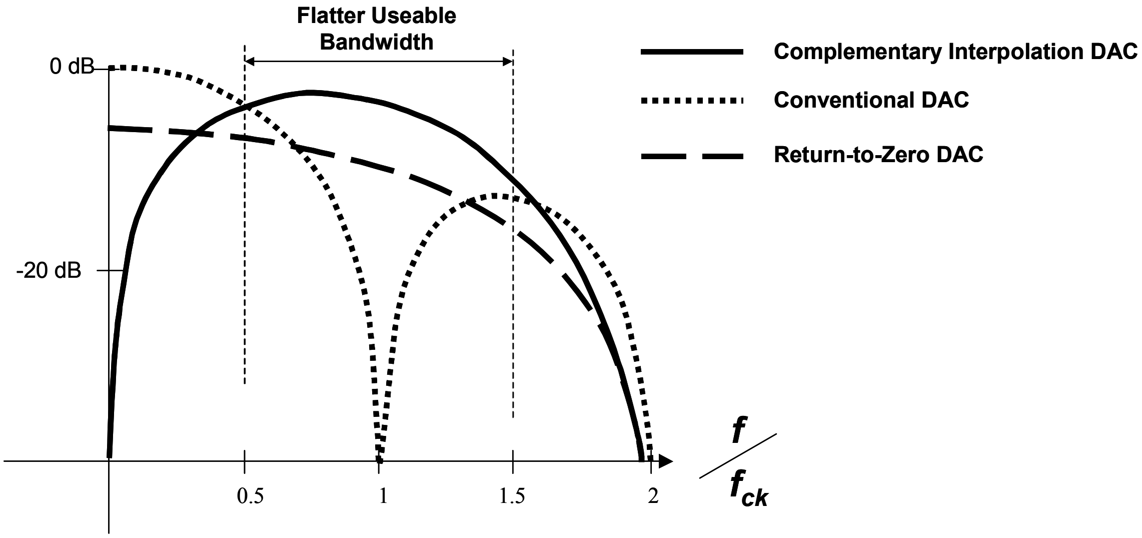

Fig.3. Comparison of spectrum envelop between conventional non-return-to-zero (**MD651D/MD652D**), return-to-zero (**MD653*RZ***) and complementary interpolation (**MD653*CI***) outputs.

To toggle the DAC current switches between complementary digital input codes within one clock cycles, a polyphase splitter and XOR gates were used to generate a clock source which double the frequency of the externally supplied clock source, as shown in the Block Diagram in page.3.

To provide temperature measurement in application a temperature sensing diode is provided in the DAC portion of the chip. **TMPI** is the anode and **TMPO** is the cathode.

The output signals should be connected with 50-Ω terminations to ground. Once terminated each output will produce a typical full-scale voltage range of 600 mV_{PP}. This full-scale output voltage can be adjusted between 400 and 800 mV_{PP} by a control voltage at **AVC**. If **AVC** is left open the output amplitude will be 600 mV_{PP}.

OPERATION TIMING

The 48 pairs of differential digital data inputs are sampled and latched every four input clock cycles. The sampling instance is user selectable to be aligned to input data. The latched data are multiplexed to 12-bit data according to the clock. The 12-bit data are then converted to analog signals with a delay of one clock latency.

The following timing diagram shows the relative operation timing of data latching and multiplexing from parallel input data to serial data available to DAC section. The divided-by-4 clocks are generated by dividing the input main clock and sent out directly to output clock **CK4P/N.** The divided-by-8 output clock **CK8P/N** are generated by dividing divide-by-4 output clock. **SEL1** and **SEL2** are used to select one of the possible 4 different phases of divide-by-4 clocks as the best internal sampling clock phase relative to input data. The divided-by-4 output clock phase **CK4P/N** and divided-by-8 output clock phase **CK8P/N** are continuous and independent of **SEL1** and **SEL2** selection. The 4 pairs of 12-bit differential data inputs, **A[0:11]**, **B[0:11]**, **C[0:11]**, and **D[0:11]**, are sampled and latched into the internal registers on the positive transition of internal divide-by-4 sampling clock. The internal registers are multiplexed to 12-bit data that are converted to analog outputs **OUTP** and **OUTN** after a clock cycle.

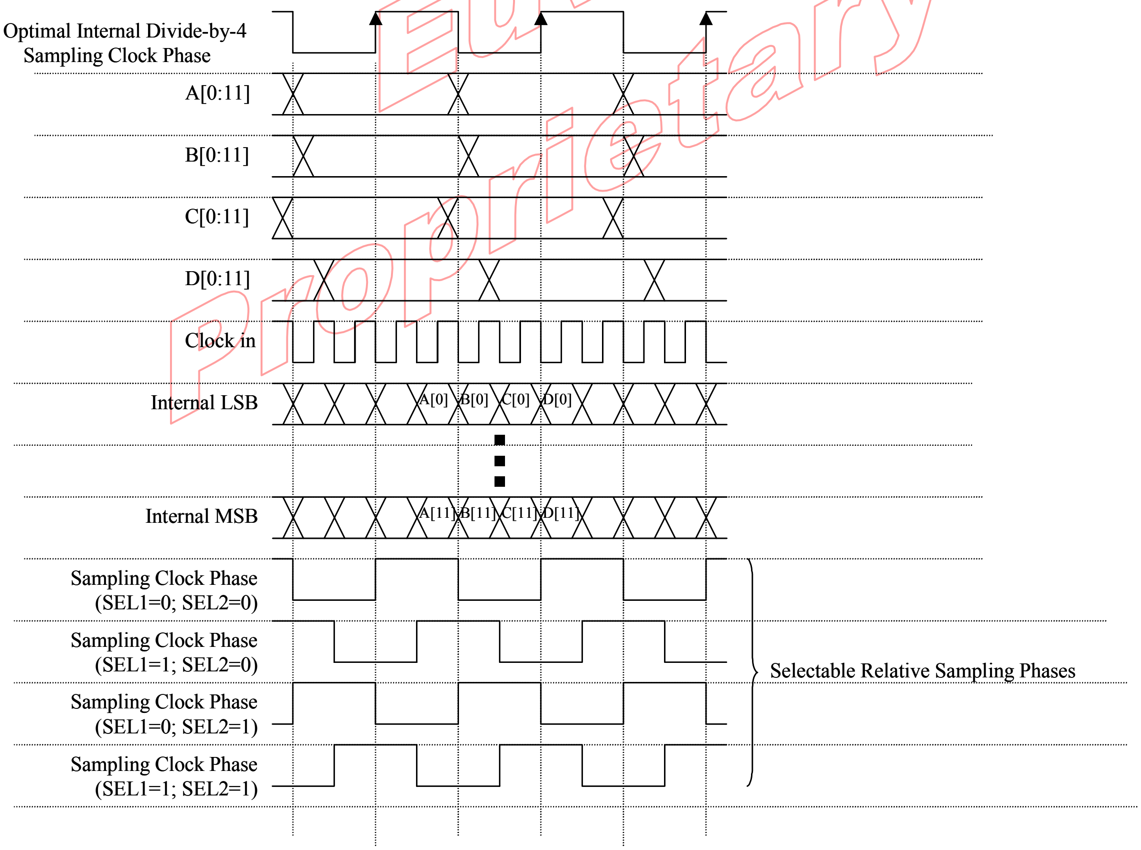

DIGITAL TIMING SELECTION AND RESET OPERATION

The multiplexer operation provides for the sampling clock phase to be manually selected. Relative to the full rate input clock the data sampling clock is 1/4th the rate and can be digitally set to one of four phase: 0, 90, 180, 270 degrees. The actual data sampling clock edge is determined by a combination of the full rate clock edge and the multiplexing flip-flop input selection line. Two selection pins **SEL1** and **SEL2**, are provided to the user to determine which phase for the data sampling will be used. When the full rate clock is divided by 4, a quadrature divided-by-4 clock is also generated. Using OR gates four pulse signals are generated by the dived-by-4 clocks. Each signal is high for a different quarter of the signal cycle. The phase selection bits control a multiplexer that chooses one of the pulse signals as the multiplexer input selection line. As shown in the BLOCK DIAGRAM in page 1, the divided-by-4 and divided-by-8 output clocks bypass the **SEL1** and **SEL2** functions. Their output phase are continuous, not affected by **SEL1** and **SEL2** selections.

Synchronization is provided by means of a RESET function. The reset function stops all input latching, holding the DAC output constant, and sets all sampling clocks and output divide-by-4 and divide-by-8 clocks low. The reset function is applied by setting the **RESETP** pin lower than the **RESETN** pin. Application of the RESET function makes the output low for the divide-by-4 flip-flops which guarantee multiple chips starting from the same internal states once the RESET is released. Upon return to free running the chip will be in phase 0 degrees. This function allows for synchronization of multiple chips by ensuring each will be in the same digital phase state.

PIN DESCRIPTION

Name	Function	I/O/A	Signal
VCC	Ground, General		DC
VCCA	Ground, DAC Analog		DC
VCCD	Ground, DAC Digital		DC
VEE	Negative Power Supply, General (-5.2V)		DC
VEEA	Negative Power Supply, Analog (-5.2V)		DC
VEED	Negative Power Supply, Digital (-5.2V)		DC
VCCP	Positive Power Supply (+3.3V)		DC
A[0:11]	Differential Data Input (A11P/N MSB)	I	RF
B[0:11]	Differential Data Input (B11P/N MSB)	I	RF
C[0:11]	Differential Data Input (C11P/N MSB)	I	RF
D[0:11]	Differential Data Input (D11P/N MSB)	I	RF
TMPI	Temperature Diode Anode	I	DC
TMPO	Temperature Diode Cathode	I	DC
SEL1, SEL2	Sample Phase Select	I	DC
RESET	Differential Reset Input	I	RF
AVC	Analog Output Control	A	DC
CKIP/N	Differential Clock Input	I	RF
CK4P/N	Differential Divide-by-4 Clock Output	O	RF
CK8P/N	Differential Divide-by-8 Clock Output	O	RF
OUTP/N	Differential Analog Output	O	RF

MD653*CI* Drawing

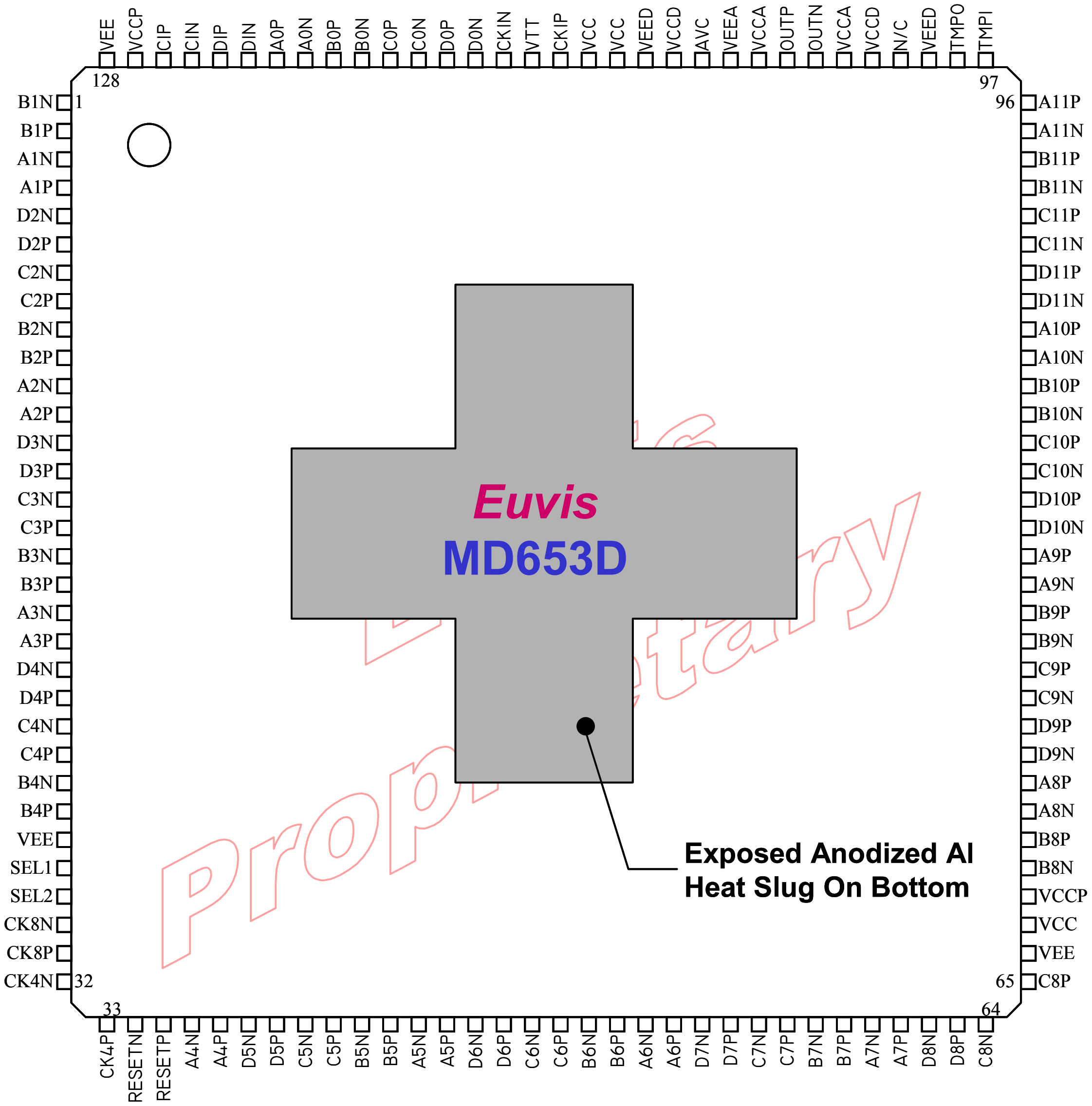

Top view (not to scale)

Note: The device name was marked as MD653D

DATA INPUT

A simplified schematic of differential data input and differential RESET input circuit is shown below. It accepts LVPECL, LVDS, and CML-compatible differential data. The 100 ohm termination resistor between each differential input pair is implemented on chip.

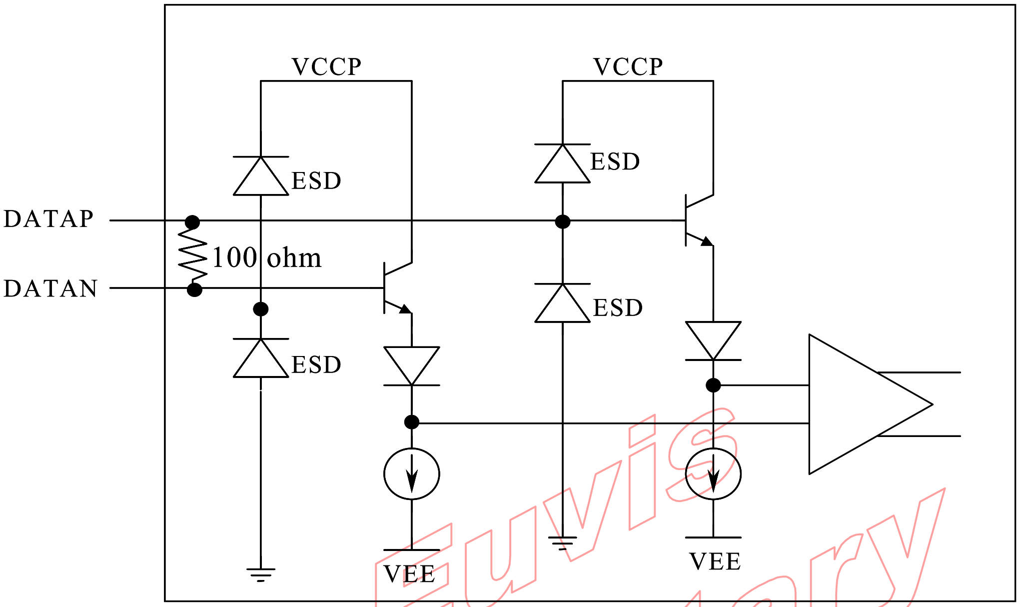

CLOCK INPUT

A simplified schematic of clock input circuit is shown below. It has input impedance of 50Ω terminated to VTT- which can be used to set clock input DC level. VTT should be grounded when clock signals are AC coupled.

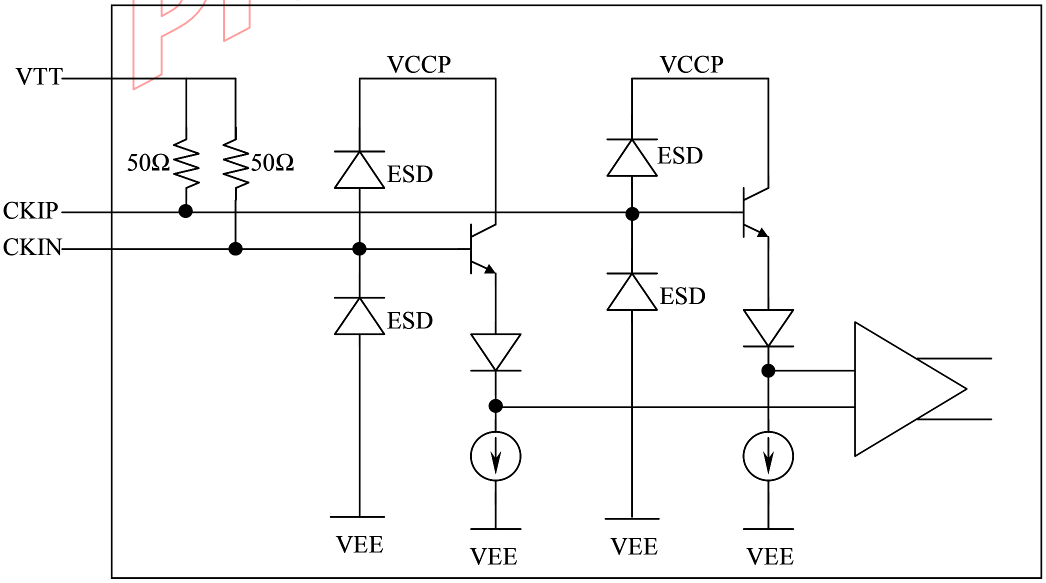

Temperature Sensing Diode

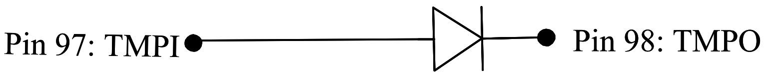

TYPICAL CIRCUIT CONNECTION

A recommended circuit connection is shown below.

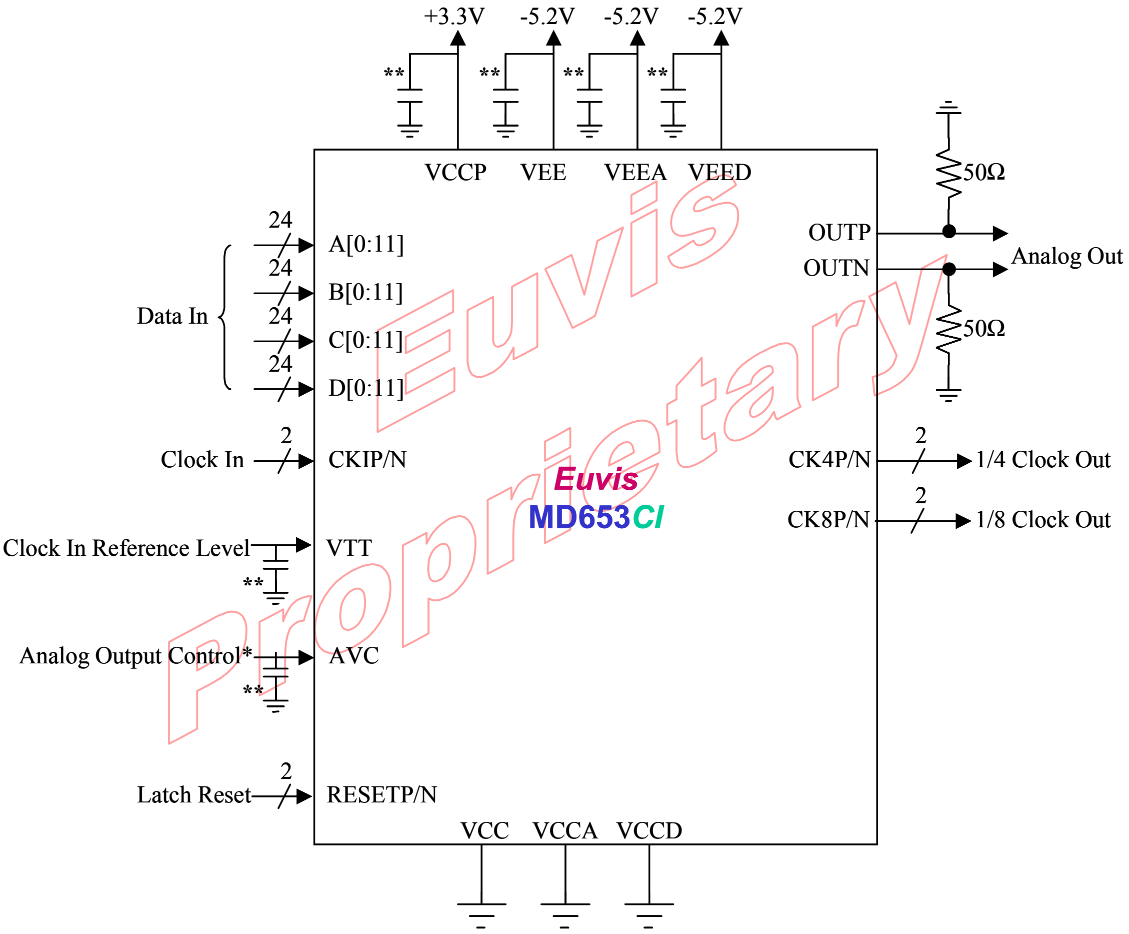

*AVC should be left floating if conditions are met.
** Very good bypasses are required for VCCP, VEEA, VEED, VEE, VTT and AVC pins. The bypass capacitors should be placed as close as possible to the pins of the package on the PCB.

PACKAGE DIMENSIONS

Package type: LQFP, 14 mm x 14 mm, Exposed Anodized Al Heat Slug
Pin count: 128

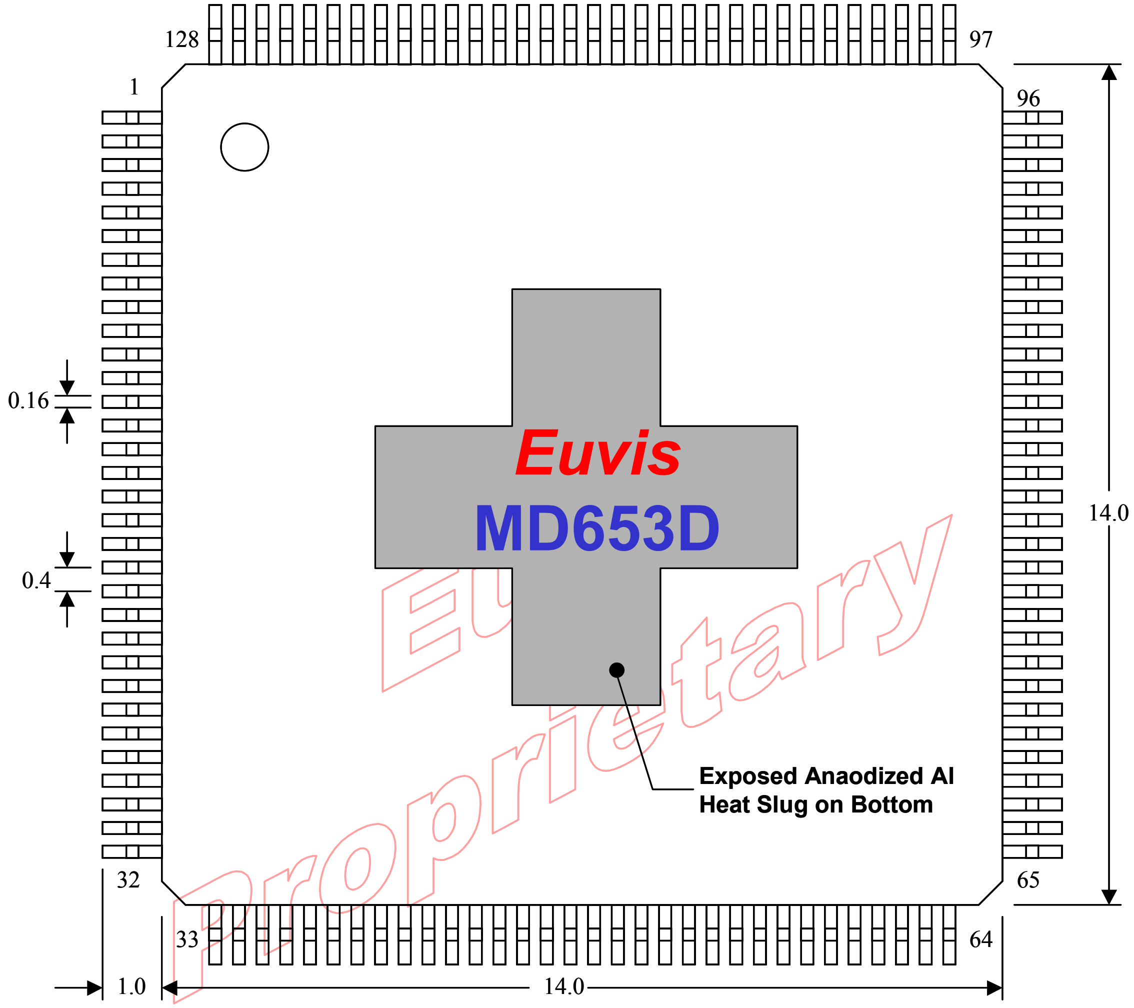

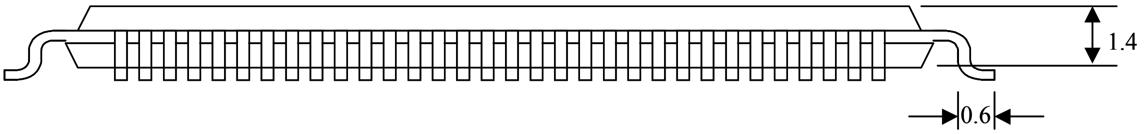

Unit: mm

Note: The bottom of the package is exposed anaodized heat slug which is not solderable. Heat should be removed through the printed circuit board (PCB) by copper pad with through-vias to the ground plan. The solder mask underneath the heat slug need to be open. In operation, it is recommended to apply a heat sink on the bottom or both top and bottom of the package with good air circulation.

MEASUREMENT RESULTS

RF Spectrum

The RF performance was characterized by four **AC701**s functioning in parallel. **AC701** is a high-speed digital waveform generator which can generate sine waveforms or saw-tooth waveforms up to 2.0 Gsps. The initial phase of the generated waveform can be preset to zero degree or can be preset to all possible phase values. With the initial phase of the four **AC701**s preset at interleaved values, these four **AC701**s clocked at ¼ of the master clock rate will generate four pairs of sampled sine-waveform with interleaved phase values resulted in interleaved magnitudes. These four pairs of data were then multiplexed by **MD653*CI*** to interpolate these four pairs of data in time domain resulted in four times of the data rate and then synthesized by the DAC to form the sine-wave at the DAC outputs for SFDR measurements.

The following figures show typical SFDR versus signal frequency at clock rates of 1.0 GHz, 1.6 GHz and 2.0 GHz respectively. The SFDR was derived based on the difference of the single-ended signal output and the highest (or the 2nd highest) spur within each 1st, 2nd and 3rd Nyquist band without filtering. The highest spurs (data in red) are 2nd harmonics related spurs for each output frequency. These 2nd harmonic related highest spurs can be reduced by converting the differential outputs into the single-ended output with a broadband balun.

Spectrum Sweep

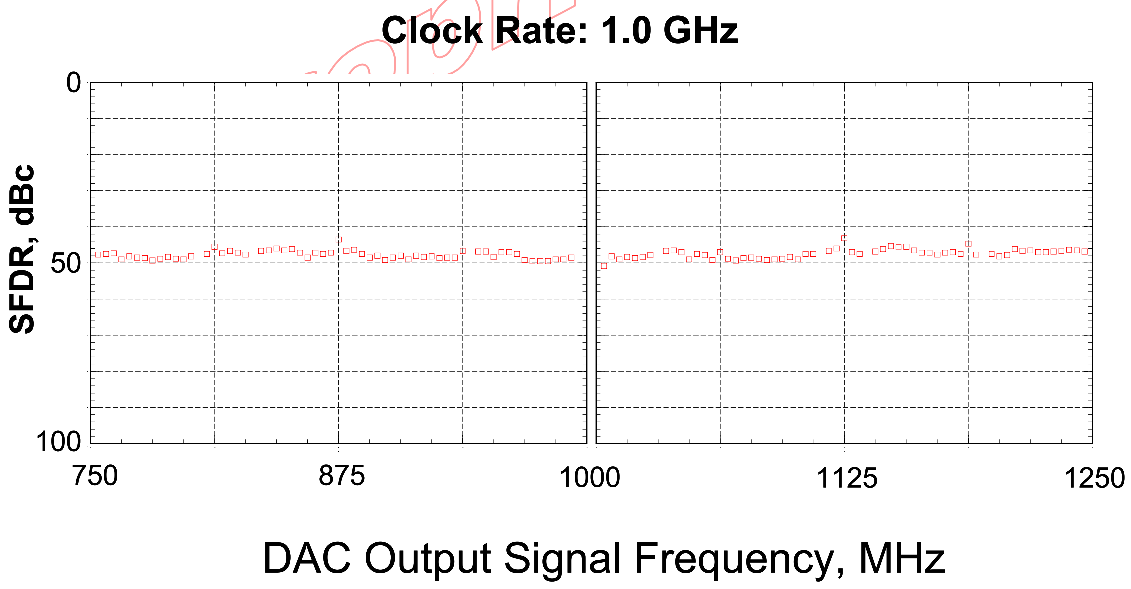

Spectrum Sweep

Clock Rate: 1.5 GHz

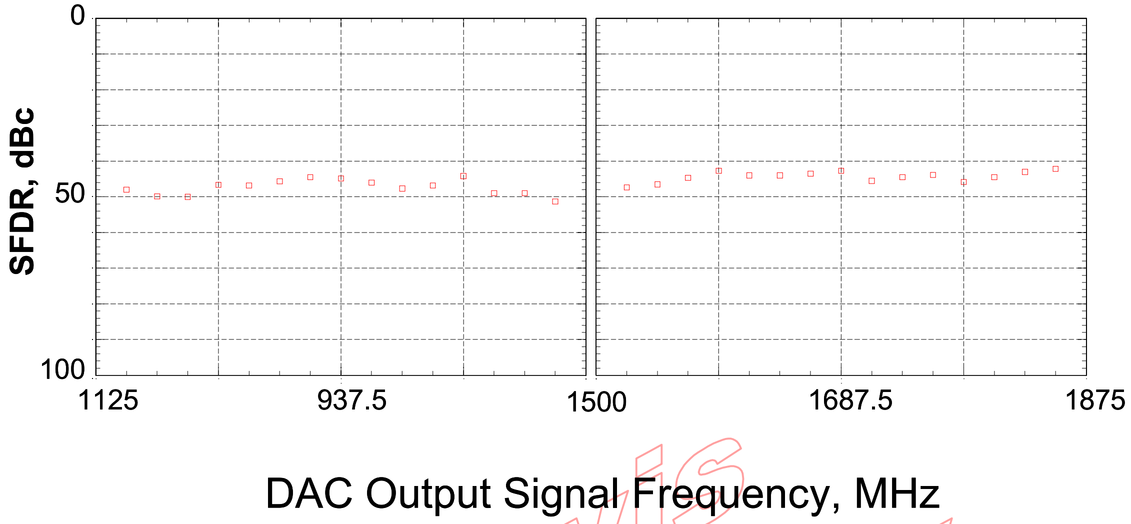

Spectrum Sweep

Clock Rate: 2.0 GHz

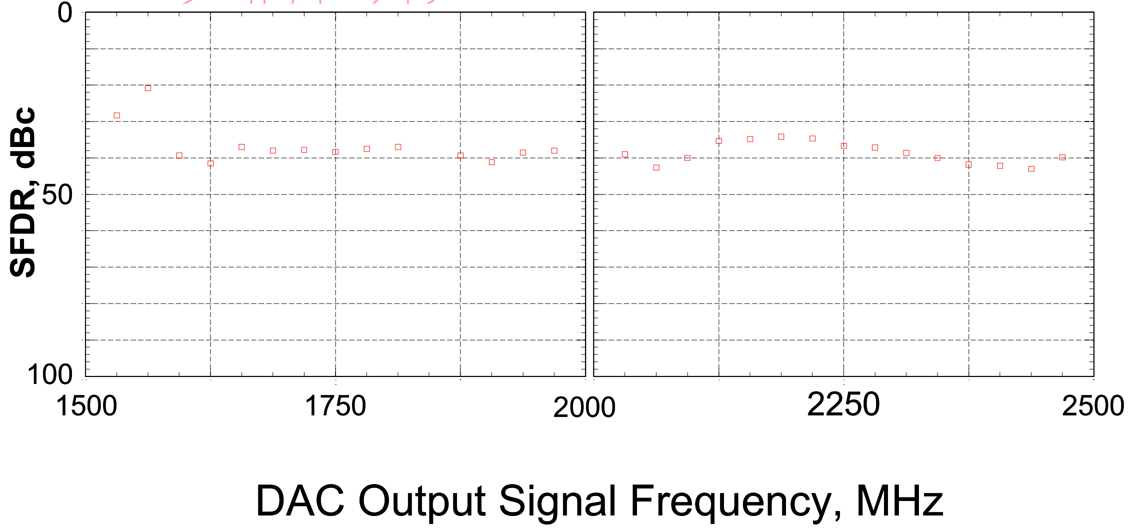

Euvis

Ordering Information:

Email to: Sales@euvis.com
Or call: (805) 552-0725 Sales Department
Or fax: (805) 552-0752

The information contained in this document is based on preliminary product test results. Characteristic data and other specifications are subject to change without notice. Customers are advised to confirm information in this advanced datasheet prior to using this information or placing the order.

Euvis Inc. does not assume any liability arising from the application or use of any product or circuit described herein, neither does it convey any license under its patents or any other rights.

Author/s:
McFadden, Rebecca Angela

Title:
UHE neutrino detection using the lunar erenkov technique

Date:
2009

Citation:
McFadden, R. A. (2009). UHE neutrino detection using the lunar erenkov technique. PhD thesis, School of Physics, The University of Melbourne.

Publication Status:
Unpublished

Persistent Link:
http://hdl.handle.net/11343/39808

File Description:
UHE neutrino detection using the lunar Cherenkov technique